Electromechanical Modeling of Piezoelectric Energy Harvesters

Alper Erturk

Dissertation submitted to the faculty of the
Virginia Polytechnic Institute and State University
in partial fulfillment of the requirements for the degree of

Doctor of Philosophy
in
Engineering Mechanics

Daniel J. Inman, Chair
Scott L. Hendricks
Michael W. Hyer
Ishwar K. Puri
Liviu Librescu (deceased)

November 20, 2009
Blacksburg, VA

Keywords: Piezoelectricity, vibration energy harvesting, structural dynamics, electromechanical modeling

Electromechanical Modeling of Piezoelectric Energy Harvesters

Alper Erturk

Abstract

Vibration-based energy harvesting has been investigated by several researchers over the last decade. The ultimate goal in this research field is to power small electronic components (such as wireless sensors) by using the vibration energy available in their environment. Among the basic transduction mechanisms that can be used for vibration-to-electricity conversion, piezoelectric transduction has received the most attention in the literature. Piezoelectric materials are preferred in energy harvesting due to their large power densities and ease of application. Typically, piezoelectric energy harvesters are cantilevered structures with piezoceramic layers that generate alternating voltage output due to base excitation. This work presents distributed-parameter electromechanical models that can accurately predict the coupled dynamics of piezoelectric energy harvesters. First the issues in the existing models are addressed and the lumped-parameter electromechanical formulation is corrected by introducing a dimensionless correction factor derived from the electromechanically uncoupled distributed-parameter solution. Then the electromechanically coupled closed-form analytical solution is obtained based on the thin-beam theory since piezoelectric energy harvesters are typically thin structures. The multi-mode electromechanical frequency response expressions obtained from the analytical solution are reduced to single-mode expressions for modal vibrations. The analytical solutions for the electromechanically coupled voltage response and vibration response are validated experimentally for various cases. The single-mode analytical equations are then used for deriving closed-form relations for parameter identification and optimization. Asymptotic analyses of the electromechanical frequency response functions are given along with expressions for the short-circuit and the open-circuit resonance frequencies. A simple experimental technique is presented to identify the optimum load resistance using only a single resistor and an open-circuit voltage measurement. A case study is given to compare the power generation performances of

commonly used monolithic piezoceramics and novel single crystals with a focus on the effects of plane-stress material constants and mechanical damping. The effects of strain nodes and electrode configuration on piezoelectric energy harvesting are discussed theoretically and demonstrated experimentally. An approximate electromechanical solution using the assumed-modes method is presented and it can be used for modeling of asymmetric and moderately thick energy harvester configurations. Finally, a piezo-magneto-elastic energy harvester is introduced as a non-conventional broadband energy harvester.

Acknowledgements

First and foremost, I would like to extend my deepest gratitude to Prof. Daniel J. Inman for he has been more than an academic advisor over the last three years. Prof. Inman has been a great advisor who was always available to discuss and support the technical problems came to my mind. He *did* make me feel like his colleague, more than a graduate student, throughout my entire PhD study. He provides a very pleasant research environment in the lab and he really knows how to communicate with his students. He has been a great mentor who was available to discuss and advise on non-technical problems of life as well. Prof. Inman has given me the opportunity to work on several research problems other than the subject of this dissertation and he has offered the freedom to start developing my own academic style. He has given me the opportunity to co-teach classes with him, to attend conferences several times and to take responsibilities in the research community. I cannot think of a more fruitful and joyful post-masters research than my last three years under the guidance of Prof. Inman at the Center for Intelligent Material Systems and Structures (CIMSS).

Ms. Beth Howell, the program manager at CIMSS, has been very helpful since the first day I started working at CIMSS. The friendly office environment and numerous beautiful aspects of CIMSS have a lot to do with her presence and energy. She keeps so many things running simultaneously with an amazing performance. I am indebted to Beth for several things she has helped with.

The experience I have gained as a graduate student in the Department of Engineering Science and Mechanics (ESM) is invaluable. I know that I am only at the beginning of my academic career but my appreciation of *Engineering Mechanics* as a part of my life has been enhanced dramatically after attending several classes by the pioneers of this field, such as Prof. Liviu Librescu, Prof. Michael W. Hyer, Prof. Dean T. Mook, Prof. Raymond H. Plaut and Prof. Ali H. Nayfeh, among others. I have been very proud of being an ESM student during my entire graduate study.

I would like to thank Prof. Scott L. Hendricks, Prof. Michael W. Hyer, and Prof. Ishwar K. Puri for serving on my PhD committee.

I would like to extend my appreciation to my Department, particularly the Graduate Committee, once again, for honoring me with the “Liviu Librescu Memorial Scholarship.”

Words are not enough to express the value of being the first recipient of a scholarship named in memory of the late member of my PhD committee and my teacher, Prof. Librescu. I will have to work very hard to honor Prof. Librescu's memory…

I truly enjoyed sharing the same office and the lab with several colleagues and friends at CIMSS over the last three years and I have had research collaborations with some of them (on topics not discussed in this dissertation). I owe thanks to Dr. Pablo Tarazaga (presently with the University of Bristol, England) for introducing me the lab equipment when I was a junior PhD student. It was in those days when he helped me with conducting the experiments of the strain nodes demonstration together with Justin Farmer. Justin was also a great colleague during the short period of time we were at CIMSS together. Dr. Jamil Renno (presently with the University of Southampton, England) was an outstanding colleague and a wonderful desk neighbor when we shared the same office before his graduation. I could not count how many nights we spent in lab Steve Anton while developing the concept of self-charging structures (a novel energy harvesting concept that is not discussed in this dissertation). Steve has been a fantastic colleague to collaborate with. It was also a great pleasure to work with Na Kong (a PhD student in the VLSI for Telecommunications Group) and observe how a skillful electrical engineer can improve that electrical domain (that we mechanical engineers often simplify) with efficient regulator circuits. If one is interested in how brittle single crystals can be, he/she should find me or Onur Bilgen. We have had long nights of research collaboration with Onur as well on macro-fiber composites and single crystals. The gentlemen presently sitting close to me in the office, Austin Creasy and Kahlil Detrich, are the best office neighbors one can find. I really enjoyed the break chats with Austin every time and I am very glad that the tower of books and papers on my desk has not yet collapsed onto Kahlil's desk. I would like to thank also Andy Sarles, Andy Duncan, Woon Kim, Zach Hills, Mana Afshari, Amin Karami, Brad Butrym and all the members of the CIMSS community I could not mention here, for making CIMSS what it has been.

I met another great colleague during his visit to our lab for about a year: Prof. Carlos De Marqui Junior, an aeroelasticity professor of the University of São Paulo in São Carlos, Brazil. I have enjoyed collaborating with him on piezo-aero-elasticity (not covered here) during my PhD study as much as I enjoyed the *caipirinha* when I visited his university to give a lecture last summer.

I would like to thank Julien Hoffmann, a student (presently an engineer) I advised during his visit as a senior engineering student from the Institut Catholique d'Arts et Métiers in Lille, France, for his help in planning and rapidly completing the manufacturing of the piezo-magneto-elastic device with the ESM Machine Shop (which reminds me that I owe thanks to Mr. David Simmons as well). If Julien had not undertaken the manufacturing process of the piezo-magneto-elastic device, the idea of using the magneto-elastic structure for energy harvesting (dates back to the summer of 2008 when I had taken Prof. Francis Moon's book from Prof. Inman's library at a party) was going wait for at least one more year!

I owe special thanks to my parents, Selma and Hikmet, for their patience and support during my PhD study. It was wonderful to visit them in my hometown (Eskisehir, Turkey) every July to regain the energy I needed. This work is dedicated to them.

This work has been supported by the U.S. Air Force Office of Scientific Research MURI under grant number F 9550-06-1-0326 "*Energy Harvesting and Storage Systems for Future Air Force Vehicles*" monitored by Dr B.L. Lee and recently by the U.S. Department of Commerce, National Institute of Standards and Technology, Technology Innovation Program, under the Cooperative Agreement Number 70NANB9H9007: "*Self-Powered Wireless Sensor Network for Structural Health Prognosis*."

"These oscillations arise freely, and I have determined various conditions, and have performed a great many beautiful experiments on the position of the knot points and the pitch of the tone, which agree beautifully with the theory." [1]

– Daniel Bernoulli (from a letter to Leonhard Euler)

Table of Contents

List of Figures

List of Tables

CHAPTER 1

INTRODUCTION

1.1 Vibration Energy Harvesting Using Piezoelectric Transduction

Vibration-based energy harvesting has received growing attention over the last decade. The research motivation in this field is due to the reduced power requirement of small electronic components, such as the wireless sensor networks used in structural health monitoring* applications. The ultimate goal in this research field is to power such small electronic devices by using the vibration energy available in their environment. If this can be achieved, the requirement of an external power source as well as the maintenance requirement for periodic battery replacement can be minimized.

It appears from the literature that the idea of vibration-to-electricity conversion first appeared in a journal article by Williams and Yates [2] in 1996. They described the basic transduction mechanisms that can be used for this purpose and provided a lumped-parameter base excitation model to simulate the electrical power output for electromagnetic energy harvesting. As stated by Williams and Yates [2], the three basic vibration-to-electric energy conversion mechanisms are the electromagnetic [2-4], electrostatic [5,6] and piezoelectric [7,8] transductions. Over the last decade, several articles have appeared on the use of these transduction mechanisms for low power generation from ambient vibrations. Two of the review articles covering mostly the experimental research on all transduction mechanisms are given by Beeby et al. [9] and Cook-Chennault et al. [10]. Comparing the number of publications appeared using each of these three transduction alternatives, it can be seen that the piezoelectric transduction has received the greatest attention especially in the last five years. Four review

* As an example, one of the recently started energy harvesting projects in the Center for Intelligent Material Systems and Structures at Virginia Tech aims to harvest ambient vibration energy to power the acoustic emission sensor nodes in bridges for structural health prognosis (supported by the National Institute of Standards and Technology, Technology Innovation Program, Cooperative Agreement Number 70NANB9H9007: *Self-Powered Wireless Sensor Network for Structural Health Prognosis*).

articles [10-13] have appeared in four years (2004-2008) with an emphasis on piezoelectric transduction to generate electricity from vibrations.

Piezoelectricity is a form of coupling between the mechanical and electrical behaviors of certain materials. The materials exhibiting the *piezoelectric effect* are called the piezoelectric materials. The piezoelectric effect is usually divided into two parts as the *direct* and the *converse* piezoelectric effects. In the simplest terms, when a piezoelectric materials is squeezed (i.e. mechanically strained) an electric charge collects at the electrodes located on its surface. This is called the direct piezoelectric effect and it was first demonstrated by the Currie brothers in 1880. If the same material is subjected to a voltage drop (i.e. an electrical potential difference applied across its electrodes), it deforms mechanically. This is called the converse piezoelectric effect and it was deduced mathematically (after the discovery of the direct piezoelectric effect) from the fundamental principles of thermodynamics by Gabriel Lippmann in 1881 and then confirmed experimentally by the Curie brothers. It is important to note that these two effects usually co-exist in a piezoelectric material. Therefore in an application where the direct piezoelectric effect is of the particular interest (which is the case in energy harvesting) ignoring the presence of the converse piezoelectric effect would be thermodynamically inconsistent.

Several natural crystals have been observed to exhibit the piezoelectric effect in the first half of the last century, e.g. Rochelle salt, quartz, etc. However, in order to use them in engineering applications, the *electromechanical coupling* between the mechanical and the electrical behaviors of the material has to be sufficiently strong. As a result, man-made piezoelectric ceramics have been developed in the second half of the last century. The most popular of engineering ceramics, PZT (lead zirconate titanate) was developed at the Tokyo Institute of Technology in the 1950s and various versions of it (particularly PZT-5A and PZT-5H) are today the most commonly used engineering piezoceramics. As far as energy harvesting research is concerned, PZT-5A and PZT-5H are the most widely implemented piezoceramics according to the literature [10].

The main advantages of piezoelectric materials in energy harvesting (compared to using the other two transduction mechanisms) are their large power densities and ease of application. When vibration input is applied, usable voltage output can be obtained directly from the piezoelectric material itself based on the direct piezoelectric effect. In electrostatic energy harvesting, for instance, an input voltage is required so that it can be alternated due to the relative

vibratory motion between the capacitor elements [5,6]. The voltage output in piezoelectric energy harvesting emerges from the constitutive law of the material which eliminates the requirement of an external voltage input. In addition, unlike electromagnetic devices, piezoelectric devices can be fabricated both in macro-scale and micro-scale owing to the well-established thin-film and thick-film fabrication techniques [8,14].

Typically, a piezoelectric energy harvester is a cantilevered beam with one or two piezoceramic layers. The harvester beam is located on a vibrating host structure and the dynamic strain induced in the piezoceramic layer(s) generates an alternating voltage output across the electrodes covering the piezoceramic layer(s). An example of a cantilever tested under base excitation is shown in Fig. 1.1 (referred from Chapter 4) along with its schematic view. An alternating voltage output is obtained due to the oscillatory base motion applied to the structure. In the mechanics research on piezoelectric energy harvesting as well as in the experimental research conducted to estimate the device performance for power generation, it is a common practice to consider a resistive load in the electrical domain [6-8,15-22] as depicted in Fig. 1.1b (which is also the case in this dissertation). From the electrical engineering point of view, it is often required to convert the alternating voltage output to a constant voltage using a rectifier bridge (AC-to-DC converter) and a smoothing capacitor in order to reach a constant level of voltage for charging a small battery or a capacitor using the harvested energy. Since the voltage levels for charging batteries and capacitors are not arbitrary, it is usually required to use a DC-to-DC converter (step-up or step-down) in order to regulate the rectified voltage output of the piezoceramic according to the voltage requirement of the specific charging application. These electrical engineering and power electronics aspects are beyond the scope of this dissertation and the relevant electrical engineering work can be found in the literature [23-25].

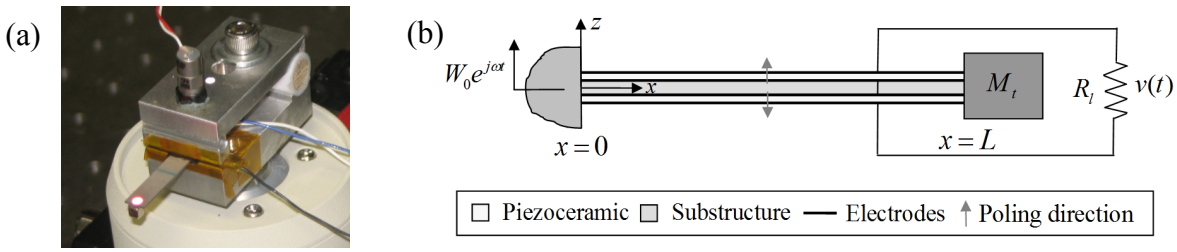

Fig. 1.1 (a) A cantilevered piezoelectric energy harvester tested under base excitation (photo by A. Erturk, 2009) and (b) its schematic view (referred from Chapter 4)

1.2 Review of the Existing Piezoelectric Energy Harvesting Models

Research in the area of piezoelectric energy harvesting involves understanding the mechanics of vibrating structures, the fundamental electrical circuit theory and the constitutive behavior of piezoelectric materials. This promising way of powering small electronic components and remote sensors has attracted researchers from different disciplines of engineering including mechanical, electrical and civil as well as researchers from the field of material science [10-13] and various modeling approaches have appeared as summarized in the following.

As shown with Fig. 1.1b, the modeling problem of vibration energy harvesting using piezoelectric transduction is to estimate the voltage output across the resistive load in terms of the base motion input. The voltage output can then be used to calculate the power delivered to the given electrical load. The coupled problem of predicting the voltage across the resistive load connected to the electrodes of a vibrating energy harvester (under base excitation) has been investigated by several researchers. In the early mathematical modeling treatments, researchers [15,16] employed lumped-parameter (single-degree-of-freedom) solutions. Lumped-parameter modeling is a convenient modeling approach since the electrical domain already consists of lumped parameters: a capacitor due to the internal (or inherent) capacitance of the piezoceramic and a resistor due to an external load resistance. Hence, the only thing required is to obtain the lumped parameters representing the mechanical domain so that the mechanical equilibrium and electrical loop equations can be coupled through the piezoelectric constitutive relations [26] (Appendix A) and a transformer relation can be established. This was the main procedure followed by Roundy et al. [15] and duToit et al. [16] in their lumped-parameter model derivations. Although lumped-parameter modeling gives initial insight into the problem by allowing simple expressions, it is an approximation limited to a single vibration mode and it lacks important aspects of the coupled physical system, such as the information of dynamic mode shapes and accurate strain distribution as well as their effects on the electrical response.

Since cantilevered energy harvesters are basically excited due to the motion of their base, the well-known lumped parameter harmonic base excitation relation taken from the elementary vibration texts has been used in the energy harvesting literature both for modeling [16] and studying the maximum power generation and parameter optimization [27,28]. In both lumped-parameter models [15,16] (derived for the transverse vibrations and longitudinal vibrations,

respectively), the contribution of the distributed mass (spring mass in the lumped-parameter sense) to the forcing amplitude in the base excitation problem is neglected. The contribution of the distributed mass to the excitation amplitude can be important especially if the harvester does not have a very large proof mass.

As an improved modeling approach, the Rayleigh-Ritz type discrete formulation originally derived by Hagood et al. [29] for piezoelectric actuation (based on the generalized Hamilton's principle for electromechanical systems given by Crandall et al. [30]) was employed by Sodano et al. [17] and duToit et al. [15,21] for modeling of cantilevered piezoelectric energy harvesters (based on the Euler-Bernoulli beam theory). The Rayleigh-Ritz model gives a discrete model of the distributed parameter system and it is a more accurate approximation compared to lumped-parameter modeling with a single degree of freedom. It can be seen that the modeling the force acting on the beam due to base excitation in the distributed-parameter formulation caused some confusion [17]. The Rayleigh-Ritz model gives an approximate representation of the distributed-parameter system (Fig. 1.1) as a discretized system by reducing its mechanical degrees of freedom from infinity[†] to a finite dimension and usually it is computationally more expensive than the analytical solution (if available).

In order to obtain an analytical expressions, Lu et al. [18] used the vibration mode shapes obtained from the Euler-Bernoulli beam theory along with the piezoelectric constitutive relation [26] that gives the electric displacement to relate the electrical outputs to the vibration mode shape. Due to the derivation issues in Lu et al. [18], the most important concept in structural dynamics, the resonance phenomenon, is completely lost and the resulting frequency response curves do not have any peak. Another problem in the same work is due to the oversimplified modeling of piezoelectric coupling as viscous damping (this work remains very frequently cited regardless of these very important issues). Similar models were presented by Chen et al. [19] and Lin et al. [20] where the electrical response is expressed in terms of the beam vibration response in an effort to obtain an analytical representation. The deficiencies in these analytical modeling attempts can be summarized as the lack of consideration of the resonance phenomenon, ignorance of modal expansion (higher mode effects) and oversimplified modeling of piezoelectric coupling in the beam equation as viscous damping. Representing the effect of

[†] Indeed the electromechanical system shown in Fig. 1.1b has infinite mechanical degrees of freedom from all vibration modes and one electrical degree of freedom due to the *RC* circuit.

electromechanical coupling on the harvester structure as an electrically induced viscous damping effect is a reasonable approximation for certain electromagnetic energy harvesters [2] where the transduction force is proportional to the velocity. However, several other researchers [8,13,31] represented the piezoelectric energy harvester problem referring to the early electromagnetic energy harvesting model by Williams and Yates [2] although in the original work [2] the authors explicitly state that they focus on electromagnetic energy harvesting. The experiments [32] show that the form of the damping induced in the structure due to piezoelectric power generation is considerably different from the effect of viscous damping. In a more recent work aiming to obtain an analytical representation, Ajitsaria et al. [22] presented a cantilevered energy harvester model, where they combined the static sensing/actuation equations (with constant radius of curvature due to a static tip force) with the dynamic Euler-Bernoulli beam equation (where the radius of curvature varies) under base excitation (where there is no tip force). Their model [22] uses the static actuation formulation given by DeVoe and Pisano [33] (which is based on an analogy that uses Timoshenko's approach of modeling bi-metal thermostats [34]) clearly fails in the dynamic problem of vibration energy harvesting.

The aforementioned papers are frequently cited modeling papers from the literature of piezoelectric energy harvesting. Since this dissertation focuses on electromechanical modeling of piezoelectric energy harvesters, several papers related to experimentation, materials research and circuit design for piezoelectric energy harvesting are not reviewed here and such work can be found in the existing review articles [10-13]. Based on the modeling review given in this section, it can be seen that highly different modeling approaches have appeared in the literature of vibration energy harvesting over the last five years. These modeling papers have originated from different disciplines such as mechanical, electrical, civil and materials engineering. Considering the propagation rate of some of the fundamentally incorrect results, there seems to be an urgent need to develop reliable piezoelectric energy harvester models for the use of this particular research community from different disciplines of engineering.

1.3 Objectives of the Dissertation

Considering the issues in the existing literature of mathematical modeling of piezoelectric energy harvesters, the primary objective of this dissertation is to develop reliable mathematical models

for predicting the electromechanically coupled system dynamics of cantilevers used for piezoelectric energy harvesting. For the particular research community of this rapidly growing and multi-disciplinary area of engineering, developing computationally efficient but accurate models that can be implemented by the researchers in academia and industry is essential. Analytical solutions, as long as they are available, are usually much faster than the numerical solution techniques such as the finite element modeling and other energy-based discretization techniques. Moreover, the closed-form expressions associated with the analytical solutions often provide an explicit understanding of the effects of systems parameters and the physics of the problem clearly. Therefore the focus is placed on analytical modeling and a major part of this work covers analytical formulations and their validations.

In addition to deriving and experimentally validating the analytical solutions, another objective is to study the effects of system parameters such as the piezoelectric, elastic and dielectric properties of the piezoceramic layers as well as mechanical damping. It is also aimed to obtain closed-form expressions that can be used to identify the critical system parameters (e.g. the optimum electrical load, the maximum voltage, mechanical damping ratio in the presence of an electrical load, etc.) accurately from the experimental data. Such equations can be considered as relations for experimental modal analysis in the presence of electromechanical coupling.

It is also aimed in this dissertation to compare the performances of the existing piezoelectric materials for power generation in order to provide the materials scientists a physical understanding of how different properties of various piezoceramics affect the resulting power output so that the composition of the piezoelectric materials can be optimized using the models developed here. Therefore, the models given here are for designing and optimizing not only the mechanical structure of an energy harvester but also the materials aspects.

Since the analytical solutions are not available for all configurations, it is aimed to develop the mathematical background for the relatively complicated problem of energy harvesting using asymmetric and moderately thick beams based on an electromechanical version of the assumed-modes method. Even though piezoelectric energy harvesters are usually designed and manufactured as thin structures for larger flexibility and larger power, there might be need to use configurations where the structure might have moderate thickness (e.g. due to the limitations in the active material dimensions) where the shear deformation and the rotary inertia effects are pronounced. It is also aimed to validate the predictions of the approximate formulation against

the experimental cases of the analytical solution part to observe the convergence of the assumed-modes solution to the analytical solution (hence to the experimental results) with the increasing number of modes.

1.4 Layout of the Dissertation

The main body of this work consists of eight chapters mostly focusing of modeling and analysis of piezoelectric energy harvesters along with experimental validations. Starting with the second chapter, the contents of the main body are as follows:

The second chapter of this dissertation improves the existing lumped-parameter piezoelectric energy harvester model by considering the electromechanically uncoupled distributed-parameter base excitation problem. The inaccuracy of the frequently referred lumped-parameter base excitation equation is shown and correction factors are derived to improve it. Experimental validations are given for the corrected lumped-parameter base excitation equation. An amplitude correction factor is then introduced to the lumped-parameter piezoelectric energy harvester equations.

The third chapter presents electromechanically coupled analytical solutions of symmetric bimorph piezoelectric energy harvester configurations under base excitation for the series and parallel connections of the piezoceramics layers. The formulation is given based on the thin-beam theory since piezoelectric energy harvesters are typically thin structures. The multi-mode solutions (for arbitrary excitation frequencies) and the single-mode solutions (approximately valid for resonance excitation) are obtained and an extensive theoretical case study is provided.

The fourth chapter provides detailed experimental validations for the analytical expressions derived in Chapter 3. Three case studies are given with a focus on a brass-reinforced PZT-5H cantilever without and with a tip mass and a PZT-5A cantilever. Validations of the electromechanical frequency response equations are given along with the electrical performance diagrams.

In Chapter 5, the analytical solutions are first expressed in dimensionless forms. The asymptotic forms of the FRFs (frequency response functions) are obtained for the short-circuit and the open-circuit conditions, which are then used to derive closed-form

expressions for identifying system parameters such as the short-circuit and the open-circuit resonance frequencies, mechanical damping ratio and the optimum load resistance for the maximum power output. Experimental validations of the closed-form modal electromechanical expressions are also provided.

The electromechanical model is used in Chapter 6 for simulating and comparing the performance results of conventional monolithic piezoceramics and commonly used single crystals for energy harvesting. The effects of piezoelectric constant, elastic compliance, permittivity and mechanical damping on the power output are addressed. The importance of the reduced (plane-stress) piezoelectric stress constant (rather that the well-known d_{31} strain constant) is highlighted since single crystals have not only very large d_{31} constant but also very large elastic compliance (which tends to reduce the effective piezoelectric stress constant). An experimental demonstration is given to demonstrate the effect of mechanical damping with a focus on two bimorphs using PZT-5A and PZT-5H piezoceramics.

In Chapter 7, the effects of strain nodes are discussed in detail with an experimental demonstration for the cancellation of the electrical output in the second vibration mode of a cantilever. The cancellation problem due to the presence of the strain nodes is discussed and dimensionless data for the strain node positions of thin beams are provided. The relationship between this chapter and a recent paper on energy harvesting from the static deflection of a clamped plate is explained. How to avoid the cancellation problem in the electrical circuit is also discussed.

For relatively complicated structural configurations which do not allow analytical solutions, an approximate analytical solution using an electromechanical version of the assumed-modes method is given in Chapter 8. Euler-Bernoulli, Rayleigh and Timoshenko solutions are presented. The formulation given here should be preferred for asymmetric energy harvesters, moderately thick energy harvesters as well as energy harvesters with varying cross section. Two of the experimental cases given in Chapter 4 are revisited for validation of the approximate solutions using the electromechanical assumed-modes method. Convergence of the assumed-modes solution to the analytical solution is also shown.

Chapter 9 introduces a piezo-magneto-elastic structure for broadband vibration energy harvesting. The lumped-parameter equations describing the nonlinear system dynamics are given along with the theoretical simulations. Experimental results are also presented to verify

the presence of high-energy orbits of the piezo-magneto-elastic energy harvester over a range of frequencies. Energy harvesting from the large-amplitude oscillations on these orbits yields an order of magnitude larger power compared to energy harvesting from the conventional piezo-elastic configuration.

Finally, Chapter 10 summarizes the results of this work and draws conclusions from the chapters.

CHAPTER 2

CORRECTION OF THE EXISTING LUMPED-PARAMETER PIEZOELECTRIC ENERGY HARVESTER MODEL

The goal of this chapter is to improve the existing electromechanical lumped-parameter piezoelectric energy harvester model by considering the (electromechanically) uncoupled distributed-parameter formulation. First the general solution of the base excitation problem for the transverse vibrations of a cantilevered Euler-Bernoulli beam is reviewed. The formal treatment of mechanical damping as a combination of internal (strain-rate) and external (air) damping mechanisms is addressed. The base motion is described by translation in the transverse direction with superimposed small rotation and it is not restricted to be harmonic in time. The general solution is then reduced to the particular case of harmonic base translation and the results of the distributed-parameter model are compared with those of the lumped-parameter model in a dimensionless basis. It is shown that the lumped-parameter model may yield highly inaccurate results and an amplitude correction factor is derived for improving the lumped-parameter base excitation model for transverse vibrations. The variation of correction factor with tip mass – to – beam mass ratio is also given and it is observed that the uncorrected lumped-parameter model can be accurate only when this ratio is sufficiently large. Case studies are presented for experimental validation of the dimensionless correction factor. Then the base excitation problem is summarized for the case of longitudinal vibrations and a correction factor is introduced for the lumped-parameter harmonic base excitation model of longitudinal vibrations as well. Finally, the amplitude correction factor is introduced to the electromechanically coupled lumped-parameter piezoelectric energy harvester equations and a theoretical case study is given to demonstrate the requirement of a correction factor in the lumped-parameter electromechanical equations.

2.1 Base Excitation Problem for the Transverse Vibrations of a Cantilevered Beam

2.1.1 Response to General Base Excitation. The clamped-free Euler-Bernoulli beam shown in Fig. 2.1 is subjected to the translation $g(t)$ of its base in the transverse direction with superimposed small rotation $h(t)$. Deformations of the geometrically uniform thin beam are assumed to be small and its composite structure (of isotropic or transversely isotropic layers) exhibits linear-elastic material behavior. The shear deformation and the rotary inertia effects are neglected based on the thin-beam assumption. For the purpose of demonstration, the cantilevered beam is depicted as a symmetric bimorph with three layers. Typically the outer two layers are piezoceramics (poled in the thickness direction) and the layer bracketed in between is a metallic substructure. The distributed-parameter formulations given in this chapter do not consider the piezoelectric coupling effect as the purpose here is to investigate the accuracy of the lumped-parameter harmonic base excitation relation in the absence of electromechanical coupling.

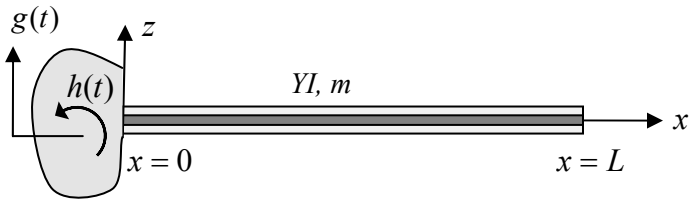

Fig. 2.1 Cantilevered beam transversely excited by the translation and small rotation of its base

The transverse displacement of the beam at any point x along neutral axis is denoted by $w(x,t)$. If the beam is assumed to be undamped, the equation of motion for free vibrations in the absolute frame of reference can be written as [35]

$$YI\frac{\partial^4 w(x,t)}{\partial x^4}+m\frac{\partial^2 w(x,t)}{\partial t^2}=0 \tag{2.1}$$

where YI is the bending stiffness and m is the mass per unit length of the beam.[*] Note that the expression of the bending stiffness of a uniform bimorph cantilever is given in the electromechanical derivations of Chapter 3.

[*] Y is preferred to denote the elastic modulus (Young's modulus) in order to avoid confusion with the electric field term (E) in the following chapters.

Two types of damping mechanisms are included to the undamped beam: viscous air damping and Kelvin-Voigt (or strain-rate) damping (then the material behavior is approximated as linear-viscoelastic hereafter). The equation of motion of the damped beam becomes

$$YI\frac{\partial^4 w(x,t)}{\partial x^4}+c_s I\frac{\partial^5 w(x,t)}{\partial x^4\partial t}+c_a\frac{\partial w(x,t)}{\partial t}+m\frac{\partial^2 w(x,t)}{\partial t^2}=0 \tag{2.2}$$

where c_a is the viscous air damping coefficient and c_s is the strain-rate damping coefficient (appears as an effective term $c_s I$ for the composite structure). Viscous air damping is a simple way of modeling the force acting on the beam due to the air particles displaced during the vibratory motion and strain-rate damping accounts for the structural damping due to the friction internal to the beam. Both of these damping mechanisms satisfy the proportional damping criterion and hence they are mathematically convenient for the modal analysis solution procedure. Other beam damping mechanisms and the identification procedures of their respective damping parameters from experimental measurements are discussed by Banks and Inman [36]. In order to use analytical modal analysis techniques, one is basically restricted with the stiffness and mass proportional damping mechanisms (often referred to as Rayleigh damping [37] especially in dynamic analysis of discrete systems).

Following Timoshenko et al. [35], the absolute transverse displacement of the beam (i.e. the transverse displacement relative to the absolute reference frame) at any point *x* and time *t* can be written as

$$w(x,t)=w_b(x,t)+w_{rel}(x,t) \tag{2.3}$$

where $w_{rel}(x,t)$ is the transverse displacement relative to the clamped end of the beam and $w_b(x,t)$ is the base displacement given by

$$w_b(x,t)=\delta_1(x)g(t)+\delta_2(x)h(t) \tag{2.4}$$

Here, $\delta_1(x)$ and $\delta_2(x)$ are the displacement influence functions for the transverse base displacement and small base rotation of the beam, respectively. For the cantilevered beam case, $\delta_1(x)=1$ and $\delta_2(x)=x$ [35]. Using Eq. (2.3) in Eq. (2.2) yields

$$YI\frac{\partial^4 w_{rel}(x,t)}{\partial x^4}+c_s I\frac{\partial^5 w_{rel}(x,t)}{\partial x^4\partial t}+c_a\frac{\partial w_{rel}(x,t)}{\partial t}+m\frac{\partial^2 w_{rel}(x,t)}{\partial t^2}=-m\frac{\partial^2 w_b(x,t)}{\partial t^2}-c_a\frac{\partial w_b(x,t)}{\partial t} \tag{2.5}$$

Note that, after expressing the absolute transverse displacement $w(x,t)$ in terms of the base displacement $w_b(x,t)$ and the relative transverse displacement $w_{rel}(x,t)$, the free vibration equation for the absolute vibratory motion of the beam given by Eq. (2.2) becomes a forced vibration equation for the relative vibratory motion of the beam. There are two important points to mention at this stage. First, the external damping acts on the absolute velocity whereas the internal damping acts on the relative velocity of the beam. Secondly, for the same reason, the excitation is not only due to the rigid body inertia of the beam but also it is due to the effect of external damping on the rigid body motion. The latter may or may not be negligible depending on the amount of external damping, which will be discussed later in this chapter.

The boundary conditions for the relative vibratory motion of the beam can be written as

$$w_{rel}(0,t)=0\,,\ \left.\frac{\partial w_{rel}(x,t)}{\partial x}\right|_{x=0}=0 \tag{2.6}$$

$$\left[YI\frac{\partial^2 w_{rel}(x,t)}{\partial x^2}+c_sI\frac{\partial^3 w_{rel}(x,t)}{\partial x^2\partial t}\right]_{x=L}=0\,,\ \left[YI\frac{\partial^3 w_{rel}(x,t)}{\partial x^3}+c_sI\frac{\partial^4 w_{rel}(x,t)}{\partial x^4\partial t}\right]_{x=L}=0 \tag{2.7}$$

Note that the strain-rate damping results in a moment as well as a transverse force term that appears in the natural boundary conditions written for the free end [36]. Based on the expansion theorem, the solution of Eq. (2.5) can be represented by an absolutely and uniformly convergent series of the eigenfunctions as

$$w_{rel}(x,t)=\sum_{r=1}^{\infty}\phi_r(x)\eta_r(t) \tag{2.8}$$

where $\phi_r(x)$ and $\eta_r(t)$ are the mass normalized eigenfunction and the modal coordinate of the clamped-free beam for the *r*-th mode, respectively. Since the system is proportionally damped, the eigenfunctions denoted by $\phi_r(x)$ are indeed the mass normalized eigenfunctions of the corresponding *undamped* free vibration problem [38] given by Eq. (2.1) along with the clamped-free boundary conditions

$$w_{rel}(0,t)=0\,,\ \left.\frac{\partial w_{rel}(x,t)}{\partial x}\right|_{x=0}=0\,,\ YI\left.\frac{\partial^2 w_{rel}(x,t)}{\partial x^2}\right|_{x=L}=0\,,\ YI\left.\frac{\partial^3 w_{rel}(x,t)}{\partial x^3}\right|_{x=L}=0 \tag{2.9}$$

Therefore, the resulting mass normalized eigenfunction of the *r*-th vibration mode is

$$\phi_r(x)=\sqrt{\frac{1}{mL}}\left[\cosh\frac{\lambda_r}{L}x-\cos\frac{\lambda_r}{L}x-\sigma_r\left(\sinh\frac{\lambda_r}{L}x-\sin\frac{\lambda_r}{L}x\right)\right] \tag{2.10}$$

where the λ_r is the dimensionless frequency parameter of the *r*-th mode obtained from the characteristic equation given by

$$1+\cos\lambda\cosh\lambda=0 \tag{2.11}$$

and σ_r is expressed as

$$\sigma_r=\frac{\sinh\lambda_r-\sin\lambda_r}{\cosh\lambda_r+\cos\lambda_r} \tag{2.12}$$

It should be noted that Eqs. (2.10)-(2.12) are valid for a clamped-free beam without a tip mass. The presence of a tip mass affects not only the eigenvalue problem but also the right hand side of Eq. (2.5) since the inertia of a possible tip mass also contributes to the excitation of the beam in that case (Section 2.2.2).

The mass normalized form of the eigenfunctions given by Eq. (2.10) satisfies the following orthogonality conditions:

$$\int_0^L m\phi_s(x)\phi_r(x)dx=\delta_{rs}\ ,\ \int_0^L YI\phi_s(x)\frac{d^4\phi_r(x)}{dx^4}dx=\omega_r{}^2\delta_{rs} \tag{2.13}$$

where δ_{rs} is the Kronecker delta, defined as being equal to unity for $s=r$ and equal to zero for $s\neq r$, and ω_r is the undamped natural frequency of the *r*-th mode given by

$$\omega_r=\lambda_r{}^2\sqrt{\frac{YI}{mL^4}} \tag{2.14}$$

Using Eqs. (2.5)-(2.7) and (2.13), the partial differential equation of motion can be reduced to an infinite set of ordinary differential equations

$$\frac{d^2\eta_r(t)}{dt^2}+2\zeta_r\omega_r\frac{d\eta_r(t)}{dt}+\omega_r{}^2\eta_r(t)=f_r(t) \tag{2.15}$$

where

$$2\zeta_r\omega_r=\frac{c_sI\omega_r{}^2}{YI}+\frac{c_a}{m} \tag{2.16}$$

Therefore, the damping ratio ζ_r includes the effects of both strain-rate damping and viscous air damping and it can be expressed as $\zeta_r=\zeta_r^s+\zeta_r^a$ where the strain-rate and the air damping components of the damping ratio are $\zeta_r^s=c_sI\omega_r/2YI$ and $\zeta_r^a=c_a/2m\omega_r$, respectively. It is clear from Eq. (2.16) that the strain-rate damping coefficient is proportional to structural stiffness

and the viscous air damping coefficient is proportional to mass per unit length. It is worth mentioning that identification of the proportional damping coefficients $c_s I$ and c_a (from experimental measurements) requires knowing the natural frequencies and modal damping ratios of two separate modes [37]. If one knows the natural frequencies (ω_j, ω_k) and the modal damping ratios† (ζ_j, ζ_k) of modes *j* and *k*, it is straightforward from Eq. (2.16) to obtain the $c_s I$ and c_a values using‡

$$\begin{Bmatrix} c_s I \\ c_a \end{Bmatrix} = \frac{2\omega_j \omega_k}{\omega_j^{\,2} - \omega_k^{\,2}} \begin{bmatrix} \dfrac{YI}{\omega_k} & -\dfrac{YI}{\omega_j} \\ -m\omega_k & m\omega_j \end{bmatrix} \begin{Bmatrix} \zeta_j \\ \zeta_k \end{Bmatrix} \tag{2.17}$$

In Eq. (2.15), the modal forcing function $f_r(t)$ can be expressed as

$$f_r(t) = f_r^m(t) + f_r^c(t) \tag{2.18}$$

Here, the inertial and the damping excitation terms are given by the following expressions, respectively,

$$f_r^m(t) = -m\left(\gamma_r^w \frac{d^2 g(t)}{dt^2} + \gamma_r^\theta \frac{d^2 h(t)}{dt^2}\right),\ f_r^c(t) = -c_a\left(\gamma_r^w \frac{dg(t)}{dt} + \gamma_r^\theta \frac{dh(t)}{dt}\right) \tag{2.19}$$

where

$$\gamma_r^w = \int_0^L \phi_r(x)dx\ ,\ \gamma_r^\theta = \int_0^L x\phi_r(x)dx \tag{2.20}$$

Then, the modal response can be obtained by using the Duhamel integral (for zero initial conditions) as

$$\eta_r(t) = \frac{1}{\omega_{rd}} \int_0^t f_r(\tau) e^{-\zeta_r \omega_r (t-\tau)} \sin \omega_{rd}(t-\tau) d\tau \tag{2.21}$$

---

† Concepts such as the quality factor, half-power points or the Nyquist plot can be used for the identification of modal damping ratio in frequency domain [39], or alternatively, logarithmic decrement can be used for its identification in time domain [37].

‡ This procedure assumes that the modal damping ratios of all the other modes can be determined if those of only two modes are known (which is practically not the case for most physical systems). The reader is referred to Banks and Inman [36] for a more realistic approach of identifying these damping coefficients. Often the damping ratios of the individual vibration modes are identified separately from experiments.

where $\omega_{rd} = \omega_r \sqrt{1-\zeta_r^{\,2}}$ is the damped natural frequency of the *r*-th mode. Eventually, the modal response obtained from Eq. (2.21) can be used in Eq. (2.8) along with the eigenfunction expression given by Eq. (2.10) and the relative response $w_{rel}(x,t)$ at any point along the beam axis can be obtained as

$$w_{rel}(x,t) = \sum_{r=1}^{\infty} \frac{\phi_r(x)}{\omega_{rd}} \int_0^t f_r(\tau) e^{-\zeta_r \omega_r (t-\tau)} \sin \omega_{rd}(t-\tau) d\tau \tag{2.22}$$

Note that the displacement at the tip of the beam (relative to the moving base) can be obtained by just setting $x = L$ in Eq. (2.22). If one is interested, the response of the beam relative to the absolute reference frame can be obtained by just using the relative displacement and the base displacement input in Eq. (2.3). However, the main concern in vibration energy harvesting is the response of the beam relative to its base. The expression obtained for the relative vibratory motion of the beam, Eq. (2.22), is not restricted to harmonic base excitation and it can handle transient base histories (including small base rotations).

2.1.2 Steady-state Response to Harmonic Base Excitation. In most of the theoretical and experimental work on piezoelectric energy harvesting, the base excitation is assumed to be harmonic translation to simplify the problem and also to estimate the maximum power generation from resonance excitation. If the base translation is of the form $g(t) = W_0 e^{j\omega t}$ (where W_0 is the base displacement amplitude, ω is the excitation frequency and $j = \sqrt{-1}$ is the unit imaginary number) and if the base does not rotate (i.e. $h(t) = 0$), the steady-state modal response can be obtained as

$$\eta_r(t) = \frac{m\omega^2 - j\omega c_a}{\omega_r^{\,2} - \omega^2 + j2\zeta_r \omega_r \omega} \gamma_r^w W_0 e^{j\omega t} \tag{2.23}$$

where

$$\gamma_r^w = \int_0^L \phi_r(x) dx = \frac{2\sigma_r}{\lambda_r} \sqrt{\frac{L}{m}} \tag{2.24}$$

is obtained by integrating Eq. (2.10) over the beam length. Using Eqs. (2.8), (2.10) and (2.23), one can obtain the expression for the relative response at point *x* and time *t* as

$$w_{rel}(x,t) = 2W_0 e^{j\omega t} \sum_{r=1}^{\infty} \left[\cosh\frac{\lambda_r}{L}x - \cos\frac{\lambda_r}{L}x - \sigma_r \left(\sinh\frac{\lambda_r}{L}x - \sin\frac{\lambda_r}{L}x \right) \right] \frac{\sigma_r \left(\omega^2 - j2\zeta_r^a \omega_r \omega \right)}{\lambda_r \left(\omega_r{}^2 - \omega^2 + j2\zeta_r \omega_r \omega \right)} \tag{2.25}$$

Then, by setting $x = L$ one obtains

$$w_{rel}(L,t) = 2W_0 e^{j\omega t} \sum_{r=1}^{\infty} \left[\cosh\lambda_r - \cos\lambda_r - \sigma_r \left(\sinh\lambda_r - \sin\lambda_r \right) \right] \frac{\sigma_r \left(\omega^2 - j2\zeta_r^a \omega_r \omega \right)}{\lambda_r \left(\omega_r{}^2 - \omega^2 + j2\zeta_r \omega_r \omega \right)} \tag{2.26}$$

which is the distributed-parameter (Euler-Bernoulli model) steady-state solution of the relative tip displacement due to harmonic base excitation (when there is no tip mass).

2.1.3 Lumped-parameter Model of the Harmonic Base Excitation Problem. Lumped-parameter modeling approach with a single degree of freedom requires describing the dynamics of the point of interest (usually the free end of the beam) in terms of certain lumped parameters which are the equivalent mass, stiffness and the damping of the beam denoted by m_{eq}, k_{eq} and c_{eq}, respectively (Fig. 2.2a). The equivalent stiffness is obtained from the static deflection relation of a cantilevered beam due to a concentrated transverse load at the tip whereas the equivalent mass is obtained by expressing the total kinetic energy of the beam in terms of the velocity at the tip through Rayleigh's quotient [40] for cantilevered end conditions where the base is not moving. It should be highlighted at this point that, in the base excitation problem (unlike the problem of a beam where the base is not moving), the cantilevered beam is excited by its own inertia and there is an inertial contribution to the excitation from its distributed mass. The contribution of this distributed inertia to the excitation amplitude can be very significant as will be shown in the next section.

The commonly referred [2,3,8,10,13,16,22,27,28,31] lumped parameter model is shown in Fig. 2.2a and the lumped parameter model with a more precise representation of damping is depicted in Fig. 2.2b. The correction made in Fig. 2.2b is due to the modeling of the external viscous damping (air damping). It is analogous to the Euler-Bernoulli model solution in the sense that the structural damping acts on the relative velocity between the mass and the base however the air damping acts on the absolute velocity of the mass.

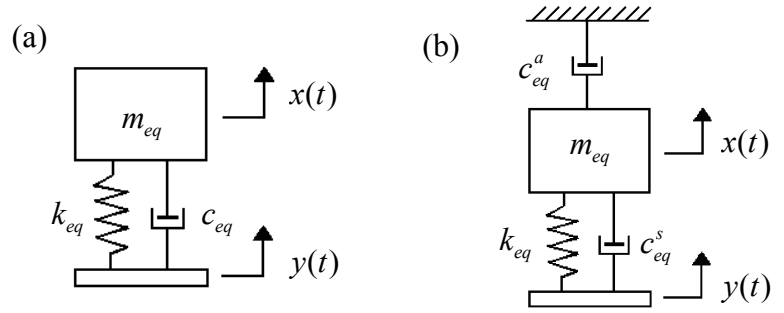

Fig. 2.2 Lumped-parameter models of the base excitation problem; (a) the commonly used representation and (b) a more precise representation of external damping

In Fig. 2.2, $y(t)$ is the harmonic base displacement ($y(t) = Y_0 e^{j\omega t}$) whereas $x(t)$ is the absolute displacement response of the mass (i.e. it is the absolute transverse displacement at the free end of the beam). Let the response of the mass relative to the base be $z(t) = x(t) - y(t)$. Then, for the system shown in Fig. 2.2a, one can obtain the relative displacement of the mass as

$$z(t) = \frac{\omega^2 m_{eq}}{k_{eq} - \omega^2 m_{eq} + j\omega c_{eq}} Y_0 e^{j\omega t} \tag{2.27}$$

which can be found in any elementary vibration text [41,42] and which has also been frequently referred in order to describe dynamics of vibration energy harvesters [2,3,8,10,13,16,22,27, 28,31]. In Eq. (2.27), the equivalent flexural stiffness of the cantilever at the tip is

$$k_{eq} = \frac{3YI}{L^3} \tag{2.28}$$

and the equivalent mass is due to Lord Rayleigh [40]:

$$m_{eq} = \frac{33}{140} mL + M_t \tag{2.29}$$

where M_t is the tip mass (if exists). The undamped natural frequency (the *fundamental* natural frequency of the structure) is[§]

[§] It can be shown that the error due to using Eq. (2.30) in predicting the fundamental natural frequency is about 1.5 % in the absence of a tip mass (relative to the Euler-Bernoulli model fundamental natural frequency ω_1 obtained for $r = 1$ in Eq. (2.14)). The prediction of Eq. (2.30) is improved in the presence of a tip mass.

$$\omega_n = \sqrt{\frac{k_{eq}}{m_{eq}}} = \sqrt{\frac{3YI/L^3}{(33/140)mL + M_t}} \tag{2.30}$$

Then the equivalent damping coefficient is $c_{eq} = 2\zeta\omega_n m_{eq}$ where ζ is the equivalent damping ratio. According to Fig. 2.2a, this model assumes a single damping coefficient which acts on the relative velocity of the tip mass.

Consider the lumped-parameter model presented in Fig. 2.2b where air damping and structural damping are treated separately; the former acts on the absolute velocity of the mass whereas the latter acts on the velocity of the mass relative to the base. The air damping coefficient c_{eq}^a is assumed to be proportional to m_{eq} ($c_{eq}^a = a_0 m_{eq}$) whereas the structural damping coefficient c_{eq}^s is assumed to be proportional to k_{eq} ($c_{eq}^s = a_1 k_{eq}$), where a_0 and a_1 are the constants of proportionality. Once again, obtaining the proportionality constants a_0 and a_1 (hence the damping coefficients c_{eq}^a and c_{eq}^s) from experimental measurements requires knowing the damping ratios and natural frequencies of two separate modes of the physical (multi-mode) system as in the case of the Euler-Bernoulli model (see Eq. (2.17)). For the lumped-parameter model shown in Fig. 2.2b, the relative response of the mass can be expressed as

$$z(t) = \frac{\omega^2 m_{eq} - j\omega c_{eq}^a}{k_{eq} - \omega^2 m_{eq} + j\omega c_{eq}} Y_0 e^{j\omega t} \tag{2.31}$$

Here, $c_{eq}^a = 2\zeta^a \omega_n m_{eq}$ and $c_{eq} = c_{eq}^a + c_{eq}^s = 2\zeta\omega_n m_{eq}$, where ζ^a is the damping ratio due to the viscous damping effect of air. Clearly, in the commonly referred Eq. (2.27), the forcing term due to air damping is missing. Therefore, representing all sources of mechanical damping by a single damping ratio acting on the relative velocity of the tip mass [16] is not the most general case. However, for the case where the damping ratio ζ^a due to the surrounding fluid (which is usually air) is very low, it is reasonable to expect the forcing term $-j\omega c_{eq}^a$ coming from the air damping to be much less than the inertial forcing term $\omega^2 m_{eq}$ and consequently Eq. (2.31) reduces to Eq. (2.27). For a dimensionless comparison, dividing both of these forcing terms by m_{eq} gives the inertia contribution as ω^2 and the air damping contribution as $-j2\zeta^a\omega_n\omega$. For the case of excitation at the natural frequency ($\omega = \omega_n$), variation of the percentage forcing contribution of

air damping with ζ^a is shown in Fig. 2.3 (which is simply the plot of $2\zeta^a/\sqrt{1+(2\zeta^a)^2}\times 100$). As can be seen from Fig. 2.3, the excitation amplitude coming from the air damping is less than 5 % of the total excitation (inertial and damping) if $\zeta^a < 0.025$. The conclusion of this brief discussion is that the lumped-parameter model of the harmonic base excitation problem given by Fig. 2.2a and Eq. (2.27) implicitly assumes the excitation component due to the damping coming from the external fluid to be sufficiently low when compared to the inertial excitation component. For the base excitation problem of cantilevers operating in viscous fluids or for micro-scale cantilevers for which the external damping effect becomes more significant, the representation given in Fig. 2.2b and Eq. (2.31) can be preferred.

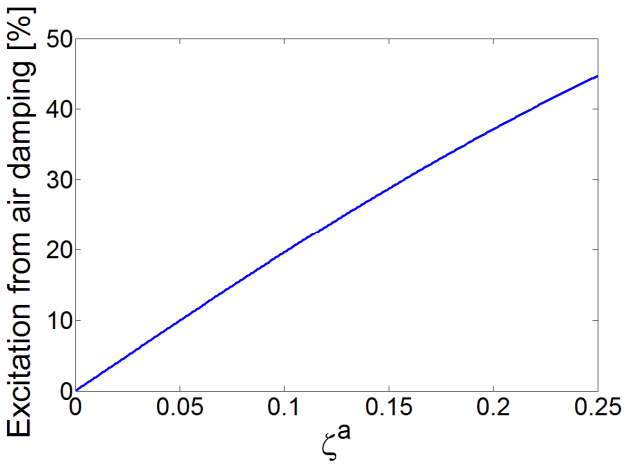

Fig. 2.3 Contribution of excitation from air (or external) damping to the total excitation term as a function of air damping ratio (for excitation at $\omega = \omega_n$)

2.1.4 Comparison of the Distributed-parameter and the Lumped-parameter Model Predictions. Consider the expressions of the relative tip displacement response obtained by using the distributed-parameter (Euler-Bernoulli) model and the lumped-parameter model, which are Eqs. (2.26) and (2.31), respectively. As mentioned previously, for the case of light air (external) damping (i.e. for $\zeta^a, \zeta_r^a \ll 1$) the excitation due to the inertia term dominates the numerators of Eqs. (2.26) and (2.31) and these equations can be reduced to

$$w_{rel}(L,t) = 2\omega^2 W_0 e^{j\omega t} \sum_{r=1}^{\infty} \frac{\sigma_r \left[\cosh\lambda_r - \cos\lambda_r - \sigma_r\left(\sinh\lambda_r - \sin\lambda_r\right)\right]}{\lambda_r\left(\omega_r{}^2 - \omega^2 + j2\zeta_r\omega_r\omega\right)} \tag{2.32}$$

$$z(t) = \frac{\omega^2}{\omega_n{}^2 - \omega^2 + j2\zeta\omega_n\omega} Y_0 e^{j\omega t} \tag{2.33}$$

respectively.

The tip displacement – to – base displacement ratio gives the *relative displacement transmissibility function*, which forms an appropriate dimensionless basis for comparing the Euler-Bernoulli and the lumped-parameter models. These relative displacement transmissibility functions can be extracted from Eqs. (2.32) and (2.33) as

$$T_{rel}^{EB}(\omega, \zeta_r) = 2\omega^2 \sum_{r=1}^{\infty} \frac{\sigma_r \left[\cosh\lambda_r - \cos\lambda_r - \sigma_r \left(\sinh\lambda_r - \sin\lambda_r\right)\right]}{\lambda_r \left(\omega_r{}^2 - \omega^2 + j2\zeta_r\omega_r\omega\right)} \tag{2.34}$$

$$T_{rel}^{LP}(\omega, \zeta) = \frac{\omega^2}{\omega_n{}^2 - \omega^2 + j2\zeta\omega_n\omega} \tag{2.35}$$

where T_{rel}^{EB} and T_{rel}^{LP} are for the Euler-Bernoulli and the lumped-parameter models, respectively. Note that the Euler-Bernoulli and the lumped-parameter natural frequencies are not identical since the natural frequency prediction of the latter model (which is due to Eq. (2.30)) is slightly different from that of the former model (which is due to Eq. (2.14) for $r = 1$). It should be noted from Eqs. (2.34) and (2.35) that these are also functions of the damping ratios. Therefore, it is required to compare the results of these transmissibility functions for different values of damping ratio. Here, we use three different values of damping ratio ($\zeta = \zeta_1 = 0.01,\ 0.025,\ 0.05$) for comparison of the models. The relative motion transmissibility functions given by Eqs. (2.34) and (2.35) are shown in Figs. 2.4a and 2.4b, respectively. For convenience, the excitation frequency ω is normalized with respect to the fundamental natural frequency (of the Euler-Bernoulli beam model as it is assumed to be the accurate one) and therefore the frequency axis is denoted by $\Omega = \omega / \omega_1$. As can be seen from Fig 2.4, the frequency of maximum relative displacement transmissibility corresponds to $\Omega \cong 1$ in both models since the lumped-parameter approach gives a good estimate of the fundamental natural frequency (from Eq. (2.30)). However, it is not possible to draw the same conclusion from the amplitude-wise results. It is clear from Fig. 2.4 that the peak values for the same damping ratios are different for the distributed-parameter and the lumped-parameter model predictions.

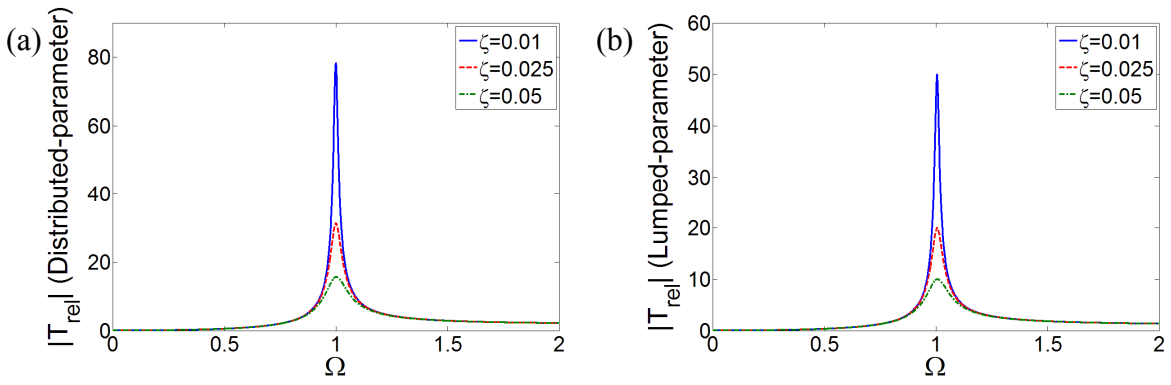

Fig. 2.4 Relative motion transmissibility functions for the transverse vibrations of a cantilevered beam without a tip mass; (a) distributed-parameter model and (b) lumped-parameter model

The percentage error in the lumped-parameter solution as a function of dimensionless frequency ratio is given by Fig. 2.5 (relative to the Euler-Bernoulli model). As can be seen from Fig 2.5, the relative error due to using the lumped-parameter approach in predicting the relative motion at the tip of the beam is very large. In the vicinity of the first natural frequency (i.e. for $\Omega \cong 1$), the error of the lumped-parameter model can be greater than 35 % regardless of the damping ratio. The interesting behavior in the relative error plot around the resonance is due to the 1.5 % error in the natural frequency predicted by the lumped-parameter approach. If the lumped-parameter natural frequency were taken to be identical to the first natural frequency of the Euler-Bernoulli model, one would obtain a smooth behavior in the error. Figure 2.5 shows

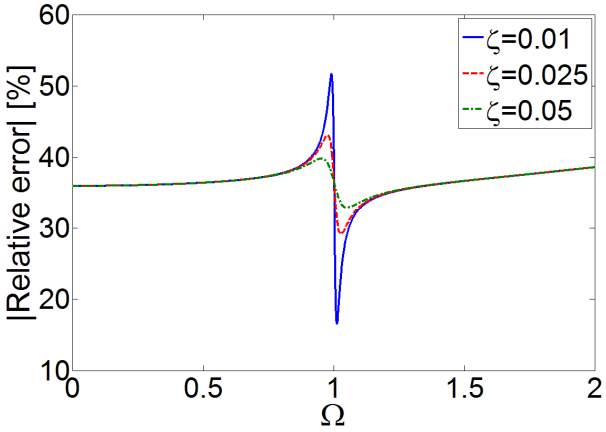

Fig. 2.5 Error in the relative motion transmissibility due to using the lumped-parameter model for a cantilevered beam without a tip mass in transverse vibrations

that the important error is in the prediction of the relative motion amplitude rather than the natural frequency. The error in the lumped-parameter model increases drastically at higher frequencies since higher vibration modes cannot be captured by the lumped-parameter approach.

2.2 Correction of the Lumped-parameter Model for Transverse Vibrations

2.2.1 Correction Factor for the Lumped-parameter Model. Since much of the vibration energy harvesting literature uses lumped-parameter modeling for design and optimization [2,3,8,10,13,16,22,27,28,31], a correction factor is presented for using the simplified lumped-parameter model. Consider the relative motion transmissibility function of the Euler-Bernoulli model given by Eq. (2.34). If the beam is excited around its first natural frequency, taking only the first term in the summation sign (neglecting the terms for $r \geq 2$) gives a good approximation for the resulting motion transmissibility. This reduced form of the Euler-Bernoulli model solution is denoted by T_{rel}^{EB*}:

$$T_{rel}^{EB*}(\omega,\zeta) = \frac{\mu_1 \omega^2}{{\omega_1}^2 - \omega^2 + j2\zeta\omega_1\omega} \tag{2.36}$$

which can reduced to

$$T_{rel}^{EB*}(\Omega,\zeta) = \frac{\mu_1 \Omega^2}{1 - \Omega^2 + j2\zeta\Omega} \tag{2.37}$$

where $\Omega = \omega/\omega_1$ is used and μ_1 corrects the excitation amplitude for the first transverse vibration mode of a cantilevered Euler-Bernoulli beam without a tip mass (for predicting the vibration response at $x = L$). Using $\lambda_1 = 1.87510407$ and $\sigma_1 = 0.734095514$ obtained from Eqs. (2.11) and (2.12) gives the *correction factor* for the first mode as

$$\mu_1 = \frac{2\sigma_1\left[\left(\cosh\lambda_1 - \cos\lambda_1\right) - \sigma_1\left(\sinh\lambda_1 - \sin\lambda_1\right)\right]}{\lambda_1} \cong 1.566 \tag{2.38}$$

It should be noted from Eqs. (2.35) and (2.36) that the reduced form of the Euler-Bernoulli solution for the first mode is indeed the correction factor μ_1 multiplied by the lumped-parameter solution (assuming that the lumped-parameter model natural frequency is accurate so that $\Omega = \omega/\omega_1 = \omega/\omega_n$). Therefore, μ_1 corrects the amplitude of the relative motion obtained from the lumped-parameter solution. The comparison of the relative motion transmissibility functions

obtained by using the Euler-Bernoulli model, the lumped-parameter model and the corrected lumped-parameter model are given in Fig. 2.6 for $\zeta = 0.05$. The agreement between the Euler-Bernoulli model (Eq. (2.34)) and the corrected lumped-parameter model (Eq. (2.36)) is very good over a wide frequency range around the fundamental resonance frequency and the corrected lumped-parameter relative motion transmissibility function starts deviating close to the region of the second natural frequency. The original lumped-parameter model prediction with Eq. (2.35) underestimates the relative motion transmissibility amplitude considerably with an error of about at least 35 % (see Fig. 2.5).

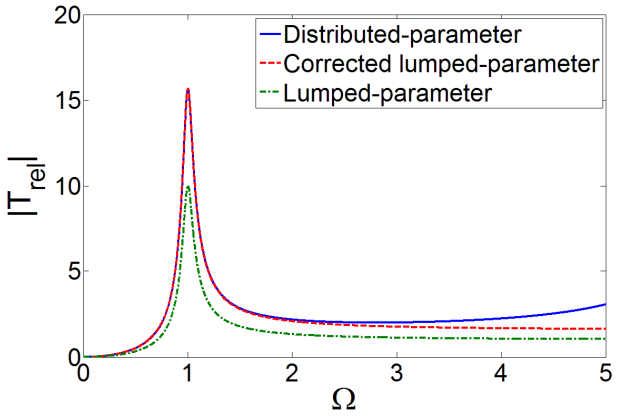

Fig. 2.6 Relative motion transmissibility functions obtained from the distributed-parameter, corrected lumped-parameter and the original lumped-parameter models for $\zeta = 0.05$

If the beam is to be excited not at the first natural frequency but at one of the higher mode frequencies, one can obtain the correction factor of the mode of interest (*r*-th mode) from the following relation

$$\mu_r = \frac{2\sigma_r\left[\left(\cosh\lambda_r - \cos\lambda_r\right) - \sigma_r\left(\sinh\lambda_r - \sin\lambda_r\right)\right]}{\lambda_r} \tag{2.39}$$

and then use it in the following expression of reduced relative motion transmissibility

$$T_{rel}^{EB*}(\Omega_r, \zeta_r) = \frac{\mu_r \Omega_r^{\,2}}{1 - \Omega_r^{\,2} + j2\zeta_r\Omega_r} \tag{2.40}$$

where the dimensionless frequency ratio is now $\Omega_r = \omega/\omega_r$ and ω_r is the undamped natural frequency of the *r*-th mode obtained from Eq. (2.14) and ζ_r is the modal damping ratio of the *r*-

th mode. Note that, since the modal parameters λ_r and σ_r do not depend on the aspect ratio of the beam in the Euler-Bernoulli beam theory, the correction factor μ_r of the *r*-th mode is unique in the absence of a tip mass. That is, the correction factor for the fundamental mode is $\mu_1 \cong 1.566$ for any uniform cantilevered Euler-Bernoulli beam without a tip mass in transverse vibrations (so long as the beam aspect ratio justifies the Euler-Bernoulli beam assumptions).[**] However, the presence of a tip mass affects the correction factor which is discussed in the following section.

2.2.2 Effect of a Tip Mass on the Correction Factor. In some cases, it is required to attach a tip mass (proof mass) to the beam in order to tune its fundamental natural frequency to the excitation frequency and to improve its dynamic flexibility. If the differential eigenvalue problem is solved for a uniform cantilevered beam with a tip mass of M_t rigidly attached at $x = L$, the eigenfunctions can be obtained as[††]

$$\phi_r(x) = C_r\left[\cos\frac{\lambda_r}{L}x - \cosh\frac{\lambda_r}{L}x + \varsigma_r\left(\sin\frac{\lambda_r}{L}x - \sinh\frac{\lambda_r}{L}x\right)\right] \tag{2.41}$$

where ς_r is obtained from

$$\varsigma_r = \frac{\sin\lambda_r - \sinh\lambda_r + \lambda_r\dfrac{M_t}{mL}\left(\cos\lambda_r - \cosh\lambda_r\right)}{\cos\lambda_r + \cosh\lambda_r - \lambda_r\dfrac{M_t}{mL}\left(\sin\lambda_r - \sinh\lambda_r\right)} \tag{2.42}$$

and C_r is a modal amplitude constant which should be evaluated by normalizing the eigenfunctions according to the following orthogonality conditions:

[**] In the discussion given here, the correction factor is defined to predict the motion exactly at the tip. It should be noted that distributed-parameter modeling allows predicting the motion transmitted from the base to any arbitrary point of the beam. In such a case the numerical value of the correction factor obviously changes (e.g. μ_1 takes a value lower that 1.566 for the fundamental mode) but it is still independent of the aspect ratio as long as the beam is sufficiently thin, geometrically and materially uniform and linear vibrations are considered.

[††] Here, it is assumed that the uniform thin beam with a tip mass can be approximated as a normal-mode system so that the eigenfunctions of the undamped problem can be used for modal analysis of the damped problem [38]. Banks et al. [43] pointed out the mathematical limitations of the normal-mode assumption for combined dynamical systems, i.e. distributed-parameter systems with discrete elements.

$$\int_0^L \phi_s(x) m \phi_r(x) dx + \phi_s(L) M_t \phi_r(L) = \delta_{rs}$$
$$\int_0^L \phi_s(x) YI \frac{d^4\phi_r(x)}{dx^4} dx - \left[\phi_s(x) YI \frac{d^3\phi_r(x)}{dx^3} \right]_{x=L} = \omega_r{}^2 \delta_{rs} \tag{2.43}$$

The natural frequency expression given by Eq. (2.14) still holds but the dimensionless eigenvalues (λ_r for the *r*-th mode) should be obtained from

$$1 + \cos\lambda \cosh\lambda + \lambda \frac{M_t}{mL} \left(\cos\lambda \sinh\lambda - \sin\lambda \cosh\lambda \right) = 0 \tag{2.44}$$

where M_t / mL is a dimensionless parameter as it is the tip mass – to – beam mass ratio. In the above equations, the rotary inertia of the tip mass is neglected for convenience, i.e. the tip mass is assumed to be a point mass.

In addition to the modification of the eigenvalue problem in the presence of a tip mass, the forcing term due to base excitation also changes since the tip mass also contributes to the inertia of the structure. Equation (2.5) becomes

$$YI \frac{\partial^4 w_{rel}(x,t)}{\partial x^4} + c_s I \frac{\partial^5 w_{rel}(x,t)}{\partial x^4 \partial t} + c_a \frac{\partial w_{rel}(x,t)}{\partial t} + m \frac{\partial^2 w_{rel}(x,t)}{\partial t^2} = -\left[m + M_t \delta(x - L) \right] \frac{\partial^2 w_b(x,t)}{\partial t^2} \tag{2.45}$$

where $\delta(x)$ is the Dirac delta function and the forcing term due to external damping is neglected. The modal forcing function corresponding to the right hand side of Eq. (2.45) is then

$$f_r(t) = -m \left(\frac{d^2 g(t)}{dt^2} \int_0^L \phi_r(x) dx + \frac{d^2 h(t)}{dt^2} \int_0^L x \phi_r(x) dx \right) - M_t \phi_r(L) \left(\frac{d^2 g(t)}{dt^2} + L \frac{d^2 h(t)}{dt^2} \right) \tag{2.46}$$

Expectedly, the foregoing modification results in variation of the correction factor defined in the previous section. Since the base is assumed to be not rotating (i.e. $h(t) = 0$) in deriving the correction factor, one can extract the expression of the correction factor μ_1 in the presence of a tip mass as

$$\mu_1 = \phi_1(L) \left(M_t \phi_1(L) + m \int_0^L \phi_1(x) dx \right) \tag{2.47}$$

The variation of the correction factor μ_1 of the fundamental transverse vibration mode given by Eq. (2.47) with tip mass (M_t) – to – beam mass (mL) ratio is shown in Fig. 2.7.

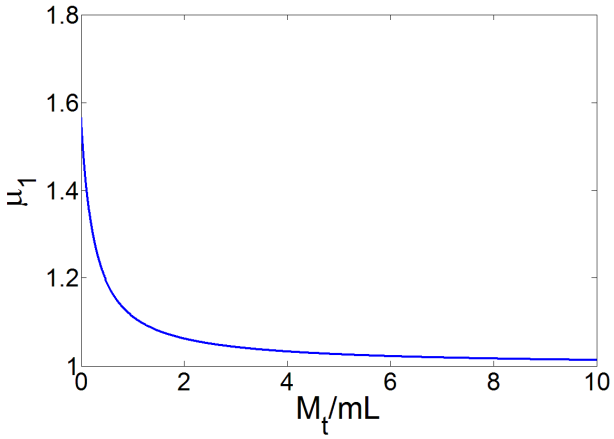

Fig. 2.7 Variation of the correction factor for the fundamental transverse vibration mode with tip mass – to – beam mass ratio

It can be read from Fig. 2.7 that when there is no tip mass ($M_t / mL = 0$), $\mu_1 \cong 1.566$ as previously obtained, whereas as M_t / mL becomes larger ($M_t / mL \to \infty$), μ_1 approaches to unity. The important conclusion drawn from Fig. 2.7 is that the *uncorrected* lumped-parameter model can be used safely only when the tip mass is sufficiently larger than the beam mass. From the physical point of view, if the tip mass is sufficiently large, the inertia of the tip mass dominates in the forcing function and the distributed inertia of the beam (as a component of excitation) becomes negligible. Table 2.1 shows the values μ_1 takes for different M_t / mL ratios. It should be noted that, for the uncorrected lumped-parameter formulation $\mu_1 = 1$, and therefore, the relative error in the motion at the tip of the beam predicted by the uncorrected lumped-parameter model is estimated from $\left(1 - \mu_1\right) / \mu_1 \times 100$.

The following quadratic polynomial ratio obtained by using the Curve Fitting Toolbox of MATLAB [44] gives an estimate of μ_1 with an error less than 9×10^{-3} % for all values of M_t / mL:

$$\mu_1 = \frac{\left(M_t / mL\right)^2 + 0.603\left(M_t / mL\right) + 0.08955}{\left(M_t / mL\right)^2 + 0.4637\left(M_t / mL\right) + 0.05718} \tag{2.48}$$

Table 2.1 Correction factor for the fundamental transverse vibration mode and the error in the uncorrected lumped-parameter model for different tip mass – to – beam mass ratios

M_t / mL	μ_1	Error in the uncorrected lumped-parameter model [%]
0	1.56598351	-36.14
0.1	1.40764886	-28.96
0.5	1.18922917	-15.91
1	1.11285529	-10.14
5	1.02662125	-2.59
10	1.01361300	-1.34

2.3 Experimental Case Studies for Validation of the Correction Factor

This section provides experimental demonstrations for the use of the correction factor in order to improve the predictions of the lumped-parameter base excitation model in the absence and presence of a tip mass. The bimorph cantilever discussed in the following is investigated extensively in Chapter 4 for validation of the distributed-parameter electromechanical models developed in Chapter 3. Detailed information regarding the cantilever and the experimental setup can therefore be found in Chapter 4. Here, only the motion transmissibility FRFs are considered in order to validate the amplitude correction factor derived in this chapter. Each one of the two cases presented here uses the measurement taken for an external electrical load close to short-circuit conditions of the electrodes (very low external impedance). Therefore, the following cases can be considered as very close to being electromechanically uncoupled (i.e. having negligible piezoelectric shunt damping effect), in agreement with the formulation given in this chapter (where the purpose is to improve the mechanical aspect of the existing lumped-parameter electromechanical model). The electromechanically coupled distributed-parameter dynamics of these configurations are modeled and validated in Chapters 3 and 4, respectively.

2.3.1 Cantilevered Beam without a Tip Mass under Base Excitation. The cantilever considered here is a T226-H4-203X type bimorph manufactured by Piezo Systems, Inc. [45].

Detailed electromechanical analysis of this sample can be found in Section 4.1. Here, the experimental data for a $470\,\Omega$ load resistance (close to short-circuit conditions) is considered to validate the corrected lumped-parameter base excitation relation given by Eq. (2.36) and to demonstrate the failure of the original relation given by Eq. (2.35) in predicting the vibration response. It should be noted from Table 4.1 that the overhang length, width and the thickness of the cantilever are 24.53 mm, 6.4 mm and 0.670 mm, respectively. Therefore the overhang length – to – total thickness ratio of the bimorph cantilever is about 37.7 and the Euler-Bernoulli formulation can safely be used as far as the fundamental vibration mode is concerned.

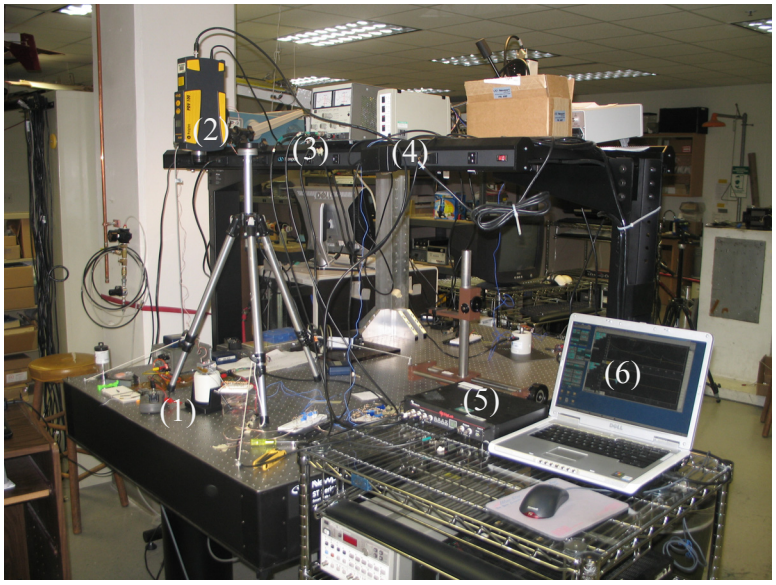

(1) Shaker with a small accelerometer and the cantilever
(2) Laser vibrometer
(3) Fixed gain amplifier (power supply)
(4) Charge amplifier
(5) Data acquisition system
(6) Frequency response analyzer (software)

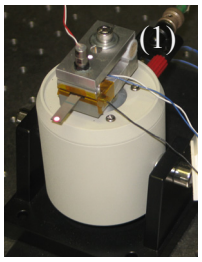

Fig. 2.8 Experimental setup used for the frequency response measurements of a uniform bimorph cantilever (photos by A. Erturk, 2009)

The experimental setup used for the frequency response measurement is shown in Fig. 2.8 (referred from Chapter 4). The bimorph cantilever is clamped onto a small electromagnetic shaker (TMC Model TJ-2 [46]). A small accelerometer (PCB Piezotronics Model U352C67 [47]) is attached via wax close to the root of the cantilever on the clamp. The tip velocity response of the cantilever is measured using a laser vibrometer (Polytec PDV100 [48]) by attaching a small reflector tape at the tip of the cantilever (see Fig. 2.9a for an enlarged view). Chirp excitation (burst type with five averages) is used for the frequency response measurement through the data acquisition system (SigLab Model 20-42) [49]. The ratio of the vibrometer measurement to the

acceleration measurement in the frequency domain defines the tip velocity – to – base acceleration FRF.

(a) 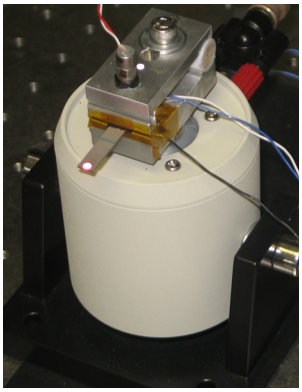 (b) 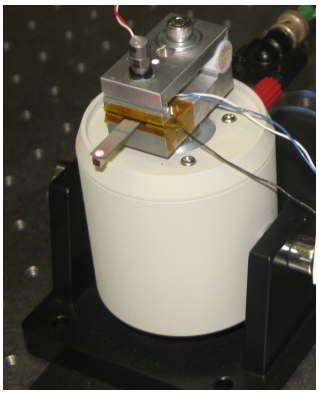

Fig. 2.9 Close views of the cantilever tested under base excitation (a) without and (b) with a tip mass attachment (photos by A. Erturk, 2009)

It is important to note that the laser vibrometer measures the velocity response at the center of the reflector tape that is attached near the tip of the cantilever (i.e. not exactly at $x = L$). If the point of the velocity measurement is $x = L_v$, Eq. (2.47) should be modified to

$$\mu_1^* = \phi_1(L_v)\left(M_t \phi_1(L) + m\int_0^L \phi_1(x)dx \right) \tag{2.49}$$

where μ_1^* is the modified form of the correction factor that accounts for the small distance of the point of velocity measurement from the tip. In the experiments, the position of the velocity measurement on the cantilever is $L_v = 23\,\text{mm}$ from the root (i.e. approximately 1.5 mm from the tip). For this point of velocity measurement, the variation of the correction factor with tip mass – to – beam mass ratio is given by Fig. 2.10. In the absence of a tip mass, the modified correction factor is $\mu_1^* = 1.431$ and it can be used in Eq. (2.36) to predict the vibratory motion at $x = L_v$.

It should also be noted at this stage that the theoretical discussion given so far is for the tip displacement – to – base displacement FRF. However, the measurements taken with this experimental setup are the tip velocity and the base acceleration of the cantilever. Moreover, the experimental velocity measurement is relative to the fixed frame, i.e. it is not the tip velocity of the cantilever relative to its moving base. One option for comparing the experimental data and the analytical predictions is to process the experimentally measured FRF to bring it to the form

of Eqs. (2.35) and (2.36). The second option is to bring the analytical relative displacement transmissibility functions given by these equations to the form of the experimental measurement. The second option is preferred in order not to create a possible noise in the experimental data due to post-processing. The relative displacement transmissibility FRF (Eqs. (2.35) and (2.36)) can be used in the following relation to give the absolute tip velocity – to – base acceleration FRF as

$$\frac{\left.\dfrac{\partial w(x,t)}{\partial t}\right|_{x=L_v}}{-\omega^2 W_0 e^{j\omega t}} = \frac{1+T_{rel}(\omega,\zeta)}{j\omega} \tag{2.50}$$

In addition, the experimental FRFs are given per gravitational acceleration ($g = 9.81\,\mathrm{m/s^2}$), i.e. Eq. (2.50) should be multiplied by g in order to compare with the experimental data.

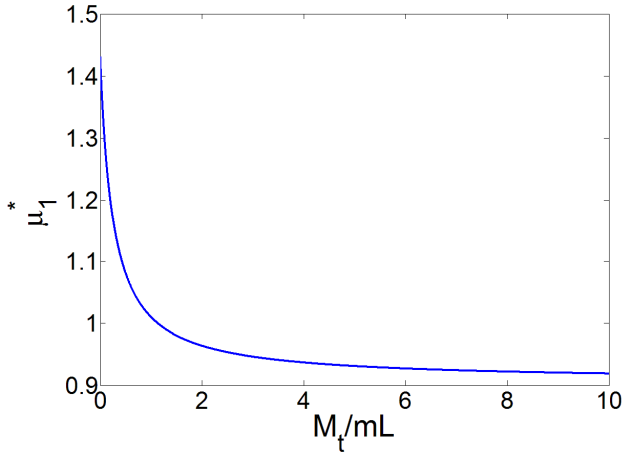

Fig. 2.10 Variation of the modified correction factor for the fundamental transverse vibration mode with tip mass – to – beam mass ratio

Figure 2.11a shows the experimental frequency response measurement and its prediction by Eqs. (2.35) and (2.36) (when used in Eq. (2.50)). The undamped natural frequency of the cantilever (close to short-circuit conditions) is 502.5 Hz ($\omega_n = 3157.3\,\mathrm{rad/s}$) and the mechanical damping ratio identified in Section 4.1 is 0.874 % ($\zeta = 0.00874$). As can be seen in Fig. 2.11b, the coherence [50,51] of the measurement is very good (unity). Therefore the measurement is reliable for the frequency range of interest.

Since the cantilever does not have a tip mass ($M_t / mL = 0$), the modified amplitude correction factor is obtained from Eq. (2.49) or from Fig 2.10 as $\mu_1^* \cong 1.431$. It is observed from Fig. 2.11a that the corrected lumped-parameter model (due to Eq. (2.36)) is in very good agreement with the experimental FRF whereas the uncorrected lumped-parameter model (due to Eq. (2.35)) underestimates the vibration amplitude considerably (note that the vertical axis in Fig. 2.11a is given in log-scale).‡‡ Therefore, in agreement with the theoretical discussion given with Fig. 2.6, the commonly referred form of the lumped-parameter base excitation model results in significantly inaccurate prediction of the vibration response in the absence of a tip mass. The inaccurate prediction is in the form of *underestimation* of the vibration response amplitude.

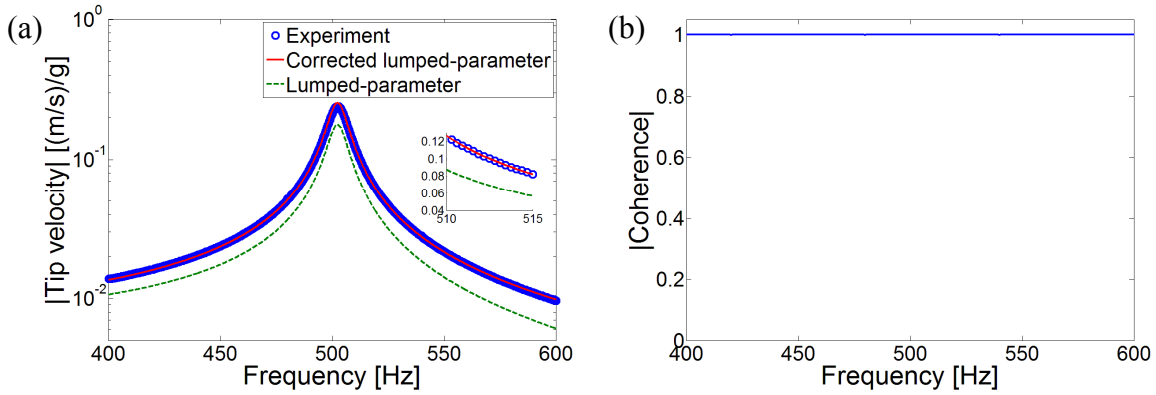

Fig. 2.11 (a) Tip velocity – to – base acceleration FRFs of a cantilever without a tip mass: experimental measurement, corrected lumped-parameter and uncorrected lumped-parameter model predictions; (b) coherence function of the experimental measurement

2.3.2 Cantilevered Beam with a Tip Mass under Base Excitation. The second case study is given for the same cantilever after a tip mass of 0.239 grams is attached at the tip using a slight amount of wax (Fig. 2.9b). Detailed electromechanical analysis of the cantilever with a tip mass is given in Section 4.2. The demonstration given here aims to estimate the correction factor and

‡‡ The form of the uncorrected lumped-parameter equation given by Eq. (2.35) is originally defined to predict the tip motion but the experimental measurement belongs to the point $x = L_v$. Nevertheless since this lumped-parameter expression underestimates the motion amplitude at $x = L_v$ it would certainly underestimate the motion amplitude at the exact point of $x = L$ where the vibration amplitude is larger for the fundamental mode.

to verify the need for using it. For this tip mass ($M_t = 0.239\times10^{-3}$ kg) and for the numerical data of the cantilever given with Table 4.4, the tip mass – to – beam mass ratio is $M_t / mL = 0.291$. This ratio yields $\mu_1^* = 1.149$ either using Eq. (2.49) or Fig. 2.10. As discussed theoretically, in the presence of a tip mass, predictions of the original lumped-parameter equation are not expected to be as inaccurate as the case when there is no tip mass. Recall that, in the extreme case of having a very large tip mass, the correction factor is not required. However, in this experimental case study, the tip mass is not large enough to ignore the excitation coming from the distributed mass of the cantilever.

Figure 2.12a shows the experimental tip velocity – to – base acceleration FRF (for a $470\,\Omega$ load resistance) along with the predictions of Eqs. (2.35) and (2.36) when used in Eq. (2.50). As can be seen from the enlarged view in Fig. 2.11a, the uncorrected lumped-parameter model underestimates the experimental measurement but the error is not as large as in the case of Fig. 2.11a. The prediction of the corrected lumped-parameter equation (obtained using $\mu_1^* = 1.149$ in Eq. (2.36)) agrees very well with the experimental data.

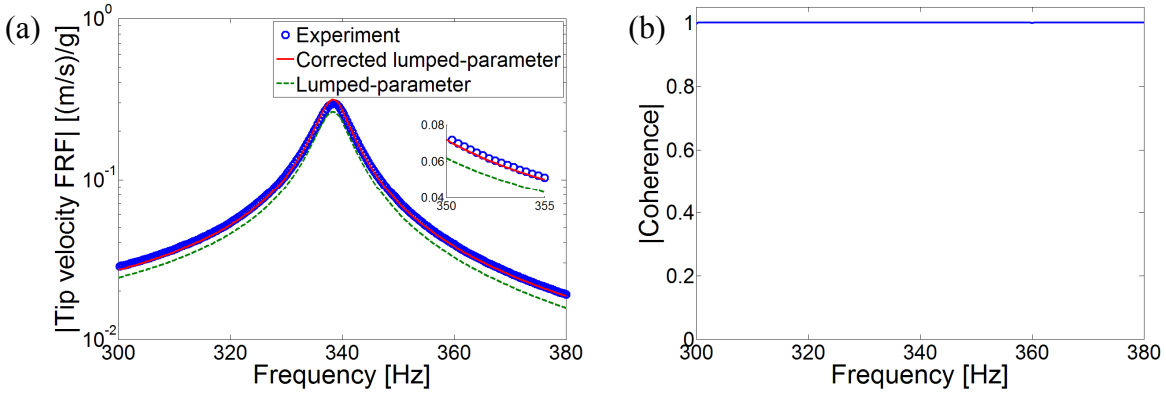

Fig. 2.12 (a) Tip velocity – to – base acceleration FRFs of a cantilever with a tip mass: experimental measurement, corrected lumped-parameter and uncorrected lumped-parameter model predictions; (b) coherence function of the experimental measurement

2.4 Base Excitation Problem for Longitudinal Vibrations and Correction of Its Lumped-parameter Model

So far the base excitation problem of a beam in transverse vibrations has been discussed in detail and experimental validations have been provided for its corrected lumped-parameter model. This section summarizes the same problem for longitudinal vibrations of a uniform cantilevered bar under base excitation (Fig. 2.13). As in the case of transverse vibrations, the electromechanically uncoupled problem is considered in order to correct the excitation amplitude of its lumped-parameter model.

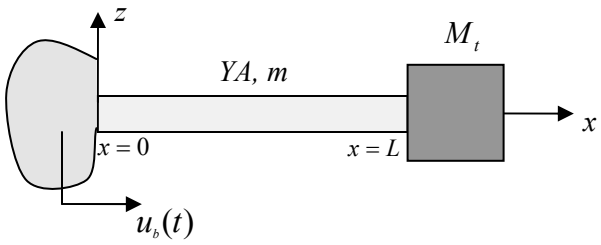

Fig. 2.13 Cantilevered bar with a tip mass longitudinally excited by the translation of its base

2.4.1 Analytical Modal Analysis and Steady-state Response to Harmonic Base Excitation. The uniform clamped-free bar shown in Fig. 2.13 is subjected to the arbitrary translation of its base, which is denoted by $u_b(t)$. The equation of motion for the longitudinal free vibrations of a uniform bar can be written as

$$YA\frac{\partial^2 u(x,t)}{\partial x^2} + c_s A\frac{\partial^3 u(x,t)}{\partial x^2 \partial t} - c_a\frac{\partial u(x,t)}{\partial t} - m\frac{\partial^2 u(x,t)}{\partial t^2} = 0 \tag{2.51}$$

where YA is the axial stiffness (Y is the elastic modulus and A is the cross-sectional area) and m is the mass per unit length of the bar. The absolute longitudinal displacement at any point x can be represented by $u(x,t) = u_b(t) + u_{rel}(x,t)$. The damping mechanism is again represented by two terms: c_s is due to internal (structural) friction and c_a accounts for external viscous (air) damping.[§§] Proportional damping is assumed as it allows analytical modal analysis.

[§§] Although the same notation is used for some of the terms (such as the damping coefficients) of the transverse vibrations case, they are not necessarily identical.

After following steps similar to the derivation given for the transverse vibrations case in Section 2.1, the longitudinal vibration response of the bar relative to its moving base can be obtained as

$$u_{rel}(x,t)=\sum_{r=1}^{\infty}\frac{\varphi_r(x)}{\omega_{rd}}\int_0^t f_r(\tau)e^{-\zeta_r\omega_r(t-\tau)}\sin\omega_{rd}(t-\tau)d\tau \tag{2.52}$$

Here, the modal forcing function is

$$f_r(t)=-\frac{d^2u_b(t)}{dt^2}\left[m\int_0^L\varphi_r(x)dx+M_t\varphi_r(L)\right] \tag{2.53}$$

where the forcing term due to air damping is neglected. It should be noted from Eq. (2.53) that the excitation coming from the tip mass is directly considered in the modal forcing.

The undamped natural frequency ω_r of the *r*-th vibration mode is obtained from

$$\omega_r=\alpha_r\sqrt{\frac{EA}{mL^2}} \tag{2.54}$$

and ω_{rd} in Eq. (2.52) is the damped natural frequency given by $\omega_{rd}=\omega_r\sqrt{1-\zeta_r{}^2}$ where ζ_r is the modal damping ratio of the *r*-th vibration mode. The mass normalized eigenfunction $\varphi_r(x)$ of the *r*-th mode can be expressed as

$$\varphi_r(x)=\frac{1}{\sqrt{\frac{mL}{2}\left(1-\frac{\sin 2\alpha_r}{2\alpha_r}\right)+M_t\sin^2\alpha_r}}\sin\frac{\alpha_r}{L}x \tag{2.55}$$

Along with the geometric and natural boundary conditions at $x=0$ and $x=L$, respectively, the eigenfunctions given by Eq. (2.55) satisfy the following orthogonality conditions:

$$\begin{aligned}\int_0^L\varphi_s(x)m\varphi_r(x)dx+\varphi_s(L)M_t\varphi_r(L)&=\delta_{rs}\\ -\int_0^L\varphi_s(x)YA\frac{d^2\varphi_r(x)}{dx^2}dx+\left[\varphi_s(x)YA\frac{d\varphi_r(x)}{dx}\right]_{x=L}&=\omega_r{}^2\delta_{rs}\end{aligned} \tag{2.56}$$

The eigenvalues (α_r for mode *r*) are the roots of the characteristic equation

$$\frac{M_t}{mL}\alpha\sin\alpha-\cos\alpha=0 \tag{2.57}$$

For a harmonic base displacement input, $u_b(t)=U_0e^{j\omega t}$, the steady-state displacement response relative to the moving base becomes

$$u_{rel}(L,t)=\sum_{r=1}^{\infty}\frac{\sin\alpha_r\left(\dfrac{1-\cos\alpha_r}{\alpha_r}+\dfrac{M_t}{mL}\sin\alpha_r\right)\omega^2U_0e^{j\omega t}}{\left[\dfrac{2\alpha_r-\sin 2\alpha_r}{4\alpha_r}+\dfrac{M_t}{mL}\sin^2\alpha_r\right]\left({\omega_r}^2-\omega^2+j2\zeta_r\omega_r\omega\right)} \tag{2.58}$$

2.4.2 Correction Factor for Longitudinal Vibrations. The relative motion transmissibility between the tip of the bar and the moving base can be extracted from Eq. (2.58) as

$$T_{rel}(\omega,\zeta_r)=\frac{u_{rel}(L,t)}{U_0e^{j\omega t}}=\sum_{r=1}^{\infty}\frac{\kappa_r\omega^2}{{\omega_r}^2-\omega^2+j2\zeta_r\omega_r\omega} \tag{2.59}$$

where

$$\kappa_r=\frac{\sin\alpha_r\left(\dfrac{1-\cos\alpha_r}{\alpha_r}+\dfrac{M_t}{mL}\sin\alpha_r\right)}{\dfrac{2\alpha_r-\sin 2\alpha_r}{4\alpha_r}+\dfrac{M_t}{mL}\sin^2\alpha_r} \tag{2.60}$$

is the correction factor for the lumped-parameter model of the *r*-th mode for longitudinal vibrations (to predict the vibratory motion at $x=L$). Note that, κ_r is a function of M_t/mL and α_r due to Eq. (2.60), and α_r is a function of M_t/mL from Eq. (2.57). Therefore, for a given vibration mode, the correction factor κ_r is a function of M_t/mL only. In the absence of a tip mass ($M_t/mL=0$), the correction factor for the fundamental mode can explicitly be obtained from Eqs. (2.57) and (2.60) as $\kappa_1=4/\pi\cong 1.273$. However, in the presence of a tip mass, the transcendental equation given by Eq. (2.57) should be solved numerically to obtain the correction factor. The variation of the correction factor of the fundamental mode (κ_1) with M_t/mL is given in Fig. 2.14.

As in the transverse vibrations case, the correction factor tends to unity as the tip mass to beam mass ratio increases, meaning that the *uncorrected* lumped-parameter model can be used only for bars whose tip mass is much larger than the bar mass. Table 2.2 shows the correction factor κ_1 for lumped-parameter modeling of the fundamental longitudinal vibration mode for different M_t/mL ratios. Note that the error in the relative motion u_{rel} at the tip of the bar predicted by using the uncorrected lumped-parameter model is simply obtained from $(1-\kappa_1)/\kappa_1\times 100$.

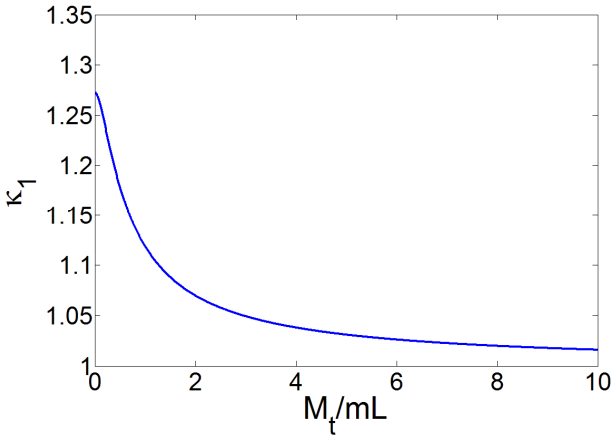

Fig. 2.14 Variation of the correction factor for the fundamental longitudinal vibration mode with tip mass – to – beam mass ratio

The following quadratic polynomial ratio obtained by using the Curve Fitting Toolbox of MATLAB [44] represents the behavior of the correction factor shown in Fig. 2.14 successfully with a maximum error less than $4.5\times10^{-2}\,\%$ for all values of M_t/mL:

$$\kappa_1 = \frac{\left(M_t/mL\right)^2 + 0.7664\left(M_t/mL\right) + 0.2049}{\left(M_t/mL\right)^2 + 0.6005\left(M_t/mL\right) + 0.161} \tag{2.61}$$

Table 2.2 Correction factor for the longitudinal vibration mode and the error in the uncorrected lumped-parameter model for different tip mass – to – bar mass ratios

M_t/mL	κ_1	Error in the uncorrected lumped-parameter model [%]
0	1.27323954	-21.46
0.1	1.26196259	-20.76
0.5	1.17845579	-15.14
1	1.11913201	-10.65
5	1.03108765	-3.02
10	1.01609422	-1.58

2.5 Correction Factor in the Electromechanically Coupled Lumped-parameter Equations and a Theoretical Case Study

This section introduces the amplitude correction factor to the electromechanically coupled lumped-parameter piezoelectric energy harvester equations. The lumped-parameter electromechanical equations of a piezoelectric energy harvester are obtained by applying Newton's second law (or d'Alembert's principle) in the mechanical domain, Kirchhoff's laws in the electrical domain and also including the electromechanical coupling effects coming from the piezoelectric constitutive relations [26].

2.5.1 An Electromechanically Coupled Lumped-parameter Model for Piezoelectric Energy Harvesting. Recently, a lumped-parameter piezoelectric energy harvester model was introduced by duToit et al. [16]. Figure 2.15 shows the schematic of their cantilevered energy harvester which is excited by the motion of its base in the longitudinal direction. Therefore, this model uses longitudinal vibrations of the piezoceramic for power generation. The design depicted in Fig. 2.15 for longitudinal vibrations (almost like an accelerometer) typically results in a very high fundamental natural frequency, which is not preferred for vibration energy harvesting as it will not match with typical ambient vibration frequencies. Nevertheless this lumped-parameter representation provides useful insight into the electromechanical problem for a simplified analysis of the coupled system dynamics.

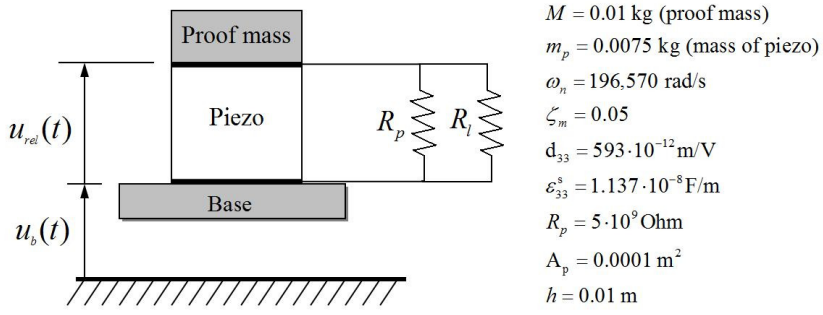

Fig. 2.15 A lumped-parameter piezoelectric energy harvester model with sample numerical values by duToit et al. [16] (reproduced by adapting the displacement variables to this text)

As the longitudinal strain and the electric field directions are the same, the device shown in Fig. 2.15 uses the 33-mode of piezoelectricity (and therefore the d_{33} constant of the piezoceramic) where 3-direction (poling direction) is the longitudinal direction. The electrodes are connected to an equivalent resistive load R_{eq} (which is the parallel combination of the piezoelectric leakage resistance R_p and the load resistance R_l where $R_l << R_p$ hence $R_{eq} \approx R_l$). The coupled lumped-parameter equations are given by duToit et al. [16] as[***]

$$\frac{d^2u_{rel}}{dt^2} + 2\zeta_m\omega_n \frac{du_{rel}}{dt} + \omega_n{}^2 u_{rel} - \omega_n{}^2 d_{33} v = -\frac{d^2u_b}{dt^2} \tag{2.62}$$

$$R_{eq}C_p \frac{dv}{dt} + v + m_{eq}R_{eq}d_{33}\omega_n{}^2 \frac{du_{rel}}{dt} = 0 \tag{2.63}$$

where m_{eq} is the equivalent mass of the bar, ζ_m is the mechanical damping ratio, ω_n is the natural frequency, d_{33} is the piezoelectric constant, R_{eq} is the equivalent resistance, C_p is the capacitance, u_b is the harmonic base excitation, u_{rel} is the relative displacement of the proof mass and v is the voltage output. One can then obtain the steady-state vibration response, voltage output and the power output FRFs (per base acceleration) by assuming $u_b(t) = U_0 e^{j\omega t}$ as

$$\left|\frac{u_{rel}}{\ddot{u}_b}\right| = \frac{1/\omega_n{}^2\sqrt{1+(r\Omega)^2}}{\sqrt{\left[1-(1+2\zeta_m r)\Omega^2\right]^2 + \left[(1+k_e^2)r\Omega + 2\zeta_m\Omega - r\Omega^3\right]^2}} \tag{2.64}$$

$$\left|\frac{v}{\ddot{u}_b}\right| = \frac{m_{eff}R_{eq}d_{33}\omega_n\Omega}{\sqrt{\left[1-(1+2\zeta_m r)\Omega^2\right]^2 + \left[(1+k_e^2)r\Omega + 2\zeta_m\Omega - r\Omega^3\right]^2}} \tag{2.65}$$

$$\left|\frac{P}{(\ddot{u}_b)^2}\right| = \frac{m_{eff}1/\omega_n r k_e^2 R_{eq}/R_l\Omega^2}{\left[1-(1+2\zeta_m r)\Omega^2\right]^2 + \left[(1+k_e^2)r\Omega + 2\zeta_m\Omega - r\Omega^3\right]^2} \tag{2.66}$$

where $\Omega = \omega/\omega_n$ is the dimensionless frequency, k_e is the lumped-parameter coupling coefficient and $r = \omega_n R_{eq} C_p$ [16].

2.5.2 Correction Factor in the Electromechanically Coupled Lumped-parameter Model and a Theoretical Case Study. From the theoretical discussion given in Section 2.4, it is known

[***] Some of the variables have been adapted to the notation of this text.

that the right hand side of the mechanical equilibrium equation given by Eq. (2.62) should have a correction factor (to be valid for all values of the proof mass). Therefore the corrected form of Eq. (2.62) is

$$\frac{d^2u_{rel}}{dt^2}+2\zeta_m\omega_n\frac{du_{rel}}{dt}+\omega_n{}^2u_{rel}-\omega_n{}^2d_{33}v=-\kappa_1\frac{d^2u_b}{dt^2} \tag{2.67}$$

Then the steady-state vibration response, voltage and the power output FRFs given by Eqs. (2.64)-(2.66) become

$$\left|\frac{u_{rel}}{\ddot{u}_b}\right|=\frac{\kappa_1/\omega_n{}^2\sqrt{1+\left(r\Omega\right)^2}}{\sqrt{\left[1-\left(1+2\zeta_m r\right)\Omega^2\right]^2+\left[\left(1+k_e^2\right)r\Omega+2\zeta_m\Omega-r\Omega^3\right]^2}} \tag{2.68}$$

$$\left|\frac{v}{\ddot{u}_b}\right|=\frac{\kappa_1 m_{eff}R_{eq}d_{33}\omega_n\Omega}{\sqrt{\left[1-\left(1+2\zeta_m r\right)\Omega^2\right]^2+\left[\left(1+k_e^2\right)r\Omega+2\zeta_m\Omega-r\Omega^3\right]^2}} \tag{2.69}$$

$$\left|\frac{P}{\left(\ddot{u}_b\right)^2}\right|=\frac{\kappa_1{}^2m_{eff}1/\omega_n r k_e^2R_{eq}/R_l\Omega^2}{\left[1-\left(1+2\zeta_m r\right)\Omega^2\right]^2+\left[\left(1+k_e^2\right)r\Omega+2\zeta_m\Omega-r\Omega^3\right]^2} \tag{2.70}$$

Note that the steady-state vibration response and the voltage response are linearly proportional to κ_1. However, since it is proportional to the square of the voltage, the power output is proportional to the square of κ_1. Hence the inaccuracy of the predicted power output due to using Eq. (2.66) is expected to be more significant than that of the vibration amplitude or the voltage output.

Using the numerical values given Fig. 2.15 (referred from duToit et al. [16]), the tip mass – to – bar mass ratio of this sample device is obtained as $M_t/mL\cong 1.33$. From Eq. (2.61), the correction factor for the fundamental mode for this ratio is $\kappa_1\cong 1.0968$. If this factor is not used, the relative error in the predicted proof mass motion and the voltage output is about 8.83 % whereas the relative error in the estimated power output is about 16.9 %. Figure 2.16 shows the vibration and the power FRFs obtained using the uncorrected and the corrected equations for an arbitrary load resistance of 10 $\mathrm{k}\Omega$ and a base acceleration of 9.81 m/s^2.

The inaccuracy due to ignoring the contribution of the distributed mass of the structure to the excitation amplitude is also the case in the lumped-parameter model given by Roundy et al. [6,7,15] for transverse vibrations (unless the tip mass is very large).

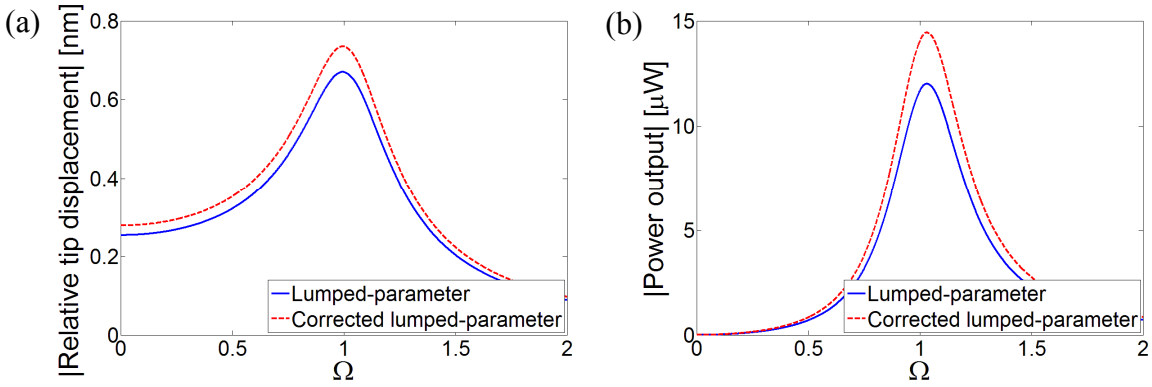

Fig. 2.16 Corrected and uncorrected (a) relative tip displacement and (b) power output FRFs obtained using the lumped-parameter electromechanical model for a load resistance of 10 kΩ and a base acceleration of 9.81 m/s^2

2.6 Summary and Conclusions

In this chapter, first the distributed-parameter modeling of the base excitation problem is reviewed for cantilevered thin-beams. The form of the base excitation assumed here is translation in the transverse direction with superimposed small rotation. After obtaining the distributed-parameter displacement transmissibility function, it is compared with the well-known lumped-parameter transmissibility function. Based on a dimensionless comparison, it is shown that the prediction of the lumped-parameter base excitation relation might have an error as high as 35 %. The error in the lumped-parameter model is due to the fact that it ignores the contribution of the distributed inertia to the excitation amplitude. A correction factor is introduced to correct the excitation amplitude in the lumped-parameter representation and the variation of the correction factor with tip mass – to – beam mass ratio is investigated. It is shown that the original form of the lumped-parameter base excitation model can be used only if the tip mass is much larger than the beam mass. Experimental validations of the corrected lumped-parameter model are given for a small cantilever in the absence and presence of a tip mass. Modeling of the base excitation problem is summarized for cantilevered bars under longitudinal vibrations and the lumped-parameter model of the longitudinal vibration case is also corrected. Finally, the correction factor is introduced to the lumped-parameter electromechanical equations and a comparative case study is given.

CHAPTER 3

DISTRIBUTED-PARAMETER ELECTROMECHANICAL MODELING OF BIMORPH PIEZOELECTRIC ENERGY HARVESTERS – ANALYTICAL SOLUTIONS

In this chapter, electromechanically coupled analytical solutions are given for symmetric bimorph piezoelectric energy harvester configurations with series and parallel connections of the piezoceramic layers. The base excitation acting on the bimorph cantilever is assumed to be translation in the transverse direction with superimposed small rotation. After describing the modeling assumptions and the bimorph configurations, the distributed-parameter thin beam equation (the Euler-Bernoulli beam equation) with piezoelectric coupling is derived and its modal analysis in short-circuit conditions is given. The electromechanically coupled circuit equation excited by infinitely many vibration modes is then derived based on the Gauss's law and the plane-stress piezoelectric constitutive relation for a thin beam. The governing electromechanical equations are then reduced to ordinary differential equations in modal coordinates and eventually an infinite set of algebraic equations are obtained for the complex modal vibration response and the complex voltage response amplitudes of the energy harvester beam. For the series and parallel connections of the piezoceramic layers, the closed-form electromechanical expressions are first obtained for the steady-state response to harmonic excitation at arbitrary frequencies. The resulting analytical multi-mode expressions are then simplified to single-mode expressions by assuming modal excitation (i.e. excitation at or very close to a particular natural frequency), which is the main concern in vibration-based energy harvesting. The single-mode relations derived here are easier to use compared to the multi-mode solutions but they provide approximations only around the respective resonance frequency. The electromechanical FRFs which relate the voltage output and the vibration response of the bimorph to the translational and the rotational base acceleration components are extracted both for the multi-mode and single-mode solutions. A detailed theoretical case study is presented at the end of this chapter. Experimental validations of the analytical solutions derived here are presented in Chapter 4.

3.1 Fundamentals of the Electromechanically Coupled Distributed-parameter Model

3.1.1 Modeling Assumptions and Bimorph Configurations. The symmetric bimorph cantilever configurations shown in Fig. 3.1 are modeled here as uniform composite beams based on the Euler-Bernoulli beam theory. This is a reasonable assumption since typical cantilevered piezoelectric energy harvesters are designed and manufactured as fairly thin beams and most of the commercially available bimorphs are also thin structures (e.g. the samples used in Chapter 4 for model validation). Deformations are assumed to be small and the composite structure exhibits linear-elastic material behavior. The mechanical losses are represented by internal and external damping mechanisms as done in the electromechanically uncoupled discussion of Chapter 2. The internal damping mechanism is assumed to be in the form of strain-rate (or Kelvin-Voigt) damping and the effect of external (air) damping is considered with a separate damping coefficient. The piezoceramic and the substructure layers are assumed to be perfectly bonded to each other. The electrodes covering the opposite faces of piezoceramic layers are assumed to be very thin when compared to the overall thicknesses of the harvester so that their contribution to the thickness dimension is negligible. In the following formulation, therefore, only the substructure and piezoceramic layers are assumed to be present. However, presence of additional structural epoxy and Kapton layers can be handled easily.*

The continuous electrode pairs covering the top and the bottom faces of the piezoceramic layers are assumed to be perfectly conductive so that a single electric potential difference can be defined across them. Therefore, the instantaneous electric fields induced in the piezoceramic layers are assumed to be uniform throughout the length of the beam. A resistive electrical load (denoted by R_l in Fig. 3.1) is considered in the circuit along with the internal capacitances of the piezoceramic layers. Note that, considering a resistive load in the electrical domain is a common practice in modeling of vibration-based energy harvesters [14-22]. As a consequence, it is assumed that the base motion input is persistent so that continuous electrical outputs can be extracted from the electromechanical system. The leakage resistance of the piezoceramic is ignored here as it is typically very large. It can easily be added as an additional resistance parallel

* With the inclusion of additional inactive layers, the bending stiffness and the mass per length terms will be altered. In addition, distance of the piezoceramic layers from the neutral axis will be modified, which changes the piezoelectric coupling terms in the derivation.

to the load resistance (as in the lumped-parameter model of duToit et al. [16] discussed in Section 2.5).

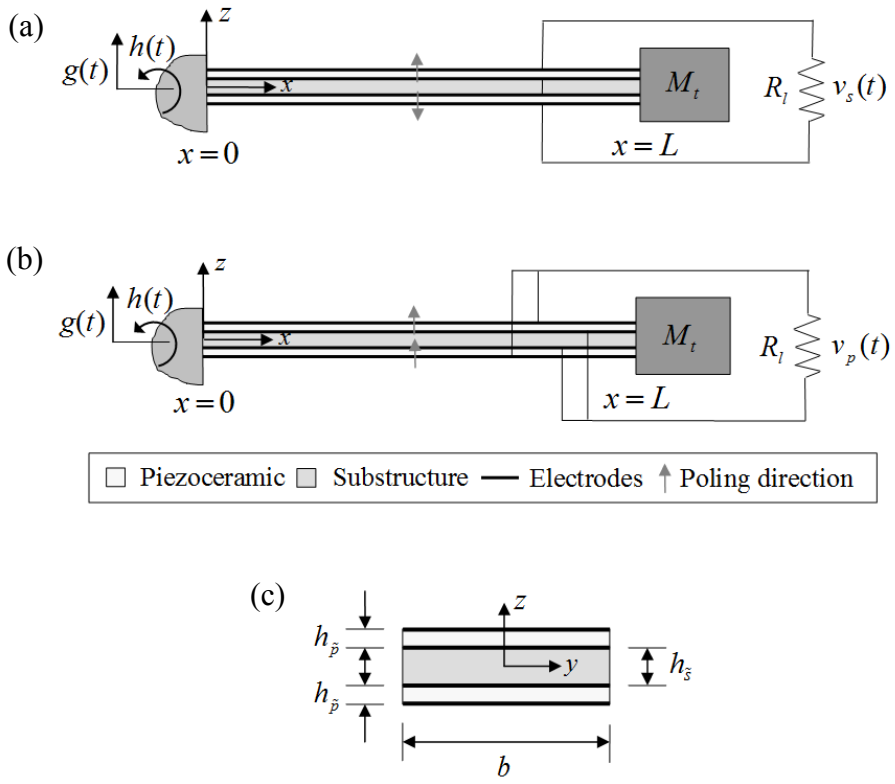

Fig. 3.1 Bimorph piezoelectric energy harvester configurations with (a) series connection of piezoceramic layers, (b) parallel connection of piezoceramic layers and the (c) cross-sectional view of a uniform bimorph cantilever

It is known from the literature of static sensing and actuation that, depending on the voltage or current requirements, the piezoceramic layers of a symmetric bimorph can be combined in series or in parallel (see, for instance, Wang and Cross [52]). This common practice of static sensing and actuation problems is valid for the dynamic piezoelectric energy harvesting problem as well. Each of the two bimorph configurations displayed in Figs. 3.1a and 3.1b undergoes bending vibrations due to the motion of its base. The piezoceramic layers are assumed to be identical and their conductive electrodes are assumed to be fully covering the respective surfaces of these layers (top and bottom). The instantaneous bending strain in the top and the bottom layers at an arbitrary position x over the beam length have the opposite sign (i.e. one is in

tension whereas the other is in compression). As a consequence, since the piezoceramic layers of the bimorph shown in Fig. 3.1a are poled oppositely in the thickness direction (i.e. *z*-direction), this configuration represents the *series connection* of the piezoceramic layers. Likewise, Fig. 3.1b represents the *parallel connection* of the piezoceramic layers because the layers are poled in the same direction. The configuration in Fig. 3.1a produces a larger voltage output whereas the one in Fig. 3.1b produces a larger current output under the optimal conditions.

3.1.2 Coupled Mechanical Equation and Modal Analysis of Bimorph Cantilevers. As far as the purely mechanical aspect of the problem is concerned, the bimorph configurations shown in Figs. 3.1a and 3.1b are identical. That is, they have the same geometric and material properties. However, the *backward* piezoelectric coupling effect[†] in the beam equation due to piezoelectric constitutive relations is different for series and parallel connections of the piezoceramic layers, and expectedly, this affects the vibration response of the cantilever. In the following, the beam equations are derived for these two configurations and the analytical modal analysis relations are presented.

The motion of the base for each of the cantilevers shown in Figs. 3.1a and 3.1b is represented by translation $g(t)$ in the transverse direction with superimposed small rotation $h(t)$. Therefore, the effective base displacement $w_b(x,t)$ in the transverse direction can be written as

$$w_b(x,t) = g(t) + xh(t) \tag{3.1}$$

The partial differential equation governing the forced vibrations of a uniform cantilevered bimorph (with a tip mass) under base excitation is

$$-\frac{\partial^2 M(x,t)}{\partial x^2} + c_s I \frac{\partial^5 w_{rel}(x,t)}{\partial x^4 \partial t} + c_a \frac{\partial w_{rel}(x,t)}{\partial t} + m\frac{\partial^2 w_{rel}(x,t)}{\partial t^2} = -\left[m + M_t \delta(x-L)\right]\frac{\partial^2 w_b(x,t)}{\partial t^2} \tag{3.2}$$

[†] Throughout this text, the term *backward coupling* represents the electrical effect induced in the harvester structure due to the converse piezoelectric effect (feedback sent from the electrical domain to the mechanical domain due to power generation). Hence the *forward coupling* term (to be defined later) is the term in the circuit equation due to the direct piezoelectric effect.

where $w_{rel}(x,t)$ is the transverse displacement of the beam (neutral axis) relative to its base at position x and time t, c_a is the viscous air damping coefficient, c_s is the strain-rate damping coefficient (appears as an effective term $c_s I$ for the composite structure), m is the mass per unit length of the beam, M_t it is tip mass and $\delta(x)$ is the Dirac delta function and $M(x,t)$ is the internal bending moment[‡] (excluding the strain-rate damping effect). Recall from Eq. (2.7) that the effect of strain-rate damping is an internal bending moment, which, in Eq. (3.2), is directly written outside the undamped bending moment term $M(x,t)$.

The bimorph cantilevers shown in Fig. 3.1 are assumed to be proportionally damped so that these configurations are normal-mode systems. Hence the eigenfunctions of the respective undamped problem can be used for modal analysis. Indeed, instead of defining the damping coefficients in the physical equation of motion, one could consider the corresponding undamped equation (by setting $c_s I = c_a = 0$ in Eq. (3.2)) and introduce modal damping to the equation of motion in modal coordinates as a common practice in structural dynamics [55]. It is worth recalling that the foregoing consideration of the mechanical damping components results in an additional excitation term (peculiar to base excitation problems) due to external damping as shown in Section 2.1.1. For cantilevers operating in air, the external damping excitation is negligible when compared to the inertial excitation term (Fig. 2.3). Therefore the damping excitation term is directly omitted in Eq. (3.2) for simplicity.

The internal bending moment term in Eq. (3.2) is the first moment of axial strain over the cross-section:

$$M(x,t) = b\left(\int_{-h_{\tilde{p}}-h_{\tilde{s}}/2}^{-h_{\tilde{s}}/2} T_1^{\tilde{p}} z dz + \int_{-h_{\tilde{s}}/2}^{h_{\tilde{s}}/2} T_1^{\tilde{s}} z dz + \int_{h_{\tilde{s}}/2}^{h_{\tilde{p}}+h_{\tilde{s}}/2} T_1^{\tilde{p}} z dz \right) \tag{3.3}$$

where b is the width, $h_{\tilde{p}}$ is the thickness of each piezoceramic layer and $h_{\tilde{s}}$ is the thickness of each substructure layer (Fig. 1c). Furthermore, $T_1^{\tilde{p}}$ and $T_1^{\tilde{s}}$ are the axial stress components in the piezoceramic and the substructure layers, respectively (1-direction is the longitudinal direction, i.e. x-direction), and they are given by the following constitutive relations:

[‡] The convention for the bending moment is such that the *positive bending moment creates negative curvature* as in Sokolnikoff [53] and Dym and Shames [54], among others.

$$T_1^{\tilde{s}} = Y_{\tilde{s}} S_1^{\tilde{s}} \quad , \quad T_1^{\tilde{p}} = \overline{c}_{11}^{E} S_1^{\tilde{p}} - \overline{e}_{31} E_3 \tag{3.4}$$

where Y_s is the elastic modulus (i.e., Young's modulus) of the substructure layer (which can be isotropic or orthotropic), $\overline{c}_{11}^{E}$ is the elastic modulus of the piezoceramic layer at constant electric field, $\overline{e}_{31}$ is the effective piezoelectric stress constant and E_3 is the electric field component in the 3-direction (i.e. *z*-direction or the *poling* direction). Here and hereafter, the subscripts and superscripts $\tilde{p}$ and $\tilde{s}$ stand for the piezoceramic and the substructure layers, respectively. Based on the plane-stress assumption for a transversely isotropic thin piezoceramic beam (about the *z*-direction), the elastic modulus component of the piezoceramic can be expressed as $\overline{c}_{11}^{E} = 1/s_{11}^{E}$, where s_{11}^{E} is the elastic compliance at constant electric field. Furthermore, based on the same assumption, $\overline{e}_{31}$ can be given in terms of the more commonly used piezoelectric strain constant d_{31} as $\overline{e}_{31} = d_{31}/s_{11}^{E}$ (Appendix A.2). The axial strain components in the piezoelectric and substructure layers are defined as $S_1^{\tilde{p}}$ and $S_1^{\tilde{s}}$, respectively, and they are due to bending only. Hence the axial strain at a certain level (*z*) from the neutral axis of the symmetric composite beam is simply proportional to the curvature of the beam at that position (*x*):[§]

$$S_1(x,z,t) = -z\frac{\partial^2 w_{rel}(x,t)}{\partial x^2} \tag{3.5}$$

The electric field component E_3 should be expressed in terms of the respective voltage term for each bimorph configuration (Figs. 3.1a and 3.1b). This is the point where the resulting mechanical equations for the series and parallel connections of the piezoceramic layers differ from each other. Since the piezoceramic layers are assumed to be identical, voltage across the electrodes of each piezoceramic layer is $v_s(t)/2$ in the series connection case (Fig. 3.1a). Expectedly, for the parallel connection case (Fig. 3.1b), voltage across the electrodes of each piezoceramic layer is $v_p(t)$. It is worth adding that $\overline{e}_{31}$ has the opposite sign for the top and the bottom piezoceramic layers for the series connection case (due to opposite poling) so that the

[§] An independent axial displacement variable (in *x*-direction) is not included in the strain expression since it decouples from the equation of motion for transverse vibrations due to the symmetric composite structure [56]. Since there is no excitation in the axial direction, there is no strain contribution from the decoupled axial displacement.

instantaneous electric fields are in the same direction (i.e. $E_3(t) = -v_s(t)/2h_{\tilde{p}}$ in both layers). For the configuration with parallel connection, since $\overline{e}_{31}$ has the same sign in top and bottom piezoceramic layers, the instantaneous electric fields are in the opposite directions (i.e., $E_3(t) = -v_p(t)/h_{\tilde{p}}$ in the top layer and $E_3(t) = v_p(t)/h_{\tilde{p}}$ in the bottom layer). Another important point is that, for both configurations, the piezoelectric coupling term coming from Eq. (3.3) is a function of time only. Hence, before substituting Eq. (3.3) into Eq. (3.2), the electrical term must be multiplied by $\left[H(x) - H(x-L)\right]$, where $H(x)$ is the Heaviside function. Since the voltage outputs of the series and parallel connection cases are different, the piezoelectric coupling effect in the mechanical equation (Eq. (3.2)) is expected to be different. Thus, in the rest of this chapter, the mechanical response expressions of the series and parallel connection configurations are denoted by $w_{rel}^{s}(x,t)$ and $w_{rel}^{p}(x,t)$, respectively. Note that, here and hereafter, the subscripts and superscripts *s* and *p*, respectively, stand for the *series* and *parallel* connections of the piezoceramic layers (which should not be confused with $\tilde{s}$ and $\tilde{p}$ formerly introduced for the substructure and the piezoceramic layers, respectively). The internal bending moment terms are then obtained from Eq. (3.3) as

$$M^{s}(x,t) = YI\frac{\partial^2 w_{rel}^{s}(x,t)}{\partial x^2} + \vartheta_s v_s(t)\left[H(x) - H(x-L)\right] \tag{3.6}$$

$$M^{p}(x,t) = YI\frac{\partial^2 w_{rel}^{p}(x,t)}{\partial x^2} + \vartheta_p v_p(t)\left[H(x) - H(x-L)\right] \tag{3.7}$$

where the coefficients of the backward coupling terms (ϑ_s and ϑ_p) for the series and parallel connection cases can be expressed as

$$\vartheta_s = \frac{\overline{e}_{31} b}{2h_{\tilde{p}}}\left[\frac{h_{\tilde{s}}^{\,2}}{4} - \left(h_{\tilde{p}} + \frac{h_{\tilde{s}}}{2}\right)^2\right] \tag{3.8}$$

$$\vartheta_p = 2\vartheta_s = \frac{\overline{e}_{31} b}{h_{\tilde{p}}}\left[\frac{h_{\tilde{s}}^{\,2}}{4} - \left(h_{\tilde{p}} + \frac{h_{\tilde{s}}}{2}\right)^2\right] \tag{3.9}$$

The bending stiffness term *YI* of the composite cross section for the constant electric field condition of the piezoceramic is

$$YI = \frac{2b}{3}\left[Y_{\tilde{s}} \frac{h_{\tilde{s}}^{\,3}}{8} + \bar{c}_{11}^{E}\left(\left(h_{\tilde{p}} + \frac{h_{\tilde{s}}}{2} \right)^3 - \frac{h_{\tilde{s}}^{\,3}}{8} \right) \right] \tag{3.10}$$

From Eq. (3.2), the coupled beam equation can be obtained for the series connection case (Fig. 3.1a) as follows:

$$YI \frac{\partial^4 w_{rel}^{s}(x,t)}{\partial x^4} + c_s I \frac{\partial^5 w_{rel}^{s}(x,t)}{\partial x^4 \partial t} + c_a \frac{\partial w_{rel}^{s}(x,t)}{\partial t} + m \frac{\partial^2 w_{rel}^{s}(x,t)}{\partial t^2} + \vartheta_s v_s(t)\left[\frac{d\delta(x)}{dx} - \frac{d\delta(x-L)}{dx} \right] =$$
$$-\left[m + M_t \delta(x-L) \right] \frac{\partial^2 w_b(x,t)}{\partial t^2} \tag{3.11}$$

Similarly, one can obtain the equation of motion for the case (Fig. 3.1b) with the parallel connection of the piezoceramic layers as

$$YI \frac{\partial^4 w_{rel}^{p}(x,t)}{\partial x^4} + c_s I \frac{\partial^5 w_{rel}^{p}(x,t)}{\partial x^4 \partial t} + c_a \frac{\partial w_{rel}^{p}(x,t)}{\partial t} + m \frac{\partial^2 w_{rel}^{p}(x,t)}{\partial t^2} + \vartheta_p v_p(t)\left[\frac{d\delta(x)}{dx} - \frac{d\delta(x-L)}{dx} \right] =$$
$$-\left[m + M_t \delta(x-L) \right] \frac{\partial^2 w_b(x,t)}{\partial t^2} \tag{3.12}$$

It is useful to notice at this stage that the *n*-th distributional derivative of the Dirac delta function satisfies [57,58]

$$\int_{-\infty}^{\infty} \frac{d^{(n)}\delta(x-x_0)}{dx^{(n)}} \gamma(x) dx = (-1)^n \frac{d\gamma^{(n)}(x_0)}{dx^{(n)}} \tag{3.13}$$

where $\gamma(x)$ is a smooth test function. The mass per unit length term *m* is simply

$$m = b\left(\rho_{\tilde{s}} h_{\tilde{s}} + 2\rho_{\tilde{p}} h_{\tilde{p}} \right) \tag{3.14}$$

where $\rho_{\tilde{s}}$ and $\rho_{\tilde{p}}$ are the mass densities of the substructure and the piezoceramic, respectively.

Based on the proportional damping (or modal damping) assumption, the vibration response relative to the base of the bimorph (Figs. 3.1a and 3.1b) can be represented as an absolutely and uniformly convergent series of the eigenfunctions as

$$w_{rel}^{s}(x,t) = \sum_{r=1}^{\infty} \phi_r(x) \eta_r^{s}(t) \ , \ w_{rel}^{p}(x,t) = \sum_{r=1}^{\infty} \phi_r(x) \eta_r^{p}(t) \tag{3.15}$$

where $\phi_r(x)$ is the mass normalized eigenfunction of the *r*-th vibration mode, and $\eta_r^{s}(t)$ and $\eta_r^{p}(t)$ are the modal mechanical response expressions of the series and parallel connection cases,

respectively. The eigenfunctions denoted by $\phi_r(x)$ are the mass normalized eigenfunctions of the corresponding undamped free vibration problem:

$$\phi_r(x) = C_r\left[\cos\frac{\lambda_r}{L}x - \cosh\frac{\lambda_r}{L}x + \varsigma_r\left(\sin\frac{\lambda_r}{L}x - \sinh\frac{\lambda_r}{L}x\right)\right] \tag{3.16}$$

where ς_r is obtained from

$$\varsigma_r = \frac{\sin\lambda_r - \sinh\lambda_r + \lambda_r\dfrac{M_t}{mL}\left(\cos\lambda_r - \cosh\lambda_r\right)}{\cos\lambda_r + \cosh\lambda_r - \lambda_r\dfrac{M_t}{mL}\left(\sin\lambda_r - \sinh\lambda_r\right)} \tag{3.17}$$

and C_r is a modal amplitude constant which should be evaluated by normalizing the eigenfunctions according to the following orthogonality conditions:

$$\begin{aligned}
&\int_0^L \phi_s(x)m\phi_r(x)dx + \phi_s(L)M_t\phi_r(L) + \left[\frac{d\phi_s(x)}{dx}I_t\frac{d\phi_r(x)}{dx}\right]_{x=L} = \delta_{rs} \\
&\int_0^L \phi_s(x)YI\frac{d^4\phi_r(x)}{dx^4}dx - \left[\phi_s(x)YI\frac{d^3\phi_r(x)}{dx^3}\right]_{x=L} + \left[\frac{d\phi_s(x)}{dx}YI\frac{d^2\phi_r(x)}{dx^2}\right]_{x=L} = \omega_r{}^2\delta_{rs}
\end{aligned} \tag{3.18}$$

Here, I_t is the mass moment of inertia of the tip mass M_t about the free end and δ_{rs} is the Kronecker delta. Furthermore, ω_r is the undamped natural frequency of the *r*-th vibration mode in the short-circuit conditions (i.e. $R_l \to 0$) given by

$$\omega_r = \lambda_r{}^2\sqrt{\frac{YI}{mL^4}} \tag{3.19}$$

where the eigenvalues of the system (λ_r for mode *r*) are obtained from

$$\begin{aligned}
&1 + \cos\lambda\cosh\lambda + \lambda\frac{M_t}{mL}\left(\cos\lambda\sinh\lambda - \sin\lambda\cosh\lambda\right) - \frac{\lambda^3 I_t}{mL^3}\left(\cosh\lambda\sin\lambda + \sinh\lambda\cos\lambda\right) \\
&+ \frac{\lambda^4 M_t I_t}{m^2L^4}\left(1 - \cos\lambda\cosh\lambda\right) = 0
\end{aligned} \tag{3.20}$$

It should be mentioned that the foregoing modal analysis is given for the short-circuit conditions (i.e. for $R_l \to 0$) so that the conventional form of the eigenfunctions given by Eq. (3.16) is obtained since

$$\lim_{R_l\to 0} v_s(t) = 0, \quad \lim_{R_l\to 0} v_p(t) = 0 \tag{3.21}$$

in Eqs. (3.11) and (3.12), respectively (i.e. the voltage output vanishes for zero load resistance). Note that the short-circuit condition is indeed a constant electric field condition ($E_3 \to 0$ as $R_l \to 0$), in agreement with the piezoelectric constitutive relation used here.

For a given bimorph, the form of the eigenfunctions given by $\phi_r(x)$ and their mass normalization conditions are the same regardless of the series or parallel connections of the piezoceramic layers. For non-zero values of load resistance, the voltage terms in the mechanical equations take finite values, generating *point moment excitations* at the boundaries of the piezoceramic layer according to Eqs. (3.11) and (3.12), and yielding two different modal mechanical response functions for these equations as $\eta_r^s(t)$ and $\eta_r^p(t)$, respectively. The feedback received from the voltage response for a given load resistance alters the mechanical response as well as the resonance frequency of the energy harvester, as discussed theoretically here and validated experimentally in the next chapter.

3.1.3 Coupled Electrical Circuit Equation of a Thin Piezoceramic Layer under Dynamic Bending. In order to derive the governing electrical circuit equations of the bimorph configurations for the series and parallel connections of the piezoceramic layers, one should first examine the electrical dynamics of a single layer under bending vibrations. Consider Fig. 3.2a, where the electrodes of a single layer are connected to a resistive electrical load. The deflections are exaggerated to highlight the space- and time-dependent radius of curvature at an arbitrary point *x* on the neutral axis at time *t*.

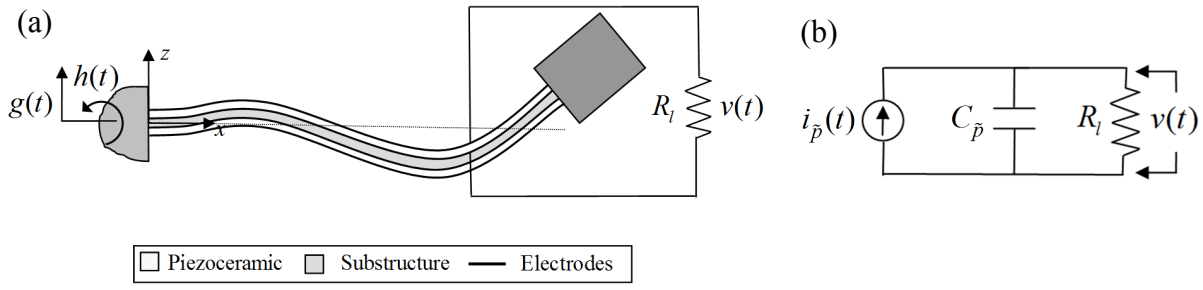

Fig. 3.2 (a) Bimorph cantilever with a single layer connected to a resistive load and (b) the corresponding electrical circuit

Since the only source of mechanical strain is assumed to be the axial strain due to bending, the tensorial representation of the relevant piezoelectric constitutive relation [26] that gives the vector of electric displacements can be reduced to the following scalar equation (Appendix A.2):

$$D_3 = \overline{e}_{31} S_1^{\tilde{p}} + \overline{\varepsilon}_{33}^S E_3 \tag{3.22}$$

where D_3 is the electric displacement component and $\overline{\varepsilon}_{33}^S$ is the permittivity component at constant strain with the plane-stress assumption for a beam ($\overline{\varepsilon}_{33}^S = \varepsilon_{33}^T - d_{31}^2 / s_{11}^E$ where ε_{33}^T is the permittivity component at constant stress as given in Appendix A.2) .

As the circuit admittance across the electrodes is $1/R_l$, the electric current output can be obtained from the Gauss's law [26] as

$$\frac{d}{dt}\left(\int_A \mathbf{D} \cdot \mathbf{n} dA \right) = \frac{v(t)}{R_l} \tag{3.23}$$

where **D** is the vector of electric displacement components in the piezoceramic layer, **n** is the unit outward normal and the integration is performed over the electrode area *A*. As can be anticipated, the only contribution to the inner product of the integrand in Eq. (3.23) is from D_3, since the electrodes are perpendicular to 3-direction (i.e. *z*-direction). After expressing the average bending strain in the piezoceramic layer in terms of the curvature (see Eq. (3.5)) and the uniform electric field in terms of the electric potential difference ($E_3(t) = -v(t)/h_{\tilde{p}}$), Eq. (3.22) can be used in equation Eq. (3.23) to obtain

$$\frac{\overline{\varepsilon}_{33}^S bL}{h_{\tilde{p}}} \frac{dv(t)}{dt} + \frac{v(t)}{R_l} = -\overline{e}_{31} h_{\tilde{p}c} b \int_0^L \frac{\partial^3 w_{rel}(x,t)}{\partial x^2 \partial t} dx \tag{3.24}$$

where b, $h_{\tilde{p}}$ and L are the width, thickness and the length of the piezoceramic layer, respectively, and $h_{\tilde{p}c}$ is the distance between the neutral axis and the center of the piezoceramic layer ($h_{\tilde{p}c} = (h_{\tilde{p}} + h_{\tilde{s}})/2$). One can then substitute the modal expansion form of the transverse vibration response (relative to the base) given by

$$w_{rel}(x,t) = \sum_{r=1}^{\infty} \phi_r(x) \eta_r(t) \tag{3.25}$$

into Eq. (3.24) to obtain

$$\frac{\overline{\varepsilon}_{33}^{S} bL}{h_{\tilde{p}}} \frac{dv(t)}{dt} + \frac{v(t)}{R_l} = \sum_{r=1}^{\infty} \kappa_r \frac{d\eta_r(t)}{dt} \tag{3.26}$$

where κ_r is the modal coupling term in the electrical circuit equation:

$$\kappa_r = -\overline{e}_{31} h_{\tilde{p}c} b \int_0^L \frac{d^2 \phi_r(x)}{dx^2} dx = -\overline{e}_{31} h_{\tilde{p}c} b \left. \frac{d\phi_r(x)}{dx} \right|_{x=L} \tag{3.27}$$

The *forward* coupling term κ_r has important consequences as discussed in Chapter 7 extensively. According to Eq. (3.24), which originates from the Gauss's law given by Eq. (3.23), the excitation of the simple *RC* circuit considered here as well as that of more sophisticated energy harvesting circuit topologies [23-25] is proportional to the integral of the dynamic strain distribution over the electrode area. For vibration modes of a cantilevered beam other than the fundamental (first) vibration mode, the dynamic strain distribution over the beam length changes sign at the *strain nodes*. It is known from Eq. (3.5) that the curvature at a point is a direct measure of the bending strain. Hence, for modal excitations, strain nodes are the *inflection points* of the eigenfunctions and the integrand in Eq. (3.27) is the curvature eigenfunction. If the electric charge developed at the opposite sides of a strain node is collected by continuous electrodes for vibrations with a certain mode shape, cancellation occurs due to the phase difference in the mechanical strain distribution. Mathematically, the partial areas under the integrand function of the integral in Eq. (3.27) cancel each other over the domain of integration. As an undesired consequence, the excitation of the electrical circuit, and therefore the electrical outputs might diminish drastically. In order to avoid cancellations, segmented electrodes can be used in harvesting energy from the modes higher than the fundamental mode. The leads of the segmented electrodes can be combined in the circuit in an appropriate manner. Note that the *r*-th vibration mode of a clamped-free beam has $r-1$ strain nodes, and consequently, the first mode of a cantilevered beam has no cancellation problem. Some boundary conditions are more prone to strong cancellations. For instance, a beam with clamped-clamped boundary conditions has $r+1$ strain nodes for the *r*-th vibration mode. A detailed discussion related to the strain nodes of thin beams is given in Chapter 7.

Based on Eq. (3.26), it is very useful to represent the electrical domain of the coupled system by the simple circuit shown in Fig. 3.2b. It is known in the circuitry-based energy harvesting literature that a piezoelectric element can be represented as a current source in parallel

with its internal capacitance [23-25] (Norton equivalent[**]). Therefore, the simple circuit shown in Fig. 3.2b is the complete circuit of the electrical domain for a single resistive load case. Note that, this representation considers the electrical domain *only* and the electromechanical representation of the coupled system is actually a *transformer* because of the voltage feedback sent to the mechanical domain due to the piezoelectric coupling (which will be incorporated in the formulation here). The components of the circuit are the internal capacitance $C_{\tilde{p}}$ of the piezoceramic layer, the resistive load R_l and the current source $i_{\tilde{p}}(t)$. In agreement with Fig. 3.2a, the voltage across the resistive load is denoted by $v(t)$. Then, the Kirchhoff laws can be applied to the electrical circuit shown in Fig. 3.2b to obtain

$$C_{\tilde{p}} \frac{dv(t)}{dt} + \frac{v(t)}{R_l} = i_{\tilde{p}}(t) \tag{3.28}$$

where the internal capacitance and the current source terms can be extracted by matching Eqs. (3.26) and (3.28) as

$$C_{\tilde{p}} = \frac{\bar{\varepsilon}_{33}^{S} bL}{h_{\tilde{p}}} \quad , \quad i_{\tilde{p}}(t) = \sum_{r=1}^{\infty} \kappa_r \frac{d\eta_r(t)}{dt} \tag{3.29}$$

Identification of the above terms (especially the current source term) has an important use for modeling of multi-morph piezoelectric energy harvesters. This way, for a given number of piezoceramic layers, there is no need to derive the electrical circuit equation by using the constitutive relation and the Gauss's law given by equations Eqs. (3.23) and (3.24), respectively. Each piezoceramic layer will have a similar capacitance and current source term and the layers can be combined to the resistive electrical load(s) in a desired way.

3.2 Series Connection of the Piezoceramic Layers

Based on the fundamentals given in Section 3.1, this section presents the derivation of the closed-form expressions for the coupled voltage response $v_s(t)$ and vibration response $w_{rel}^{s}(x,t)$ of the bimorph configuration shown in Fig. 3.1a. First the coupled mechanical equation is given in modal coordinates and then the coupled circuit equation is derived. The resulting

[**] The alternative representation is the Thévenin equivalent (voltage source in series with its internal capacitance). See a discussion in Section 5.4.6 regarding a misuse of these representations to obtain the optimum load resistance.

electromechanical equations are then solved for the steady-state voltage response and vibration response for harmonic base motion inputs.

3.2.1 Coupled Beam Equation in Modal Coordinates. After substituting Eq. (3.15a) into Eq. (3.11) and applying the orthogonality conditions of the eigenfunctions, the mechanical equation of motion in modal coordinates can be obtained as

$$\frac{d^2\eta_r^s(t)}{dt^2} + 2\zeta_r\omega_r\frac{d\eta_r^s(t)}{dt} + \omega_r{}^2\eta_r^s(t) + \chi_r^s v_s(t) = f_r(t) \tag{3.30}$$

where the modal electromechanical coupling term is[††]

$$\chi_r^s = \vartheta_s \left.\frac{d\phi_r(x)}{dx}\right|_{x=L} \tag{3.31}$$

The modal mechanical forcing function can be expressed as

$$f_r(t) = -m\left(\frac{d^2g(t)}{dt^2}\int_0^L \phi_r(x)dx + \frac{d^2h(t)}{dt^2}\int_0^L x\phi_r(x)dx\right) - M_t\phi_r(L)\left(\frac{d^2g(t)}{dt^2} + L\frac{d^2h(t)}{dt^2}\right) \tag{3.32}$$

In Eq. (3.30), ζ_r is the modal mechanical damping ratio that includes the combined effects of strain-rate and air damping. In the absence of a tip mass, how to relate the modal damping ratio to the strain-rate and air damping terms c_sI and c_a mathematically based on the assumption of proportional damping was described in Chapter 2. However, as a common experimental modal analysis practice, one can identify the modal damping ratio ζ_r of a desired mode directly from the frequency response or time domain measurements (which avoids the requirement of defining and obtaining the physical damping terms c_sI and c_a). Chapter 5 provides closed-form relations to identify modal mechanical damping ratio from electromechanical FRF measurements in the presence of a resistive electrical load.

3.2.2 Coupled Electrical Circuit Equation. As described in Section 3.1.1, the piezoceramic layers of the bimorph configuration shown in Fig. 3.1a are connected in series. We know from the practice given in Section 3.1.3 that each piezoceramic layer can be represented as a current

[††] Note that, here, Eq. (3.13) is used to obtain the modal backward coupling term χ_r^s where the test function is the eigenfunction ($\gamma(x) = \phi_r(x)$) multiplying the partial differential equation in the modal analysis solution procedure.

source in parallel with its internal capacitance. Therefore, Fig. 3.3 displays the series connection of the identical piezoceramic layers of the bimorph configuration shown in Fig. 3.1a.

The Kirchhoff laws can be applied to the circuit depicted in Fig. 3.3 to obtain

$$\frac{C_{\tilde{p}}}{2}\frac{dv_s(t)}{dt}+\frac{v_s(t)}{R_l}=i_{\tilde{p}}^s(t) \tag{3.33}$$

where the internal capacitance and the current source terms of the bimorph (for each layer) are

$$C_{\tilde{p}}=\frac{\bar{\varepsilon}_{33}^S bL}{h_{\tilde{p}}} \quad , \quad i_{\tilde{p}}^s(t)=\sum_{r=1}^{\infty}\kappa_r\frac{d\eta_r^s(t)}{dt} \tag{3.34}$$

The modal electromechanical coupling term is then

$$\kappa_r=-\bar{e}_{31}h_{\tilde{p}c}b\int_0^L\frac{d^2\phi_r(x)}{dx^2}dx=-\frac{\bar{e}_{31}\left(h_{\tilde{p}}+h_{\tilde{s}}\right)b}{2}\frac{d\phi_r(x)}{dx}\bigg|_{x=L} \tag{3.35}$$

where $h_{\tilde{p}c}$ (the distance between the neutral axis and the center of the piezoceramic layer) is expressed in terms of the piezoceramic and the substructure layer thicknesses $h_{\tilde{p}}$ and $h_{\tilde{s}}$ (Fig. 3.1c). Hence, Eq. (3.34) is the electrical circuit equation of the bimorph cantilever for the series connection of the piezoceramic layers.

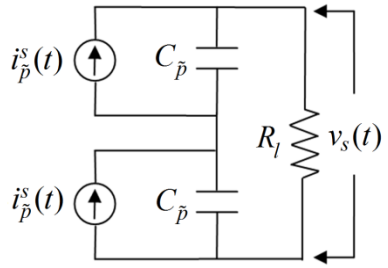

Fig. 3.3 Electrical circuit representing the series connection of the piezoceramic layers

3.2.3 Closed-form Voltage Response and Vibration Response at Steady State. Equations (3.31) and (3.33) constitute the coupled equations for the modal mechanical response $\eta_r^s(t)$ of the bimorph and the voltage response $v_s(t)$ across the resistive load. In this section, the steady-state solution of these terms for harmonic motion inputs is derived. If the translational and rotational components of the base displacement given by Eq. (3.1) are harmonic of the forms $g(t)=W_0e^{j\omega t}$ and $h(t)=\theta_0e^{j\omega t}$, where W_0 and θ_0 are the translational and the small rotational

displacement amplitudes of the base, ω is the excitation frequency and j is the unit imaginary number, then the modal forcing function given by Eq. (3.32) can be expressed as $f_r(t) = F_r e^{j\omega t}$ where the amplitude F_r is

$$F_r = \omega^2 \left[m\left(W_0 \int_0^L \phi_r(x)dx + \theta_0 \int_0^L x\phi_r(x)dx \right) + M_t \phi_r(L)\left(W_0 + L\theta_0\right) \right] \tag{3.36}$$

For the harmonic base motions at frequency ω, the steady-state modal mechanical response of the beam and the steady-state voltage response across the resistive load are assumed to be harmonic at the same frequency as $\eta_r^s(t) = \mathrm{H}_r^s e^{j\omega t}$ and $v_s(t) = V_s e^{j\omega t}$ (linear system assumption), respectively, where the amplitudes H_r^s and V_s are complex valued. Therefore, Eqs. (3.30) and (3.33) yield the following two equations for H_r^s and V_s:

$$\left(\omega_r{}^2 - \omega^2 + j2\zeta_r\omega_r\omega\right)\mathrm{H}_r^s + \chi_r^s V_s = F_r \tag{3.37}$$

$$\left(\frac{1}{R_l} + j\omega\frac{C_{\tilde{p}}}{2}\right)V_s - j\omega\sum_{r=1}^{\infty}\kappa_r \mathrm{H}_r^s = 0 \tag{3.38}$$

The complex modal mechanical response amplitude H_r^s can be extracted from Eq. (3.37) and it can be substituted into Eq. (3.38) to obtain the complex voltage amplitude V_s explicitly. The resulting complex voltage amplitude can then be used in $v_s(t) = V_s e^{j\omega t}$ to express the steady-state voltage response as

$$v_s(t) = \frac{\displaystyle\sum_{r=1}^{\infty}\frac{j\omega\kappa_r F_r}{\omega_r{}^2 - \omega^2 + j2\zeta_r\omega_r\omega}}{\displaystyle\frac{1}{R_l} + j\omega\frac{C_{\tilde{p}}}{2} + \sum_{r=1}^{\infty}\frac{j\omega\kappa_r\chi_r^s}{\omega_r{}^2 - \omega^2 + j2\zeta_r\omega_r\omega}} e^{j\omega t} \tag{3.39}$$

The complex voltage amplitude V_s can be substituted into Eq. (3.37) to obtain the steady-state modal mechanical response of the bimorph as

$$\eta_r^s(t) = \left(F_r - \chi_r^s \frac{\displaystyle\sum_{r=1}^{\infty}\frac{j\omega\kappa_r F_r}{\omega_r{}^2 - \omega^2 + j2\zeta_r\omega_r\omega}}{\displaystyle\frac{1}{R_l} + j\omega\frac{C_{\tilde{p}}}{2} + \sum_{r=1}^{\infty}\frac{j\omega\kappa_r\chi_r^s}{\omega_r{}^2 - \omega^2 + j2\zeta_r\omega_r\omega}} \right) \frac{e^{j\omega t}}{\omega_r{}^2 - \omega^2 + j2\zeta_r\omega_r\omega} \tag{3.40}$$

The transverse displacement response (relative to the base) at point *x* on the bimorph can be obtained in physical coordinates by substituting Eq. (3.40) into Eq. (3.15a):

$$w_{rel}^{s}(x,t)=\sum_{r=1}^{\infty}\left[\left(F_r-\chi_r^{s}\frac{\sum_{r=1}^{\infty}\frac{j\omega\kappa_r F_r}{\omega_r{}^2-\omega^2+j2\zeta_r\omega_r\omega}}{\frac{1}{R_l}+j\omega\frac{C_{\tilde{p}}}{2}+\sum_{r=1}^{\infty}\frac{j\omega\kappa_r\chi_r^{s}}{\omega_r{}^2-\omega^2+j2\zeta_r\omega_r\omega}}\right)\frac{\phi_r(x)e^{j\omega t}}{\omega_r{}^2-\omega^2+j2\zeta_r\omega_r\omega}\right] \tag{3.41}$$

Note that the vibration response given by Eq. (3.41) is the displacement response of the beam relative to its moving base. If one is interested in the coupled beam displacement in the absolute physical coordinates (relative to the fixed frame), it is the superposition of the base displacement and the vibratory displacement relative to base:

$$w^{s}(x,t)=w_b(x,t)+w_{rel}^{s}(x,t) \tag{3.42}$$

where $w_b(x,t)$ is the effective base displacement given by Eq. (3.1).

3.3. Parallel Connection of the Piezoceramic Layers

This section aims to derive the steady-state voltage response $v_p(t)$ and the vibration response $w_{rel}^{p}(x,t)$ of the bimorph configuration shown in Fig. 3.1b to harmonic base motions. The coupled beam equation in modal coordinates and the electrical circuit equations are derived and the closed-form solutions are obtained in the following.

3.3.1 Coupled Beam Equation in Modal Coordinates. After substituting Eq. (3.15b) in Eq. (3.11), the partial differential equation given by Eq. (3.11) can be reduced to an infinite set of ordinary differential equations in modal coordinates as follows:

$$\frac{d^2\eta_r^{p}(t)}{dt^2}+2\zeta_r\omega_r\frac{d\eta_r^{p}(t)}{dt}+\omega_r{}^2\eta_r^{p}(t)+\chi_r^{p}v_p(t)=f_r(t) \tag{3.43}$$

where the modal electromechanical coupling term is

$$\chi_r^{p}=\vartheta_p\left.\frac{d\phi_r(x)}{dx}\right|_{x=L} \tag{3.44}$$

and the modal mechanical forcing function is given by Eq. (3.32). The discussion regarding the mechanical damping ratio ζ_r is the same as given in Section 3.2.1. Thus, Eq. (3.43) is the coupled beam equation in modal coordinates for the bimorph configuration with the parallel connection of the piezoceramic layers.

3.3.2 Coupled Electrical Circuit Equation. It was mentioned in Section 3.1.1 that the piezoceramic layers of the bimorph configuration shown in Fig. 3.1b are connected in parallel. Since each of the piezoceramic layers can be represented as a current source in parallel with its internal capacitance (Section 3.1.3), Fig. 3.4 represents the parallel connection of the identical top and bottom piezoceramic layers of the bimorph configuration shown in Fig. 3.1b.

One can then derive the governing electrical circuit equation based on the Kirchhoff laws as follows:

$$C_{\tilde{p}} \frac{dv_p(t)}{dt} + \frac{v_p(t)}{2R_l} = i_{\tilde{p}}^p(t) \tag{3.45}$$

where the internal capacitance and the current source terms for each layer are

$$C_{\tilde{p}} = \frac{\bar{\varepsilon}_{33}^S bL}{h_{\tilde{p}}} \quad , \quad i_{\tilde{p}}^p(t) = \sum_{r=1}^{\infty} \kappa_r \frac{d\eta_r^p(t)}{dt} \tag{3.46}$$

The modal coupling term κ_r is given by Eq. (3.34). Equation (3.45) is the electrical circuit equation of the bimorph cantilever for the parallel connection of the piezoceramic layers.

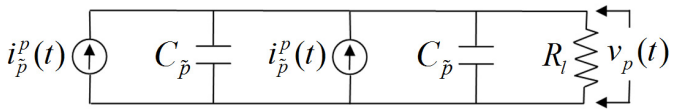

Fig. 3.4 Electrical circuit representing the parallel connection of the piezoceramic layers

3.3.3 Closed-form Voltage Response and Vibration Response at Steady State. In order to solve for $\eta_r^p(t)$ and $v_p(t)$ in Eqs. (3.43) and (3.45), the same procedure of Section 3.2 is followed by assuming the base excitation components in Fig. 3.1b to be harmonic as $g(t) = W_0 e^{j\omega t}$ and $h(t) = \theta_0 e^{j\omega t}$. For these harmonic base motion inputs of the same frequency, the modal forcing is harmonic as $f_r(t) = F_r e^{j\omega t}$ where the amplitude F_r is given by Eq. (3.36).

Based on the linear system assumption, the modal mechanical response $\eta_r^p(t)$ and the voltage response $v_p(t)$ are assumed to be harmonic at the frequency of excitation such that

$\eta_r^p(t) = \mathrm{H}_r^p e^{j\omega t}$ and $v_p(t) = V_p e^{j\omega t}$, where the amplitudes H_r^p and V_p are complex valued. Hence, Eqs. (3.43) and (3.45) yield the following equations for H_r^p and V_p:

$$\left(\omega_r{}^2 - \omega^2 + j2\zeta_r\omega_r\omega\right)\mathrm{H}_r^p + \chi_r^p V_p = F_r \tag{3.47}$$

$$\left(\frac{1}{2R_l} + j\omega C_{\tilde{p}}\right)V_p - j\omega\sum_{r=1}^{\infty}\kappa_r \mathrm{H}_r^p = 0 \tag{3.48}$$

where H_r^p and V_p can be obtained explicitly. Using the resulting complex voltage amplitude in $v_p(t) = V_p e^{j\omega t}$ gives the steady-state voltage response as

$$v_p(t) = \frac{\displaystyle\sum_{r=1}^{\infty}\frac{j\omega\kappa_r F_r}{\omega_r{}^2 - \omega^2 + j2\zeta_r\omega_r\omega}}{\displaystyle\frac{1}{2R_l} + j\omega C_{\tilde{p}} + \sum_{r=1}^{\infty}\frac{j\omega\kappa_r\chi_r^p}{\omega_r{}^2 - \omega^2 + j2\zeta_r\omega_r\omega}} e^{j\omega t} \tag{3.49}$$

Then the steady-state modal mechanical response of the bimorph can be obtained by using V_p in Eq. (3.47) as

$$\eta_r^p(t) = \left(F_r - \chi_r^p \frac{\displaystyle\sum_{r=1}^{\infty}\frac{j\omega\kappa_r F_r}{\omega_r{}^2 - \omega^2 + j2\zeta_r\omega_r\omega}}{\displaystyle\frac{1}{2R_l} + j\omega C_{\tilde{p}} + \sum_{r=1}^{\infty}\frac{j\omega\kappa_r\chi_r^p}{\omega_r{}^2 - \omega^2 + j2\zeta_r\omega_r\omega}}\right)\frac{e^{j\omega t}}{\omega_r{}^2 - \omega^2 + j2\zeta_r\omega_r\omega} \tag{3.50}$$

The modal mechanical response expression can then be used in Eq. (3.15b) to obtain the transverse displacement response (relative to the base) at point *x* on the bimorph:

$$w_{rel}^p(x,t) = \sum_{r=1}^{\infty}\left[\left(F_r - \chi_r^p \frac{\displaystyle\sum_{r=1}^{\infty}\frac{j\omega\kappa_r F_r}{\omega_r{}^2 - \omega^2 + j2\zeta_r\omega_r\omega}}{\displaystyle\frac{1}{2R_l} + j\omega C_{\tilde{p}} + \sum_{r=1}^{\infty}\frac{j\omega\kappa_r\chi_r^p}{\omega_r{}^2 - \omega^2 + j2\zeta_r\omega_r\omega}}\right)\frac{\phi_r(x)e^{j\omega t}}{\omega_r{}^2 - \omega^2 + j2\zeta_r\omega_r\omega}\right] \tag{3.51}$$

Having obtained the vibration response relative to the moving base, one can easily use superimpose the base motion and the relative response to obtain the transverse displacement response at point *x* relative to the fixed frame as follows:

$$w^p(x,t) = w_b(x,t) + w_{rel}^p(x,t) \tag{3.52}$$

where the base displacement $w_b(x,t)$ is given by Eq. (3.1).

3.4 Single-mode Electromechanical Expressions for Modal Excitations

The steady-state voltage response and vibration response expressions obtained in Sections 3.2 and 3.3 are valid for harmonic excitations at any arbitrary frequency ω. That is, Eqs. (3.39) and (3.41) for the series connection of the piezoceramic layers (Fig. 3.1a) and Eqs. (3.49) and (3.51) for the parallel connection of the piezoceramic layers (Fig. 3.1b) are the *multi-mode* solutions as they include all vibration modes of the bimorph harvester. Hence, these equations can predict the coupled system dynamics at steady state not only for resonance excitation but also for excitations at the off-resonance frequencies of the energy harvester.

In order to obtain the maximum electrical response, it is preferable to excite a given energy harvester at its fundamental resonance frequency (or at one of the higher resonance frequencies). Most of the studies in the literature have focused on the resonance excitation at the fundamental resonance frequency in order to investigate the maximum power generation performance. Consequently, excitation of a bimorph at or very close to one of its natural frequencies is a very useful problem to investigate through the resulting equations derived here. This is the *modal excitation* condition and mathematically it implies $\omega \cong \omega_r$. With this assumption for the excitation frequency, the major contribution in the summation terms of Eqs. (3.39), (3.41), (3.49) and (3.51) are from the *r*-th vibration mode. This approximation allows simplifications in the coupled voltage response and vibration response expressions.

In the following, the reduced *single-mode* expressions are given for excitations at or very close to the *r*-th natural frequency, however, it should be noted that the fundamental mode is the main concern in the energy harvesting problem (which corresponds to $r = 1$).

3.4.1 Series Connection of the Piezoceramic Layers. If the bimorph configuration shown in Fig. 3.1a is excited at $\omega \cong \omega_r$, the contribution of all vibration modes other than the *r*-th mode can be ignored in the summation terms. Then, the steady-state voltage response given by Eq. (3.39) can be reduced to

$$\hat{v}_s(t) = \frac{j2\omega R_l \kappa_r F_r e^{j\omega t}}{\left(2 + j\omega R_l C_{\tilde{p}}\right)\left(\omega_r^{\,2} - \omega^2 + j2\zeta_r \omega_r \omega\right) + j2\omega R_l \kappa_r \chi_r^s} \tag{3.53}$$

and the transverse displacement relative to the moving base is simply obtained from Eq. (3.41) as

$$\hat{w}_{rel}^{s}(x,t)=\frac{\left(2+j\omega R_l C_{\tilde{p}}\right)F_r\phi_r(x)e^{j\omega t}}{\left(2+j\omega R_l C_{\tilde{p}}\right)\left(\omega_r{}^2-\omega^2+j2\zeta_r\omega_r\omega\right)+j2\omega R_l\kappa_r\chi_r^s} \tag{3.54}$$

where the relevant terms can be found in Section 3.2. Here and hereafter, a hat (^) denotes that the respective term is reduced from the full solution to a single mode for excitations very close to a natural frequency.

3.4.2 Parallel Connection of the Piezoceramic Layers. Similarly, if the bimorph configuration displayed in Fig. 3.1b is excited at $\omega\cong\omega_r$, the steady-state voltage response given by Eq. (3.49) can be reduced to

$$\hat{v}_p(t)=\frac{j2\omega R_l\kappa_r F_r e^{j\omega t}}{\left(1+j2\omega R_l C_{\tilde{p}}\right)\left(\omega_r{}^2-\omega^2+j2\zeta_r\omega_r\omega\right)+j2\omega R_l\kappa_r\chi_r^p} \tag{3.55}$$

and the transverse displacement relative to the base is obtained from Eq. (3.51) as

$$\hat{w}_{rel}^{p}(x,t)=\frac{\left(1+j2\omega R_l C_{\tilde{p}}\right)F_r\phi_r(x)e^{j\omega t}}{\left(1+j2\omega R_l C_{\tilde{p}}\right)\left(\omega_r{}^2-\omega^2+j2\zeta_r\omega_r\omega\right)+j2\omega R_l\kappa_r\chi_r^p} \tag{3.56}$$

where the relevant terms can be found in Section 3.3.

3.5 Multi-mode and Single-mode Electromechanical FRFs

In the electromechanical model proposed here, the two excitation inputs to the system are the translation of the base in the transverse direction and its small rotation (Figs. 3.1a and 3.1b). For these two inputs, the resulting electromechanical outputs are the voltage response and the vibration response. Therefore, for harmonic base excitations, one can define four electromechanical FRFs between these two outputs and two inputs: voltage output – to – translational base acceleration, voltage output – to – rotational base acceleration, vibration response – to – translational base acceleration and vibration response – to – rotational base acceleration. This section extracts these FRFs from the multi-mode (for arbitrary frequency excitations) and single-mode (for modal excitations) steady-state solutions derived in the previous sections.

3.5.1 Multi-mode Electromechanical FRFs. Since the translational and the small rotational displacements of the base are given by $g(t) = W_0 e^{j\omega t}$ and $h(t) = \theta_0 e^{j\omega t}$, the modal forcing function has the form of $f_r(t) = F_r e^{j\omega t}$ where F_r is given by Eq. (3.36). Before identifying the aforementioned FRFs, one should first rearrange the complex modal forcing amplitude given by Eq. (3.36) as follows:

$$F_r = -\sigma_r \omega^2 W_0 - \tau_r \omega^2 \theta_0 \tag{3.57}$$

where

$$\sigma_r = -m\int_0^L \phi_r(x)dx - M_t \phi_r(L) \tag{3.58}$$

$$\tau_r = -m\int_0^L x\phi_r(x)dx - M_t L \phi_r(L) \tag{3.59}$$

3.5.1.1 Series Connection of the Piezoceramic Layers. The steady-state voltage response given by Eq. (3.39) can be written in terms of the translational and rotational base accelerations as

$$v_s(t) = \alpha_s(\omega)\left(-\omega^2 W_0 e^{j\omega t}\right) + \mu_s(\omega)\left(-\omega^2 \theta_0 e^{j\omega t}\right) \tag{3.60}$$

where the FRF that relates the voltage output to the translational base acceleration is

$$\alpha_s(\omega) = \frac{\sum_{r=1}^{\infty} \dfrac{j\omega \kappa_r \sigma_r}{\omega_r^2 - \omega^2 + j2\zeta_r \omega_r \omega}}{\dfrac{1}{R_l} + j\omega \dfrac{C_{\tilde{p}}}{2} + \sum_{r=1}^{\infty} \dfrac{j\omega \kappa_r \chi_r^s}{\omega_r^2 - \omega^2 + j2\zeta_r \omega_r \omega}} \tag{3.61}$$

and the voltage output per rotational base acceleration input can be given by

$$\mu_s(\omega) = \frac{\sum_{r=1}^{\infty} \dfrac{j\omega \kappa_r \tau_r}{\omega_r^2 - \omega^2 + j2\zeta_r \omega_r \omega}}{\dfrac{1}{R_l} + j\omega \dfrac{C_{\tilde{p}}}{2} + \sum_{r=1}^{\infty} \dfrac{j\omega \kappa_r \chi_r^s}{\omega_r^2 - \omega^2 + j2\zeta_r \omega_r \omega}} \tag{3.62}$$

Similarly, the steady-state vibration response relative to the base of the bimorph given by Eq. (3.41) can be expressed as

$$w_{rel}^s(x,t) = \beta_s(\omega, x)\left(-\omega^2 W_0 e^{j\omega t}\right) + \psi_s(\omega, x)\left(-\omega^2 \theta_0 e^{j\omega t}\right) \tag{3.63}$$

where the relative transverse displacement response – to – translational base acceleration FRF is

$$\beta_s(\omega,x)=\sum_{r=1}^{\infty}\left[\left(\sigma_r-\chi_r^s\frac{\sum_{r=1}^{\infty}\frac{j\omega\kappa_r\sigma_r}{\omega_r{}^2-\omega^2+j2\zeta_r\omega_r\omega}}{\frac{1}{R_l}+j\omega\frac{C_{\tilde{p}}}{2}+\sum_{r=1}^{\infty}\frac{j\omega\kappa_r\chi_r^s}{\omega_r{}^2-\omega^2+j2\zeta_r\omega_r\omega}}\right)\frac{\phi_r(x)}{\omega_r{}^2-\omega^2+j2\zeta_r\omega_r\omega}\right] \tag{3.64}$$

The relative transverse displacement response and the rotational base acceleration are related by

$$\psi_s(\omega,x)=\sum_{r=1}^{\infty}\left[\left(\tau_r-\chi_r^s\frac{\sum_{r=1}^{\infty}\frac{j\omega\kappa_r\tau_r}{\omega_r{}^2-\omega^2+j2\zeta_r\omega_r\omega}}{\frac{1}{R_l}+j\omega\frac{C_{\tilde{p}}}{2}+\sum_{r=1}^{\infty}\frac{j\omega\kappa_r\chi_r^s}{\omega_r{}^2-\omega^2+j2\zeta_r\omega_r\omega}}\right)\frac{\phi_r(x)}{\omega_r{}^2-\omega^2+j2\zeta_r\omega_r\omega}\right] \tag{3.65}$$

3.5.1.2 Parallel Connection of the Piezoceramic Layers. It is possible to derive similar FRFs for the parallel connection of the piezoceramic layers. The steady-state voltage response given by Eq. (3.49) can be rearranged to yield

$$v_p(t)=\alpha_p(\omega)\left(-\omega^2W_0e^{j\omega t}\right)+\mu_p(\omega)\left(-\omega^2\theta_0e^{j\omega t}\right) \tag{3.66}$$

where the voltage output – to – translational base acceleration FRF is

$$\alpha_p(\omega)=\frac{\sum_{r=1}^{\infty}\frac{j\omega\kappa_r\sigma_r}{\omega_r{}^2-\omega^2+j2\zeta_r\omega_r\omega}}{\frac{1}{2R_l}+j\omega C_{\tilde{p}}+\sum_{r=1}^{\infty}\frac{j\omega\kappa_r\chi_r^p}{\omega_r{}^2-\omega^2+j2\zeta_r\omega_r\omega}} \tag{3.67}$$

and the voltage output – to – rotational base acceleration FRF can be given by

$$\mu_p(\omega)=\frac{\sum_{r=1}^{\infty}\frac{j\omega\kappa_r\tau_r}{\omega_r{}^2-\omega^2+j2\zeta_r\omega_r\omega}}{\frac{1}{2R_l}+j\omega C_{\tilde{p}}+\sum_{r=1}^{\infty}\frac{j\omega\kappa_r\chi_r^p}{\omega_r{}^2-\omega^2+j2\zeta_r\omega_r\omega}} \tag{3.68}$$

From Eq. (3.51), the steady-state vibration response relative to the base of the bimorph can be expressed as

$$w_{rel}^p(x,t)=\beta_p(\omega,x)\left(-\omega^2W_0e^{j\omega t}\right)+\psi_p(\omega,x)\left(-\omega^2\theta_0e^{j\omega t}\right) \tag{3.69}$$

where the relative transverse displacement response – to – translational base acceleration FRF is

$$\beta_p(\omega,x)=\sum_{r=1}^{\infty}\left[\left(\sigma_r-\chi_r^p\frac{\sum_{r=1}^{\infty}\frac{j\omega\kappa_r\sigma_r}{\omega_r{}^2-\omega^2+j2\zeta_r\omega_r\omega}}{\frac{1}{2R_l}+j\omega C_{\tilde{p}}+\sum_{r=1}^{\infty}\frac{j\omega\kappa_r\chi_r^p}{\omega_r{}^2-\omega^2+j2\zeta_r\omega_r\omega}}\right)\frac{\phi_r(x)}{\omega_r{}^2-\omega^2+j2\zeta_r\omega_r\omega}\right] \tag{3.70}$$

and the relative transverse displacement response – to – rotational base acceleration FRF is

$$\psi_p(\omega,x)=\sum_{r=1}^{\infty}\left[\left(\tau_r-\chi_r^p\frac{\sum_{r=1}^{\infty}\frac{j\omega\kappa_r\tau_r}{\omega_r{}^2-\omega^2+j2\zeta_r\omega_r\omega}}{\frac{1}{2R_l}+j\omega C_{\tilde{p}}+\sum_{r=1}^{\infty}\frac{j\omega\kappa_r\chi_r^p}{\omega_r{}^2-\omega^2+j2\zeta_r\omega_r\omega}}\right)\frac{\phi_r(x)}{\omega_r{}^2-\omega^2+j2\zeta_r\omega_r\omega}\right] \tag{3.71}$$

3.5.2 Single-mode Electromechanical FRFs. In order to extract the respective FRFs of the single-mode expressions, one should use Eqs. (3.53)-(3.56) along with Eq. (3.57). In the following, Eq. (3.57) is substituted into each of Eqs. (3.53)-(3.56) and the relevant FRFs are extracted as done for the multi-mode solution case. Note that the single-mode electromechanical FRFs given here provide approximation of the full solution for modal excitations ($\omega\cong\omega_r$) only.

3.5.2.1 Series Connection of the Piezoceramic Layers. Equation (3.53) can be rearranged to give the single-mode steady-state voltage response as

$$\hat{v}_s(t)=\hat{\alpha}_s(\omega)\left(-\omega^2W_0e^{j\omega t}\right)+\hat{\mu}_s(\omega)\left(-\omega^2\theta_0e^{j\omega t}\right) \tag{3.72}$$

where the single-mode FRF that relates the voltage output to the translational base acceleration is

$$\hat{\alpha}_s(\omega)=\frac{j2\omega R_l\kappa_r\sigma_r}{\left(2+j\omega R_lC_{\tilde{p}}\right)\left(\omega_r{}^2-\omega^2+j2\zeta_r\omega_r\omega\right)+j2\omega R_l\kappa_r\chi_r^s} \tag{3.73}$$

and the single-mode voltage output – to – rotational base acceleration FRF is

$$\hat{\mu}_s(\omega)=\frac{j2\omega R_l\kappa_r\tau_r}{\left(2+j\omega R_lC_{\tilde{p}}\right)\left(\omega_r{}^2-\omega^2+j2\zeta_r\omega_r\omega\right)+j2\omega R_l\kappa_r\chi_r^s} \tag{3.74}$$

The single-mode steady-state vibration response relative to the base of the bimorph given by Eq. (3.54) can be rearranged to give

$$\hat{w}_{rel}^s(x,t)=\hat{\beta}_s(\omega,x)\left(-\omega^2W_0e^{j\omega t}\right)+\hat{\psi}_s(\omega,x)\left(-\omega^2\theta_0e^{j\omega t}\right) \tag{3.75}$$

where the single-mode relative transverse displacement response – to – translational base acceleration FRF is

$$\hat{\beta}_s(\omega,x)=\frac{\left(2+j\omega R_lC_{\tilde{p}}\right)\sigma_r\phi_r(x)}{\left(2+j\omega R_lC_{\tilde{p}}\right)\left(\omega_r{}^2-\omega^2+j2\zeta_r\omega_r\omega\right)+j2\omega R_l\kappa_r\chi_r^s} \tag{3.76}$$

and the single-mode relative transverse displacement response – to – rotational base acceleration FRF can be given by

$$\hat{\psi}_s(\omega,x)=\frac{\left(2+j\omega R_l C_{\tilde{p}}\right)\tau_r\phi_r(x)}{\left(2+j\omega R_l C_{\tilde{p}}\right)\left(\omega_r{}^2-\omega^2+j2\zeta_r\omega_r\omega\right)+j2\omega R_l\kappa_r\chi_r^s} \tag{3.77}$$

3.5.2.2 Parallel Connection of the Piezoceramic Layers. The single-mode steady-state voltage response given by Eq. (3.55) can be expressed in terms of the translational and the rotational base accelerations as

$$\hat{v}_p(t)=\hat{\alpha}_p(\omega)\left(-\omega^2 W_0 e^{j\omega t}\right)+\hat{\mu}_p(\omega)\left(-\omega^2\theta_0 e^{j\omega t}\right) \tag{3.78}$$

Here, the single-mode FRF that relates the voltage output to the translational base acceleration is

$$\hat{\alpha}_p(\omega)=\frac{j2\omega R_l\kappa_r\sigma_r}{\left(1+j2\omega R_l C_{\tilde{p}}\right)\left(\omega_r{}^2-\omega^2+j2\zeta_r\omega_r\omega\right)+j2\omega R_l\kappa_r\chi_r^p} \tag{3.79}$$

and the single-mode FRF that relates the voltage output to the rotational base acceleration is

$$\hat{\mu}_p(\omega)=\frac{j2\omega R_l\kappa_r\tau_r}{\left(1+j2\omega R_l C_{\tilde{p}}\right)\left(\omega_r{}^2-\omega^2+j2\zeta_r\omega_r\omega\right)+j2\omega R_l\kappa_r\chi_r^p} \tag{3.80}$$

Similarly, the single-mode steady-state vibration response relative to the base of the bimorph given by Eq. (3.56) can be rewritten as

$$\hat{w}_{rel}^p(x,t)=\hat{\beta}_p(\omega,x)\left(-\omega^2 W_0 e^{j\omega t}\right)+\hat{\psi}_p(\omega,x)\left(-\omega^2\theta_0 e^{j\omega t}\right) \tag{3.81}$$

where the single-mode relative transverse displacement response – to – translational base acceleration FRF can be given by

$$\hat{\beta}_p(\omega,x)=\frac{\left(1+j2\omega R_l C_{\tilde{p}}\right)\sigma_r\phi_r(x)}{\left(1+j2\omega R_l C_{\tilde{p}}\right)\left(\omega_r{}^2-\omega^2+j2\zeta_r\omega_r\omega\right)+j2\omega R_l\kappa_r\chi_r^p} \tag{3.82}$$

and the single-mode relative transverse displacement response – to – rotational base acceleration FRF is

$$\hat{\psi}_p(\omega,x)=\frac{\left(1+j2\omega R_l C_{\tilde{p}}\right)\tau_r\phi_r(x)}{\left(1+j2\omega R_l C_{\tilde{p}}\right)\left(\omega_r{}^2-\omega^2+j2\zeta_r\omega_r\omega\right)+j2\omega R_l\kappa_r\chi_r^p} \tag{3.83}$$

3.6 Equivalent Representation of the Series and Parallel Connection Expressions

This section aims to obtain an equivalent (or a unified) representation of the distributed-parameter analytical solutions derived for the series and the parallel connection cases. For this

purpose, the equivalent electromechanical coupling and the capacitance terms are obtained first and then the resulting equivalent representation is given.

3.6.1 Modal Electromechanical Coupling Terms. A careful investigation of the coefficient of backward coupling term for the series connection case (Eq. (3.8)) yields

$$\vartheta_s = \frac{\bar{e}_{31} b}{2h_{\tilde{p}}}\left[\frac{h_{\tilde{s}}^{\,2}}{4} - \left(h_{\tilde{p}} + \frac{h_{\tilde{s}}}{2}\right)^2\right] = -\frac{\bar{e}_{31} b}{2h_{\tilde{p}}}\left[\left(h_{\tilde{p}} + h_{\tilde{s}}\right) h_{\tilde{p}}\right] = -\bar{e}_{31} b \frac{h_{\tilde{p}} + h_{\tilde{s}}}{2} = -\bar{e}_{31} b h_{\tilde{p}c} \tag{3.84}$$

Then, Eq. (3.9) for the parallel connection case becomes

$$\vartheta_p = 2\vartheta_s = -2\bar{e}_{31} b h_{\tilde{p}c} \tag{3.85}$$

From Eqs. (3.31) and (3.44), the backward modal coupling terms lead to

$$\chi_r^s = -\bar{e}_{31} b h_{\tilde{p}c} \left.\frac{d\phi_r(x)}{dx}\right|_{x=L} \tag{3.86}$$

$$\chi_r^p = -2\bar{e}_{31} b h_{\tilde{p}c} \left.\frac{d\phi_r(x)}{dx}\right|_{x=L} \tag{3.87}$$

One can then notice the similarity of these expressions to the forward modal coupling term given by Eq. (3.35):

$$\kappa_r = -\bar{e}_{31} b h_{\tilde{p}c} \left.\frac{d\phi_r(x)}{dx}\right|_{x=L} \tag{3.88}$$

3.6.2 Equivalent Capacitance for Series and Parallel Connections. The circuit equation for the series connection case given by Eq. (3.33) can be re-written as

$$C_{\tilde{p}}^{eq,s} \frac{dv_s(t)}{dt} + \frac{v_s(t)}{R_l} = \sum_{r=1}^{\infty} \kappa_r \frac{d\eta_r^s(t)}{dt} \tag{3.89}$$

where

$$C_{\tilde{p}}^{eq,s} = \frac{C_{\tilde{p}}}{2} = \frac{\bar{\varepsilon}_{33}^S b L}{2h_{\tilde{p}}} \tag{3.90}$$

is the equivalent capacitance of two capacitors ($C_{\tilde{p}}$) connected in series.

Likewise, the circuit equation for the parallel connection case given by Eq. (3.45) can be re-arranged to give

$$C_{\tilde{p}}^{eq,p}\frac{dv_p(t)}{dt}+\frac{v_p(t)}{R_l}=\sum_{r=1}^{\infty}2\kappa_r\frac{d\eta_r^p(t)}{dt} \tag{3.91}$$

where

$$C_{\tilde{p}}^{eq,p}=2C_{\tilde{p}}=\frac{2\bar{\varepsilon}_{33}^{S}bL}{h_{\tilde{p}}} \tag{3.92}$$

is the equivalent capacitance of two capacitors ($C_{\tilde{p}}$) connected in parallel. Note that the difference between the representations of Eqs. (3.89) and (3.91) is a factor of two in the coupling terms, as in the backward coupling terms given by Eqs. (3.86) and (3.87). Indeed, from Eqs. (3.86)-(3.88), $\kappa_r=\chi_r^s$ and $2\kappa_r=\chi_r^p$.

3.6.3 Equivalent Representation of the Electromechanical Expressions. The equivalent electromechanical equations governing the modal mechanical response and the voltage response of a bimorph can be given by

$$\frac{d^2\eta_r(t)}{dt^2}+2\zeta_r\omega_r\frac{d\eta_r(t)}{dt}+\omega_r{}^2\eta_r(t)+\tilde{\theta}_r v(t)=f_r(t) \tag{3.93}$$

$$C_{\tilde{p}}^{eq}\frac{dv(t)}{dt}+\frac{v(t)}{R_l}=\sum_{r=1}^{\infty}\tilde{\theta}_r\frac{d\eta_r(t)}{dt} \tag{3.94}$$

where the modal electromechanical coupling term $\tilde{\theta}_r$ and the equivalent capacitance $C_{\tilde{p}}^{eq}$ depend on the way piezoceramic layers are connected (Table 3.1). In Eqs. (3.93) and (3.94), $\eta_r(t)$ is the modal mechanical response that gives the transverse displacement response of the cantilever relative to its moving base when used in Eq. (3.25) whereas $v(t)$ is the voltage across the load resistance (i.e. $v(t)=v_s(t)$ in Fig. 3.1a and $v(t)=v_p(t)$ in Fig. 3.1b).

As mentioned previously, for harmonic base displacement inputs of $g(t)=W_0e^{j\omega t}$ and $h(t)=\theta_0e^{j\omega t}$, the modal forcing function is harmonic of the form $f_r(t)=F_re^{j\omega t}$ where the amplitude F_r is given by Eq. (3.36). Substituting the steady-state response expressions $\eta_r(t)=\mathrm{H}_re^{j\omega t}$ and $v(t)=Ve^{j\omega t}$ into Eqs. (3.93) and (3.94) gives $\infty+1$ coupled linear algebraic equations for the complex amplitudes H_r and V (infinite mechanical degrees of freedom due to $r=1...\infty$ and one electrical degree of freedom):

$$\left(\omega_r{}^2 - \omega^2 + j2\zeta_r\omega_r\omega\right)\mathrm{H}_r + \tilde{\theta}_r V = F_r \tag{3.95}$$

$$\left(\frac{1}{R_l} + j\omega C_{\tilde{p}}^{eq}\right)V - j\omega\sum_{r=1}^{\infty}\tilde{\theta}_r\mathrm{H}_r = 0 \tag{3.96}$$

Eventually one obtains the steady-state voltage response and the vibration response expressions as follows:

$$v(t) = \frac{\displaystyle\sum_{r=1}^{\infty}\frac{j\omega\tilde{\theta}_r F_r}{\omega_r{}^2 - \omega^2 + j2\zeta_r\omega_r\omega}}{\dfrac{1}{R_l} + j\omega C_{\tilde{p}}^{eq} + \displaystyle\sum_{r=1}^{\infty}\frac{j\omega\tilde{\theta}_r^2}{\omega_r{}^2 - \omega^2 + j2\zeta_r\omega_r\omega}}e^{j\omega t} \tag{3.97}$$

$$w_{rel}(x,t) = \sum_{r=1}^{\infty}\left[\left(F_r - \tilde{\theta}_r\frac{\displaystyle\sum_{r=1}^{\infty}\frac{j\omega\tilde{\theta}_r F_r}{\omega_r{}^2 - \omega^2 + j2\zeta_r\omega_r\omega}}{\dfrac{1}{R_l} + j\omega C_{\tilde{p}}^{eq} + \displaystyle\sum_{r=1}^{\infty}\frac{j\omega\tilde{\theta}_r^2}{\omega_r{}^2 - \omega^2 + j2\zeta_r\omega_r\omega}}\right)\frac{\phi_r(x)e^{j\omega t}}{\omega_r{}^2 - \omega^2 + j2\zeta_r\omega_r\omega}\right] \tag{3.98}$$

For modal excitations (i.e. $\omega \cong \omega_r$), Eqs. (3.97) and (3.98) reduce to

$$\hat{v}(t) = \frac{j\omega R_l\tilde{\theta}_r F_r e^{j\omega t}}{\left(1 + j\omega R_l C_{\tilde{p}}^{eq}\right)\left(\omega_r{}^2 - \omega^2 + j2\zeta_r\omega_r\omega\right) + j\omega R_l\tilde{\theta}_r^2} \tag{3.99}$$

$$\hat{w}_{rel}(x,t) = \frac{\left(1 + j\omega R_l C_{\tilde{p}}^{eq}\right)F_r\phi_r(x)e^{j\omega t}}{\left(1 + j\omega R_l C_{\tilde{p}}^{eq}\right)\left(\omega_r{}^2 - \omega^2 + j2\zeta_r\omega_r\omega\right) + j\omega R_l\tilde{\theta}_r^2} \tag{3.100}$$

Table 3.1 Modal electromechanical coupling and equivalent capacitance of a bimorph energy harvester for the series and the parallel connections of the piezocermaic layers

	Series connection	**Parallel connection**
$\tilde{\theta}_r$	$-\overline{e}_{31}bh_{\tilde{p}c}\left.\dfrac{d\phi_r(x)}{dx}\right\|_{x=L}$	$-2\overline{e}_{31}bh_{\tilde{p}c}\left.\dfrac{d\phi_r(x)}{dx}\right\|_{x=L}$
$C_{\tilde{p}}^{eq}$	$\dfrac{\overline{\varepsilon}_{33}^{S}bL}{2h_{\tilde{p}}}$	$\dfrac{2\overline{\varepsilon}_{33}^{S}bL}{h_{\tilde{p}}}$

3.6.4 Equivalent Representation of the Multi-mode Electromechanical FRFs. Equation (3.97) can be re-expressed as

$$v(t) = \alpha(\omega)\left(-\omega^2 W_0 e^{j\omega t}\right) + \mu(\omega)\left(-\omega^2 \theta_0 e^{j\omega t}\right) \tag{3.101}$$

where the voltage output – to – translational base acceleration FRF is

$$\alpha(\omega) = \frac{\displaystyle\sum_{r=1}^{\infty} \frac{j\omega\tilde{\theta}_r \sigma_r}{\omega_r{}^2 - \omega^2 + j2\zeta_r\omega_r\omega}}{\dfrac{1}{R_l} + j\omega C_{\tilde{p}}^{eq} + \displaystyle\sum_{r=1}^{\infty} \frac{j\omega\tilde{\theta}_r^2}{\omega_r{}^2 - \omega^2 + j2\zeta_r\omega_r\omega}} \tag{3.102}$$

and the voltage output – to – rotational base acceleration FRF can be given by

$$\mu(\omega) = \frac{\displaystyle\sum_{r=1}^{\infty} \frac{j\omega\tilde{\theta}_r \tau_r}{\omega_r{}^2 - \omega^2 + j2\zeta_r\omega_r\omega}}{\dfrac{1}{R_l} + j\omega C_{\tilde{p}}^{eq} + \displaystyle\sum_{r=1}^{\infty} \frac{j\omega\tilde{\theta}_r^2}{\omega_r{}^2 - \omega^2 + j2\zeta_r\omega_r\omega}} \tag{3.103}$$

Similarly, Eq. (3.98) can be written as

$$w_{rel}(x,t) = \beta(\omega,x)\left(-\omega^2 W_0 e^{j\omega t}\right) + \psi(\omega,x)\left(-\omega^2 \theta_0 e^{j\omega t}\right) \tag{3.104}$$

where the relative transverse displacement response – to – translational base acceleration FRF is

$$\beta(\omega,x) = \sum_{r=1}^{\infty}\left[\left(\sigma_r - \tilde{\theta}_r \frac{\displaystyle\sum_{r=1}^{\infty} \frac{j\omega\tilde{\theta}_r \sigma_r}{\omega_r{}^2 - \omega^2 + j2\zeta_r\omega_r\omega}}{\dfrac{1}{R_l} + j\omega C_{\tilde{p}}^{eq} + \displaystyle\sum_{r=1}^{\infty} \frac{j\omega\tilde{\theta}_r^2}{\omega_r{}^2 - \omega^2 + j2\zeta_r\omega_r\omega}}\right)\frac{\phi_r(x)}{\omega_r{}^2 - \omega^2 + j2\zeta_r\omega_r\omega}\right] \tag{3.105}$$

and the relative transverse displacement response – to – rotational base acceleration FRF is

$$\psi(\omega,x) = \sum_{r=1}^{\infty}\left[\left(\tau_r - \tilde{\theta}_r \frac{\displaystyle\sum_{r=1}^{\infty} \frac{j\omega\tilde{\theta}_r \tau_r}{\omega_r{}^2 - \omega^2 + j2\zeta_r\omega_r\omega}}{\dfrac{1}{R_l} + j\omega C_{\tilde{p}}^{eq} + \displaystyle\sum_{r=1}^{\infty} \frac{j\omega\tilde{\theta}_r^2}{\omega_r{}^2 - \omega^2 + j2\zeta_r\omega_r\omega}}\right)\frac{\phi_r(x)}{\omega_r{}^2 - \omega^2 + j2\zeta_r\omega_r\omega}\right] \tag{3.106}$$

3.6.5 Equivalent Representation of the Single-mode Electromechanical FRFs. From Eq. (3.99):

$$\hat{v}(t) = \hat{\alpha}(\omega)\left(-\omega^2 W_0 e^{j\omega t}\right) + \hat{\mu}(\omega)\left(-\omega^2 \theta_0 e^{j\omega t}\right) \tag{3.107}$$

where the single-mode voltage output – to – translational base acceleration FRF is

$$\hat{\alpha}(\omega) = \frac{j\omega R_l \tilde{\theta}_r \sigma_r}{\left(1 + j\omega R_l C_{\tilde{p}}^{eq}\right)\left(\omega_r{}^2 - \omega^2 + j2\zeta_r\omega_r\omega\right) + j\omega R_l \tilde{\theta}_r^2} \tag{3.108}$$

and the single-mode voltage output – to – rotational base acceleration FRF is

$$\hat{\mu}(\omega) = \frac{j\omega R_l \tilde{\theta}_r \tau_r}{\left(1 + j\omega R_l C_{\tilde{p}}^{eq}\right)\left(\omega_r{}^2 - \omega^2 + j2\zeta_r \omega_r \omega\right) + j\omega R_l \tilde{\theta}_r^2} \tag{3.109}$$

Likewise, from Eq. (3.100):

$$\hat{w}_{rel}(x,t) = \hat{\beta}(\omega, x)\left(-\omega^2 W_0 e^{j\omega t}\right) + \hat{\psi}(\omega, x)\left(-\omega^2 \theta_0 e^{j\omega t}\right) \tag{3.110}$$

where the single-mode relative transverse displacement response – to – translational base acceleration FRF is

$$\hat{\beta}(\omega, x) = \frac{\left(1 + j\omega R_l C_{\tilde{p}}^{eq}\right)\sigma_r \phi_r(x)}{\left(1 + j\omega R_l C_{\tilde{p}}^{eq}\right)\left(\omega_r{}^2 - \omega^2 + j2\zeta_r \omega_r \omega\right) + j\omega R_l \tilde{\theta}_r^2} \tag{3.111}$$

and the single-mode relative transverse displacement response – to – rotational base acceleration FRF can be given by

$$\hat{\psi}(\omega, x) = \frac{\left(1 + j\omega R_l C_{\tilde{p}}^{eq}\right)\tau_r \phi_r(x)}{\left(1 + j\omega R_l C_{\tilde{p}}^{eq}\right)\left(\omega_r{}^2 - \omega^2 + j2\zeta_r \omega_r \omega\right) + j\omega R_l \tilde{\theta}_r^2} \tag{3.112}$$

3.7 Theoretical Case Study

This section presents theoretical demonstrations of the analytical model developed in this chapter. An extensive electromechanical analysis of a bimorph cantilever configuration is presented in the following subsections. First the series and the parallel connections of the piezoceramic layers are studied with a focus on multiple vibration modes. Then the electrical and mechanical response simulations of the multi-mode and single-mode FRFs are compared. The damping effect of piezoelectric power generation on the harvester beam is also investigated.

3.7.1 Properties of the Bimorph Cantilever. The geometric properties of the bimorph cantilever investigated in this case study are given in Table 3.2. The overhang length – to – total thickness ratio of the harvester is about 85.7 which makes it reasonable to neglect the shear deformation and the rotary inertia effects for the practical vibration modes (in agreement with the Euler-Bernoulli beam theory). The substructure layer is assumed to be aluminum, the piezoceramic layer is taken to be PZT-5A and the configuration does not have a tip mass (i.e. $M_t = I_t = 0$). The material properties of the substructure and the piezoceramic layers are shown in Table 3.3. The elastic, piezoelectric and permittivity constants of PZT-5A are obtained from

Table B.2 in the Appendix (reduced constants for the Euler-Bernoulli beam theory). The analysis given here considers the frequency range of 0-5000 Hz. It can easily be shown that this cantilever has three vibration modes in this frequency range. The first three mechanically and electrically *undamped* natural frequencies of the bimorph cantilever (for $R_l \to 0$) are $f_1 = 185.1\,\text{Hz}$, $f_2 = 1159.8\,\text{Hz}$ and $f_3 = 3247.6\,\text{Hz}$ (where $f_r = \omega_r / 2\pi$). For the purpose of simulation, if one takes $\zeta_1 = 0.010$ and $\zeta_2 = 0.012$ as the mechanical damping ratios of the first two modes and assumes proportional damping based on the discussion of Chapter 2, the proportionality constants $c_s I / YI$ and c_a / m are obtained from Eq. (2.17) (by using ζ_1, ζ_2, ω_1 and ω_2) as $c_s I / YI = 2.93 \times 10^{-6}$ s/rad and $c_a / m = 19.295$ rad/s. Closed-form identification of mechanical damping in the presence of an arbitrary load resistance based on the single-mode approximation is presented in Chapter 5. Here, it can be assumed that the damping ratios are identified by setting the electrical boundary condition to short circuit ($R_l \to 0$) and using conventional techniques (e.g. half-power points of the mechanical FRF [39]).

Before the simulation results are presented and discussed, it is worth adding a few words regarding the assumption of proportional damping. The restriction about the proportional damping assumption is such that, once the proportionality constants are identified using the modal properties of two vibration modes, the rest of the damping ratios are not arbitrary and they are automatically set equal to the following numbers due to Eq. (2.17): $\zeta_3 = 0.030$, $\zeta_4 = 0.059$, $\zeta_5 = 0.097$ and so on. It should be noted that the concept of proportional damping is a convenient *mathematical* modeling assumption (to force the system to be a normal-mode system) and the *physical* system may not agree with this assumption [36]. In other words, the damping ratios of higher modes identified experimentally from the physical system may not converge to the aforementioned values. Therefore, as a relaxation in the proportional damping assumption, one might prefer to use the identified damping ratios of the vibration modes of interest (to be used in the modal expressions) directly without obtaining $c_s I / YI$ and c_a / m since the resulting electromechanical expressions developed here need only the ζ_r values. This is the modal damping assumption and it is identical to starting with the respective undamped equation (the normal-mode problem by definition) and introducing damping in the modal domain. The proportional damping (in the form of Rayleigh damping) and modal damping assumptions are

often used in vibration engineering regardless of their practical limitations. As far as the problem of vibration energy harvesting is concerned, it is the fundamental vibration mode that has the highest importance and proportional damping (or modal damping) is a reasonable assumption to establish the bridge between the partial differential equation and its closed-form analytical solution given in this chapter.

Table 3.2 Geometric properties of the bimorph cantilever

	Piezoceramic	**Substructure**
Length (L) [mm]	30	30
Width (b) [mm]	5	5
Thickness (h_p , h_s) [mm]	0.15 (each)	0.05

Table 3.3 Material properties of the bimorph cantilever

	Piezoceramic	**Substructure**
Material	PZT-5A	Aluminum
Elastic modulus ($\overline{c}_{11}^E$, Y_s) [GPa]	61	70
Mass density (ρ_p , ρ_s) [kg/m^3]	7750	2700
Piezoelectric constant ($\overline{e}_{31}$) [C/m^2]	-10.4	-
Permittivity constant ($\overline{\varepsilon}_{33}^S$) [nF/m]	13.3	-

3.7.2 Frequency Response of the Voltage Output. In the simulations given here, the base of the cantilever is assumed to be not rotating (i.e. $h(t) = 0$ in Fig. 3.1) and the series connection case is considered first. The multi-mode voltage FRFs (per base acceleration) shown in Fig. 3.5 are obtained from

$$\frac{v(t)}{-\omega^2 W_0 e^{j\omega t}} = \frac{\sum_{r=1}^{\infty} \frac{j\omega \tilde{\theta}_r \sigma_r}{\omega_r{}^2 - \omega^2 + j2\zeta_r \omega_r \omega}}{\frac{1}{R_l} + j\omega C_{\tilde{p}}^{eq} + \sum_{r=1}^{\infty} \frac{j\omega \tilde{\theta}_r^2}{\omega_r{}^2 - \omega^2 + j2\zeta_r \omega_r \omega}} \tag{3.113}$$

where $\tilde{\theta}_r$ and $C_{\tilde{p}}^{eq}$ are as given in the first column of Table 3.1 for the series connection of the piezoceramic layers. Note that, here and hereafter, the electromechanical FRFs are given in the modulus form and the base acceleration in the frequency response graphs is normalized with respect to the gravitational acceleration for a convenient representation (i.e. the voltage FRF given by the foregoing equation is multiplied by the gravitational acceleration, $g = 9.81\,\mathrm{m/s^2}$). The set of electrical load resistance considered here ranges from $100\,\Omega$ to $10\,\mathrm{M}\Omega$. As far as the fundamental vibration mode of this particular bimorph is concerned, the lowest resistance ($R_l = 100\,\Omega$) used here is very close to the short-circuit conditions whereas the largest load ($R_l = 10\,\mathrm{M}\Omega$) is very close to the open-circuit conditions.

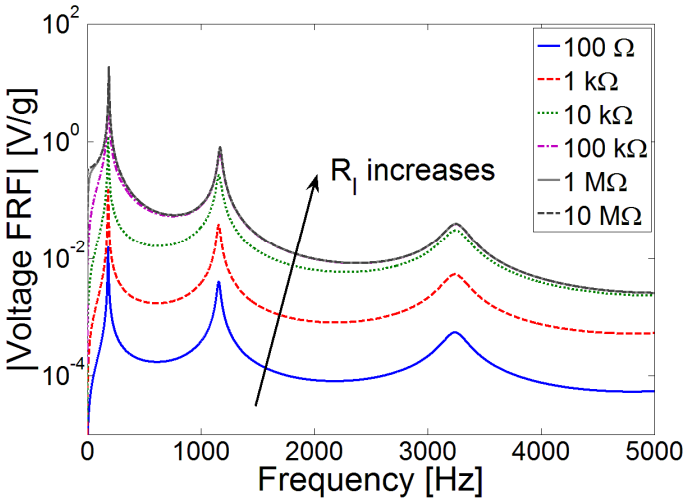

Fig. 3.5 Voltage FRFs of the bimorph for a broad range of load resistance (series connection of the piezoceramic layers)

As the load resistance is increased from the short-circuit to the open-circuit conditions, the voltage output at each frequency increases monotonically. To be precise, the voltage output for the exact short-circuit condition with zero external resistance ($R_l = 0$) would be zero, which would not allow defining a voltage FRF. Consequently, throughout this text, the short-circuit condition is defined as $R_l \to 0$. At the other extremum, the open-circuit condition ($R_l \to \infty$), the voltage output at each frequency converges to its maximum value. Another important aspect of the voltage FRFs plotted in Fig. 3.5 is that, with increasing load resistance, the resonance

frequency of each vibration mode moves from the short-circuit resonance frequency (ω_r^{sc} for $R_l \to 0$) to the open-circuit resonance frequency (ω_r^{oc} for $R_l \to \infty$). The short-circuit and the open-circuit resonance frequencies of the first three modes read from Fig. 3.5 are listed in Table 3.4 (where $f_r^{sc} = \omega_r^{sc} / 2\pi$ and $f_r^{oc} = \omega_r^{oc} / 2\pi$). The direct conclusion based on this observation is that the resonance frequency of a given piezoelectric energy harvester depends on the external load resistance. Moreover, depending on the external load resistance, the resonance frequency of each mode can take a value only between the short-circuit and the open-circuit resonance frequencies f_r^{sc} and f_r^{oc}. Closed-form identification of the frequency shift ($\Delta f_r = f_r^{oc} - f_r^{sc}$) based on the single-mode approximation is given in Chapter 5. Here, the data in Table 3.4 are read from the from the resulting frequency response graph given by Fig. 3.5.

Table 3.4 First three short-circuit and open-circuit resonance frequencies read from the voltage FRF of the bimorph piezoelectric energy harvester

Mode (r)	f_r^{sc} [Hz]	f_r^{oc} [Hz]
1	185.1	191.1
2	1159.7	1171.6
3	3245.3	3254.1

Two enlarged views of the voltage FRFs with a focus of the first two vibration modes are shown in Fig. 3.6 in order to display the resonance frequency shift from the short-circuit to the open-circuit conditions clearly. Note that the voltage FRFs of the largest two values of load resistance are almost indifferent especially for the second vibration mode, implying a convergence of the curves to the open-circuit voltage FRF. That is, if the voltage FRF for 100 $\mathrm{M}\Omega$ case was also plotted, it would not be any different from that of the 10 $\mathrm{M}\Omega$ case. Again, these numbers are for this particular cantilever. For a different configuration, it might be the case that even a load of 100 $\mathrm{k}\Omega$ might be sufficient to represent the open-circuit conditions.

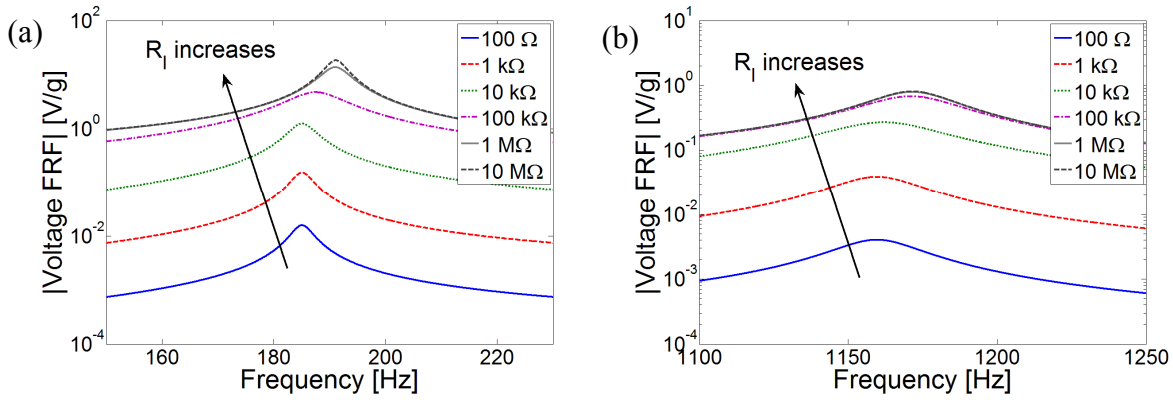

Fig. 3.6 Voltage FRFs of the bimorph with a focus on the first two vibration modes: (a) mode 1 and (b) mode 2 (series connection)

As far as the fundamental vibration mode is concerned, the short-circuit and the open-circuit resonance frequencies are 185.1 Hz and 191.1 Hz, respectively. Excitation at these two frequencies will be of particular interest in this section as well as in the experimental validations to be discussed in the next chapter. Variation of the voltage output for excitations at the *fundamental short-circuit resonance frequency* and at the *fundamental open-circuit resonance frequency* are plotted in Fig. 3.7. As can be seen from the figure, for low values of load resistance, the voltage output at the short-circuit resonance frequency is larger since the system (i.e. the electrical boundary condition) is close to short-circuit conditions. With increasing load resistance, the curves intersect at a certain point (around 120 kΩ) and for the values of load resistance larger than the value at the intersection point, the voltage output at the open-circuit resonance frequency is larger. It is important at this stage to notice the linear asymptotic trends at the extrema of $R_l \to 0$ and $R_l \to \infty$ (which will be proved mathematically in Chapter 5). The graph given here in log-log scale shows a linear increase in the voltage output with increasing load resistance for low values of load resistance (both for the short-circuit and the open-circuit resonance frequencies). The voltage output becomes less sensitive to the variations in the load resistance for its large values due to the horizontal asymptotes of the $R_l \to \infty$ extremum.

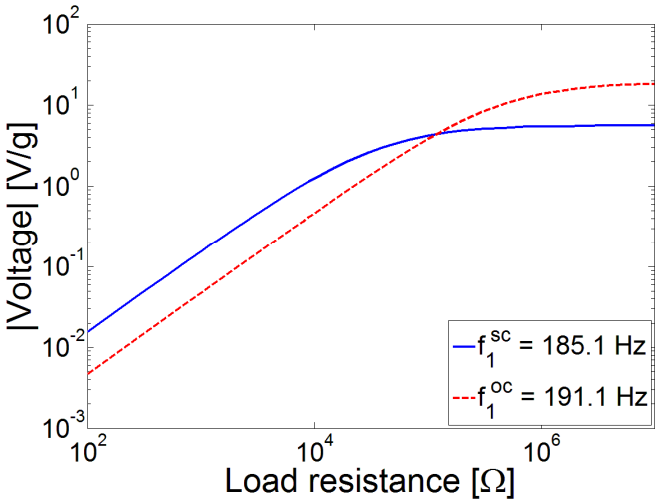

Fig. 3.7 Variation of the voltage output with load resistance for excitations at the short-circuit and the open-circuit resonance frequencies of the first vibration mode (series connection)

3.7.3 Frequency Response of the Current Output. If the voltage FRF given by Eq. (3.113) is divided by the load resistance, the multi-mode current FRF is obtained as

$$\frac{i(t)}{-\omega^2 W_0 e^{j\omega t}} = \frac{1}{R_l}\left(\frac{\sum_{r=1}^{\infty} \frac{j\omega\tilde{\theta}_r\sigma_r}{\omega_r{}^2 - \omega^2 + j2\zeta_r\omega_r\omega}}{\frac{1}{R_l} + j\omega C_{\tilde{p}}^{eq} + \sum_{r=1}^{\infty} \frac{j\omega\tilde{\theta}_r^2}{\omega_r{}^2 - \omega^2 + j2\zeta_r\omega_r\omega}} \right) \tag{3.114}$$

The modulus of the current FRF is plotted against the frequency in Fig. 3.8. Unlike the voltage FRF shown in Fig. 3.5, the amplitude of the current at every frequency decreases with increasing load resistance. Indeed this is the opposite of the voltage behavior shown in Fig. 3.8 but the behavior is still monotonic. For every excitation frequency, the maximum value of the current is obtained when the system is close to short-circuit conditions. The enlarged views of the current FRFs around the first two resonance frequencies are plotted in Fig. 3.9, showing the change in the resonance frequency with increasing load resistance. Moreover, being analogous to the behavior of voltage output close to open-circuit conditions, the current FRFs become indifferent close to short-circuit conditions. That is, if one plotted the current FRF of the 10 Ω case, the resulting graph would not look any different than that of the 100 Ω case.

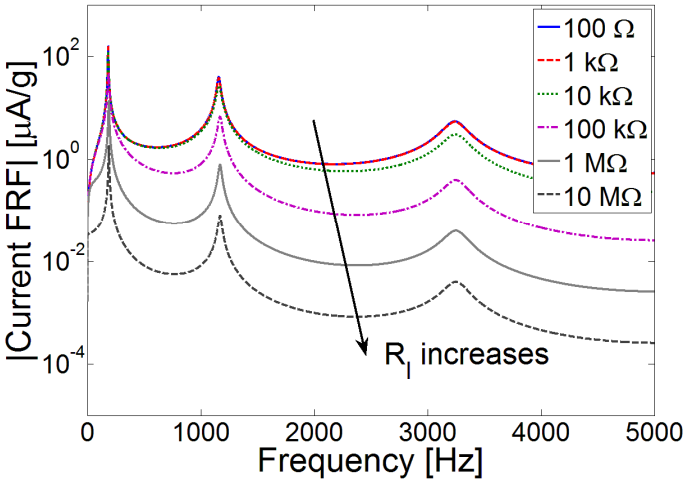

Fig. 3.8 Current FRFs of the bimorph for a broad range of load resistance (series connection of the piezoceramic layers)

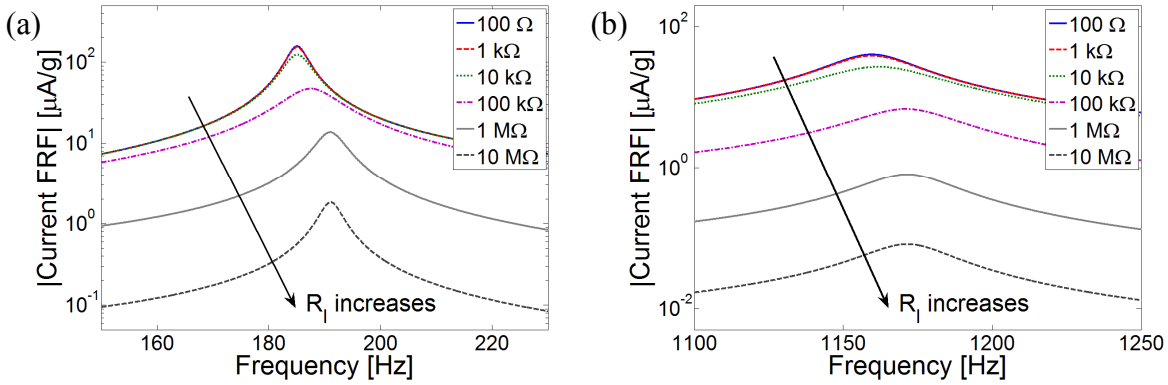

Fig. 3.9 Current FRFs of the bimorph with a focus on the first two vibration modes: (a) mode 1 and (b) mode 2 (series connection)

Figure 3.10 shows the current output as a function of load resistance for excitations at the fundamental short-circuit and the open-circuit resonance frequencies. It is clear from Fig. 3.10 that the current output is very insensitive to the variations of the region of low load resistance (i.e. the slope is almost zero for $R_l \to 0$). In this region of relatively low load resistance, the current output is larger at the short-circuit resonance frequency, as in the case of the voltage output (in Fig. 3.7), since the system is close to short-circuit conditions. Then, the current output starts decreasing with increasing load resistance until the curves intersect at a certain value of

load resistance (around 120 kΩ). For the values of load resistance larger than the value at this intersection point, the current output at the open-circuit resonance frequency becomes larger since the system approaches the open-circuit conditions. As in the voltage vs. load resistance graph, the asymptotic trends for $R_l \to 0$ and $R_l \to \infty$ appear to be linear.

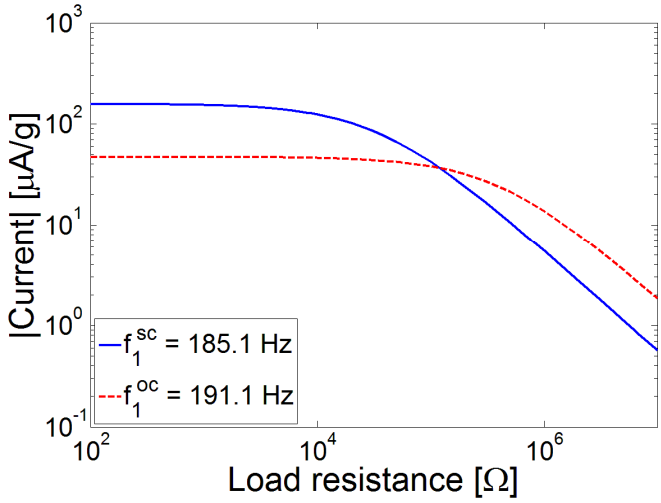

Fig. 3.10 Variation of the current output with load resistance for excitations at the short-circuit and the open-circuit resonance frequencies of the first vibration mode (series connection)

3.7.4 Frequency Response of the Power Output. The expression for the multi-mode power FRF is obtained from Eq. (3.113) as

$$\frac{p(t)}{\left(-\omega^2 W_0 e^{j\omega t}\right)^2} = \frac{1}{R_l}\left(\frac{\sum_{r=1}^{\infty}\frac{j\omega\tilde{\theta}_r\sigma_r}{\omega_r^{\,2}-\omega^2+j2\zeta_r\omega_r\omega}}{\frac{1}{R_l}+j\omega C_{\tilde{p}}^{eq}+\sum_{r=1}^{\infty}\frac{j\omega\tilde{\theta}_r^2}{\omega_r^{\,2}-\omega^2+j2\zeta_r\omega_r\omega}}\right)^2 \tag{3.115}$$

Therefore the power output is proportional to the square of the voltage output. As a result, the moduli of power FRFs plotted in Fig. 3.11 are normalized with respect to the square of base acceleration (i.e. g^2). According to Eq. (3.115), the power output is a product of two FRFs (current and voltage) with the opposite trends against the load resistance. It is clear from Fig. 3.11 that the power output FRF does not necessarily exhibit a monotonic behavior with increasing (or decreasing) load resistance for a given frequency. Among the sample values of the load resistance considered in this work, the maximum power output for the first vibration mode

corresponds to the load of 100 kΩ (see the enlarged view in Fig. 3.12a) at 187.5 Hz which is expectedly a frequency in between the fundamental short-circuit and open-circuit resonance frequencies. Considering the second vibration mode (see the second enlarged view in Fig. 3.12b), one observes that the maximum power output is obtained for 10 kΩ at frequency 1161.9 Hz. It should be noted that the values of the load resistance used in this analysis are taken arbitrarily to observe the general trends. Therefore, the maximum power outputs obtained from each vibration mode are for these sample values and they are *not* necessarily for the maximum possible (or the optimized) power outputs.[‡‡] Another interesting aspect of the power FRFs given in Fig. 3.11 is that they intersect one another. These intersections are observed not only around the resonance frequencies (e.g. the curves of 10 kΩ and 1 MΩ intersect at 190.2 Hz and 193.9 Hz in Fig. 3.12a) but also they are observed at the *off-resonance* frequencies (e.g. the curves of 10 kΩ and 100 kΩ intersect at 723.7 Hz in Fig. 3.11). At these intersection frequencies, the two respective load resistance values yield the same power output.

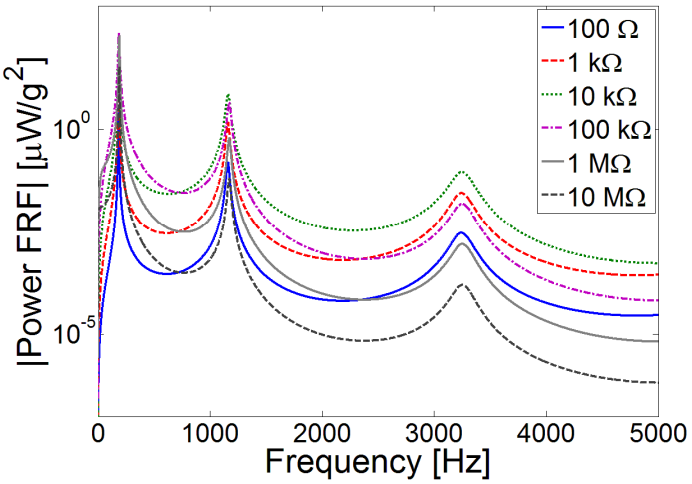

Fig. 3.11 Power FRFs of the bimorph for a broad range of load resistance (series connection of the piezoceramic layers)

The behavior of power output with changing load resistance for excitations at the fundamental short-circuit and open-circuit resonance frequencies are given in Fig. 3.13. It can be

[‡‡] Expressions of the optimum load resistance for modal excitations are given in Chapter 5.

recalled from Figs. 3.7 and 3.10 that the voltage and the current outputs obtained at the short-circuit resonance frequency are larger than the ones obtained at the open-circuit resonance frequency up to a certain load resistance (approximately 120 kΩ in this case) after which the opposite is valid. Since the power output is simply the product of the voltage and current, this observation is valid for the power versus load resistance curves as well. As can be seen form Fig. 3.13, the power output at the short-circuit resonance frequency is larger before the intersection point (at 120 kΩ) whereas the power output at the open-circuit resonance frequency is larger after this point. The asymptotic trends for $R_l \to 0$ and $R_l \to \infty$ are again linear and they appear to have the same slope in log-log scale.

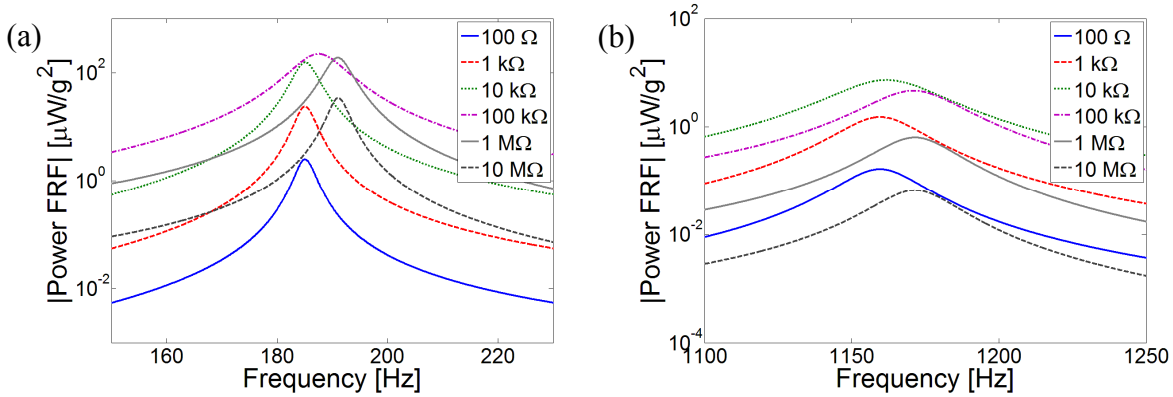

Fig. 3.12 Power FRFs of the bimorph with a focus on the first two vibration modes: (a) mode 1 and (b) mode 2 (series connection)

Since the behavior of power with changing load resistance is not monotonic, both of the power graphs shown in Fig. 3.13 exhibit peak values, which correspond to the optimum values of load resistance at the fundamental short-circuit and open-circuit resonance frequencies. When the optimum values of load resistance are used for each of the cases (short-circuit and open-circuit excitations), both of them yield the same power output. Considering Figs. 3.7 and 3.10, it can be observed that neither the voltages nor the currents are identical at these optimum values of load resistance for excitations at the two special frequencies. Therefore, in practice, if one is flexible in terms of the excitation frequency within this narrow frequency band, the short-circuit resonance frequency is preferable for larger current whereas the open-circuit resonance frequency is preferable for larger voltage (both yielding the same power output). Another aspect

of Fig. 3.13 is that the optimum values of load resistance at these two frequencies are considerably different (around 36 kΩ for excitation at 185.1 Hz and around 405 kΩ for excitation at 191.1 Hz). From another perspective, therefore, if the load resistance is a constraint, one can select the frequency of operation accordingly for the maximum power output.

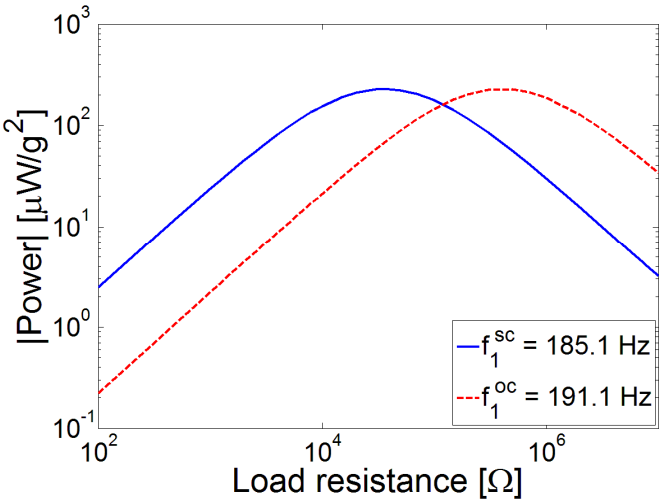

Fig. 3.13 Variation of the power output with load resistance for excitations at the short-circuit and the open-circuit resonance frequencies of the first vibration mode (series connection)

It is worth adding a few words on the advantage of using the fundamental vibration mode for energy harvesting compared to higher vibration modes. Figure 3.14 shows the power vs. load resistance curves obtained for excitation at the six frequencies listed in Table 3.4 (i.e. the short-circuit and the open-circuit resonance frequencies of the first three modes). The maximum power for mode 1 excitation is around 0.23 mW/g^2 at 185.1 Hz or at 191.1 Hz (for different optimum loads). For mode 2 excitation, the maximum power output is around 7.5 μW/g^2 (at 1159.7 Hz or at 1171.6 Hz). The maximum power output for mode 3 excitation is as low as 98 nW/g^2 (at 3245.3 Hz or at 3254.1 Hz). As the moduli of the voltage and current FRFs decay by one order of magnitude with increasing mode number according to Figs. 3.5 and 3.8, the modulus of the power FRF decays by around two orders of magnitude with the increasing mode number. Expectedly, the maximum power output is obtained for the fundamental vibration mode. For this reason, the focus is usually placed on this vibration mode in practical considerations (as well as in the experimental validations presented in the next chapter).

While considering the substantial difference between the moduli of the power FRFs for different vibration modes, one should also note that these FRFs are normalized with respect to base acceleration. A base acceleration input of 1g at 185.1 Hz implies a base displacement amplitude of 7.25 μm. This base displacement amplitude, for instance, creates a base acceleration input of 39.3g at 1159.7 Hz (which may or may not be sustained by the brittle piezoceramic layers[§§]). As a result, one should define the electromechanical FRF according to the application and normalize with respect to the constant kinematic variable (displacement, velocity or acceleration). In short, part of the reason of diminishing moduli at higher vibration modes is that these FRFs are given here per base acceleration input (rather than displacement or velocity).

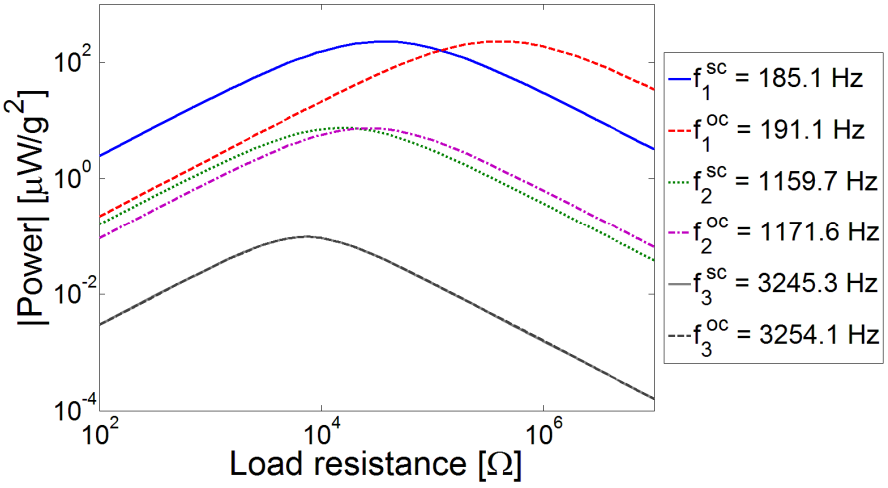

Fig. 3.14 Variation of the power output with load resistance for excitations at the short-circuit and the open-circuit resonance frequencies of the first vibration mode (series connection)

3.7.5 Frequency Response of the Relative Tip Displacement. The multi-mode expression for the tip displacement FRF (relative to the base) is

[§§] Given the bending strength of the piezoceramic and a safety factor, one can obtain a critical stress FRF as a function of load resistance by using the displacement and electric fields in the reduced piezoelectric constitutive equation. This way, an estimate of the maximum acceleration level can be obtained for a given excitation frequency and load resistance.

$$\frac{w_{rel}(L,t)}{-\omega^2 W_0 e^{j\omega t}} = \sum_{r=1}^{\infty} \left[\left(\sigma_r - \tilde{\theta}_r \frac{\sum_{r=1}^{\infty} \frac{j\omega \tilde{\theta}_r \sigma_r}{\omega_r{}^2 - \omega^2 + j2\zeta_r \omega_r \omega}}{\frac{1}{R_l} + j\omega C_{\tilde{p}}^{eq} + \sum_{r=1}^{\infty} \frac{j\omega \tilde{\theta}_r^2}{\omega_r{}^2 - \omega^2 + j2\zeta_r \omega_r \omega}} \right) \frac{\phi_r(L)}{\omega_r{}^2 - \omega^2 + j2\zeta_r \omega_r \omega} \right] \quad (3.116)$$

This FRF differs from the solution of the electromechanically uncoupled vibration FRF due to the voltage output induced as a result of piezoelectric coupling. The solution of the uncoupled base excitation problem (addressed in Chapter 2) is obtained by neglecting the electrical term as

$$\frac{w_{rel}(L,t)}{-\omega^2 W_0 e^{j\omega t}} = \sum_{r=1}^{\infty} \frac{\sigma_r \phi_r(L)}{\omega_r{}^2 - \omega^2 + j2\zeta_r \omega_r \omega} \quad (3.117)$$

which is therefore identical to Eq. (3.116) for $R_l \to 0$. The feedback of piezoelectric power generation in the mechanical equation is associated with the $\tilde{\theta}_r$ term in Eq. (3.116) and it is basically a form of power dissipation due to Joule heating in the resistor. Therefore what happens to the beam response due to power generation with a non-zero and finite load resistance is damping of the structure, which has a relatively sophisticated form compared to conventional viscous damping and structural damping mechanisms as demonstrated in the following.

Figure 3.15 shows the tip displacement FRFs[***] (per base acceleration) for the set of resistors and the frequency range of interest. One can see the three vibration modes in this figure but it is not possible to distinguish between the curves of different load resistance. The enlarged views of the first two vibration modes are shown in Fig. 3.16. The resistive shunt damping effect results in both frequency shift and vibration attenuation. With increasing load resistance, the electromechanical system moves from the short-circuit to the open-circuit conditions. In Fig. 3.16a, the peak vibration amplitude of 566.4 μm for 100 Ω (at 185.1 Hz) is attenuated to a peak amplitude of 214.7 μm for 100 kΩ (at 187.4 Hz), which means a damping effect by a factor of about 2.6. In the second vibration mode, the peak amplitude of 6.67 μm for 100 Ω (at 1159 Hz) is attenuated to 4.97 μm for 10 kΩ (at 1160.8 Hz). One thing that is useful to mention is that,

[***] The vibration FRFs investigated here are for the response at the tip of the cantilever ($x = L$). However, the distributed-parameter solution given here allows obtaining the coupled vibration response at any point x_p on the beam by setting $x = x_p$ in the eigenfunction on the right hand side of Eq. (3.116). However, the motion at the tip of the beam is of practical interest since it is the position of maximum deflection in the most flexible mode.

since the forms of the voltage and tip displacement FRFs are different, the resonance frequencies in these FRFs are slightly different (Chapter 5). This is distinguishable only in the presence of large mechanical damping. For instance, the short-circuit and the open-circuit resonance frequencies of the third vibration mode in Fig. 3.15 are 3252.6 Hz and 3264.3 Hz, respectively. Compared to those of the voltage FRF given in Table 3.4 (3245.3 Hz and 3254.1 Hz) these numbers, respectively, are 0.2 % and 0.3 % larger. The difference is not considerable for the fundamental vibration mode. Since the main concern in energy harvesting is the electrical response, the short-circuit and the open-circuit resonance frequencies are defined here based on the voltage FRF (as listed in Table 3.4).

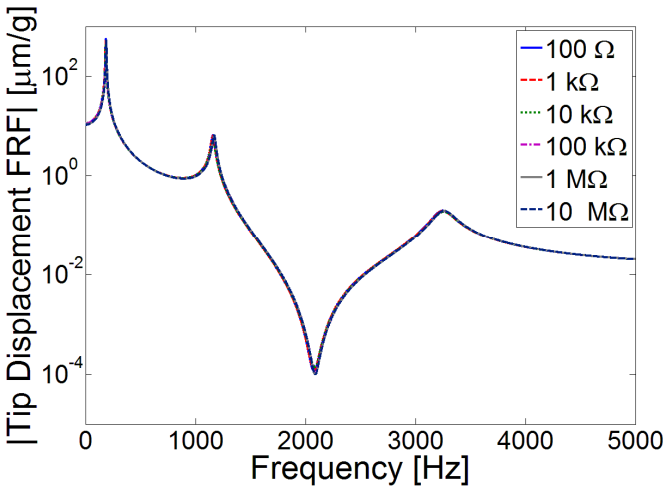

Fig. 3.15 Tip displacement FRFs (relative to the vibrating base) of the bimorph for a broad range of load resistance (series connection of the piezoceramic layers)

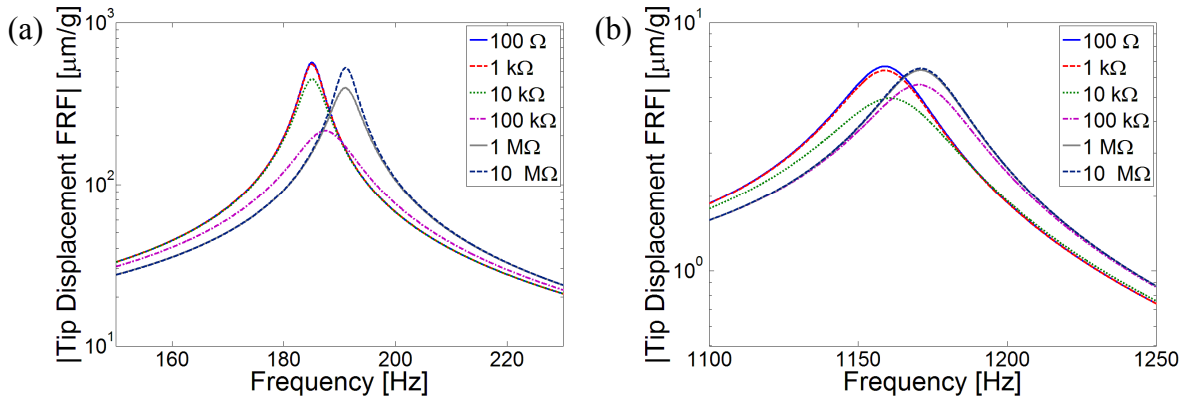

Fig. 3.16 Tip displacement FRFs of the bimorph with a focus on the first two vibration modes: (a) mode 1 and (b) mode 2 (series connection)

It is important to notice from the behavior around the modal frequencies of the vibration FRFs that the form of damping caused by piezoelectric power generation (or power dissipation in the resistor due to Joule heating) is more sophisticated that of viscous damping (although oversimplification of the problem with the *electrically induced viscous damping* assumption has been made by several researchers [18-20,22] over the last decade). First, with increasing load resistance, the frequency of peak vibration amplitude changes considerably (and shifts to the right in the FRF, unlike the case of viscous damping). Secondly, with further increase in the load resistance, although the vibration amplitude at the original (short-circuit) resonance frequency is attenuated to a certain amplitude, the vibration amplitude at the open-circuit resonance frequency is amplified considerably. The reason is the frequency shift due to changing electrical boundary condition. Indeed if one changes the load from one extremum ($R_l \to 0$) to the other extremum ($R_l \to \infty$), the only modification in the energy harvester is a stiffness change. Physically, the elastic modulus of the piezoceramic increases from the constant electric field value to the constant electric displacement value and there is no overall energy dissipation. Only for non-zero and finite values of load resistance, there is power dissipation in the mechanical domain (and hence power generation in the electrical domain). All together with these, the resonance frequency shift (from the mechanically damped natural frequency) associated with the presence of a finite electrical resistance *cannot* be represented by a real-valued viscous damping ratio or loss factor. Having discussed the mechanism of power dissipation in the mechanical domain, it is worthwhile to point out the presence of a mechanical *anti-resonance frequency* between modes 2 and 3. Just like the resonance frequencies, this anti-resonance frequency also exhibits a shift (from 2078.8 Hz to 2090.2 Hz) as the electrical load is changed from the short-circuit to the open-circuit condition.

The behavior of vibration response at the tip of the beam is further studied for excitations at the short-circuit and the open-circuit resonance frequencies of the fundamental vibration mode in Fig. 3.17. It is interesting to note that the trends are not completely monotonic. For instance, the minimum vibration amplitude at 185.1 Hz is obtained as 156.8 μm for an electrical load of about 500 kΩ and a further increase of load resistance up to 10 MΩ slightly amplifies the vibration amplitude at this frequency (to 162 μm). Likewise, before it is amplified due to the shift in the resonance frequency, the vibration amplitude at 191.1 Hz is slightly attenuated until

40 kΩ (from 162 μm to 157.7 μm). Then it is strongly amplified as the load resistance is further increased. It is also useful to note that these electrical loads of maximum vibration attenuation are *not* those of the maximum power generation. That is, the nature of electromechanical coupling is such that, for the electrical load of maximum power generation, the vibration amplitude at the tip of the beam does *not* necessarily take its minimum value.

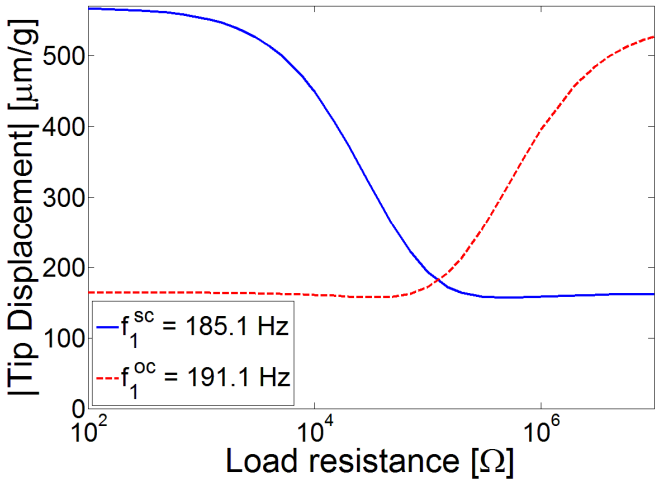

Fig. 3.17 Variation of the tip displacement (relative to the vibrating base) with load resistance for excitations at the short-circuit and the open-circuit resonance frequencies of the first vibration mode (series connection)

3.7.6 Parallel Connection of the Piezoceramic Layers. In this section, the electromechanical coupling and the equivalent capacitance terms used in Eqs. (3.113)-(3.116) are replaced by those of the parallel connection case (from the second column in Table 3.1) and sample results are presented. Figures 3.18-3.21 display the voltage, current, power and tip displacement FRFs along with the enlarged views of the behavior around the fundamental vibration mode.

The short-circuit and the open-circuit resonance frequencies read from Fig. 3.18 for the parallel connection case are identical to those listed in Table 3.4. The mathematical justification is given in Chapter 5, where the single-mode approximation of the frequency shift ($\Delta f_r = f_r^{oc} - f_r^{sc}$) is shown to be proportional to $\tilde{\theta}_r^2 / C_{\tilde{p}}^{eq}$. As a result, from Table 3.1, the single-mode approximation of the resonance frequency shift for the series and parallel connection cases are identical (in agreement with Figs. 3.18-3.21).

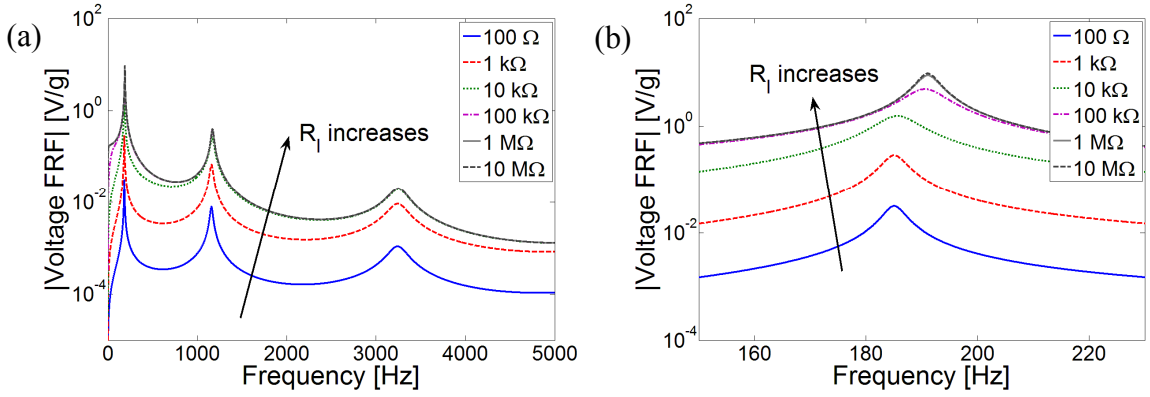

Fig. 3.18 (a) Voltage FRFs for the parallel connection of the piezoceramic layers and (b) an enlarged view around the first vibration mode

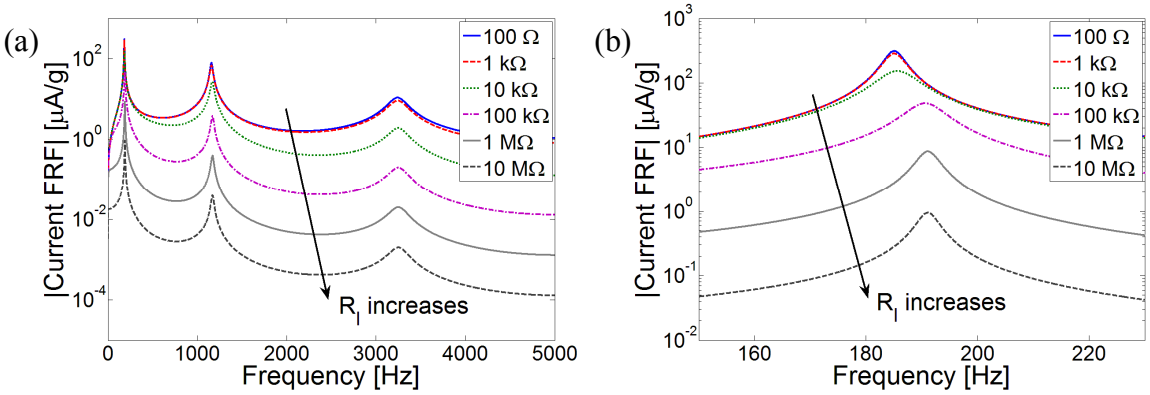

Fig. 3.19 (a) Current FRFs for the parallel connection of the piezoceramic layers and (b) an enlarged view around the first vibration mode

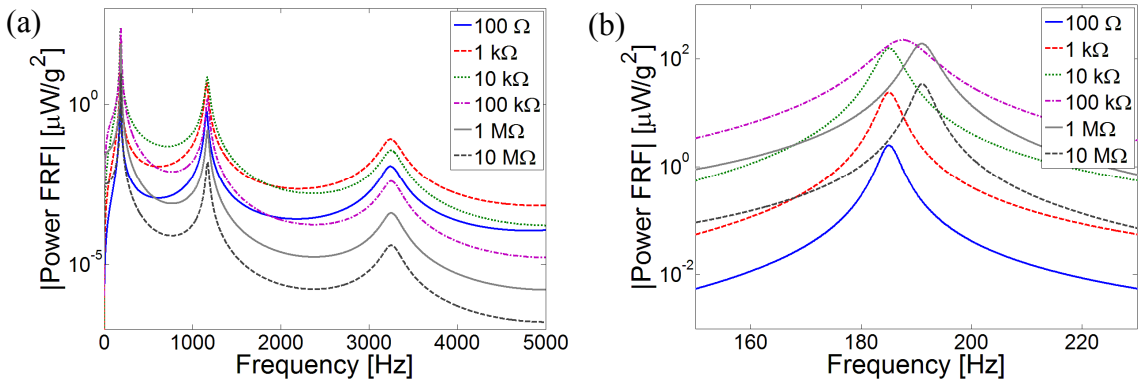

Fig. 3.20 (a) Power FRFs for the parallel connection of the piezoceramic layers and (b) an enlarged view around the first vibration mode

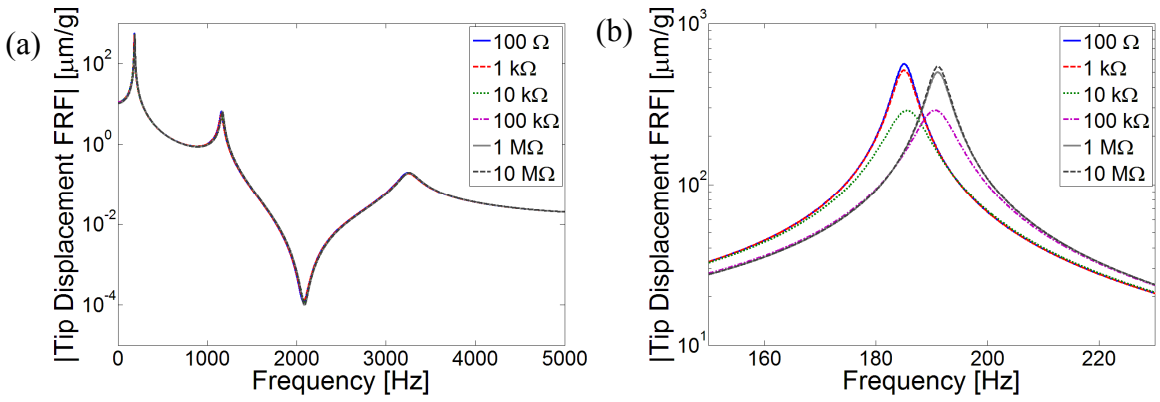

Fig. 3.21 (a) Tip displacement FRFs for the parallel connection of the piezoceramic layers and (b) an enlarged view around the first vibration mode

Comparisons of the series and the parallel connection cases for excitation at the fundamental short-circuit resonance frequency are given in Fig. 3.22. As can be anticipated, the maximum power outputs of the series connection and parallel connection cases are identical but they correspond to different values of optimum load. A maximum of 0.23 mW/g^2 is delivered to a resistive load of 36 kΩ in the series connection case whereas the same maximum power output is delivered to a resistive load of 9 kΩ in the parallel connection case. The series connection case generates this power with a current amplitude of 0.08 mA/g and a voltage amplitude of 2.8 V/g. In the parallel connection case, the same power output is obtained with a current amplitude of 0.16 mA/g and a voltage amplitude of 1.4 V/g. Reasonably, series connection should be preferred for large voltage output whereas parallel connection should be used for large current output. The last graph in Fig. 3.22 shows that the resistive damping effect starts for lower values of load resistance in the parallel connection case, which agrees with the behavior of maximum power generation.

Piezoelectric energy harvesters, as observed in this case study, are poor current generators.[†††] For instance, in the series connection case, for a base acceleration of 1g (achieved for the base displacement amplitude of 7.25 μm at 185.1 Hz) the voltage output is around 2.8 V while the current associated with it is just 0.08 mA. While this voltage level is fairly good for

[†††] This fundamental fact about piezoelectric materials is indeed well known by the experimentalist vibration engineer. It is the particular reason that piezoelectric-based transducers (such as accelerometers and impulse hammers) are usually connected to a *charge amplifier* before the data acquisition system.

charging a small battery, it is the current output that will make the duration of charging substantially long (compared to a commercial battery charger). Several orders of magnitude difference between the voltage and the current outputs of the generator is a very typical case in piezoelectric energy harvesting. Therefore, if the purpose is to charge a battery using the piezoelectric power output, parallel connection of the piezoceramic layers can be preferred so long as the voltage limit for charging the battery is reached for a given excitation input.

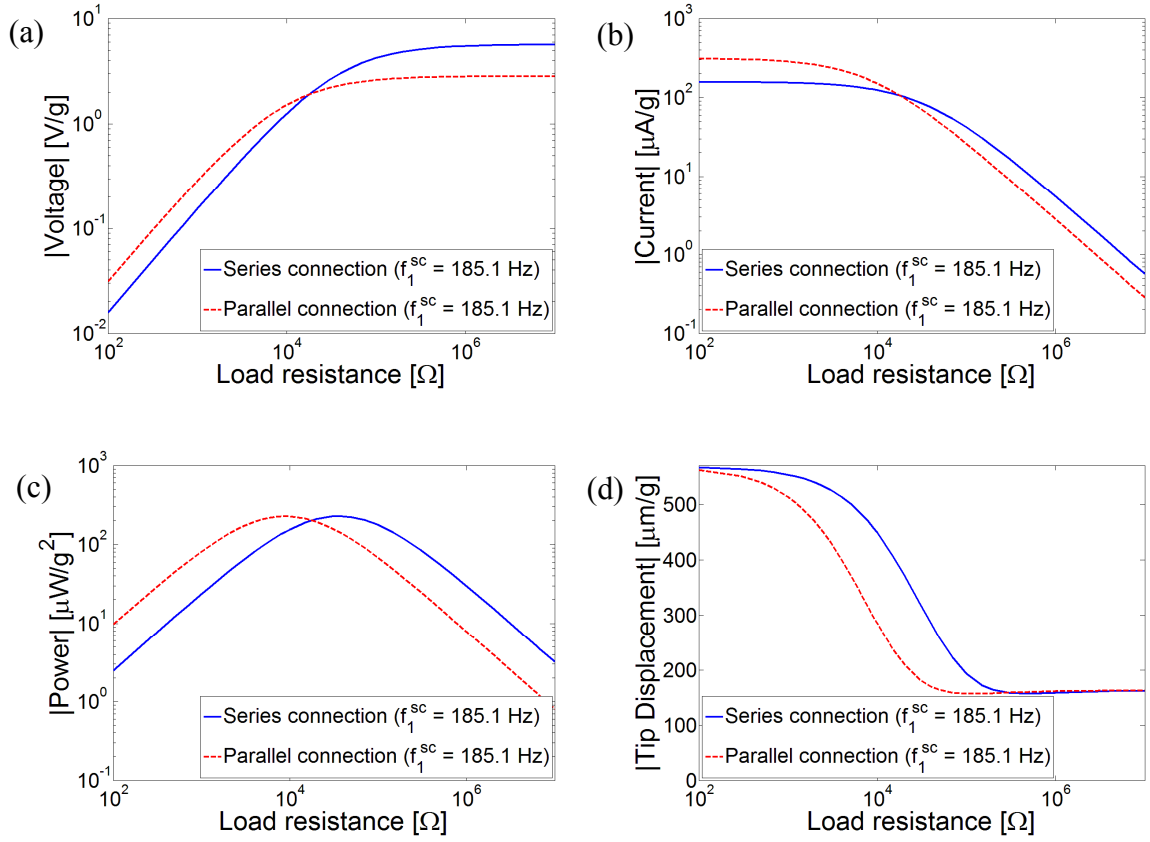

Fig. 3.22 Comparison of the series and the parallel connection cases for excitations at the short-circuit resonance frequency of the first vibration mode: (a) voltage vs. load resistance; (b) current vs. load resistance; (c) power vs. load resistance; (d) tip displacement vs. load resistance

3.7.7 Single-mode FRFs. In the absence of base rotation, the single-mode voltage FRF can be expressed as

$$\frac{\hat{v}(t)}{-\omega^2 W_0 e^{j\omega t}} = \frac{j\omega R_l \tilde{\theta}_r \sigma_r}{\left(1 + j\omega R_l C_{\tilde{p}}^{eq}\right)\left(\omega_r^{\,2} - \omega^2 + j2\zeta_r \omega_r \omega\right) + j\omega R_l \tilde{\theta}_r^2} \tag{3.118}$$

and the single-mode tip displacement FRF (relative to the base) is

$$\frac{\hat{w}_{rel}(L,t)}{-\omega^2 W_0 e^{j\omega t}} = \frac{\left(1+j\omega R_l C_{\tilde{p}}^{eq}\right)\sigma_r \phi_r(L)}{\left(1+j\omega R_l C_{\tilde{p}}^{eq}\right)\left(\omega_r{}^2 - \omega^2 + j2\zeta_r \omega_r \omega\right) + j\omega R_l \tilde{\theta}_r^2} \tag{3.119}$$

In the following, the simulations of these single-mode expressions are compared with those of the multi-mode expressions for the first three vibration modes in the series connection case (i.e. $\tilde{\theta}_r$ and $C_{\tilde{p}}^{eq}$ are read from the first column of Table 3.1). Figure 3.23 shows the single-mode FRFs obtained from Eq. (3.118) for $r=1$, $r=2$ and $r=3$ along with the multi-mode solution for all values of load resistance considered here. As can be seen in this figure, the single-mode solutions agree with the multi-mode solution only around the resonance frequency of the respective mode of interest.

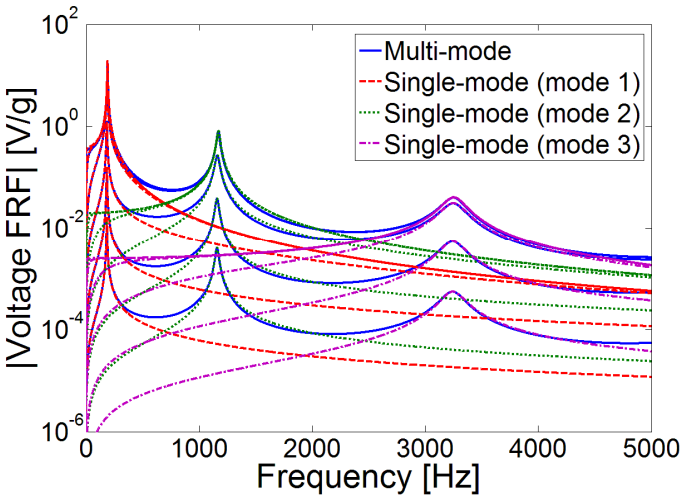

Fig. 3.23 Comparison of the multi-mode and the single-mode voltage FRFs (series connection)

Figures 3.24a and 3.24b, respectively, show the enlarged views of the single-mode and the multi-mode voltage FRF comparisons for the first two modes. The single-mode approximations work very well for all values of load resistance, yielding only slight overestimations of the resonance frequency and the voltage amplitude. The single-mode approximation for mode 1 shown in Fig. 3.24a predicts the short-circuit resonance frequency accurately as 185.1 Hz and it overestimates the open-circuit resonance frequency as 191.3 Hz (with an error of 0.1 %). In mode 2 prediction given by Fig. 3.24b, the short-circuit resonance

frequency is predicted as 1159.8 Hz (with an error of 0.009 %) whereas the open-circuit resonance frequency is predicted as 1171.9 Hz (with an error of 0.03 %). The single-mode voltage expression given by Eq. (3.118) can therefore successfully represent the resonance behavior of the multi-mode voltage expression given by Eq. (3.113) for a given mode of interest as a first approximation. The slight inaccuracy in the single-mode predictions is due to the residual effects of the neighboring modes, which are ignored in the single-mode representation given here.

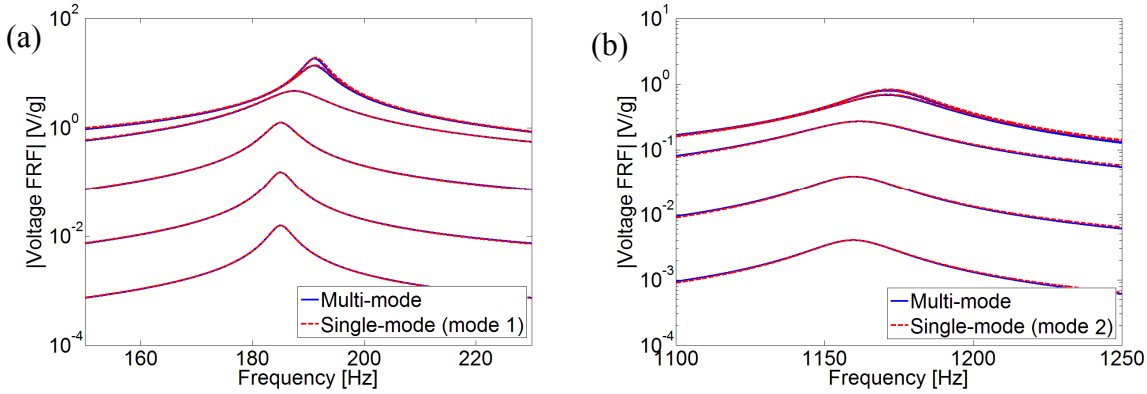

Fig. 3.24 Comparison of the multi-mode and single-mode voltage FRFs with a focus on the first two vibration modes: (a) mode 1 and (b) mode 2 (series connection)

The frequency response predictions of the single-mode tip displacement FRFs obtained from Eq. (3.119) (for $r=1$, $r=2$ and $r=3$) are shown in Fig. 3.25 along with the multi-mode tip displacement FRFs. Again, the single-mode FRFs exhibit agreement with the multi-mode FRF around the modes of interest. The enlarged views for modes 1 and 2 are provided in Fig. 3. 26 for a clear view of the quality of agreement. The slight overestimation of the resonance frequencies due to ignoring the neighboring vibration modes is the case here too and the error in the single-mode resonance frequencies is less than 0.1 % for these practical vibration modes.

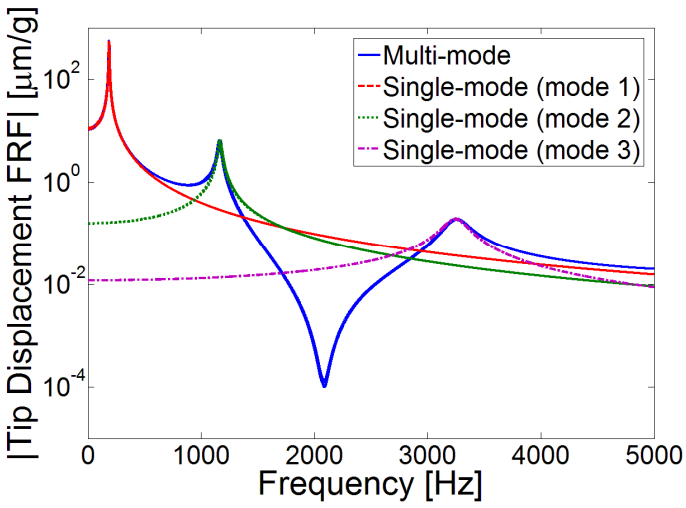

Fig. 3.25 Comparison of the multi-mode and the single-mode tip displacement FRFs (series connection)

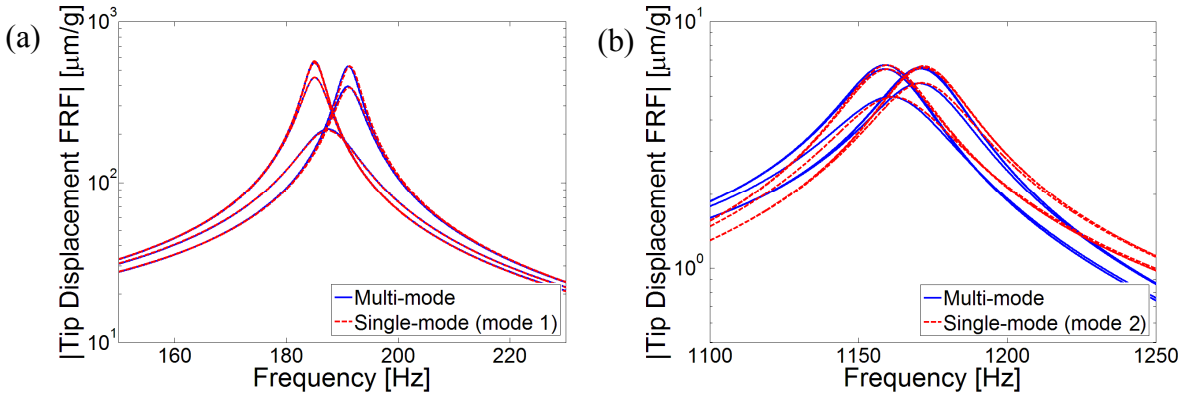

Fig. 3.26 Comparison of the multi-mode and the single-mode tip displacement FRFs with a focus on the first two vibration modes: (a) mode 1 and (b) mode 2 (series connection)

As a final comparison of the single-mode and the multi-mode simulations, the focus is placed back on the fundamental vibration mode and variations of the electrical power and the vibration response with load resistance are plotted in Figs. 3.27a and 3.27b, respectively, for excitations at the fundamental short-circuit and open-circuit resonance frequencies. Note that the slightly overestimated open-circuit resonance frequency is used in the single-mode simulations. The predictions of the single-mode FRFs for this most important vibration mode are very

accurate. Therefore, Eqs. (3.118) and (3.119) can comfortably be used as a first approximation in modeling of a piezoelectric energy harvester beam for modal excitations.

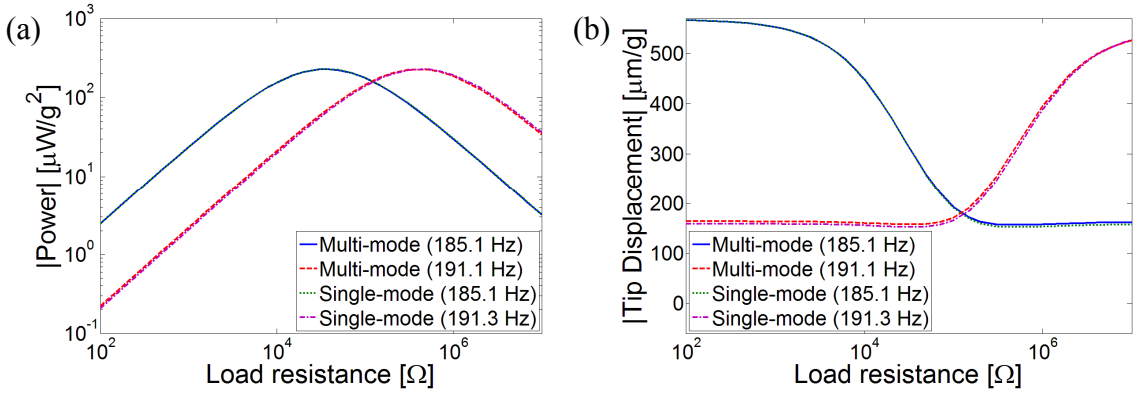

Fig. 3.27 Variations of the (a) power output and (b) tip displacement with load resistance for the multi-mode and the single mode-solutions (excitations at the fundamental short-circuit and open-circuit resonance frequencies)

3.8 Summary and Conclusions

Analytical modeling of symmetric bimorph piezoelectric energy harvesters is presented in this chapter. The distributed-parameter electromechanical formulation is based on the Euler-Bernoulli beam theory and it is valid for thin piezoelectric energy harvesters for the typical vibration modes of interest in practice. The major steps of the analytical formulation are given for the series and the parallel connection cases of the piezoceramic layers independently. An equivalent representation of the series and the parallel connections is then given in a single form. The distributed-parameter electromechanical equations are first obtained for excitation at any arbitrary frequency (including all vibration modes in the analytical solution). Then, for the practical problem of resonance excitation, the multi-mode solutions are reduced to the single-mode expressions (which are approximately valid only around the resonance frequencies). Electromechanical FRFs relating the steady-state electrical and mechanical response to translational and rotational base acceleration components are extracted both from the multi-mode and single-mode solutions. A detailed theoretical case study is presented where simulations for the series and the parallel connection cases are given using both the multi-mode and the single-

mode electromechanical FRFs. Accuracy of the single-mode FRFs in predicting the multi-mode FRFs for modal excitations is also shown.

CHAPTER 4

EXPERIMENTAL VALIDATIONS OF THE ANALYTICAL SOLUTIONS FOR CANTILEVERED BIMORPH PIEZOELECTRIC ENERGY HARVESTERS

This chapter presents experimental validations of the analytical electromechanical relations derived in Chapter 3. The first two experimental cases consider a brass-reinforced PZT-5H bimorph cantilever without and with a tip mass attachment in two separate sections. The voltage, current, power and the tip velocity FRFs of the bimorph (per base acceleration input) are analyzed extensively for both configurations and the focus is placed on the fundamental vibration mode in the frequency range of 0-1000 Hz. The general trends in the FRFs are addressed and model predictions in the absence and presence of a tip mass are shown. Excitations at the fundamental short-circuit and open-circuit resonance frequencies are investigated in detail and the electrical performance diagrams at these two frequencies are extracted. The shunt damping effect of piezoelectric power generation on the cantilever is also studied based on the experimental measurements and model predictions. The effect of rotary inertia of the tip mass is demonstrated by comparing the model predictions with the experimental results (for the PZT-5H bimorph cantilever with a tip mass) including and excluding the rotary inertia of the tip mass attachment. The electrical performance results of the same bimorph without and with the tip mass are compared. The last case study investigates a brass-reinforced PZT-5A bimorph cantilever with a focus on a wider frequency range (0-4000 Hz) covering the first two vibration modes. The model predictions are compared with the experimental results both using the multi-mode and the single-mode analytical FRFs.

4.1 PZT-5H Bimorph Cantilever without a Tip Mass

4.1.1 Experimental Setup. The first cantilever used for validation of the analytical model developed in Chapter 3 is a brass-reinforced bimorph (T226-H4-203X) manufactured by Piezo systems Inc. [45]. The experimental setup used for the electromechanical FRF measurements given in this chapter is shown in Fig. 4.1 and the enlarged views of the equipments used in the experiments are displayed in Fig. 4.2. A small electromagnetic shaker (TMC solution [46] TJ-2) is used for excitation of the bimorph cantilever and the acceleration at the base of the cantilever is measured by employing a small accelerometer (PCB Piezotronics [47] Model U352C67) attached onto the aluminum clamp of the cantilever using wax. The tip velocity of the cantilever in the transverse direction is measured using a laser vibrometer (Polytec [48] PDV100) by attaching a small reflector tape at the tip of the cantilever. The data acquisition box (SigLab [49] Model 20-42) has four input and two output channels. The base acceleration signal measured by the accelerometer is sent to the reference channel after being processed by a charge amplifier (PCB Piezotronics [47] Model 482A16). The reference channel automatically becomes the denominator of the resulting FRFs in the frequency response analyzer. Two of the remaining input channels are used for the laser vibrometer and the piezoelectric voltage output signals. Therefore the two FRFs obtained using these three signal outputs are the tip velocity – to – base acceleration FRF (or simply the *tip velocity FRF*) and the voltage output – to – base acceleration FRF (or simply the *voltage FRF*). Therefore, in all frequency response measurements provided here, the reference input is the base acceleration in agreement with the derivations of Chapter 3. Chirp excitation (burst type with five averages) is provided to the shaker from the output channel of the data acquisition box (which is connected to a Hewlett-Packard 6826A [59] fixed gain amplifier before the electromagnetic shaker).

The bimorph used in the first two sections of the experimental validations given here consists of two oppositely poled PZT-5H piezoelectric elements bracketing a brass substructure layer. The brass layer provides electrical conductivity between the bottom electrode of the top layer and the top electrode of the bottom layer. Therefore, collecting the charge output from the outermost electrodes becomes the series connection case described in Fig. 3.1a (and that is what is used here). The geometric and the material properties of the piezoceramic and the substructure layers in the cantilevered condition are given in Table 4.1. The data sheet of the manufacturer

provides limited information regarding the elastic properties of the piezoceramic. Therefore, typical properties of PZT-5H referred from the literature (Appendix B) are used here. The reduced (plane-stress) properties of the piezoceramic for the Euler-Bernoulli beam theory are referred from Table B.2 in Appendix B. Note that, in agreement with the formulation given in the previous chapter, the length described by L is the overhang length of the harvester, i.e. it is not the total free length (31.8 mm) of the bimorph as received from the manufacturer. The overhang length of the cantilever is measured as 24.53 mm. A reflector tape of negligible mass is attached close to the tip surface of the beam and the position of velocity measurement on the reflector is approximately 1.5 mm from the free end ($L_v = 23\,\text{mm}$). A close view of the bimorph cantilever with the reflector tape is given in Fig. 4.3 along with the resistive loads.

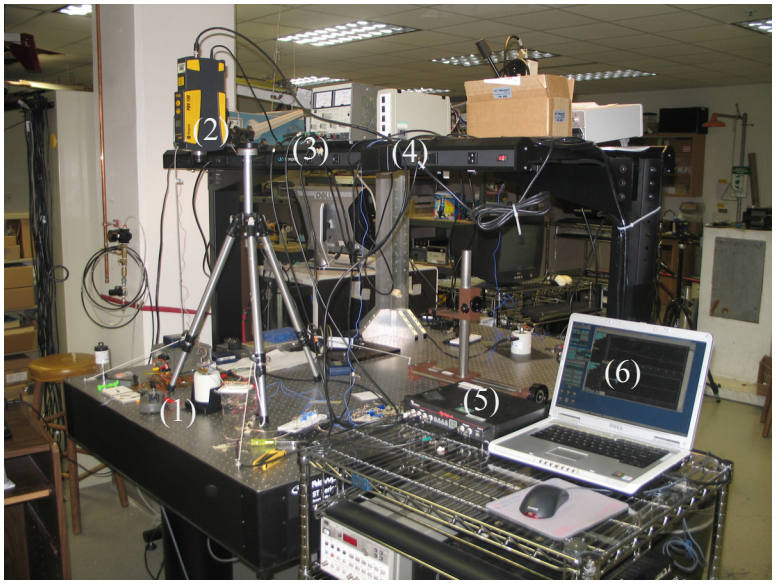

(1) Shaker with a small accelerometer and the cantilever
(2) Laser vibrometer
(3) Fixed gain amplifier (power supply)
(4) Charge amplifier
(5) Data acquisition system
(6) Frequency response analyzer (software)

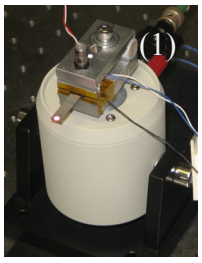

Fig. 4.1 Experimental setup used for the electromechanical frequency response measurements (photos by A. Erturk, 2009)

According to the geometric parameters in Table 4.1, the structure is assumed to be perfectly symmetric. The nickel electrodes are covering the surfaces of the piezoceramic layers are very thin and the thicknesses of the bonding layers are assumed to be neglibible. The total thickness of the beam is 0.67 mm and therefore the overhang length – to – thickness ratio is about 37.7. Since the focus in this case study (as well as in most energy harvesting applications) is placed on the fundamental vibration mode, shear deformation and rotary inertia effects are

assumed to be negligible. This is in agreement with the model presented in the previous chapter based on the Euler-Bernoulli beam assumptions.

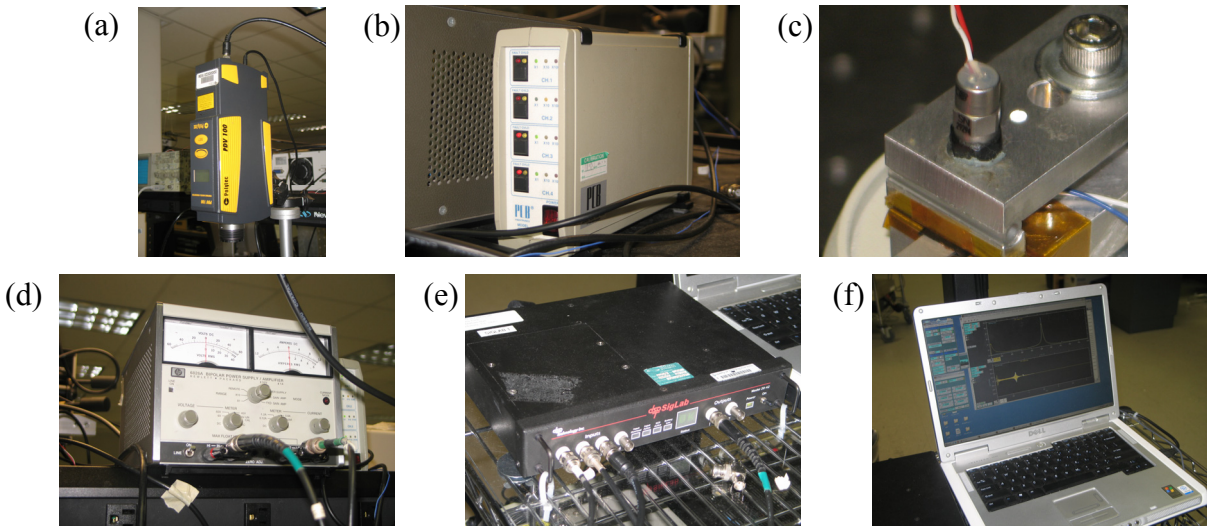

Fig. 4.2 Equipments used in the experiments: (a) laser vibrometer, (b) charge amplifier, (c) accelerometer, (d) fixed-gain amplifier, (e) data acquisition system, (f) computer with a frequency response analyzer (photos by A. Erturk, 2009)

Table 4.1 Geometric and material properties of the PZT-5H bimorph cantilever without a tip mass

	Piezoceramic (PZT-5H)	**Substructure (brass)**
Length (L) [mm]	24.53	24.53
Width (b) [mm]	6.4	6.4
Thickness (h_p, h_s) [mm]	0.265 (each)	0.140
Tip mass (M_t) [kg]	(none)	
Mass density (ρ_p, ρ_s) [kg/m^3]	7500	9000
Elastic modulus ($\bar{c}_{11}^E$, Y_s) [GPa]	60.6	105
Piezoelectric constant ($\bar{e}_{31}$) [C/m^2]	-16.6	-
Permittivity constant ($\bar{\varepsilon}_{33}^S$) [nF/m]	25.55	-

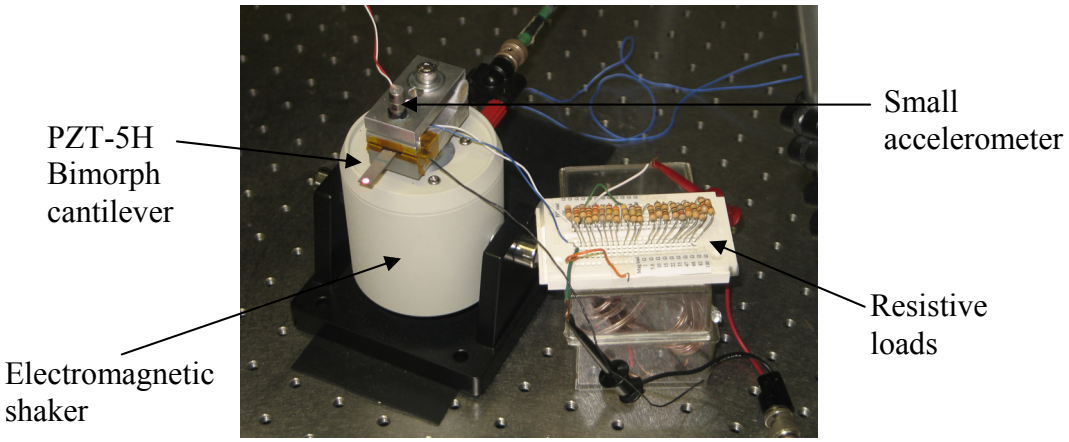

Fig. 4.3 A view of the shaker, low-mass accelerometer, PZT-5H bimorph cantilever without a tip mass, its clamp and a set of resistors (photo by A. Erturk, 2009)

For a resistive load of $470\,\Omega$, the experimentally measured tip velocity and voltage output FRFs are shown in Fig. 4.4a. This resistive load is very close to the short-circuit conditions for this particular cantilever, therefore the resonance frequency of 502.5 Hz read from Fig. 4.4a is the fundamental short-circuit resonance frequency of the PZT-5H bimorph cantilever shown in Fig. 4.3 ($f_1^{sc} = 502.5\,\text{Hz}$). It should be mentioned that, for the frequency range of measurement (0-1000 Hz), the data acquisition system automatically adjusts the frequency increment to 0.325 Hz (which is a device limitation). According to Fig. 4.4b, the coherence [50,51] of the tip velocity measurement is very good (unity) over the frequency range except for a slight reduction around 715 Hz. Around the resonance frequency, the voltage FRF also exhibits a perfect coherence, which decays away from the resonance. The relatively poor coherence of the voltage output – to – base acceleration measurement is expected and it is due to the low value of load resistance (deliberately chosen to realize a case close to the short-circuit conditions). For a load resistance of $470\,\Omega$, therefore, the system is close to short-circuit conditions so that the signal from the piezoceramic is an acceptable measurement output (i.e. it is identified to be due to the input) only around the resonance frequency. Indeed, for a resistance of $10\,\Omega$, the voltage coherence becomes extremely low almost for the entire frequency range since the piezoelectric voltage output turns out to be at the noise level of the input channel for such a low resistance. As can be anticipated, with increasing load resistance, the coherence of the voltage measurement becomes as good as that of the tip velocity measurement due to the level of the signal output.

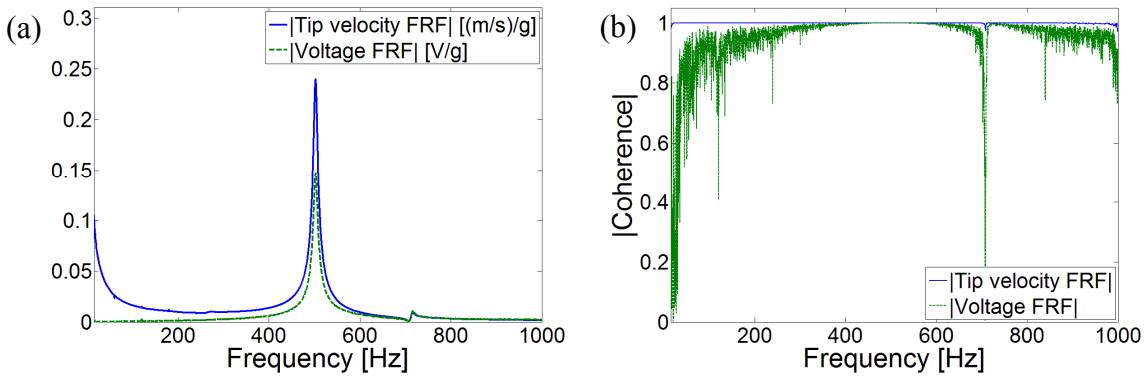

Fig. 4.4 (a) Tip velocity and voltage output FRFs of the PZT-5H bimorph cantilever without a tip mass and (b) their coherence functions (for a load resistance of 470 Ω)

The sudden reduction in the coherence around 715 Hz in Fig. 4.4b is the case for both FRF measurements and it corresponds to a very small peak in the FRFs of Fig. 4.4a. As will be seen from the model predictions shortly, the bimorph is not expected to have a mode around that frequency. The fundamental resonance of the shaker itself (without the attachment on it) is not expected for frequencies less than 15 kHz according to the manufacturer [46]. Therefore, the only possible source of the low-amplitude peak around 715 Hz is the clamp of the bimorph that is attached onto the shaker with a screw. This is checked very easily by pointing the laser vibrometer to the clamp after attaching a reflector tape on it. Figure 4.5a shows the location of the velocity measurement on the clamp and Fig. 4.5b shows the FRF obtained using the laser vibrometer and the accelerometer measurements taken on the clamp. It can be seen from Fig. 4.5b that the unexpected peak around 715 Hz in Fig. 4.4a is indeed due to the clamp itself. If the clamp behaved ideally for the purpose intended here (i.e. if all the points on it moved identically in the vertical direction with a rigid body translation), the velocity – to – acceleration measurement would be a monotonically decaying function of frequency without any peaks. More precisely, this decaying function would be $1/j\omega$ (ratio of the velocity to acceleration in the frequency domain). This ideal behavior agrees with the measurement shown in Fig. 4.5b very well for all frequencies away from the unexpected peak around 715 Hz. The source of the peak in the clamp FRF might be a possible rotation of the clamp as a result of the joint flexibility at the clamp-shaker interface or it might be due to the dynamic interaction of the clamp components. In either case the small peak appearing in the FRFs around this frequency is not a

vibration mode of the bimorph cantilever. This imperfection will be ignored throughout this chapter since it is sufficiently away from the fundamental vibration mode of the bimorph (which is the main concern here).

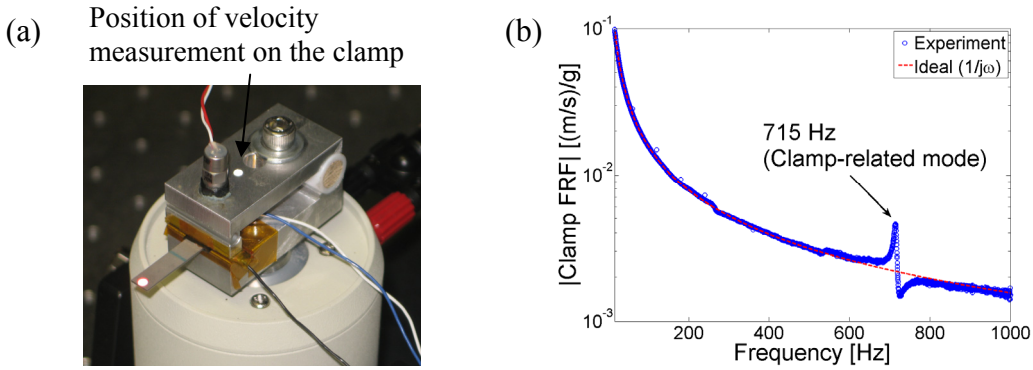

Fig. 4.5 (a) A close view of the clamp showing the point of velocity measurement (photo by A. Erturk, 2009) and (b) the clamp velocity – to – acceleration FRF capturing the clamp-related imperfection

Before the model predictions are compared with the experimental measurements, it is important to note that the tip velocity measurement taken by the laser vibrometer is the velocity response of the cantilever relative to the *absolute* reference frame. In other words, it is not the velocity response *relative* to the base of the beam. Therefore, the relative tip displacement FRF given by Eq. (3.105), $\beta(\omega,x)$, should be modified to express the velocity response at the tip of the beam relative to the absolute frame of reference:

$$\beta^{\text{modified}}(\omega,x)=\frac{\dfrac{\partial w(x,t)}{\partial t}}{-\omega^2 W_0 e^{j\omega t}}=\frac{\dfrac{\partial}{\partial t}\left[W_0 e^{j\omega t}+w(x,t)\right]}{-\omega^2 W_0 e^{j\omega t}}=\frac{1}{j\omega}+j\omega\beta(\omega,x) \tag{4.1}$$

where $x=L_v$ (the point of velocity measurement) should be used to predict the measurement taken by the laser vibrometer. Note that, instead of modifying the analytical FRF expression given by by Eq. (3.105), one could as well process the experimental tip velocity FRF to obtain a relative tip displacement FRF. However, post-processing of the analytical data is preferable in order not to amplify any noise by further processing the experimental data.

The last item to mention on the experimental setup is regarding the resistance seen across the electrodes of the piezoceramic. A measurement taken on the input channel of the data

acquisition system (when nothing is connected) shows a device resistance of 995 $\mathrm{k}\Omega$. Therefore, if the wires coming from the electrodes of the piezoceramic are directly connected to the data acquisition system in the experiments (without a probe), the effective load resistance seen across the electrodes of the piezoceramic is the equivalent resistance of the resistive load used and 995 $\mathrm{k}\Omega$ (which see each other in parallel): $R_l = 1/(1/R_l^{\text{used}} + 1/995\times10^3)$. This observation implies that the maximum resistance used in the experiments cannot exceed 995 $\mathrm{k}\Omega$. As a consequence, the equivalent of the resistor used and the device resistance constitutes the R_l value to be used in the model and these effective values are listed in the second column of Table 4.2. Therefore the load resistance (R_l) ranges from 470 Ω (close to short-circuit conditions) to 995 $\mathrm{k}\Omega$ (close to open-circuit conditions) in the experiments.

Table 4.2 The resistors used in the experiment and their effective values due to the impedance of the data acquisition system

Resistance of the resistor used [$\mathrm{k}\Omega$]	**Effective load resistance (R_l) seen by the piezoceramic [$\mathrm{k}\Omega$]**
0.470	0.470
1.2	1.2
6.7	6.7
10	9.9
22	21.5
47	44.9
100	90.9
330	247.8
470	319.2
680	403.9
1000	498.7
Open	995.0

4.1.2 Validation of the Electromechanical FRFs for a Set of Resistors. In this first case study, the focus is placed on the fundamental vibration mode seen around 502.5 Hz for a load resistance of $470\,\Omega$. Since the performance of the harvester at resonance is the main concern, accurate identification of the modal mechanical damping ratio is very important. It is a common practice to extract the mechanical damping ratio from the first measurement in experimental structural dynamics. The model developed here allows identifying mechanical damping in the presence of an arbitrary load resistance. The FRFs of the resistance that are most close to $R_l \to 0$ is used here for damping identification (i.e. the FRFs given by Fig. 4.4a for $470\,\Omega$). The mechanical damping ratio identified graphically by matching the peaks of the experimental and analytical tip velocity FRFs in Fig. 4.6a is $\zeta_1 = 0.00874$. For the numerical data given in Table 4.1, the analytical model predicts the fundamental short-circuit resonance frequency as 502.6 Hz with a relative error of 0.02 % compared to the experimental short-circuit resonance frequency (502.5 Hz). If the electromechanical model is consistent, the analytical voltage FRF should predict the peak amplitude of the experimental voltage FRF for the damping ratio of 0.874 % accurately. This mechanical damping ratio identified from the velocity FRF is substituted into the voltage FRF expressed by Eq. (3.102) and the model prediction given in Fig. 4.6b is obtained. The agreement is very good considering the fact that the two FRFs of Figs. 4.6a and 4.6b are independent measurements (velocity and voltage) and the damping is identified from the former one. One could as well identify the mechanical damping ratio from the voltage FRF (Fig. 4.6b) since a piezoelectric energy harvester itself is a *transducer*. That is, the information of the velocity response of the cantilever is included in the voltage response due to piezoelectric coupling. As long as the linear electromechanical system assumption holds, analytical predictions of the voltage and tip velocity has to be in agreement with each other for a given load resistance.

It is worth adding that, instead of identifying the modal mechanical damping ratio by matching the peak values of the experimental and the analytical electromechanical FRFs (or using the closed-form expressions of Chapter 5), one could as well follow a classic time domain procedure to identify mechanical damping. For instance, without worrying about the voltage output, one could set the electrical boundary condition as close to $R_l \to 0$ as possible and perform a time domain damping identification (e.g. logarithmic decrement). However, it should

be mentioned that even a wire (that can be used to short the electrodes to realize $R_l \to 0$) has a certain resistance. Therefore the demonstration here is given for the presence of a finite load resistance (that is still very close to $R_l \to 0$), which is the general case. Indeed, using a resistive load that generates an acceptable voltage output (larger than the noise level) allows checking whether or not the analytical model can predict the voltage output when the same damping ratio is substituted into the voltage FRF (as done here in Fig. 4.6b). The upshot of this discussion is that the mechanical damping can be identified in the presence of an arbitrary load resistance using the electromechanical model. However, if one prefers to identify mechanical damping using conventional techniques (e.g. half-power points of the vibration FRF, logarithmic decrement in time domain, etc), the electrical boundary condition should be set to $R_l \to 0$ as close as possible (which gives a noisy piezoelectric voltage output and does not allow checking the voltage prediction). The important point is that the conventional techniques of damping identification should *not* be used in the presence of *arbitrary* values of load resistance. In such a case, damping due to piezoelectric coupling contributes to the mechanical damping in the vibration response and the identified value would not be a pure mechanical damping ratio and it *cannot* be used as ζ_r in the equations derived in this dissertation.

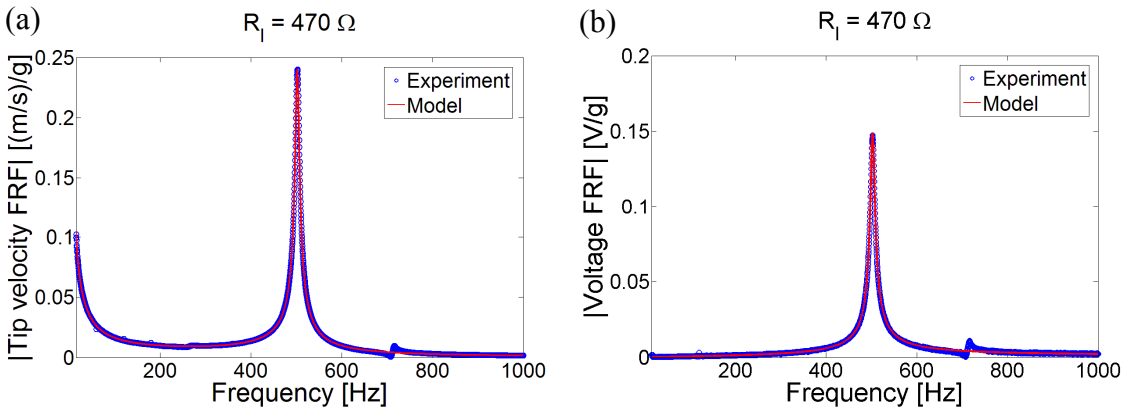

Fig. 4.6 Measured and predicted (a) tip velocity and (b) voltage output FRFs of the PZT-5H bimorph cantilever without a tip mass for a load resistance of 470 Ω

Having identified the mechanical damping ratio for a certain electrical load resistance, the next step is to keep the damping ratio fixed and predict the tip velocity and voltage FRFs for

different values of load resistance. Figure 4.7 displays experimental measurements and model predictions for resistors of three different orders of magnitude: 1.2 $\mathrm{k}\Omega$, 44.9 $\mathrm{k}\Omega$ and 995 $\mathrm{k}\Omega$. In all cases, the mechanical damping ratio is kept at $\zeta_1 = 0.00874$ and the model predictions are very good. Note that, among these three different values of load resistance, 44.9 $\mathrm{k}\Omega$ results in the strongest attenuation of the peak vibration amplitude. The peak voltage amplitude, as expected from the theoretical case study of Chapter 3, increases monotonically with increasing load resistance. The peak voltage amplitude increases by two orders of magnitude as the load resistance is increased from 470 Ω (Fig. 4.6b) to 995 $\mathrm{k}\Omega$ (Fig. 4.7c).

As the load resistance is increased from 470 Ω to 995 $\mathrm{k}\Omega$, the experimentally measured fundamental resonance frequency moves from the short-circuit value of 502.5 Hz to the open-circuit value of 524.7 Hz. The analytical model predicts these two resonance frequencies as 502.6 Hz and 524.5 Hz. Table 4.3 summarizes these results along with the errors in the model prediction compared to the experimental frequencies. It will be seen from the modal approximations given in Chapter 5 that the amount of the resonance frequency shift from the short-circuit to the open-circuit value is directly proportional to the square of the electromechanical coupling and is inversely proportional to the capacitance and the respective undamped natural frequency. Although the errors in Table 4.3 are negligible for most practical purposes, possible inaccuracies in the piezoelectric and permittivity constants contribute to the error. In addition, the fact that the undamped natural frequency is slightly overestimated results in underestimation of the open-circuit resonance frequency (as the frequency sift is inversely proportional to the undamped natural frequency). The experimental source of error might be more significant than all these, since the frequency increment is automatically set equal to 0.325 Hz when the frequency range of interest is adjusted to 0-1000 Hz.

Table 4.3 Fundamental short-circuit and open-circuit resonance frequencies of the PZT-5H bimorph cantilever without a tip mass

Fundamental resonance frequency	Experiment	Model	% Error
f_1^{sc} (short circuit) [Hz]	502.5	502.6	+0.02
f_1^{oc} (open circuit) [Hz]	524.7	524.5	-0.04

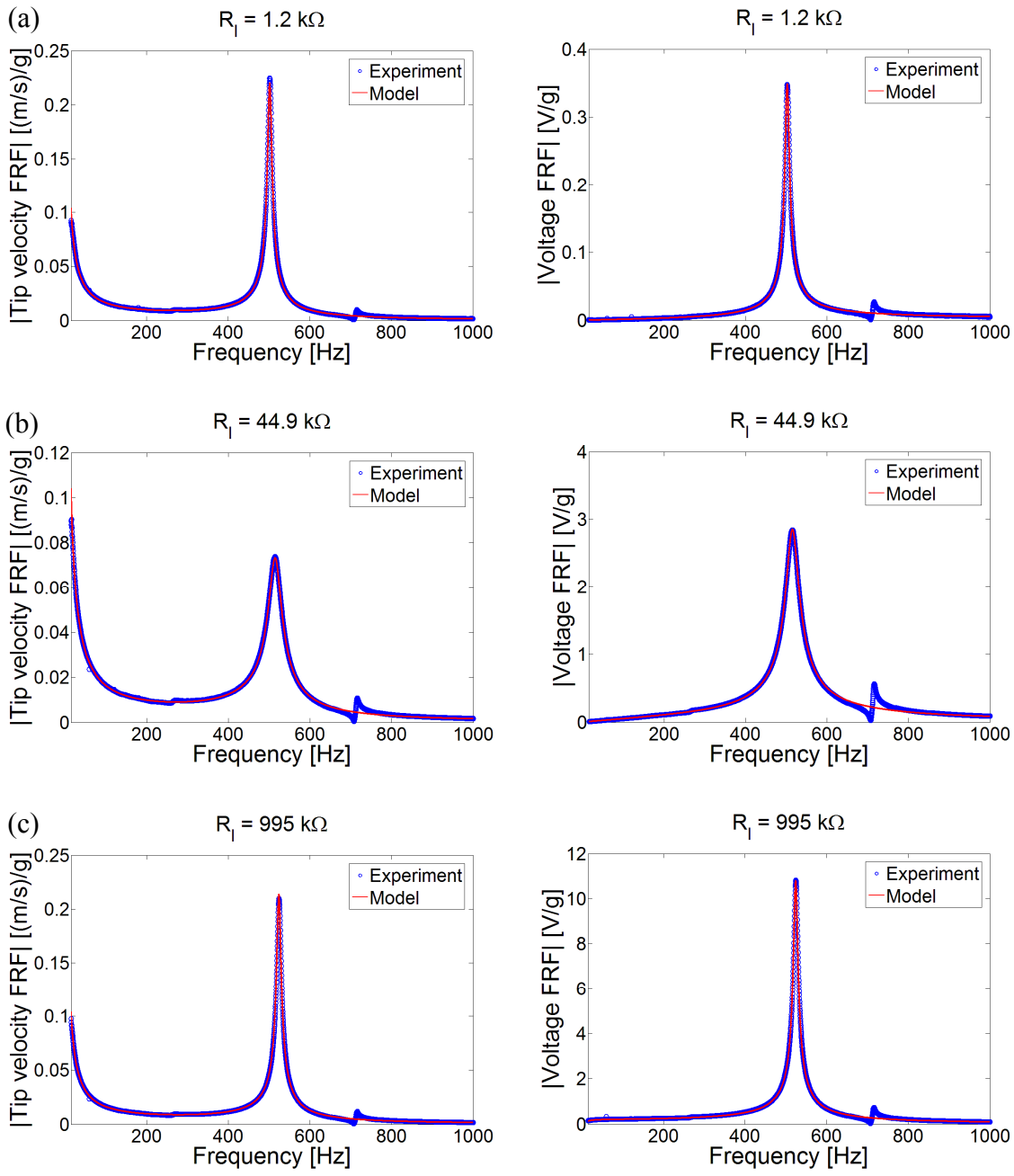

Fig. 4.7 Measured and predicted tip velocity and voltage output FRFs of the PZT-5H bimorph cantilever without a tip mass for various resistors: (a) 1.2 kΩ, (b) 44.9 kΩ and (c) 995 kΩ

The piezoelectric voltage output and tip velocity FRFs measured experimentally and predicted analytically for all resistors used here are given by Figs. 4.8 and 4.9, respectively. The gradual increase of the voltage output with increasing load resistance (Fig. 4.8) is associated with a gradual attenuation of the vibration amplitude at the short-circuit resonance frequency (Fig.

4.9). However, after a certain value of load resistance, the vibration amplitude at the short-circuit resonance frequency get saturated and that at the open-circuit resonance frequency is amplified. Hence, if one focuses on the fundamental open-circuit resonance frequency, both the vibration amplitude and the voltage amplitude increase with increasing load resistance. Consequently, modeling the effect of piezoelectric coupling in the form of an electrically induced viscous damping term [18-20,22] fails in predicting what happens to the piezoelectric energy harvester when it generates electricity (which also affects the electrical predictions in the coupled system).

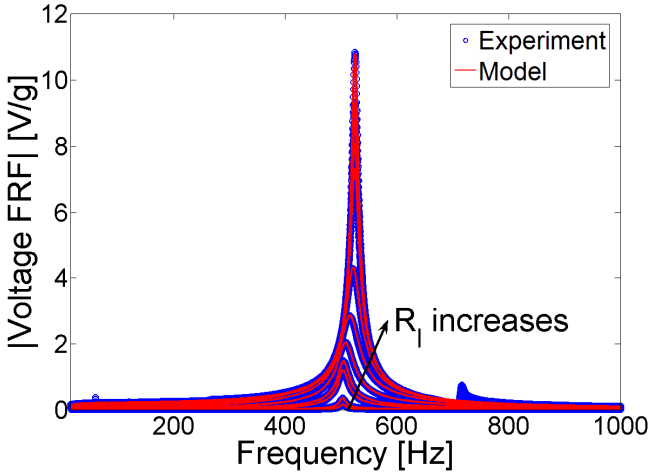

Fig. 4.8 Voltage output FRFs of the PZT-5H bimorph cantilever without a tip mass for 12 different resistive loads (ranging from 470 Ω to 995 kΩ)

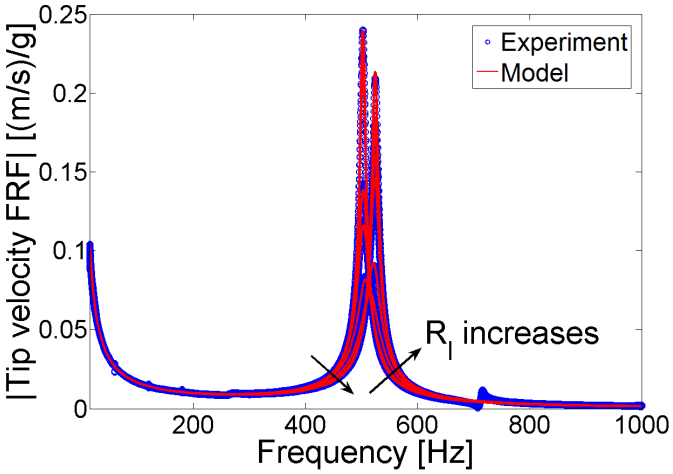

Fig. 4.9 Tip velocity FRFs of the PZT-5H bimorph cantilever without a tip mass for 12 different resistive loads (ranging from 470 Ω to 995 kΩ)

The enlarged views of the voltage, current, power and the tip velocity FRFs are given in Fig. 4.10 for all values of load resistance (in the 400-600 Hz region) with semi-log scale. It is clear from Fig. 4.10a that the voltage FRFs monotonically converge to a single open-circuit voltage FRF as the load resistance increases toward the $R_l \to \infty$ extremum. The current FRFs in Fig. 4.10b also behave monotonically and they become similar to a single short-circuit current FRF for the $R_l \to 0$ extremum. The product of the voltage and the current FRFs gives the power FRF, which results in a relatively complicated picture when all 12 curves are plotted together in Fig. 4.10c. For a given frequency and range of load resistance, the behavior is not necessarily monotonic, resulting in the intersections of the curves. One can define different values of

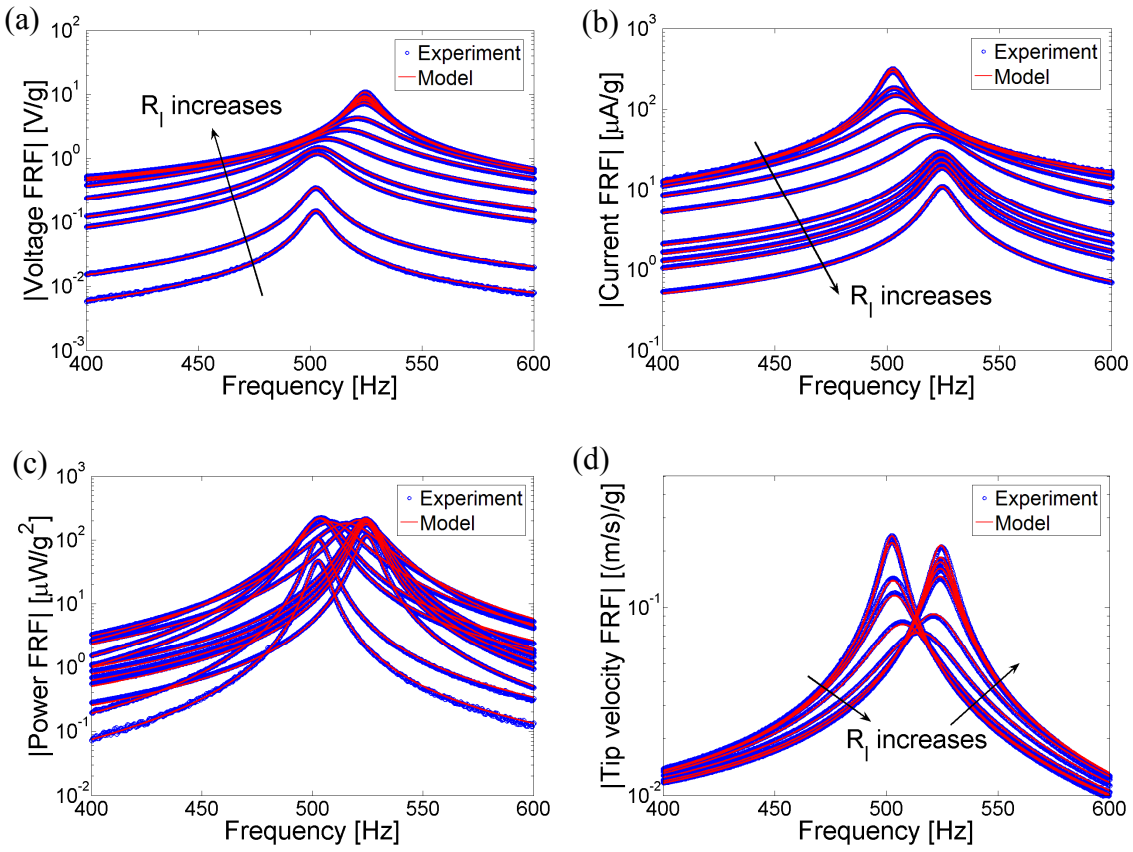

Fig. 4.10 Enlarged views of the (a) voltage output, (b) current output, (c) power output and (d) tip velocity FRFs of the PZT-5H bimorph cantilever without a tip mass for 12 different resistive loads (ranging from 470 Ω to 995 kΩ)

optimum load resistance at different frequencies. The short-circuit and the open-circuit resonance frequencies are of interest for the maximum power. Variation of the vibration response is also non-monotonic and the trend of the peak vibration amplitude with load resistance is shown in Fig. 4.10d. For a given excitation frequency, one can define an optimum load for the maximum vibration attenuation.

4.1.3 Electrical Performance Diagrams at the Fundamental Short-Circuit and Open-Circuit Resonance Frequencies. Focusing on the fundamental short-circuit and open-circuit resonance frequencies, the electrical performance diagrams are extracted next. These diagrams can be useful for the electrical engineer to obtain an idea about the maximum voltage, current and power output levels of the energy harvester as well as the optimum electrical load resistance to design a sophisticated energy harvesting circuit. Figure 4.11 shows the variation of the voltage amplitude at the fundamental short-circuit and open-circuit resonance frequencies. The model predictions are in very good agreement with the experimental data points (for 12 resistors). The linear asymptotic trends can be noted from the experimental data as well. The model predicts the maximum voltage outputs ($R_l \to \infty$) as 2.6 V/g and 12.8 V/g for excitations at the fundamental short-circuit and open-circuit resonance frequencies, respectively.

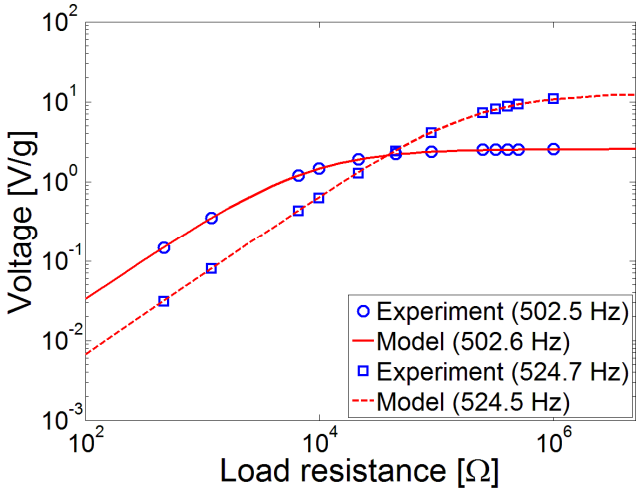

Fig. 4.11 Variation of the voltage output with load resistance for excitations at the fundamental short-circuit and open-circuit resonance frequencies of the PZT-5H bimorph cantilever without a tip mass

Variations of the electric current passing through the resistor for excitations at the fundamental short-circuit and open-circuit resonance frequencies are plotted in Fig. 4.12. For excitations at the fundamental short-circuit and open-circuit resonance frequencies, the maximum current outputs ($R_l \to 0$) are predicted as 336 μA/g and 68 μA/g. Just like the asymptotic voltage behavior for $R_l \to \infty$, the asymptotic current trends are horizontal lines as $R_l \to 0$.

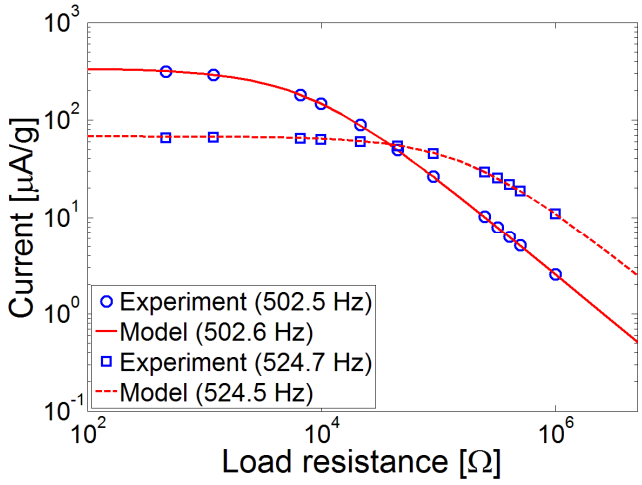

Fig. 4.12 Variation of the current output with load resistance for excitations at the fundamental short-circuit and open-circuit resonance frequencies of the PZT-5H bimorph cantilever without a tip mass

The final electrical performance diagram is the power versus load resistance diagram shown in Fig. 4.13. According to the model, for excitations at the fundamental short-circuit and open-circuit resonance frequencies, the maximum power output of about 0.22 mW/g^2 is delivered to the optimum electrical loads of 7.6 kΩ and 189 kΩ, respectively. Although these exact values of load resistance are not used in the experiments, the loads of 6.7 kΩ and 247.8 kΩ are relatively close to these optimum ones. The resistive load of 6.7 kΩ yields an experimental power output of 0.218 mW/g^2 at the fundamental short-circuit resonance frequency whereas the resistive load of 247.8 kΩ yields 0.212 mW/g^2 at the fundamental open-circuit resonance frequency. The model predicts the power outputs for 6.7 kΩ and 247.8 kΩ as 0.217

mW/g^2 and 0.215 mW/g^2, respectively, with relative errors of -0.5 % and +1.4 % (compared to the experimental power amplitudes).

It is useful to report two normalized power measures: the *power density* and the *specific power* outputs. The former is defined as the power output divided by the overhang volume of the device whereas the latter is the power output divided by the total overhang mass. The overhang volume of the cantilever is obtained from the data in Table 4.1 as 0.105 cm^3 and the overhang mass is 0.822 grams. Therefore the maximum power density of this configuration for resonance excitation is about 2.1 mW/(g^2cm^3). The maximum specific power output is about 0.27 mW/(g^2g).*

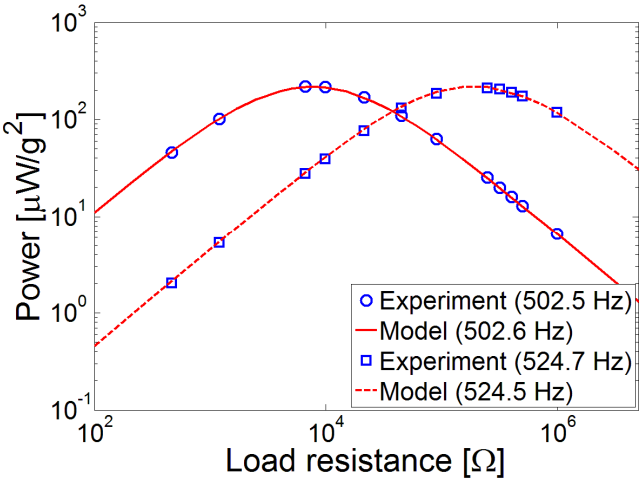

Fig. 4.13 Variation of the power output with load resistance for excitations at the fundamental short-circuit and open-circuit resonance frequencies of the PZT-5H bimorph cantilever without a tip mass

4.1.4 Vibration Response Diagrams at the Fundamental Short-Circuit and Open-Circuit Resonance Frequencies. Although the main concern in energy harvesting is the electrical performance outputs, it is interesting to summarize what happens to the piezoelectric energy harvester beam due to power generation. It was underlined while discussing the tip velocity FRF that the form of piezoelectric coupling is substantially different than conventional damping mechanisms such as viscous or structural damping.

* Here, g stands for "grams" and it should not be confused with the italic *g* for the gravitational acceleration.

Figure 4.14 shows that the vibration amplitude at the fundamental short-circuit resonance frequency is attenuated as the load resistance is increased. At the fundamental short-circuit resonance frequency, the experimental vibration amplitude of 0.240 (m/s)/g for 470 Ω is attenuated to of 0.050 (m/s)/g as the load resistance is increased to 995 kΩ. The model predicts these amplitudes as 0.240 (m/s)/g[†] and 0.051 (m/s)/g, respectively. As $R_l \to \infty$, the vibration amplitude at this frequency converges to 0.052 (m/s)/g after a slight increase. For excitation at the fundamental open-circuit resonance frequency, the experimental vibration amplitude of 0.047 (m/s)/g for 470 Ω increases to of 0.210 (m/s)/g for 995 kΩ. The model predicts these two amplitudes as 0.050 (m/s)/g and 0.223 (m/s)/g, respectively. As $R_l \to \infty$, the vibration amplitude at the fundamental open-circuit resonance frequency settles to 0.265 (m/s)/g (from the model).

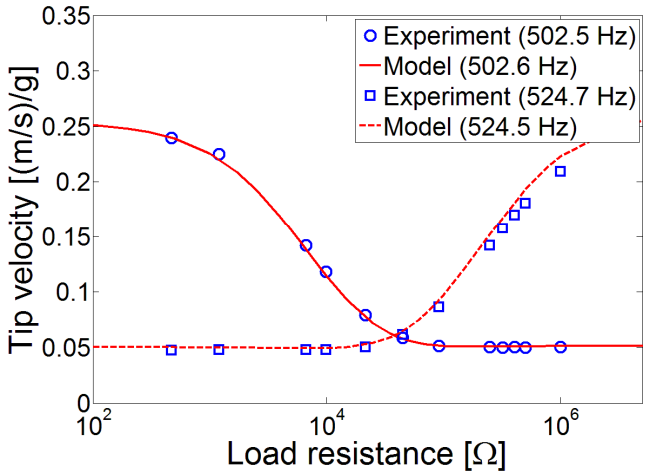

Fig. 4.14 Variation of the tip velocity with load resistance for excitations at the fundamental short-circuit and open-circuit resonance frequencies of the PZT-5H bimorph cantilever without a tip mass

4.2 PZT-5H Bimorph Cantilever with a Tip Mass

4.2.1 Experimental Setup. In order to investigate the effect of a tip mass and to demonstrate the validity of the model in the presence of a tip mass, a cube-shaped rectangular mass of 0.239

[†] The mechanical damping ratio was identified for this data point as can be recalled from Fig. 4.6a.

grams is attached at the tip of the PZT-5H bimorph cantilever investigated in the previous section (Fig. 4.15). The experimental setup and the devices used for the measurements are as described in Section 4.1.1. The purpose here is to introduce the tip mass information to the model directly and check the accuracy of the model predictions without changing the overhang length of the beam (as well as the clamping condition).

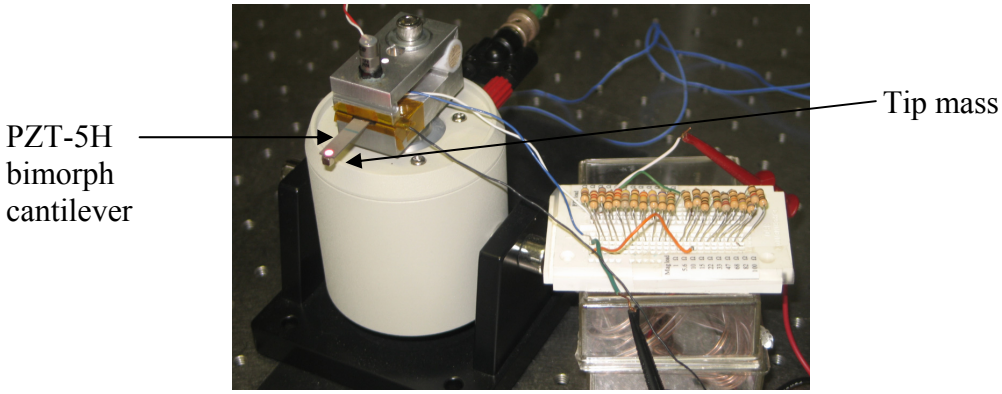

Fig. 4.15 A view of the experimental setup for the PZT-5H bimorph cantilever with a tip mass (photo by A. Erturk, 2009)

A close view of the PZT-5H bimorph cantilever with the tip mass is shown in Fig. 4.16a and a schematic showing the configuration with the tip mass is given by Fig. 4.16b. Tip mass is attached to the tip of the cantilever with a slight amount of wax (with negligible mass) such that the center line of the cube is at the tip of the beam. Each edge of the tip mass (simply a rare-earth magnet [60]) is 0.125 inch long ($a = 3.2$ mm). As the center line of the tip mass lies on the tip of the cantilever, the mass moment of inertia about the center axis of the bimorph is obtained from

$$I_t = M_t \left[\frac{a^2}{6} + \left(\frac{a + h_s}{2} + h_p \right)^2 \right] \tag{4.2}$$

where $M_t = 0.239 \times 10^{-3}$ kg (measured), the first term inside the parenthesis is for the mass moment of inertia about the center axis of the cube and the second term is due to the parallel axis theorem [61] to account for the offset of the tip mass to one side.‡ Substituting the numerical data

‡ Although the offset of the tip mass is taken into account in calculating the mass moment of inertia to improve the model predictions, it can still be argued that the structural symmetry of the bimorph is distorted as the model in the previous chapter is given for a symmetrically located tip mass. It should be noted that the tip mass is a mathematical

into Eq. (4.2), the mass moment of inertia at the tip is calculated as 1.285×10^{-9} kg.m^2. Therefore, the numerical values of the mass and the mass moment of inertia at the tip are the only additions to the data of the previous section as listed in Table 4.4. Following the same procedure, the first step is to obtain the experimental tip velocity and voltage output FRFs for the load resistance of 470 Ω.

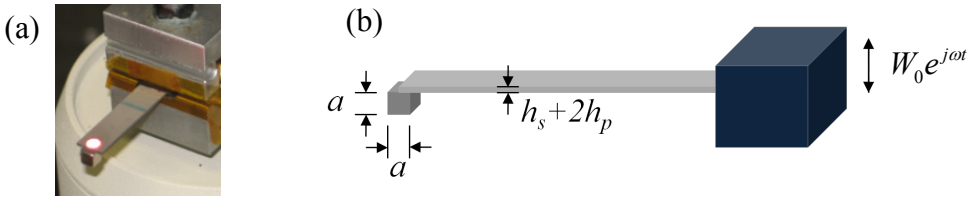

Fig. 4.16 (a) A close view of the PZT-5H bimorph cantilever with a tip mass (photo by A. Erturk, 2009) and (b) a schematic view showing the geometric detail of the cube-shaped tip mass

Table 4.4 Geometric and material properties of the PZT-5H bimorph cantilever with a tip mass

	Piezoceramic (PZT-5H)	**Substructure (brass)**
Length (L) [mm]	24.53	24.53
Width (b) [mm]	6.4	6.4
Thickness (h_p, h_s) [mm]	0.265 (each)	0.140
Tip mass (M_t) [kg]	0.239×10^{-3}	
Mass moment of inertia at the tip (I_t) [kg·m^2]	1.285×10^{-9}	
Mass density (ρ_p, ρ_s) [kg/m^3]	7500	9000
Elastic modulus ($\bar{c}_{11}^E$, Y_s) [GPa]	60.6	105
Piezoelectric constant ($\bar{e}_{31}$) [C/m^2]	-16.6	-
Permittivity constant ($\bar{\varepsilon}_{33}^S$) [nF/m]	25.55	-

singularity at $x = L$ (normally associated with the Dirac delta function) and the analytical model takes it into account through the eigenvalues and normalization of the eigenfunctions. Although the symmetry distortion is a singularity only at the tip, it might be significant for a very large tip mass. This configuration is studied here to check whether the formulation still works by comparing the model predictions with the experimental results.

Figure 4.17a shows the tip velocity and the voltage FRFs of the PZT-5H bimorph cantilever with a tip mass for the same frequency range as before (0-1000 Hz) by connecting the outermost electrodes to a resistive load of 470 Ω. The resonance frequency of the fundamental mode is measured for this low value of load resistance is 338.4 Hz. For this tip mass (which is about 29 % of the overhang mass of the beam), the reduction of the fundamental short-circuit resonance frequency compared to that of the configuration without a tip mass is about 33 %. The coherence of the velocity FRF is very good and the reduction of the coherence in the voltage FRF is due to the low value of resistance as in the previous case. The clamp-related imperfection (recall Fig. 4.5) appears in the tip velocity and the voltage FRFs and it is to be ignored as the resonance frequency is sufficiently away from it. The set of resistors used in the experiments is the same as the one given by Table 4.2.

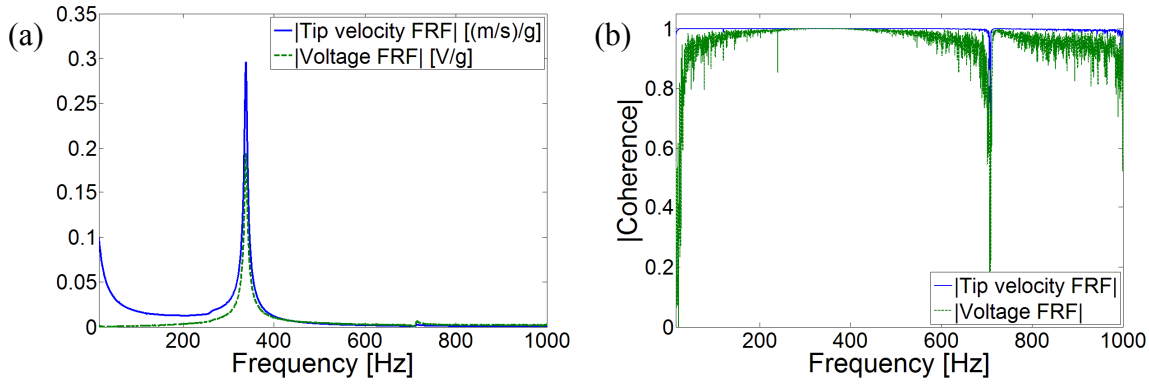

Fig. 4.17 (a) Tip velocity and voltage output FRFs of the PZT-5H bimorph cantilever with a tip mass and (b) their coherence functions (for a load resistance of 470 Ω)

4.1.2 Validation of the Electromechanical FRFs for a Set of Resistors. When the tip mass and the moment of inertia data are used in the model for a resistive load of 470 Ω (which is close to short-circuit conditions), the fundamental resonance frequency of the PZT-5H bimorph cantilever with a tip mass is obtained as 338.5 Hz (with an error of 0.03 % compared to the experimental resonance frequency). Therefore, the analytical model predicts the resonance frequency shift due to the addition of the tip mass very accurately as shown in Fig. 4.18a. Since this work does not aim to verify the stationarity or the overall behavior of mechanical damping, the damping ratio of the original configuration without the tip mass is slightly tuned to

$\zeta_1 = 0.00845$ in order to better match the peak amplitude in Fig. 4.18a. This damping ratio is then used in the analytical voltage FRF expression and the experimental voltage FRF shown in Fig. 4.18b is predicted with very good accuracy. Therefore, the model exhibits consistency between the vibration response and the electrical response in the presence of a tip mass as well.

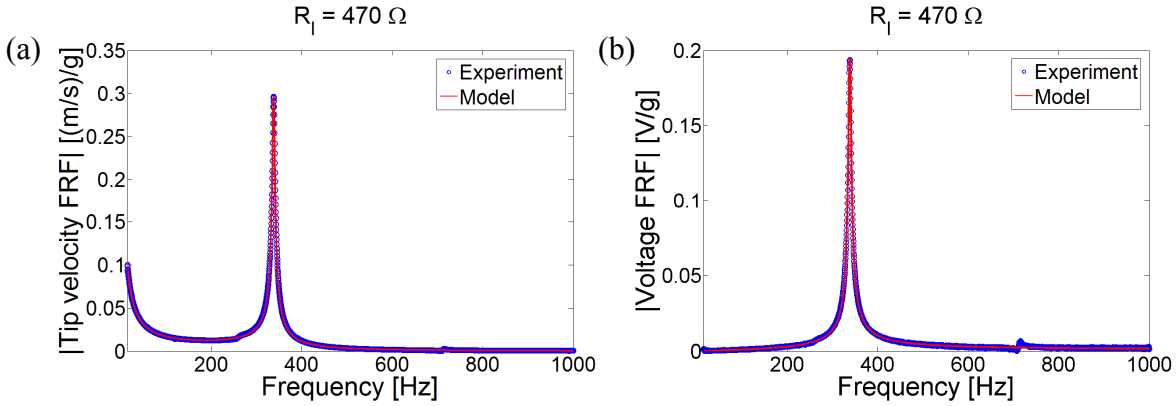

Fig. 4.18 Measured and predicted (a) tip velocity and (b) voltage output FRFs of the PZT-5H bimorph cantilever with a tip mass for a load resistance of 470 Ω

To further study the performance of the electromechanical model, three particular resistive loads are investigated next: 1.2 kΩ, 44.9 kΩ and 995 kΩ. Figure 4.19 shows the tip velocity and the voltage FRFs for these resistive loads (with fixed mechanical damping). The trend is very similar to the previous case (bimorph without a tip mass). Compared to Fig. 4.7, both the vibration and the voltage amplitudes are larger in Fig. 4.19. The main reason is the increased forcing amplitude for the same acceleration input since the force amplitude in the base excitation problem of a cantilever is proportional to the mass of the structure according to Eq. (3.36). Once again, among the loads used here, 44.9 kΩ results in a very strong attenuation of the peak vibration amplitude. The electromechanical FRFs for these three resistive loads are successfully predicted in Fig. 4.19. The experimentally measured fundamental short-circuit and open-circuit resonance frequencies are 338.4 Hz and 356.3 Hz and the model predicts these frequencies as 338.5 Hz and 355.4 as listed in Table 4.5. Once again, although the error levels are very low for practical purposes, the primary theoretical sources of the slight inaccuracy in predicting the frequency shift are the possible inaccuracies of the piezoelectric and permittivity constants. Overestimation of the short-circuit resonance also results in underestimation of the frequency shift as mentioned

earlier. As an experimental source of error, the frequency increment of the data acquisition system for frequency range of interest is 0.325 Hz.

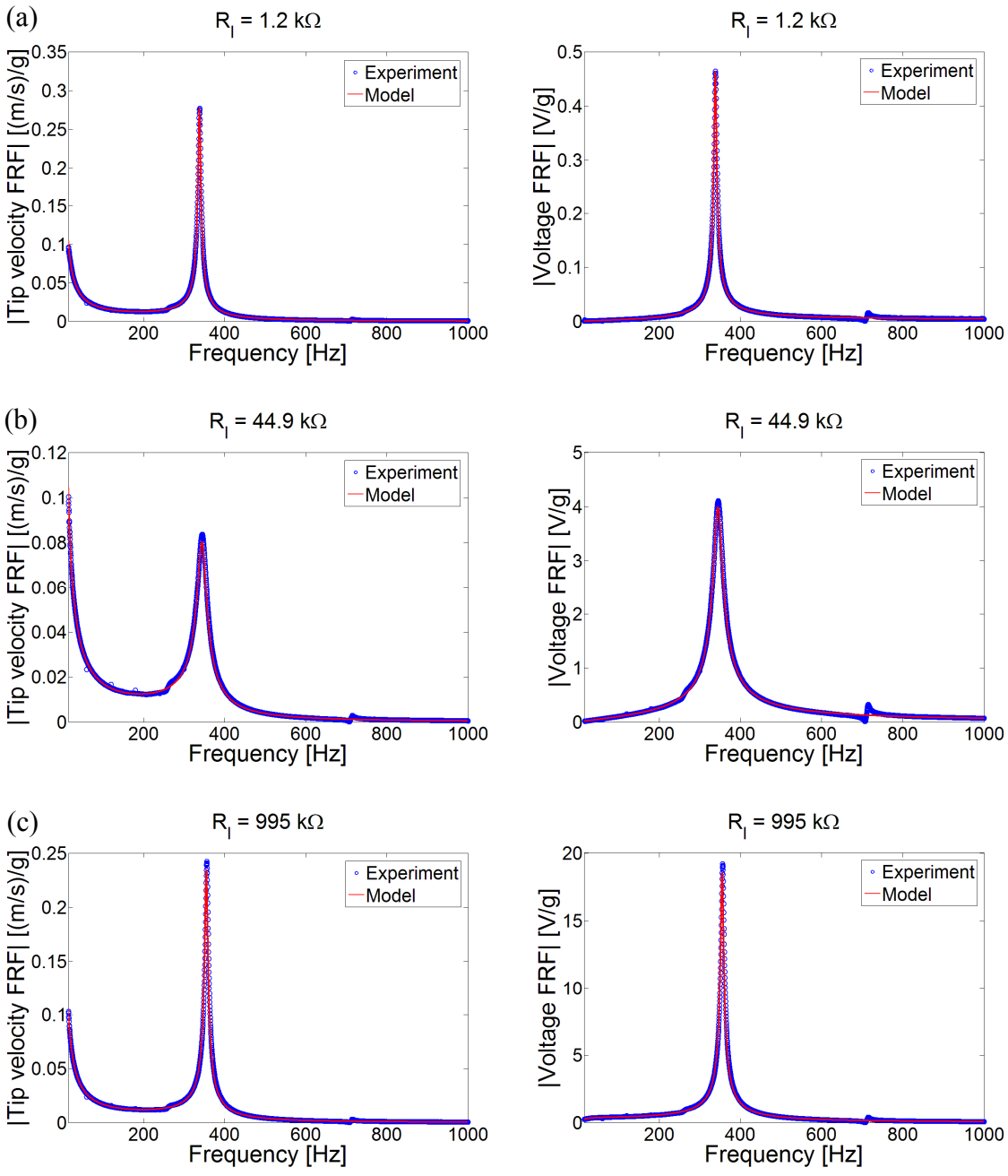

Fig. 4.19 Measured and predicted tip velocity and voltage output FRFs of the PZT-5H bimorph cantilever with a tip mass for various resistors: (a) 1.2 kΩ, (b) 44.9 kΩ and (c) 995 kΩ

Table 4.5 Fundamental short-circuit and open-circuit resonance frequencies of the PZT-5H bimorph cantilever with a tip mass

Fundamental resonance frequency	Experiment	Model	% Error
f_1^{sc} (short circuit) [Hz]	338.4	338.5	+0.03
f_1^{oc} (open circuit) [Hz]	356.3	355.4	-0.25

Figures 4.20 and 4.21, respectively, display the tip velocity and the voltage output FRFs of the PZT-5H bimorph cantilever with a tip mass for all values of load resistance used here. Variation of the peak amplitudes and the resonance frequencies are successfully predicted in both figures. The enlarged views of the voltage, current, power and the tip velocity FRFs for the frequency range of 200-500 Hz are given in Fig. 4.22, where the variation of the resonance frequency with load resistance is better visualized. All together with these graphs, one can conclude that the model can successfully predict the amplitude-wise and the frequency-wise coupled system dynamics of the bimorph cantilever in the presence of a tip mass as well.

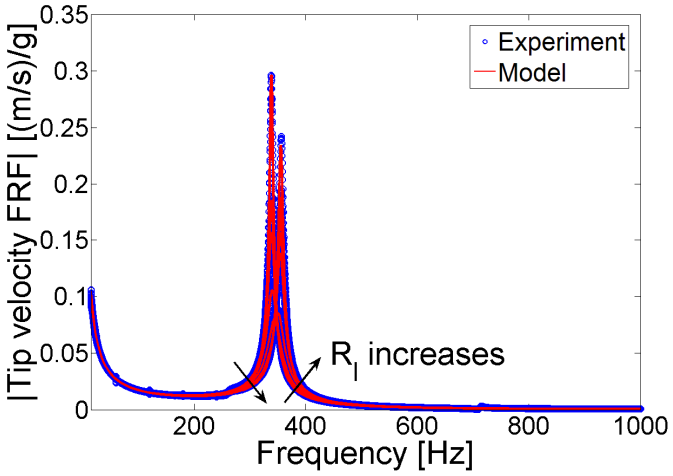

Fig. 4.20 Tip velocity FRFs of the PZT-5H bimorph cantilever with a tip mass for 12 different resistive loads (ranging from 470 Ω to 995 kΩ)

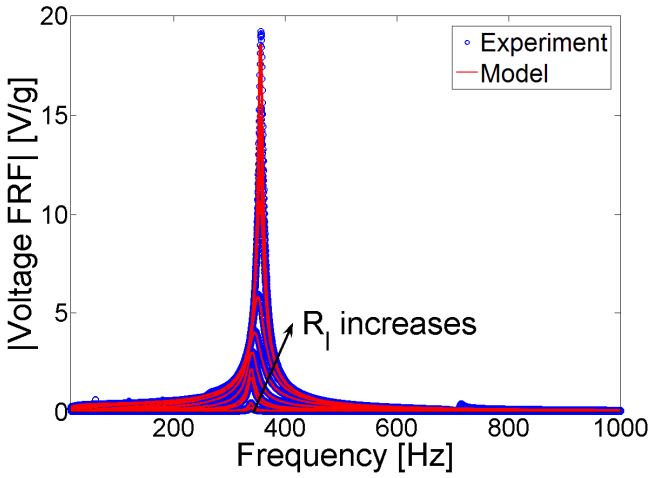

Fig. 4.21 Voltage output FRFs of the PZT-5H bimorph cantilever with a tip mass for 12 different resistive loads (ranging from 470 Ω to 995 kΩ)

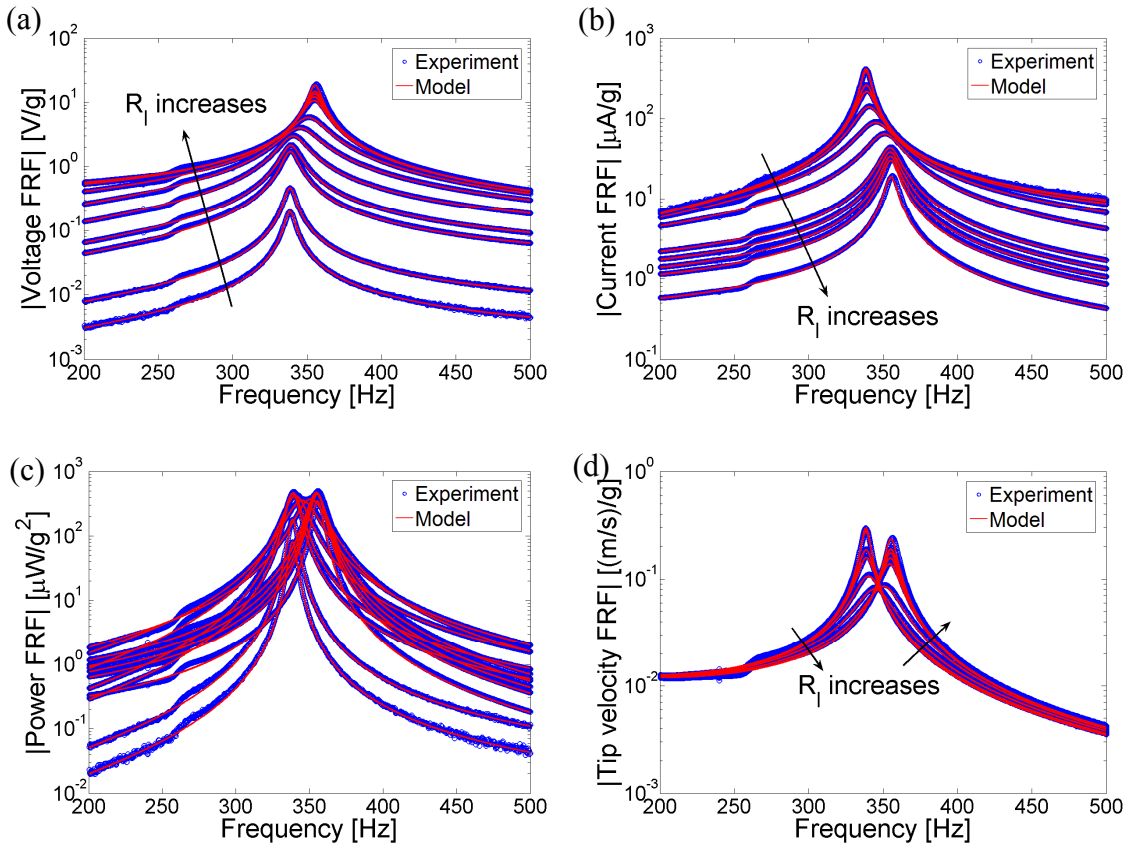

Fig. 4.22 Enlarged views of the (a) voltage output, (b) current output, (c) power output and (d) tip velocity FRFs of the PZT-5H bimorph cantilever with a tip mass for 12 different resistive loads (ranging from 470 Ω to 995 kΩ)

4.2.3 Electrical Performance Diagrams at the Fundamental Short-Circuit and Open-Circuit Resonance Frequencies. In the electromechanical curves plotted in Fig. 4.22, the focus is placed on the amplitude-wise results for excitations at the fundamental short-circuit and open-circuit resonance frequencies.

Variations of the voltage amplitude at these two frequencies are plotted in Fig. 4.23 along with the experimental data points for the 12 resistive loads. The analytical curve agrees very well with the experimental data points and the analytical asymptotes of $R_l \to \infty$ for excitations at the short-circuit and the open-circuit resonance frequencies are 4.2 V/g and 24.7 V/g, respectively.

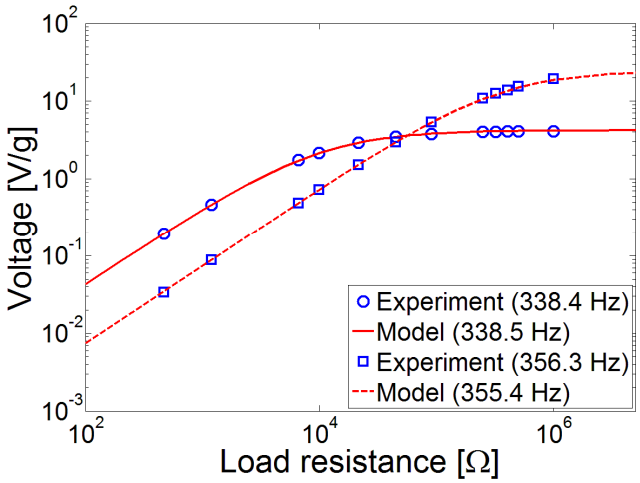

Fig. 4.23 Variation of the voltage output with load resistance for excitations at the fundamental short-circuit and open-circuit resonance frequencies of the PZT-5H bimorph cantilever with a tip mass

The current versus load resistance diagrams for excitations at the fundamental short-circuit and open-circuit resonance frequencies are plotted in Fig. 2.24, where the asymptotes of $R_l \to 0$ for these frequencies are 435 μA/g and 75 μA/g, respectively.

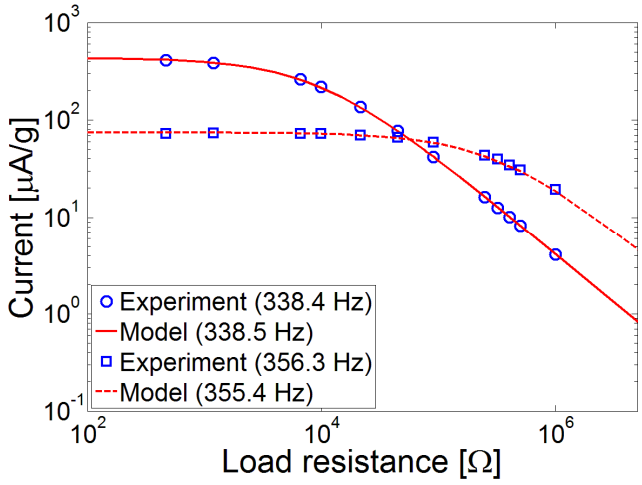

Fig. 4.24 Variation of the current output with load resistance for excitations at the fundamental short-circuit and open-circuit resonance frequencies of the PZT-5H bimorph cantilever with a tip mass

The analytical power versus load resistance diagrams are shown in Fig. 4.25 for excitations at the fundamental short-circuit and open-circuit resonance frequencies of the PZT-5H bimorph with a tip mass. The analytical curves exhibit good agreement with the experimental data points and predict a peak power amplitude of 0.46 mW/g^2 for the optimum resistive loads of 9.7 kΩ and 331 kΩ, respectively, at the fundamental short-circuit and open-circuit resonance frequencies. These exact values of the predicted optimum loads are not available in the set of resistors used here. The experimental results for the nearest resistive loads are 0.460 mW/g^2 for 9.9 kΩ at the short-circuit resonance frequency and 0.463 mW/g^2 for 319.2 kΩ at the open-circuit resonance frequency. These resistors are very close to the optimum ones and their power outputs are in good agreement with the predicted maximum power output.

With the volume of the tip mass, the overhang volume of the cantilever becomes 0.137 cm^3 and the overhang mass becomes 1.061 grams. Therefore the maximum power density of this configuration for resonance excitation is about 3.4 mW/(g^2cm^3) and the maximum specific power output is about 0.43 mW/(g^2g).

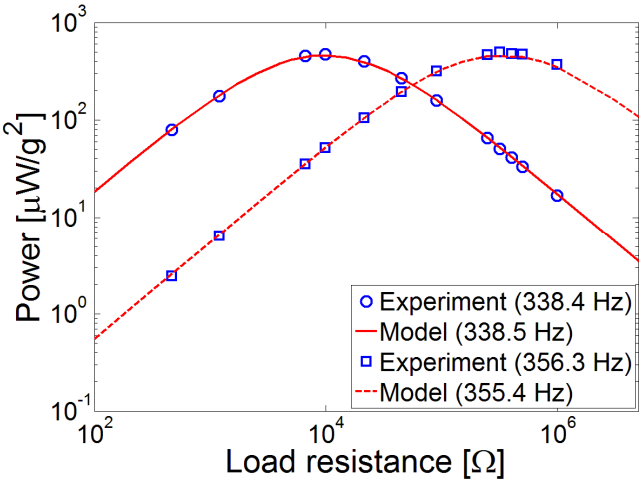

Fig. 4.25 Variation of the power output with load resistance for excitations at the fundamental short-circuit and open-circuit resonance frequencies of the PZT-5H bimorph cantilever with a tip mass

4.2.4 Vibration Response Diagrams at the Fundamental Short-Circuit and Open-Circuit Resonance Frequencies. Variation of the tip velocity amplitude with load resistance for excitations at the short-circuit and the open-circuit resonance frequencies are plotted in Fig. 4.26. At the fundamental short-circuit resonance frequency, the experimental vibration amplitude of 0.296 (m/s)/*g* for 470 Ω is attenuated to 0.054 (m/s)/*g* as the load resistance is increased to 995 kΩ. The model predicts these amplitudes as 0.296 (m/s)/*g*[§] and 0.055 (m/s)/*g*, respectively. For $R_l \to \infty$, the vibration amplitude at the fundamental short-circuit resonance frequency converges approximately to the same amplitude: 0.055 (m/s)/*g*. For excitation at the open-circuit resonance frequency, the experimental vibration amplitude of 0.048 (m/s)/*g* for 470 Ω increases to 0.242 (m/s)/*g* for 995 kΩ. The model predicts these two amplitudes as 0.051 (m/s)/*g* and 0.246 (m/s)/*g*, respectively. As $R_l \to \infty$ in the model, the vibration amplitude at the fundamental open-circuit resonance frequency reaches 0.327 (m/s)/*g*.

[§] This is the data point that was used for the identification of modal mechanical damping.

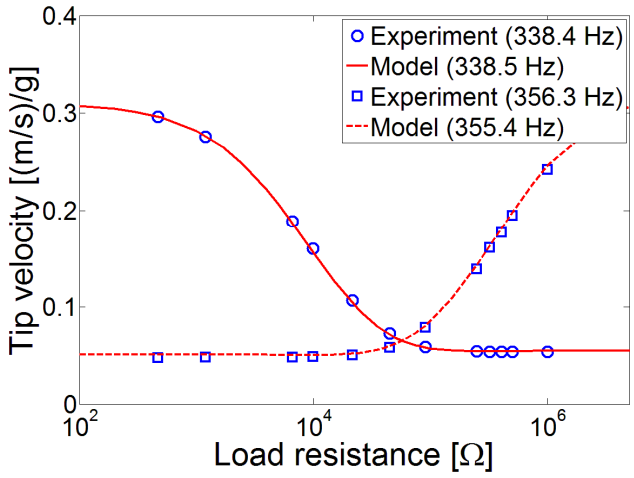

Fig. 4.26 Variation of the tip velocity with load resistance for excitations at the fundamental short-circuit and open-circuit resonance frequencies of the PZT-5H bimorph cantilever with a tip mass

4.2.5 Model Predictions with the Point Mass Assumption. In order to check the effect of the mass moment of inertia of the tip mass (therefore the rotary inertia of the tip mass), two fundamental simulations are performed using the model for the point mass assumption. That is, the mass of the tip attachment is considered in the model ($M_t = 0.239\times10^{-3}$ kg), however, its mass moment of inertia is ignored ($I_t = 0$).

Figures 4.27a and 4.27b, respectively, display the voltage FRFs and the tip velocity FRFs of the experimental measurements along with the model predictions including and excluding the rotary inertia of the tip mass. As can be expected, when the rotary inertia of the tip mass is neglected, the fundamental short-circuit resonance frequency is overestimated (as 340.2 Hz compared to the analytically obtained value of 338.5 in the presence of the rotary inertia and the experimental value of 338.4 Hz). Since the open-circuit resonance frequency was slightly underestimated for the case with the rotary inertia of the tip mass, it is now slightly overestimated with the point mass assumption. These data are given in Table 4.6. Once again, the frequency shift from the short-circuit to the open-circuit conditions depends on the piezoelectric and permittivity constants. Therefore the accuracy of the prediction with the point mass assumption should be checked considering the short-circuit resonance frequency. The short-circuit resonance frequency obtained from the analytical model with the point mass

assumption overestimates the experimentally measured short-circuit resonance frequency by 0.5 %. This error is reduced to 0.03 % when the mass moment of inertia of the tip mass is included in the model.

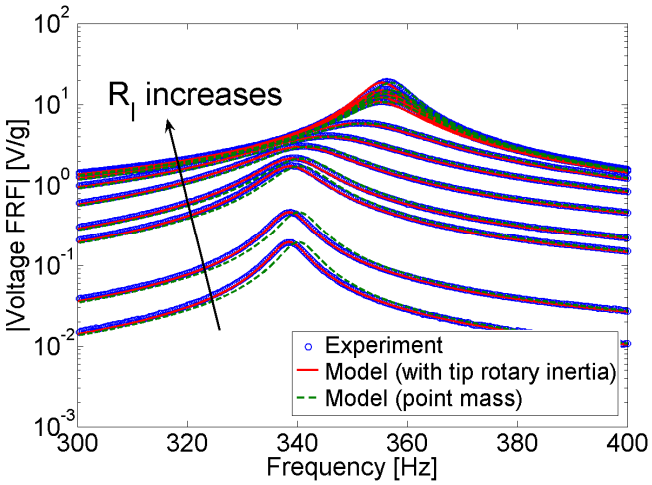

Fig. 4.27 Comparison of the voltage FRFs predicted with and without considering the rotary inertia of the tip mass

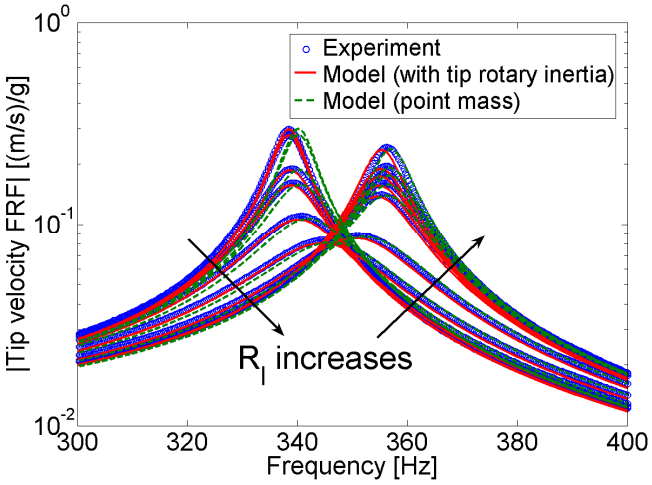

Fig. 4.28 Comparison of the tip velocity FRFs predicted with and without considering the rotary inertia of the tip mass

Table 4.6 Fundamental short-circuit and open-circuit resonance frequencies of the PZT-5H bimorph cantilever with a tip mass in the presence and absence of the tip rotary inertia

Fundamental resonance frequency	Experiment	Model (with rotary inertia)	Model (with rotary inertia)
f_1^{sc} (short circuit) [Hz]	338.4	338.5	340.2
f_1^{oc} (open circuit) [Hz]	356.3	355.4	357.0

4.2.6 Performance Comparison of the PZT-5H Bimorph without and with the Tip Mass. The electrical performance comparisons of the PZT-5H bimorph cantilever without and with the tip mass are given in this section. Table 4.7 shows the detailed performance results for the maximum power output (along with the respective optimum values of load resistance), the maximum voltage (for $R_l \to \infty$) and the maximum current (for $R_l \to 0$) outputs at the fundamental short-circuit and open-circuit resonance frequencies. The maximum power density and the specific power values are also given. It is observed that the maximum power output for resonance excitation increases by a factor of more than 2 for resonance excitation with the tip mass attachment. For both resonance frequencies (short-circuit and open-circuit), the optimum load that gives the maximum power output increases considerably in the presence of the tip mass. As will be seen in Chapter 5, the optimum load is inversely proportional to the undamped natural frequency for resonance excitation. Therefore, the increase in the optimum load due to the reduction in the resonance frequency is expected. It is worth noticing that the increase in the maximum values of the current output is not as substantial as the increase in the maximum voltage. The power density calculation accounts for the additional volume of the tip mass and it exhibits an increase of about 61% (from 2.1 mW/cm^3g^2 to 3.4 mW/cm^3g^2). The specific power calculation includes the additional mass of the tip attachment and it exhibits an increase of 59 % (from 0.27 mW/(g^2g) to 0.43 mW/(g^2g)).

Table 4.7 Electrical performance comparisons of the PZT-5H bimorph cantilever without and with a tip mass

	Without the tip mass	**With the tip mass**
f_1^{sc} (experimental) [Hz]	502.5	338.4
f_1^{oc} (experimental) [Hz]	524.7	356.3
Maximum power at f_1^{sc} [mW/g^2]	0.22	0.46
Optimum load at f_1^{sc} [kΩ]	7.6	9.7
Maximum power at f_1^{oc} [mW/g^2]	0.22	0.46
Optimum load at f_1^{oc} [kΩ]	189	331
Maximum voltage at f_1^{sc} [mV/g]	2.6	4.2
Maximum voltage at f_1^{oc} [mV/g]	12.8	24.7
Maximum current at f_1^{sc} [μA/g]	336	435
Maximum current at f_1^{oc} [μA/g]	68	75
Maximum power density [mW/(g^2cm^3)]	2.1	3.4
Maximum specific power [mW/(g^2g)]	0.27	0.43

4.3 PZT-5A Bimorph Cantilever

4.3.1 Experimental Setup. The last experimental case summarizes the analysis of a bimorph cantilever made of a different type of piezoceramic: PZT-5A. The brass-reinforced PZT-5A bimorph (T226-A4-203X) shown in Fig. 4.29 is manufactured by the same company [45]. It has the same overall geometric properties (Table 4.8) and it is also manufactured for the series connection of the oppositely poled layers (Fig. 3.1a). The main difference is due to the piezoceramic material. The reduced form of the typical PZT-5A properties are referred from Table B.2 in Appendix B (since the manufacturer provides limited data). The overhang length of the configuration shown in Fig. 4.29 is 25.35 mm and the laser vibrometer measures the response at a point that is approximately 23.2 mm away from the root ($x = L_v = 23.2$ mm in Eq. (4.1)). The

experimental setup used and the procedure followed for the frequency response measurements are identical to those of Section 4.1.1. The same set of resistors is used (Table 4.2).

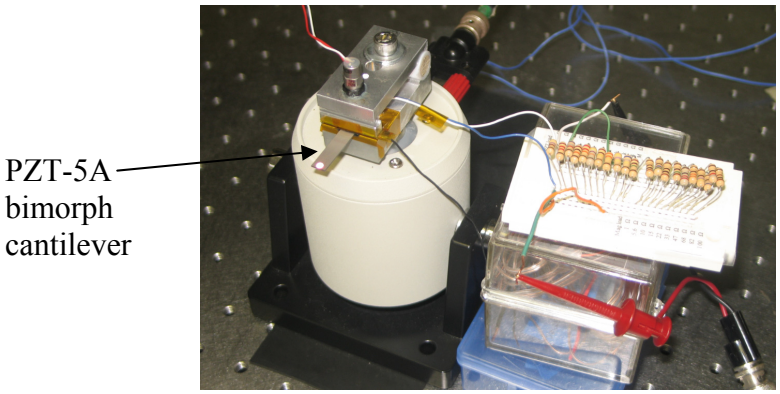

Fig. 4.29 A view of the experimental setup for the PZT-5A bimorph cantilever (photo by A. Erturk, 2009)

The two purposes of this section are to study a configuration with a different piezoelectric material (PZT-5A) and to investigate a wider frequency range to include a higher vibration mode (so that a demonstration using the single-mode FRFs can be presented). Therefore, the frequency bandwidth in the experiments is increased, which affects the frequency resolution (in an undesirable way) due to the limitations of the data acquisition system. For a frequency bandwidth of 0-5000 Hz, the frequency increment automatically becomes 1.5625 Hz (which should be taken into account as a source of error when comparing the model predictions).

For a resistive load of 470 Ω, the tip velocity and voltage FRFs of the bimorph cantilever are measured as shown in Fig. 4.30a. The FRFs are given in semi-log scale to view the second vibration mode (which has about an order of magnitude less amplitude compared to the first mode). The short-circuit resonance frequencies of the first and the second vibration modes are read from the voltage FRF as 456.6 Hz and 2921.9 Hz. The coherence functions of these measurements are given in Fig. 4.30b. The coherence of the tip velocity measurements drops around the minimum between these vibration modes and after the second mode due to low amplitude vibration response (low signal from the laser vibrometer). The poor behavior of the coherence of the voltage measurement away from the resonance frequencies is due to the low

load resistance used deliberately to be close to short-circuit conditions. However, the frequencies around the peak values have acceptable coherence (close to unity).

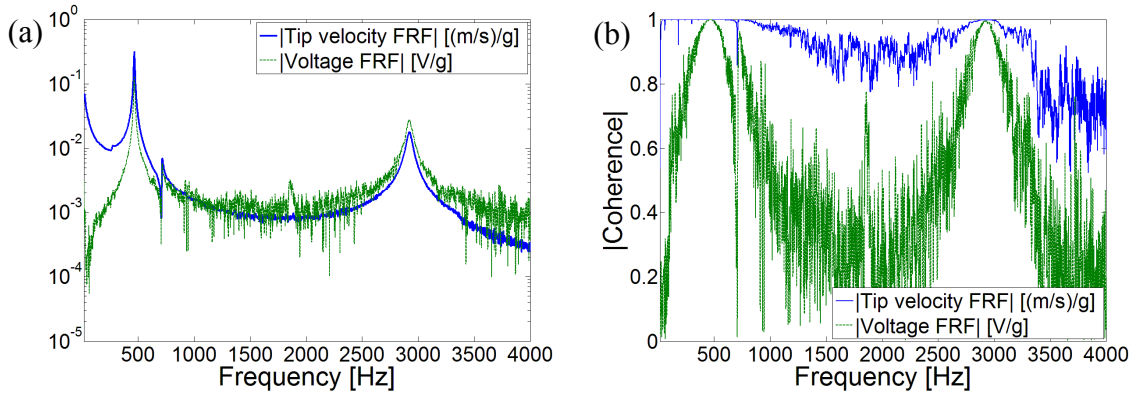

Fig. 4.30 (a) Tip velocity and voltage output FRFs of the PZT-5A bimorph cantilever and (b) their coherence functions (for a load resistance of 470 Ω)

Table 4.8 Geometric and material properties of the PZT-5A bimorph cantilever

	Piezoceramic (PZT-5A)	**Substructure (brass)**
Length (L) [mm]	25.35	25.35
Width (b) [mm]	6.4	6.4
Thickness (h_p, h_s) [mm]	0.265 (each)	0.140
Tip mass (M_t) [kg]	(none)	
Mass density (ρ_p, ρ_s) [kg/m^3]	7750	9000
Elastic modulus ($\bar{c}_{11}^E$, Y_s) [GPa]	61	105
Piezoelectric constant ($\bar{e}_{31}$) [C/m^2]	-10.4	-
Permittivity constant ($\bar{\varepsilon}_{33}^S$) [nF/m]	13.3	-

4.3.2 Validation of the Electromechanical FRFs for a Set of Resistors. When the numerical data given in Table 4.7 is used in the model, the tip velocity FRF of the 470 Ω case is predicted as shown in Fig. 4.31a. The mechanical damping ratios of these two modes are identified using

the model as $\zeta_1 = 0.00715$ and $\zeta_2 = 0.00740$. When these damping ratios are used in the voltage FRF expression, Fig. 4.31b is obtained. The voltage amplitude of the fundamental mode is predicted with good accuracy (as 0.12 V/*g* compared to the experimental value of 0.13 V/*g*) and that of the second mode is overestimated (as 0.036 V/*g* compared to the experimental value of 0.028 V/*g*) for the mechanical damping ratios identified from the tip velocity FRF. The short-circuit resonance frequencies of the first and the second vibration modes are obtained using from the model as 466.2 Hz and 2921.3 Hz, respectively. Note that the noisy behavior in Figs. 4.31a and 4.31b away from the resonance frequencies correspond to the low coherence regions in Fig. 4.30. The clamp-related imperfection is still in the FRFs (around 715 Hz) but it is sufficiently away from both vibration modes.

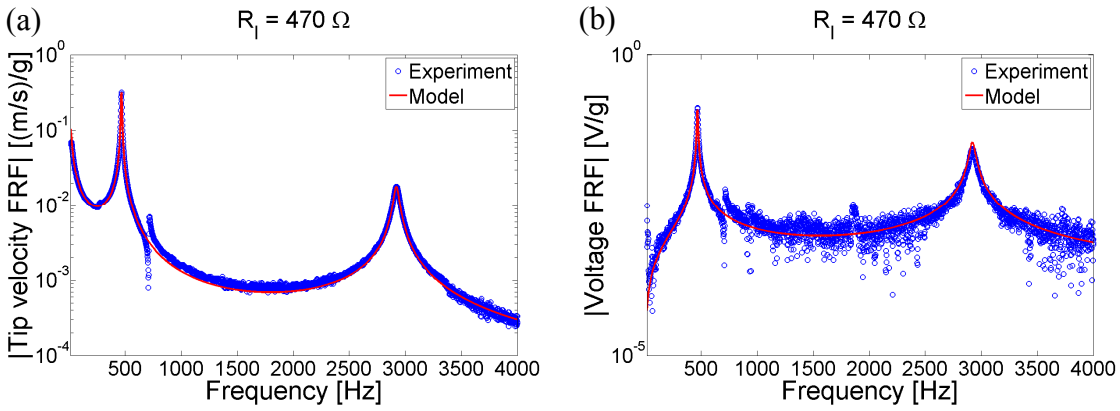

Fig. 4.31 Measured and predicted (a) tip velocity and (b) voltage output FRFs of the PZT-5A bimorph cantilever for a load resistance of 470 Ω

For the set of resistors used in the experiments (Table 4.2), the voltage, current, power and the tip velocity FRFs are obtained as shown in Fig. 4.32. The overall analytical trends are in good agreement with the experimental measurements (similar to the theoretical case study given in Chapter 3). The amplitude-wise mismatch between the experimental and the analytical results is particularly around the second vibration mode of the electrical FRFs. It should be noted that the tip velocity FRF matches the experimental FRF better than the voltage FRF around the second mode. One reason of the mismatch around the second mode in the voltage FRF (and in the electrical FRFs derived from the voltage FRF) might be the low level of the voltage output from the second vibration mode in the experiments. Another experimental source of error might

be non-modeled imperfections in the bimorph that is more pronounced at high frequencies (since the low frequency voltage predictions match perfectly around the first mode), such as possible symmetry distortion in the structure or a relatively elastic behavior of the bonding layers that becomes more important with a mode shape of larger cross-section rotation (the second mode shape compared to the first mode shape).

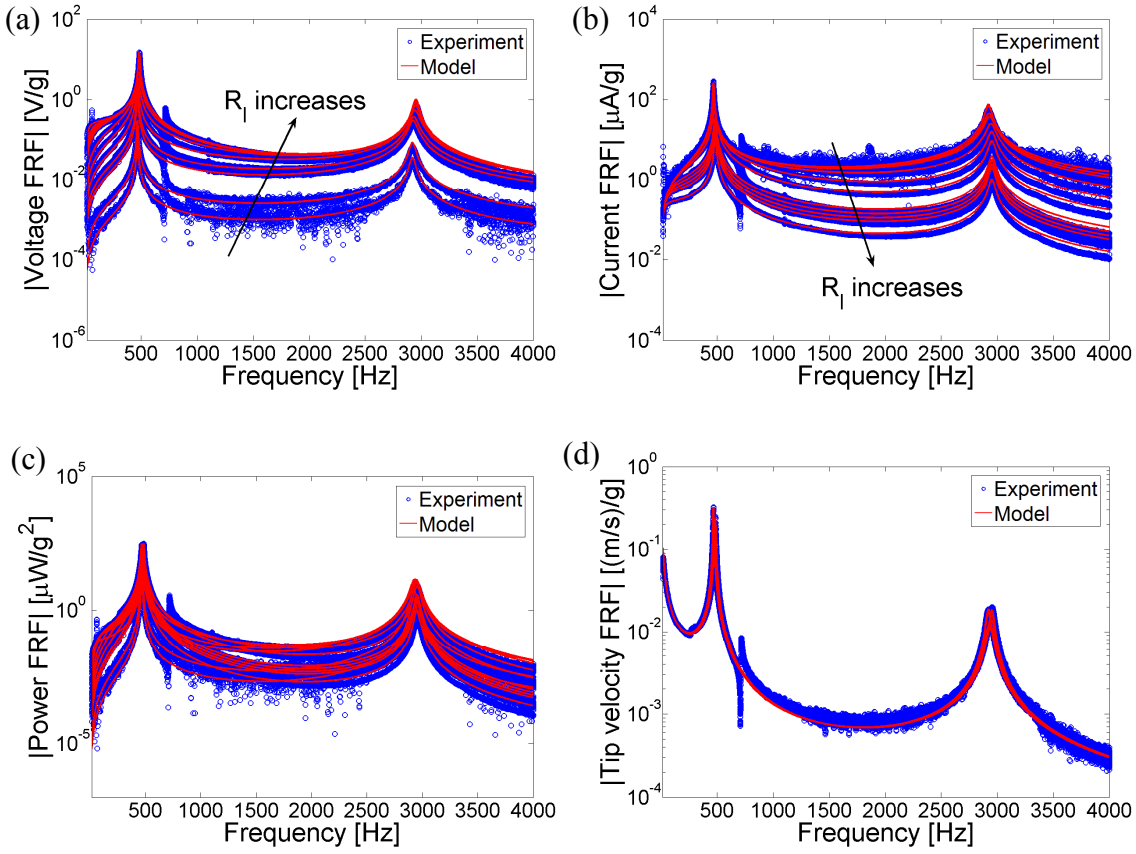

Fig. 4.32 Electromechanical FRFs of the PZT-5A bimorph cantilever: (a) voltage output, (b) current output, (c) power output and (d) tip velocity FRFs for 12 different resistive loads (ranging from 470 Ω to 995 kΩ)

The frequency-wise predictions for the PZT-5A bimorph cantilever are listed in Table 4.9. The absolute value of the relative error in the model predictions is less than 0.6 %, meaning that the Euler-Bernoulli theory works well even around the second natural frequency of this thin structure. It should also be noted that for the large frequency band considered here, the

experimental frequency increment in the measured FRFs is relatively coarse (1.5625 Hz) for this data acquisition system as mentioned previously.

Table 4.9 First two short-circuit and open-circuit resonance frequencies of the PZT-5A bimorph cantilever

Resonance frequency	Experiment	Model	% Error
f_1^{sc} (short circuit) [Hz]	465.6	466.2	+0.13
f_1^{oc} (open circuit) [Hz]	484.4	481.7	-0.56
f_2^{sc} (short circuit) [Hz]	2921.9	2921.3	-0.02
f_2^{oc} (open circuit) [Hz]	2954.7	2952.3	-0.08

4.3.3 Comparison of the Single-mode and Multi-mode Electromechanical FRFs. It is a useful practice to check the performances of the single-mode electromechanical FRFs given by Eqs. (3.108) and (3.111) for modes 1 and 2 briefly. When $r=1$ is used in the single-mode voltage FRF given by Eq. (3.108), the experimental voltage behavior is predicted as shown in Fig. 4.33a. Substituting $r=2$ into the same expression gives the single-mode curves shown in Fig. 4.33b. Note that these two separate single-mode representations (for mode 1 and mode 2 independently) are approximately valid around the respective resonance frequencies only. Figure 4.33a lacks the information of all vibration modes other than the fundamental vibration mode whereas Fig. 4.33b has the information of the second vibration mode only.

As discussed in the theoretical case study of Chapter 3, the effects of the neighboring modes are lost in the single-mode representations. The fundamental single-mode open-circuit resonance frequency is slightly overestimated as 484.3 Hz compared to the multi-mode case in Fig. 4.33a. The single-mode open-circuit resonance frequency of the second mode in Fig. 4.33b is also slightly overestimated compared to the multi-mode solution as 2953 Hz. In this case study, these open-circuit resonance frequencies of the single-mode prediction agree better with the experimental measurement compared to the multi-mode counterparts. However, one should note that the experimental results are not necessarily perfectly accurate. Secondly, it is very likely that the inaccuracy of the single-mode representation (due to excluding the residuals of the

neighboring modes) might be compensating the possible inaccuracy of the frequency shift prediction (which depends on the piezoelectric and the permittivity constants).

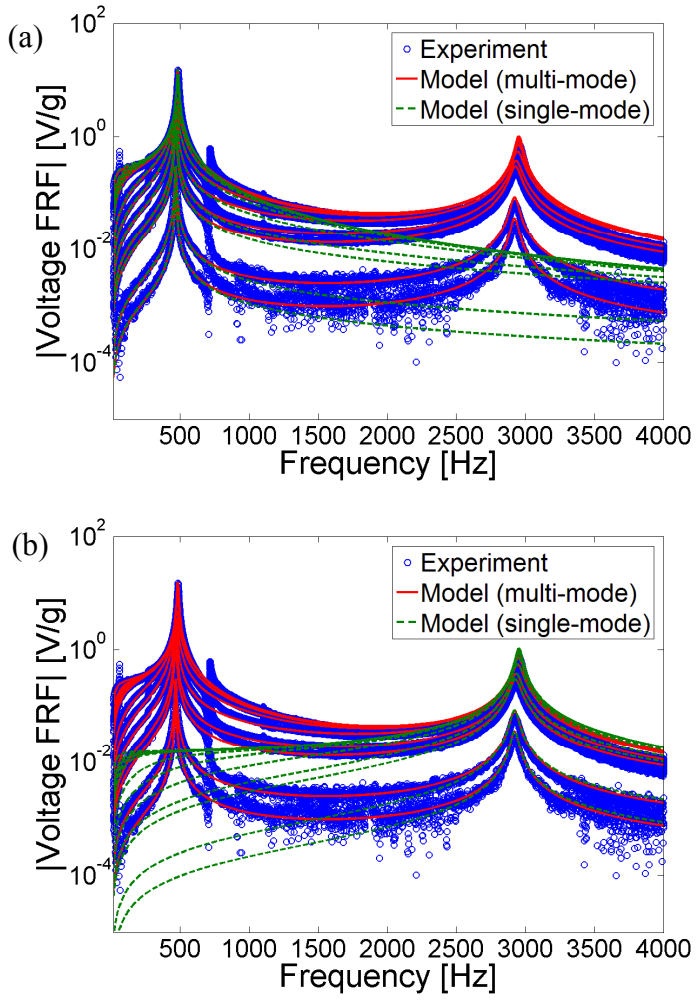

Fig. 4.33 Prediction of the modal voltage frequency response using the single-mode FRFs for (a) mode 1 and (b) mode 2 of the PZT-5A bimorph cantilever

Single-mode predictions of the tip velocity FRFs are shown in Fig. 4.34. As in the case of Fig. 4.33, the single-mode representations in Fig. 4.34a are valid strictly around the fundamental resonance frequency only whereas the single-mode representations in Fig. 4.34b are given for a narrow band around the resonance frequency of the second vibration mode only.

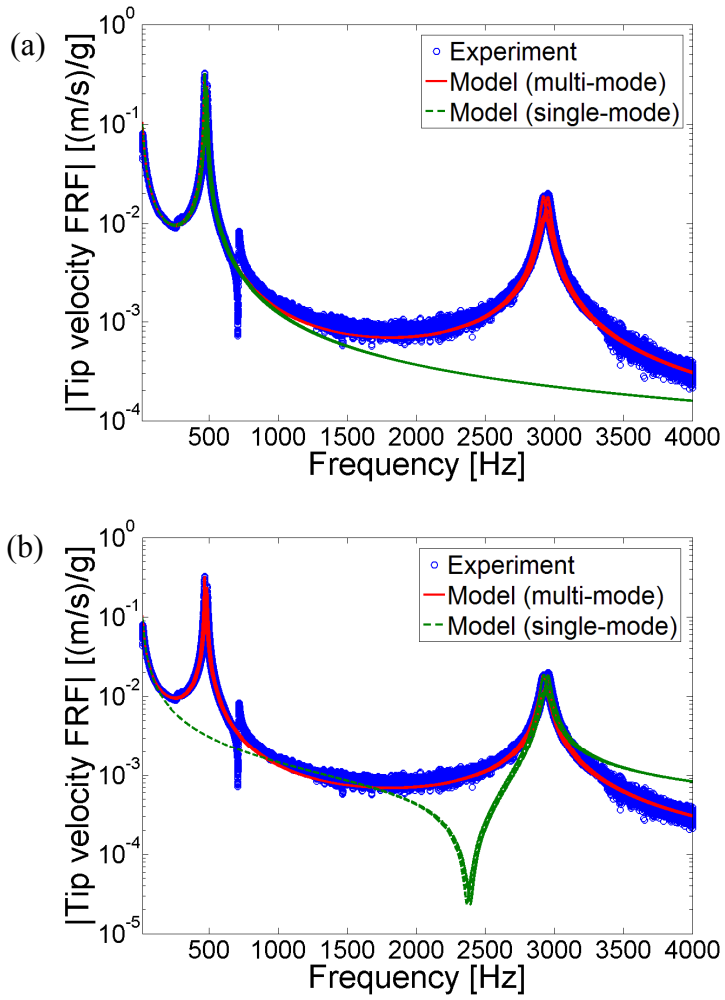

Fig. 4.34 Prediction of the single-mode tip velocity frequency response using the single-mode FRFs for (a) mode 1 and (b) mode 2 of the PZT-5A bimorph cantilever

4.4 Summary and Conclusions

The analytical solutions derived in the previous chapter are validated for various experimental cases. The first experimental case is given for a brass-reinforced PZT-5H bimorph cantilever without a tip mass. After validating the analytical model predictions using the voltage, current, power and the tip velocity FRFs for this configuration and providing an extensive electromechanical analysis, a tip mass is attached to create a configuration for the second case study. The variations of the fundamental short-circuit and open-circuit resonance frequencies after the attachment of the tip mass are successfully predicted by the model. Performance

diagrams for excitations at the fundamental short-circuit and open-circuit resonance frequencies are extracted for both configurations (without and with the tip mass) and comparisons are made. Improvement of the overall power output (as well as the power density and the specific power) due to the addition of a tip mass is shown. The analytical model predicts the electrical and the mechanical response with very good accuracy for all values of load resistance. Effect of the rotary inertia of the tip mass is also studied by providing further analytical simulations with the point mass assumption. It is shown that the resonance frequencies can be overestimated if the rotary inertia of the tip mass is neglected. The damping effect of piezoelectric power generation is discussed in detail based on the experimental measurements and the model predictions. The final case study is given for a PZT-5A bimorph cantilever and the frequency range of interest is increased to cover the second vibration mode as well. Predictions of the multi-mode and the single-mode FRFs are provided (for the first two modes independently) and good agreement is observed with the experimental results.

CHAPTER 5

DIMENSIONLESS SINGLE-MODE ELECTROMECHANICAL EQUATIONS, ASYMPTOTIC ANALYSES AND CLOSED-FORM RELATIONS FOR PARAMETER IDENTIFICATION AND OPTIMIZATION

In this chapter, mathematical analyses of the single-mode electromechanical equations are presented. Among the four FRF defined in Chapter 3, focus is placed on the voltage output and the vibration response FRFs per translational base acceleration. The single-mode relations are first expressed in the modulus-phase form and then they are represented with dimensionless terms for convenience. The asymptotic trends of the voltage output and the tip displacement FRFs are investigated and relations are obtained for the extreme conditions of load resistance. Using the asymptotic FRFs, the resonance frequencies of the voltage and the tip displacement FRFs are obtained and it is shown that they can be different. The linear asymptotes of the voltage and vibration response (at a fixed frequency) observed in the previously given theoretical and experimental case studies are mathematically verified here and the equations of these linear asymptotes are obtained. Closed-form expressions for the optimum electrical loads of the maximum power generation at the short-circuit and the open-circuit resonance frequencies at extracted. It is mathematically proven that, for excitations at these two frequencies, the intersections of the linear voltage asymptotes occur at the respective optimum load resistance. Using this result, a simple technique is introduced to identify the optimum load resistance of a piezoelectric energy harvester using a single resistive load with the open-circuit voltage measurement. The asymptotes of the vibration resonance are also studied and expressions are derived to estimate the percentage vibration attenuation/amplification at the short/open-circuit resonance frequency as the load resistance is increased from the short-circuit to the open-circuit conditions. An experimental case is visited to validate the major equations derived here. It should be noted that, all the derivations given here are based on the single-mode approximation and they are valid around the respective modal frequency (which is the fundamental natural frequency in most practical applications).

5.1 Equivalent Dimensionless Representation of the Single-mode Electromechanical FRFs

5.1.1 Complex Forms. Recall from the equivalent representations of the single-mode electromechanical equations presented for bimorph energy harvesters given by Eqs. (3.107) and (3.110) that

$$\hat{v}(t) = \hat{\alpha}(\omega)\left(-\omega^2 W_0 e^{j\omega t}\right) + \hat{\mu}(\omega)\left(-\omega^2 \theta_0 e^{j\omega t}\right) \tag{5.1}$$

$$\hat{w}_{rel}(x,t) = \hat{\beta}(\omega,x)\left(-\omega^2 W_0 e^{j\omega t}\right) + \hat{\psi}(\omega,x)\left(-\omega^2 \theta_0 e^{j\omega t}\right) \tag{5.2}$$

where the respective electromechanical FRFs are

$$\hat{\alpha}(\omega) = \frac{j\omega R_l \tilde{\theta}_r \sigma_r}{\left(1 + j\omega R_l C_{\tilde{p}}^{eq}\right)\left(\omega_r{}^2 - \omega^2 + j2\zeta_r \omega_r \omega\right) + j\omega R_l \tilde{\theta}_r^2} \tag{5.3}$$

$$\hat{\mu}(\omega) = \frac{j\omega R_l \tilde{\theta}_r \tau_r}{\left(1 + j\omega R_l C_{\tilde{p}}^{eq}\right)\left(\omega_r{}^2 - \omega^2 + j2\zeta_r \omega_r \omega\right) + j\omega R_l \tilde{\theta}_r^2} \tag{5.4}$$

$$\hat{\beta}(\omega,x) = \frac{\left(1 + j\omega R_l C_{\tilde{p}}^{eq}\right)\sigma_r \phi_r(x)}{\left(1 + j\omega R_l C_{\tilde{p}}^{eq}\right)\left(\omega_r{}^2 - \omega^2 + j2\zeta_r \omega_r \omega\right) + j\omega R_l \tilde{\theta}_r^2} \tag{5.5}$$

$$\hat{\psi}(\omega,x) = \frac{\left(1 + j\omega R_l C_{\tilde{p}}^{eq}\right)\tau_r \phi_r(x)}{\left(1 + j\omega R_l C_{\tilde{p}}^{eq}\right)\left(\omega_r{}^2 - \omega^2 + j2\zeta_r \omega_r \omega\right) + j\omega R_l \tilde{\theta}_r^2} \tag{5.6}$$

Here, the electromechanical coupling term $\tilde{\theta}_r$ and the equivalent capacitance term $C_{\tilde{p}}^{eq}$ are read from Table 3.1 for the series or parallel connection cases of the piezoceramic layers. According to Eqs. (5.1) and (5.2), $\hat{\alpha}(\omega)$, $\hat{\mu}(\omega)$, $\hat{\beta}(\omega,x)$ and $\hat{\psi}(\omega,x)$, respectively, are the single-mode voltage output – to – translational base acceleration, voltage output – to – rotational base acceleration, displacement response – to – translational base acceleration and the displacement response – to – rotational base acceleration FRF. These expressions are the *complex forms* of the single-mode electromechanical FRFs.

For convenience, in the following, the focus is placed on the FRFs for the translational acceleration input (i.e. $\hat{\alpha}(\omega)$ and $\hat{\beta}(\omega,x)$), and once can easily obtain the counterparts for $\hat{\mu}(\omega)$ and $\hat{\psi}(\omega,x)$ simply by replacing σ_r with τ_r. It is very important to note that, the single mode relations derived in the following are approximately valid only around the natural frequency (ω_r) of the respective vibration mode.

5.1.2 Modulus-Phase Forms. The single-mode voltage FRF can be expressed in the modulus-phase form as

$$\hat{\alpha}(\omega) = \left|\hat{\alpha}(\omega)\right| e^{j\Phi(\omega)} \tag{5.7}$$

where the *modulus* (magnitude) of the FRF is

$$\left|\hat{\alpha}(\omega)\right| = \frac{\omega R_l \left|\tilde{\theta}_r \sigma_r\right|}{\left\{\left[\omega_r{}^2 - \omega^2\left(1 + 2R_l C_{\tilde{p}}^{eq} \omega_r \zeta_r\right)\right]^2 + \left[2\zeta_r \omega_r \omega + R_l \omega\left(C_{\tilde{p}}^{eq} \omega_r{}^2 - C_{\tilde{p}}^{eq} \omega^2 + \tilde{\theta}_r^2\right)\right]^2\right\}^{1/2}} \tag{5.8}$$

and the phase (the argument) is the phase between the base acceleration and the voltage output

$$\Phi(\omega) = \frac{\pi}{2}\operatorname{sgn}\left(\tilde{\theta}_r \sigma_r\right) - \tan^{-1}\left(\frac{2\zeta_r \omega_r \omega + R_l \omega\left(C_{\tilde{p}}^{eq} \omega_r{}^2 - C_{\tilde{p}}^{eq} \omega^2 + \tilde{\theta}_r^2\right)}{\omega_r{}^2 - \omega^2\left(1 + 2R_l C_{\tilde{p}}^{eq} \omega_r \zeta_r\right)}\right) \tag{5.9}$$

where sgn stands for the *signum function*. The single-mode tip displacement FRF is then

$$\hat{\beta}(\omega, x) = \left|\hat{\beta}(\omega, x)\right| e^{j\Psi(\omega, x)} \tag{5.10}$$

where its modulus and the phase are

$$\left|\hat{\beta}(\omega, x)\right| = \frac{\left|\sigma_r \phi_r(x)\right|\left\{1 + \left(\omega R_l C_{\tilde{p}}^{eq}\right)^2\right\}^{1/2}}{\left\{\left[\omega_r{}^2 - \omega^2\left(1 + 2R_l C_{\tilde{p}}^{eq} \omega_r \zeta_r\right)\right]^2 + \left[2\zeta_r \omega_r \omega + R_l \omega\left(C_{\tilde{p}}^{eq} \omega_r{}^2 - C_{\tilde{p}}^{eq} \omega^2 + \tilde{\theta}_r^2\right)\right]^2\right\}^{1/2}} \tag{5.11}$$

$$\Psi(\omega, x) = \tan^{-1}\left(\frac{\omega R_l C_{\tilde{p}}^{eq} \sigma_r \phi_r(x)}{\sigma_r \phi_r(x)}\right) - \tan^{-1}\left(\frac{2\zeta_r \omega_r \omega + R_l \omega\left(C_{\tilde{p}}^{eq} \omega_r{}^2 - C_{\tilde{p}}^{eq} \omega^2 + \tilde{\theta}_r^2\right)}{\omega_r{}^2 - \omega^2\left(1 + 2R_l C_{\tilde{p}}^{eq} \omega_r \zeta_r\right)}\right) \tag{5.12}$$

5.1.3 Dimensionless Forms. Some of the terms in the modulus and phase of the voltage FRF can be put into a dimensionless form to give

$$\left|\hat{\alpha}(\tilde{\omega})\right| = \frac{\tilde{\omega}\gamma_r \upsilon_r \left|\sigma_r / \tilde{\theta}_r\right|}{\left\{\left[1 - \tilde{\omega}^2\left(1 + 2\upsilon_r \zeta_r\right)\right]^2 + \left[\left(2\zeta_r + \upsilon_r\left(1 + \gamma_r\right)\right)\tilde{\omega} - \upsilon_r \tilde{\omega}^3\right]^2\right\}^{1/2}} \tag{5.13}$$

$$\Phi(\tilde{\omega}) = \frac{\pi}{2}\operatorname{sgn}\left(\frac{\sigma_r}{\tilde{\theta}_r}\right) - \tan^{-1}\left(\frac{\left(2\zeta_r + \upsilon_r\left(1 + \gamma_r\right)\right)\tilde{\omega} - \upsilon_r \tilde{\omega}^3}{1 - \tilde{\omega}^2\left(1 + 2\upsilon_r \zeta_r\right)}\right) \tag{5.14}$$

Similarly, the modulus and the phase of the tip displacement FRF become

$$\left|\hat{\beta}(\tilde{\omega},x)\right| = \frac{\left|\tilde{f}_r(x)\right|\left\{1+\left(\tilde{\omega}\upsilon_r\right)^2\right\}^{1/2}}{\omega_r^2\left\{\left[1-\tilde{\omega}^2\left(1+2\upsilon_r\zeta_r\right)\right]^2+\left[\left(2\zeta_r+\upsilon_r\left(1+\gamma_r\right)\right)\tilde{\omega}-\upsilon_r\tilde{\omega}^3\right]^2\right\}^{1/2}} \tag{5.15}$$

$$\Psi(\tilde{\omega},x) = \tan^{-1}\left(\frac{\tilde{\omega}\upsilon_r\tilde{f}_r(x)}{\tilde{f}_r(x)}\right) - \tan^{-1}\left(\frac{\left(2\zeta_r+\upsilon_r\left(1+\gamma_r\right)\right)\tilde{\omega}-\upsilon_r\tilde{\omega}^3}{1-\tilde{\omega}^2\left(1+2\upsilon_r\zeta_r\right)}\right) \tag{5.16}$$

In Eqs. (5.13)-(5.16), the dimensionless terms are

$$\upsilon_r = R_l C_{\tilde{p}}^{eq}\omega_r \tag{5.17}$$

$$\gamma_r = \frac{\tilde{\theta}_r^2}{C_{\tilde{p}}^{eq}{\omega_r}^2} \tag{5.18}$$

$$\tilde{\omega} = \frac{\omega}{\omega_r} \tag{5.19}$$

$$\tilde{f}_r(x) = \sigma_r\phi_r(x) \tag{5.20}$$

Note that the voltage modulus given by Eq. (5.113) is dimensional due to $\sigma_r/\tilde{\theta}$ (with the unit of [Vs^2/m]) whereas the tip displacement modulus given by Eq. (5.15) is dimensional due to $1/\omega_r^2$ (and it has the unit of [s^2]).

5.2 Asymptotic Analyses, Resonance Frequencies and Closed-form Expressions for Parameter Identification and Optimization

5.2.1 Short-circuit and Open-circuit Asymptotes of the Voltage FRF. Equation (5.13) can be rewritten as

$$\left|\hat{\alpha}\left(\tilde{\omega}\right)\right| = \frac{\tilde{\omega}\gamma_r\left|\sigma_r/\tilde{\theta}_r\right|}{\left\{\left[\left(1-\tilde{\omega}^2\right)/\upsilon_r - 2\tilde{\omega}^2\zeta_r\right]^2+\left[2\zeta_r\tilde{\omega}/\upsilon_r+\left(1+\gamma_r\right)\tilde{\omega}-\tilde{\omega}^3\right]^2\right\}^{1/2}} \tag{5.21}$$

Taking the limit as $\upsilon_r \to 0$ yields the following expression for very small values of load resistance:*

* Note that, $\upsilon_r \to 0$ implies $R_l \to 0$ (close to short-circuit conditions) and $\upsilon_r \to \infty$ implies $R_l \to \infty$ (close to open-circuit conditions) according to Eq. (5.17).

$$\left|\hat{\alpha}_{sc}\left(\tilde{\omega}\right)\right| = \lim_{\upsilon_r \to 0}\left|\hat{\alpha}\left(\tilde{\omega}\right)\right| = \frac{\tilde{\omega}\gamma_r \upsilon_r \left|\sigma_r / \tilde{\theta}_r\right|}{\left[\left(1-\tilde{\omega}^2\right)^2 + \left(2\zeta_r\tilde{\omega}\right)^2\right]^{1/2}} \tag{5.22}$$

The limit as $\upsilon_r \to \infty$ leads to the following relation for very large values of load resistance:

$$\left|\hat{\alpha}_{oc}\left(\tilde{\omega}\right)\right| = \lim_{\upsilon_r \to \infty}\left|\hat{\alpha}\left(\tilde{\omega}\right)\right| = \frac{\gamma_r \left|\sigma_r / \tilde{\theta}_r\right|}{\left\{\left[\left(1+\gamma_r\right)-\tilde{\omega}^2\right]^2 + \left(2\zeta_r\tilde{\omega}\right)^2\right\}^{1/2}} \tag{5.23}$$

Here, subscripts *sc* and *oc* stand for the *short-circuit* and the *open-circuit* conditions. Equations (5.22) and (5.23) represent the moduli of the voltage FRF for the extreme cases of the load resistance ($R_l \to 0$ and $R_l \to \infty$, respectively). It is useful to note that the short-circuit voltage asymptote depends on the load resistance linearly whereas the open-circuit voltage asymptote does not depend on the load resistance.†

5.2.2 Short-circuit and Open-circuit Asymptotes of the Tip Displacement FRF. The modulus of the tip displacement FRF can be re-expressed to give

$$\left|\hat{\beta}\left(\tilde{\omega},x\right)\right| = \frac{\left|\tilde{f}_r(x)\right|\left(1/\upsilon_r{}^2 + \tilde{\omega}^2\right)^{1/2}}{\omega_r{}^2\left\{\left[\left(1-\tilde{\omega}^2\right)/\upsilon_r - 2\tilde{\omega}^2\zeta_r\right]^2 + \left[2\zeta_r\tilde{\omega}/\upsilon_r + \left(1+\gamma_r\right)\tilde{\omega} - \tilde{\omega}^3\right]^2\right\}^{1/2}} \tag{5.24}$$

The asymptotic FRF behaviors at the short-circuit and the open-circuit conditions are

$$\left|\hat{\beta}_{sc}\left(\tilde{\omega},x\right)\right| = \lim_{\upsilon_r \to 0}\left|\hat{\beta}\left(\tilde{\omega},x\right)\right| = \frac{\left|\tilde{f}_r(x)\right|}{\omega_r{}^2\left[\left(1-\tilde{\omega}^2\right)^2 + \left(2\zeta_r\tilde{\omega}\right)^2\right]^{1/2}} \tag{5.25}$$

$$\left|\hat{\beta}_{oc}\left(\tilde{\omega},x\right)\right| = \lim_{\upsilon_r \to \infty}\left|\hat{\beta}\left(\tilde{\omega},x\right)\right| = \frac{\left|\tilde{f}_r(x)\right|}{\omega_r{}^2\left\{\left[\left(1+\gamma_r\right)-\tilde{\omega}^2\right]^2 + \left(2\zeta_r\tilde{\omega}\right)^2\right\}^{1/2}} \tag{5.26}$$

Note that the short-circuit and the open-circuit asymptotes obtained for the vibration response of the beam do not depend on the load resistance.

† The asymptotes of the current FRFs are not discussed here and they can easily be derived from the voltage asymptotes.

5.2.3 Short-circuit and Open-circuit Resonance Frequencies of the Voltage FRF. Having obtained the modulus of the voltage FRF for electrical loads close to short-circuit conditions, one can find its dimensionless resonance frequency ($\tilde{\omega}_{vsc}^{res}$) as

$$\left.\frac{\partial\left|\hat{\alpha}_{sc}(\tilde{\omega})\right|}{\partial\tilde{\omega}}\right|_{\tilde{\omega}_{vsc}^{res}} = \frac{\partial}{\partial\tilde{\omega}}\left\{\frac{\tilde{\omega}\gamma_r\upsilon_r\left|\sigma_r/\tilde{\theta}_r\right|}{\left[\left(1-\tilde{\omega}^2\right)^2+\left(2\zeta_r\tilde{\omega}\right)^2\right]^{1/2}}\right\}\Bigg|_{\tilde{\omega}_{vsc}^{res}} = 0 \;\rightarrow\; \tilde{\omega}_{vsc}^{res} = 1 \tag{5.27}$$

Therefore the dimensionless resonance frequency ($\tilde{\omega}_{vsc}^{res}$) of the voltage FRF for very low values of load resistance is simply unity.

Similarly, the dimensionless resonance frequency ($\tilde{\omega}_{voc}^{res}$) of the voltage FRF for very large values of load resistance is obtained as

$$\left.\frac{\partial\left|\hat{\alpha}_{oc}(\tilde{\omega})\right|}{\partial\tilde{\omega}}\right|_{\tilde{\omega}_{voc}^{res}} = \frac{\partial}{\partial\tilde{\omega}}\left\{\frac{\gamma_r\left|\sigma_r/\tilde{\theta}_r\right|}{\left\{\left[\left(1+\gamma_r\right)-\tilde{\omega}^2\right]^2+\left(2\zeta_r\tilde{\omega}\right)^2\right\}^{1/2}}\right\}\Bigg|_{\tilde{\omega}_{voc}^{res}} = 0 \;\rightarrow\; \tilde{\omega}_{voc}^{res} = \left(1+\gamma_r-2\zeta_r^2\right)^{1/2} \tag{5.28}$$

5.2.4 Short-circuit and Open-circuit Resonance Frequencies of the Tip Displacement FRF. Using the short-circuit asymptote of the tip displacement FRF, the dimensionless resonance frequency ($\tilde{\omega}_{wsc}^{res}$) of the tip displacement response for very low values of load resistance is obtained as

$$\left.\frac{\partial\left|\hat{\beta}_{sc}(\tilde{\omega},x)\right|}{\partial\tilde{\omega}}\right|_{\tilde{\omega}_{wsc}^{res}} = \frac{\partial}{\partial\tilde{\omega}}\left\{\frac{\left|\tilde{f}_r(x)\right|}{\omega_r{}^2\left[\left(1-\tilde{\omega}^2\right)^2+\left(2\zeta_r\tilde{\omega}\right)^2\right]^{1/2}}\right\}\Bigg|_{\tilde{\omega}_{wsc}^{res}} = 0 \;\rightarrow\; \tilde{\omega}_{wsc}^{res} = \left(1-2\zeta_r^2\right)^{1/2} \tag{5.29}$$

The dimensionless resonance frequency ($\tilde{\omega}_{woc}^{res}$) of the tip displacement FRF for very large values of load resistance is

$$\left.\frac{\partial\left|\hat{\beta}_{oc}(\tilde{\omega},x)\right|}{\partial\tilde{\omega}}\right|_{\tilde{\omega}_{woc}^{res}} = \frac{\partial}{\partial\tilde{\omega}}\left\{\frac{\left|\tilde{f}_r(x)\right|}{\omega_r{}^2\left\{\left[\left(1+\gamma_r\right)-\tilde{\omega}^2\right]^2+\left(2\zeta_r\tilde{\omega}\right)^2\right\}^{1/2}}\right\}\Bigg|_{\tilde{\omega}_{woc}^{res}} = 0 \;\rightarrow\; \tilde{\omega}_{woc}^{res} = \left(1+\gamma_r-2\zeta_r^2\right)^{1/2}$$

(5.30)

Note that, the dimensionless short-circuit resonance frequencies of the voltage and the tip displacement FRFs are *not* the same. The short-circuit resonance frequency of the voltage FRF does *not* depend on mechanical damping whereas the open-circuit resonance frequencies of both FRFs depend on mechanical damping.[‡] Since the short-circuit and the open-circuit resonance frequencies are defined based on the voltage FRF in this work (where the focus is placed on the electrical response), one can express the single-mode approximations of these dimensionless frequencies as

$$\tilde{\omega}_r^{sc} = 1 \tag{5.31}$$

$$\tilde{\omega}_r^{oc} = \left(1 + \gamma_r - 2\zeta_r^2\right)^{1/2} \tag{5.32}$$

The dimensional forms are then

$$\omega_r^{sc} = \omega_r \tag{5.33}$$

$$\omega_r^{oc} = \omega_r \left(1 + \gamma_r - 2\zeta_r^2\right)^{1/2} \tag{5.34}$$

Therefore the resonance frequency shift in the voltage – to – base acceleration FRF as the load resistance is increased from $R_l \to 0$ to $R_l \to \infty$ is

$$\Delta\omega = \omega_r^{oc} - \omega_r^{sc} = \omega_r \left[\left(1 + \gamma_r - 2\zeta_r^2\right)^{1/2} - 1\right] \tag{5.35}$$

According to Eq. (5.35), the resonance frequency shift from the short-circuit to the open-circuit conditions is proportional to γ_r, which means from Eq. (5.18) that it is directly proportional to the square of the electromechanical coupling term ($\tilde{\theta}_r^2$) and inversely proportional to the equivalent capacitance (C_p^{eq}) and square of the undamped natural frequency (ω_r^2). The resonance frequency shift is affected by the modal mechanical damping ratio (ζ_r) as well.

5.2.5 Identification of Modal Mechanical Damping Ratio in the Presence of a Resistive Load. In the electromechanical system, one can identify the mechanical damping ratio either using the voltage FRF or using the vibration FRF. The following derivations provide closed-form expressions for the identification of mechanical damping at $\tilde{\omega} = \tilde{\omega}_{sc}$ in the presence of an

[‡] The mechanically undamped short-circuit and open-circuit natural frequencies of the voltage and tip displacement FRFs, however, are identical, i.e. $\tilde{\omega}_r^{sc} = 1$ and $\tilde{\omega}_r^{oc} = \left(1 + \gamma_r\right)^{1/2}$ for $\zeta_r = 0$.

arbitrary load resistance using both approaches (which can also be given for $\tilde{\omega} = \tilde{\omega}_r^{oc}$ in a similar way).

In order to identify the modal mechanical damping ratio for an arbitrary but non-zero value of υ_r, one can set $\tilde{\omega} = 1$ in the modulus of the voltage FRF given by Eq. (5.13) and obtain

$$\left|\hat{\alpha}(1)\right| = \frac{\gamma_r \upsilon_r \left|\sigma_r / \tilde{\theta}_r\right|}{\left\{\left(2\upsilon_r \zeta_r\right)^2 + \left(2\zeta_r + \upsilon_r \gamma_r\right)^2\right\}^{1/2}} \tag{5.36}$$

where $\left|\hat{\alpha}(1)\right|$ is known from the experimental measurement (i.e. it is the experimental data point used for damping identification). Equation (5.36) yields the following quadratic relation:

$$A\zeta_r^2 + B\zeta_r + C = 0 \tag{5.37}$$

where

$$A = 4\left(1 + \upsilon_r^2\right),\ B = 4\gamma_r \upsilon_r,\ C = \upsilon_r^2 \gamma_r^2 - \left(\frac{\gamma_r \upsilon_r \sigma_r}{\left|\hat{\alpha}(1)\right| \tilde{\theta}_r}\right)^2 \tag{5.38}$$

The positive root of Eq. (5.37) gives the modal mechanical damping ratio as

$$\zeta_r = \frac{\left(B^2 - 4AC\right)^{1/2} - B}{2A} \tag{5.39}$$

Although υ_r (the dimensionless measure of load resistance) is arbitrary in identifying the mechanical damping ratio from the mathematical point of view, physically, it should be large enough so that $\left|\hat{\alpha}(1)\right|$ is a meaningful voltage measurement (i.e. not noise) with acceptable coherence (recall the discussions in Chapter 4).

Identification of the modal mechanical damping from the vibration measurement requires using Eq. (5.15). Let the frequency of interest be $\tilde{\omega} = 1$ again. Equation (5.15) becomes

$$\left|\hat{\beta}(1, x)\right| = \frac{\left|\tilde{f}_r(x)\right|\left(1 + \upsilon_r^2\right)^{1/2}}{\omega_r^2 \left\{\left(2\upsilon_r \zeta_r\right)^2 + \left(2\zeta_r + \upsilon_r \gamma_r\right)^2\right\}^{1/2}} \tag{5.40}$$

which yields the following alternative quadratic equation for ζ_r

$$A\zeta_r^2 + B\zeta_r + C = 0 \tag{5.41}$$

where the coefficients are

$$A = 4\left(1+\upsilon_r^2\right),\ B = 4\gamma_r\upsilon_r,\ C = \upsilon_r^2\gamma_r^2 - \frac{\left|\tilde{f}_r(x)\right|^2\left(1+\upsilon_r^2\right)}{\omega_r^4\left|\hat{\beta}(1,x)\right|^2} \tag{5.42}$$

The modal mechanical damping ratio is the positive root of Eq. (5.41) given by Eq. (5.39). Note that the value of $\left|\hat{\beta}(1,x)\right|$ at point x on the beam is the experimental data point used in the identification process (for $\tilde{\omega}=1$). Unlike the case of mechanical damping identification using the voltage FRF, the external load resistance can be chosen very close to zero here (since such a load does not cause noise in the vibration FRF). Thus, for $\upsilon_r \to 0$, Eq. (5.41) simplifies to the purely mechanical form of

$$\zeta_r = \frac{\left|\tilde{f}_r(x)\right|}{2\omega_r^2\left|\hat{\beta}(1,x)\right|} \tag{5.43}$$

5.2.6 Electrical Power FRF. Using the dimensionless voltage FRF given by Eq. (5.13), the electrical power FRF is obtained as

$$\left|\hat{\Pi}\left(\tilde{\omega}\right)\right| = \frac{\left(\tilde{\omega}\gamma_r\upsilon_r\sigma_r/\tilde{\theta}_r\right)^2/R_l}{\left[1-\tilde{\omega}^2\left(1+2\upsilon_r\zeta_r\right)\right]^2+\left[\left(2\zeta_r+\upsilon_r\left(1+\gamma_r\right)\right)\tilde{\omega}-\upsilon_r\tilde{\omega}^3\right]^2} \tag{5.44}$$

For excitation at the short-circuit resonance frequency ($\tilde{\omega}=1$) the electrical power FRF is

$$\left|\Pi(1)\right| = \frac{\left(\gamma_r\sigma_r/\tilde{\theta}_r\right)^2/R_l}{\left(2\zeta_r\right)^2+\left(2\zeta_r/\upsilon_r+\gamma_r\right)^2} \tag{5.45}$$

and for excitation at the open-circuit resonance frequency ($\tilde{\omega}=\left(1+\gamma_r-2\zeta_r^2\right)^{1/2}$), the electrical power FRF becomes

$$\left|\hat{\Pi}\left(\left(1+\gamma_r-2\zeta_r^2\right)^{1/2}\right)\right| = \frac{\left(\gamma_r\upsilon_r\sigma_r/\tilde{\theta}_r\right)^2/R_l}{\left[1-\left(1+\gamma_r-2\zeta_r^2\right)\left(1+2\upsilon_r\zeta_r\right)\right]^2/\left(1+\gamma_r-2\zeta_r^2\right)+\left[2\zeta_r\left(1+\zeta_r\upsilon_r\right)\right]^2} \tag{5.46}$$

5.2.7 Optimum Values of Load Resistance at the Short-circuit and Open-circuit Resonance Frequencies. Equation (5.44) can be used in order to obtain the optimum load resistance for the maximum electrical power output at a given excitation frequency $\tilde{\omega}$ (around the respective

resonance frequency). The problem of interest is the resonance excitation and one can use Eq. (5.31) for excitation at $\tilde{\omega}=1$ to obtain

$$\left.\frac{\partial\left|\hat{\Pi}(1)\right|}{\partial R_l}\right|_{R_l^{opt,\tilde{\omega}=1}}=0 \quad \rightarrow \quad R_l^{opt,\tilde{\omega}=1}=\frac{1}{\omega_r C_{\tilde{p}}^{eq}\left[1+\left(\gamma_r/2\zeta_r\right)^2\right]^{1/2}} \tag{5.47}$$

which is the optimum load resistance for excitation at the short-circuit resonance frequency. A similar practice can be followed for estimating the optimum load resistance for excitation at the open-circuit resonance frequency as

$$\left.\frac{\partial\left|\hat{\Pi}\left(\left(1+\gamma_r-2\zeta_r^2\right)^{1/2}\right)\right|}{\partial R_l}\right|_{R_l^{opt,\tilde{\omega}=\left(1+\gamma_r-2\zeta_r^2\right)^{1/2}}}=0 \quad \rightarrow \quad R_l^{\tilde{\omega}=\left(1+\gamma_r-2\zeta_r^2\right)^{1/2}}=\frac{1}{\omega_r C_{\tilde{p}}^{eq}}\left[\frac{1-\zeta_r^2+\left(\gamma_r/2\zeta_r\right)^2}{\left(1+\gamma_r-\zeta_r^2\right)\left(1+\gamma_r-2\zeta_r^2\right)}\right]^{1/2} \tag{5.48}$$

For excitations at the short-circuit and the open-circuit resonance frequencies, the optimum values of load resistance are inversely proportional to the capacitance and the undamped natural frequency. The electromechanical coupling and the mechanical damping ratio also affect the optimum load resistance. The optimum resistive loads obtained in Eqs. (5.47) and (5.48) can be back substituted into Eqs. (5.45) and (5.46) to obtain the maximum power expressions for excitations at these two frequencies.

5.2.8 Vibration Attenuation from the Short-circuit to the Open-circuit Conditions. Consider the asymptotic vibration response FRFs defined for point *x* on the beam given by Eqs. (5.25) and (5.26). The ratio of the response amplitude at the open-circuit conditions to the response amplitude at the short-circuit conditions at frequency $\tilde{\omega}$ is

$$\frac{\left|\hat{\beta}_{oc}(\tilde{\omega},x)\right|}{\left|\hat{\beta}_{sc}(\tilde{\omega},x)\right|}=\frac{\left[\left(1-\tilde{\omega}^2\right)^2+\left(2\zeta_r\tilde{\omega}\right)^2\right]^{1/2}}{\left\{\left[\left(1+\gamma_r\right)-\tilde{\omega}^2\right]^2+\left(2\zeta_r\tilde{\omega}\right)^2\right\}^{1/2}} \tag{5.49}$$

Therefore the percentage variation of the vibration amplitude as the load resistance is increased from $R_l\rightarrow 0$ to $R_l\rightarrow\infty$ is

$$\delta_w(\tilde{\omega}) = \left\langle \frac{\left[\left(1-\tilde{\omega}^2\right)^2 + \left(2\zeta_r\tilde{\omega}\right)^2\right]^{1/2}}{\left\{\left[\left(1+\gamma_r\right)-\tilde{\omega}^2\right]^2 + \left(2\zeta_r\tilde{\omega}\right)^2\right\}^{1/2}} - 1 \right\rangle \times 100 \tag{5.50}$$

For excitation at the short-circuit resonance frequency ($\tilde{\omega}=1$):

$$\frac{\left|\hat{\beta}_{oc}(1,x)\right|}{\left|\hat{\beta}_{sc}(1,x)\right|} = \frac{1}{\left[1+\left(\gamma_r/2\zeta_r\right)^2\right]^{1/2}} \tag{5.51}$$

yielding a percentage vibration attenuation of

$$\delta_w(1) = \left[\frac{1}{\left(1+\gamma_r{}^2/4\zeta_r{}^2\right)^{1/2}} - 1\right] \times 100 \tag{5.52}$$

The percentage of vibration amplification for excitation at the open-circuit resonance frequency (due to an increase of the load resistance from $R_l \to 0$ to $R_l \to \infty$) can be obtained by substituting $\tilde{\omega} = \left(1+\gamma_r-2\zeta_r^2\right)^{1/2}$ into Eq. (5.49) as

$$\frac{\left|\hat{\beta}_{oc}\left(\left(1+\gamma_r-2\zeta_r^2\right)^{1/2},x\right)\right|}{\left|\hat{\beta}_{sc}\left(\left(1+\gamma_r-2\zeta_r^2\right)^{1/2},x\right)\right|} = \frac{\left[\left(\gamma_r-2\zeta_r^2\right)^2 + \left(2\zeta_r\right)^2\left(1+\gamma_r-2\zeta_r^2\right)\right]^{1/2}}{\left[\left(2\zeta_r^2\right)^2 + \left(2\zeta_r\right)^2\left(1+\gamma_r-2\zeta_r^2\right)\right]^{1/2}} = \left[\frac{\left(\gamma_r/2\zeta_r\right)^2+1-\zeta_r^2}{1+\gamma_r-\zeta_r^2}\right]^{1/2} \tag{5.53}$$

Hence the percentage vibration amplification at the open-circuit resonance frequency is

$$\delta_w\left(\left(1+\gamma_r-2\zeta_r^2\right)^{1/2}\right) = \left\{\left[\frac{\left(\gamma_r/2\zeta_r\right)^2+1-\zeta_r^2}{1+\gamma_r-\zeta_r^2}\right]^{1/2} - 1\right\} \times 100 \tag{5.54}$$

5.3 Intersection of the Voltage Asymptotes and a Simple Technique for Identification of the Optimum Load Resistance from Experimental Measurements

5.3.1 On the Intersection of the Voltage Asymptotes for Resonance Excitation. It was noticed both in the theoretical case study of Chapter 3 and in the experimental case studies of Chapter 4 that the asymptotic trends in the voltage FRF are linear, in agreement with Eqs. (5.22) and (5.23). This observation leads to an interesting result if one further examines these linear asymptotes at the short-circuit and the open-circuit resonance frequencies.

Substituting $\tilde{\omega}=1$ into the short-circuit voltage asymptote gives

$$\left|\hat{\alpha}_{sc}(1)\right|=\frac{\gamma_r\upsilon_r\left|\sigma_r/\tilde{\theta}_r\right|}{2\zeta_r} \tag{5.55}$$

Similarly, substituting $\tilde{\omega}=1$ into the open-circuit voltage asymptote yields

$$\left|\hat{\alpha}_{oc}(1)\right|=\frac{\gamma_r\left|\sigma_r/\tilde{\theta}_r\right|}{\left[\left(1+\gamma_r\right)^2+\left(2\zeta_r\right)^2\right]^{1/2}} \tag{5.56}$$

Clearly, these asymptotes intersect at a finite but non-zero value of the dimensionless load resistance

$$\left|\hat{\alpha}_{sc}(1)\right|=\left|\hat{\alpha}_{oc}(1)\right| \;\rightarrow\; \upsilon_r=\frac{2\zeta_r}{\left[\gamma_r^2+\left(2\zeta_r\right)^2\right]^{1/2}} \tag{5.57}$$

and the dimensional form of this load resistance is

$$R_l=\frac{1}{\omega_r C_{\tilde{p}}^{eq}\left[1+\left(\gamma_r/2\zeta_r\right)\right]^{1/2}} \tag{5.58}$$

which is nothing but the optimum load resistance for excitation at the short-circuit resonance frequency as derived from the power FRF in Eq. (5.47).

Substituting $\tilde{\omega}=\left(1+\gamma_r-2\zeta_r^2\right)^{1/2}$ into the short-circuit voltage asymptote gives

$$\left|\hat{\alpha}_{sc}\left(\left(1+\gamma_r-2\zeta_r^2\right)^{1/2}\right)\right|=\frac{\left(1+\gamma_r-2\zeta_r^2\right)^{1/2}\gamma_r\upsilon_r\left|\sigma_r/\tilde{\theta}_r\right|}{\left[\left(\gamma_r-2\zeta_r^2\right)^2+\left(2\zeta_r\right)^2\left(1+\gamma_r-2\zeta_r^2\right)\right]^{1/2}}=\frac{\left(1+\gamma_r-2\zeta_r^2\right)^{1/2}\gamma_r\upsilon_r\left|\sigma_r/\tilde{\theta}_r\right|}{\left(\gamma_r^2+4\zeta_r^2-4\zeta_r^4\right)^{1/2}} \tag{5.59}$$

Likewise, using $\tilde{\omega}=\left(1+\gamma_r-2\zeta_r^2\right)^{1/2}$ in the open-circuit voltage results in

$$\left|\hat{\alpha}_{oc}\left(\left(1+\gamma_r-2\zeta_r^2\right)^{1/2}\right)\right|=\frac{\gamma_r\left|\sigma_r/\tilde{\theta}_r\right|}{\left[\left(2\zeta_r^2\right)^2+\left(2\zeta_r\right)^2\left(1+\gamma_r-2\zeta_r^2\right)\right]^{1/2}}=\frac{\gamma_r\left|\sigma_r/\tilde{\theta}_r\right|}{\left(4\zeta_r^2+4\gamma_r\zeta_r^2-4\zeta_r^4\right)^{1/2}} \tag{5.60}$$

The intersection of the voltage asymptotes for excitation and the open-circuit resonance frequency gives

$$\left|\hat{\alpha}_{sc}\left(\left(1+\gamma_r-2\zeta_r^2\right)^{1/2}\right)\right|=\left|\hat{\alpha}_{oc}\left(\left(1+\gamma_r-2\zeta_r^2\right)^{1/2}\right)\right| \;\rightarrow\; \upsilon_r=\left[\frac{1-\zeta_r^2+\left(\gamma_r/2\zeta_r\right)^2}{\left(1+\gamma_r-\zeta_r^2\right)\left(1+\gamma_r-2\zeta_r^2\right)}\right]^{1/2} \tag{5.61}$$

which has the dimensional form of

$$R_l = \frac{1}{\omega_r C_{\tilde{p}}^{eq}} \left[\frac{1-\zeta_r^2+\left(\gamma_r / 2\zeta_r\right)^2}{\left(1+\gamma_r-\zeta_r^2\right)\left(1+\gamma_r-2\zeta_r^2\right)} \right]^{1/2} \tag{5.62}$$

The load resistance of the intersection point given by Equation (5.62) is the optimum load resistance for excitation at the open-circuit resonance frequency as derived in Eq. (5.48).

5.3.2 A Simple Technique for the Experimental Identification of the Optimum Load Resistance for Resonance Excitation. The observation given in the previous section leads to a very simple technique for identifying the optimum load from the experimental voltage measurements at $\tilde{\omega}=1$ or at $\tilde{\omega}=\left(1+\gamma_r-2\zeta_r^2\right)^{1/2}$. It is often required to do a resistor sweep to identify the optimum load resistance in the experiments. Either a variable resistor or a set of several resistors is used for this purpose (as done in Chapter 4). Based on the observation given in the previous section, a technique for identifying the optimum load resistance using only one resistor along with an open-circuit voltage measurement is proposed here.

It is noted in the previous section is that the intersections of the voltage asymptotes for excitations at the short-circuit and the open-circuit resonance frequencies correspond to the respective optimum loads. Suppose that the experimentalist has fixed the excitation frequency to one of these two frequencies for identifying the optimum load resistance under a certain excitation amplitude. The horizontal asymptote of the open-circuit conditions is simply obtained from the open-circuit voltage measurement (a horizontal line with the amplitude of v_{oc}). Then, a low value of resistance is chosen (R_l^*), and the respective voltage output (v^*) is measured.[§] Since the voltage output for zero load resistance (starting point of the short-circuit asymptote) is zero, one has the short-circuit asymptote, which has a slope of v^* / R_l^*. The value of load resistance for which this line intersects the open-circuit voltage amplitude is the optimum load resistance. The

[§] This test resistor of relatively low resistance should be on the linear asymptote. That is, it should be considerably lower than the optimum load (which is unknown). Usually, for configurations similar to the ones covered in the experimental cases of Chapter 4, a resistive load in the range of 10-100 Ω is sufficiently low. One can check with two different (low-valued) resistive loads to guarantee that the slope (v^* / R_l^*) is the same (so that the measurements are noise-free and on the linear asymptote).

problem is reduced to a problem of two similar triangles as depicted in Fig. 5.1. The optimum load resistance is obtained from this schematic as

$$R_l^{opt} = \frac{v_{oc}}{v^*} R_l^* \tag{5.63}$$

For an accurate open-circuit voltage measurement and a resistor chosen in the region of the linear asymptote, the foregoing approach provides predictions with very good accuracy (both at the short-circuit and the open-circuit resonance frequencies). In order to check the accuracy, one can repeat the experiment for a second resistor and compare the results or do a fine tuning around the identified value.

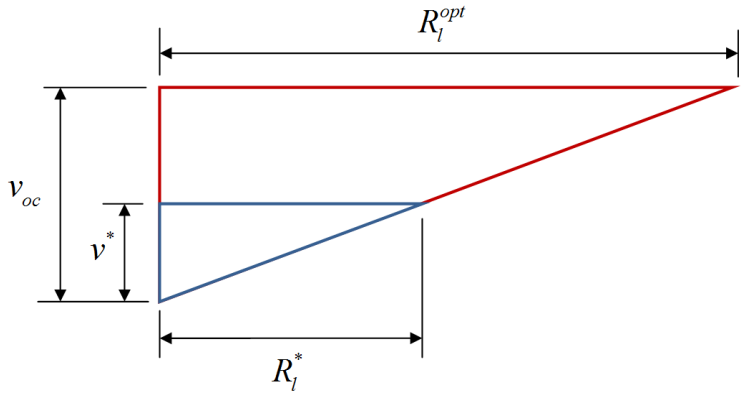

Fig. 5.1 Similar triangles describing the relationship between the voltage measurement (v^*) at a low value of load resistance (R_l^*), the open-circuit voltage output (v_{oc}) and the optimum load resistance (R_l^{opt}) for excitation at the short-circuit or open-circuit resonance frequency

5.4 Experimental Validations for a PZT-5H Bimorph Cantilever

This section revisits the case study for the PZT-5H bimorph cantilever of Section 4.1 (Fig. 5.2) for validation of the major single-mode relations derived in this chapter. Therefore the details related to this setup and the bimorph can be found in Chapter 4. Note that the following study focuses on the fundamental vibration mode ($r = 1$ in the single-mode equations).

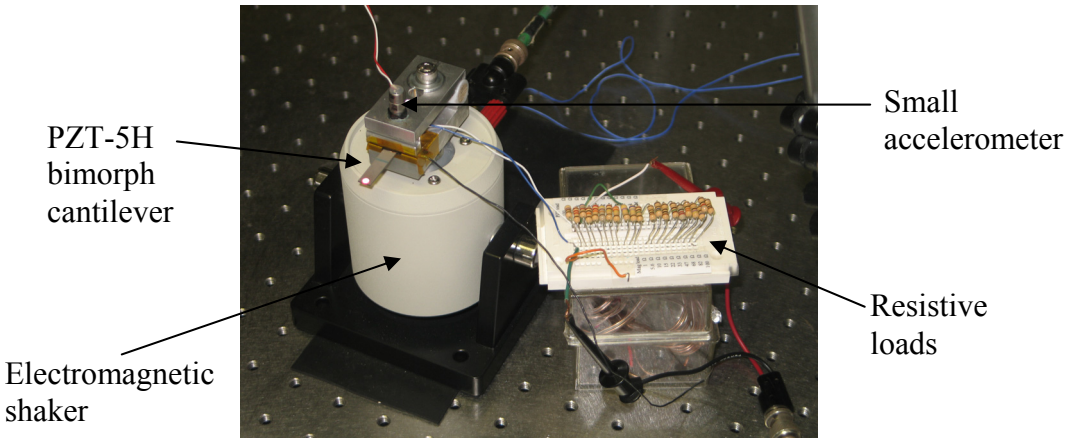

Fig. 5.2 PZT-5H bimorph cantilever without a tip mass under base excitation (revisited – photo by A. Erturk, 2009)

5.4.1 Identification of Mechanical Damping. As an alternative to identifying the mechanical damping ratio graphically by matching the peaks in the vibration FRF, here the voltage FRF is used along with the closed-form expression given by Eq. (5.39). For a resistive load of $470\,\Omega$, the experimental voltage amplitude at the short-circuit resonance frequency is 0.148 V/*g*. Therefore the experimental data point is $\left|\hat{\alpha}(1)\right| = 0.148/9.81 = 0.0151\,\text{Vs}^2/\text{m}$. For this resistive load and the remaining system parameters, the coefficients in Eq. (5.37) are $A = 2.2857\times10^7$, $B = 899.097$, and $C = -1.5705\times10^7$. For these numbers, the modal mechanical damping ratio is obtained as $\zeta_1 = 0.00880$ which is very close to the one obtained in Section 4.1 by matching the peak amplitude of the vibration FRF using the multi-mode solution ($\zeta_1 = 0.00874$).

5.4.2 Fundamental Short-circuit and Open-circuit Resonance Frequencies. The fundamental short-circuit resonance frequency (or the voltage FRF) is simply the undamped natural frequency of the cantilever as obtained in Eq. (5.34): $\omega_1^{sc} = \omega_1$. The model predicts this frequency as $f_1^{sc} = 502.6\,\text{Hz}$ (where $f_r^{sc} = \omega_r^{sc}/2\pi$). According to Eq. (5.34), the fundamental open-circuit resonance frequency depends on γ_1 in addition to ζ_1. For the given system parameters, one obtains $\gamma_1 = 0.0940$ from Eq. (5.18). The fundamental open-circuit resonance frequency is then $f_1^{oc} = 525.7\,\text{Hz}$ (from $\tilde{\omega}_1^{oc} = 1.0459$). This frequency overestimates the experimental value (524.7

Hz) and the multi-mode analytical value (524.5 Hz). The reason single-mode solution deviates from the multi-mode solution is the effect of the residuals of the neighboring modes which are excluded in this approximation (and this is what makes the single-mode solution an approximation). The relative errors in the single-mode short-circuit and the open-circuit resonance frequencies are +0.02 % and +0.2 %, respectively.

5.4.3 Amplitude and Phase of the Voltage FRF. The modulus and phase diagrams of the voltage FRFs for three different resistive loads (1.2 $k\Omega$, 44.9 $k\Omega$ and 995 $k\Omega$) are obtained and compared against the experimental and the multi-mode model results. Figures 5.3a and 5.3b, respectively, are plotted using Eqs. (5.8) and (5.9) with the damping ratio identified using a single data point of the voltage FRF for 470 Ω (Section 5.4.1). The modulus expression given by Eq. (5.8) predicts the experimental voltage amplitude successfully in Fig. 5.3a, and the slight inaccuracy is for the largest resistive load (due to the 0.2 % overestimation of the open-circuit resonance frequency). The phase diagrams of these curves are also predicted very well for all of these three resistive loads in Fig. 5.3b. It should be noted that these phase curves intersect each other at the fundamental short-circuit and open-circuit resonance frequencies.

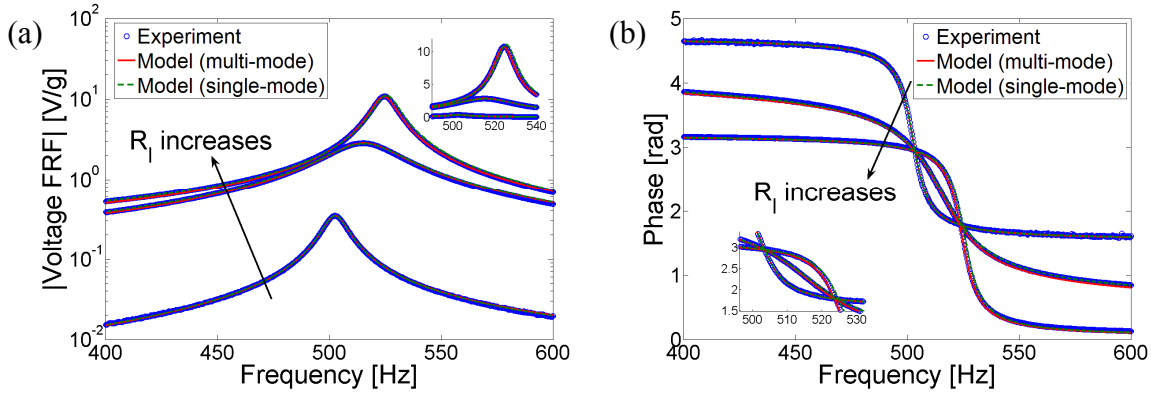

Fig. 5.3 (a) Amplitude and (b) phase diagrams of the voltage FRF for three different resistive loads: 1.2 $k\Omega$, 44.9 $k\Omega$ and 995 $k\Omega$ (experimental measurement, analytical multi-mode solution and analytical single-mode solution)

5.4.4 Voltage Asymptotes for Resonance Excitation. For excitations the fundamental short-circuit resonance frequency, the short-circuit and the open-circuit voltage asymptotes are

obtained using Eqs. (5.55) and (5.56), respectively. Variation of the single-mode voltage output with load resistance predicted using $\tilde{\omega}=1$ in Eq. (5.21) is plotted in Fig. 5.4a along with the linear asymptotes. The prediction of the single-mode expressions agrees very well with the multi-mode solution and the experimental data. The short-circuit and the open-circuit asymptotes successfully represent the limiting trends as $R_l \to 0$ and $R_l \to \infty$. Equation (5.21) is plotted against load resistance for $\tilde{\omega}=1.0459$ in Fig. 5.4b. The resulting single-mode curve exhibits good agreement with the multi-mode solution and the experimental data points. Both the single-mode and multi-mode solutions as well as the experimental data points follow the single-mode asymptotes closely for $R_l \to 0$ and $R_l \to \infty$.

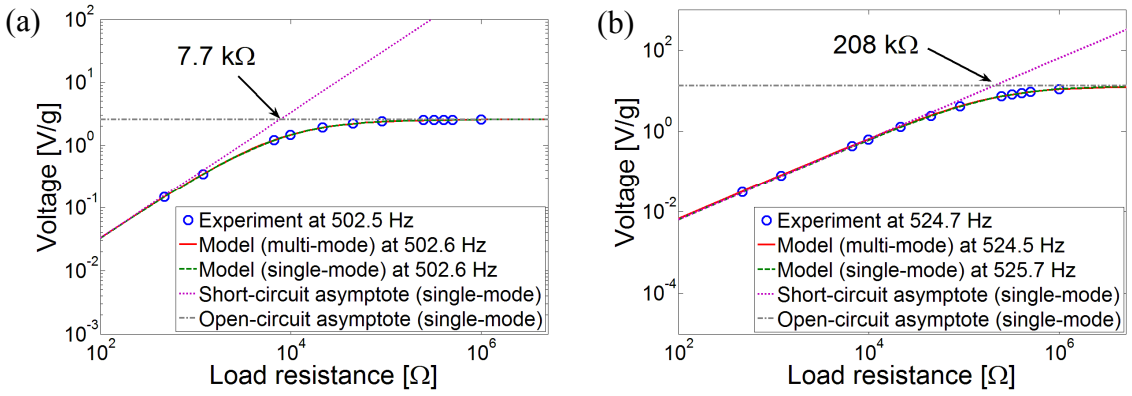

Fig. 5.4 Voltage versus load resistance diagrams for excitations (a) at the short-circuit resonance frequency and (b) at the-open circuit resonance frequency (experimental measurements, analytical multi-mode solution, analytical single-mode solution and single-mode asymptotes)

The accuracy of the single-mode prediction is better in Fig. 5.4a compared to its accuracy in Fig. 5.4b (because the single-mode prediction of the open-circuit resonance is slightly more inaccurate). The values of load resistance at the intersections of the short-circuit and the open-circuit asymptotes in Figs. 5.4a and 5.4b as 7.7 kΩ and 208 kΩ, respectively. These are expected to be the single-mode estimates of the optimum load resistance for excitations at the fundamental short-circuit and open-circuit resonance frequencies as mathematically shown in Section 5.3.1.

5.4.5 Power vs. Load Resistance Diagrams and the Optimum Loads. Variation of the single-mode power prediction with load resistance for excitation at the fundamental short-circuit resonance frequency is obtained by using $\tilde{\omega}=1$ in Eq. (5.44). Similarly, substituting $\tilde{\omega}=1.0459$ into the same equation gives the single-mode power prediction at the fundamental open-circuit resonance frequency. These predictions are plotted in Figs. 5.5a and 5.5b, respectively, and both of them exhibit good agreement with the multi-mode solutions and the experimental data points. The slight inaccuracy in Fig. 5.5b is relatively distinguishable and it is because the single-mode predictions around the open-circuit resonance are less accurate.

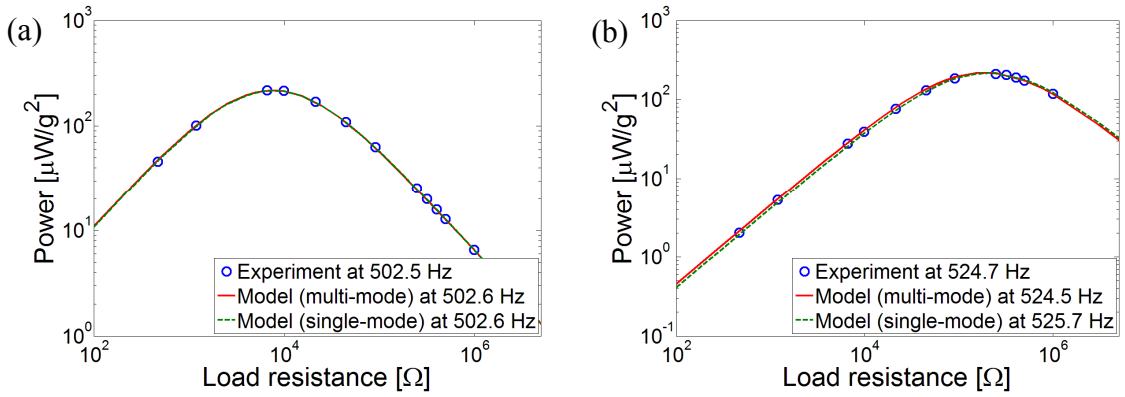

Fig. 5.5 Voltage versus load resistance diagrams for excitations (a) at the short-circuit resonance frequency and (b) at the-open circuit resonance frequency (experimental measurements, analytical multi-mode solution, analytical single-mode solution, single-mode asymptotes)

The optimum values of load resistance for excitations at the short-circuit and the open-circit resonance frequencies are calculated by using Eqs. (5.47) and (5.48) as 7.7 $\mathrm{k}\Omega$ and 208 $\mathrm{k}\Omega$, respectively. Therefore, for excitation at the fundamental short-circuit resonance frequency, the single-mode estimate of the optimum load resistance is 7.7 $\mathrm{k}\Omega$ whereas for excitation at the fundamental open-circuit resonance frequency, the single-mode estimate of the optimum load resistance is 208 $\mathrm{k}\Omega$. These values overestimate the multi-mode estimates of 7.6 $\mathrm{k}\Omega$ and 189 $\mathrm{k}\Omega$, respectively (referred from Section 4.1.3).

5.4.6 Comment on the Optimum Load Resistance obtained from the Norton and Thévenin Representations of a Piezoceramic Layer. A frequently referred expression for the optimum

load resistance ($R_l^{opt} = 1/\omega_r C_{\tilde{p}}^{eq}$, e.g. in references [9,18]) gives the optimum values of load resistance for this cantilever at the fundamental short-circuit and open-circuit resonance frequencies as 41.8 $\mathrm{k}\Omega$ and 40.1 $\mathrm{k}\Omega$ (which are highly inaccurate compared to multi-mode predictions of 7.6 $\mathrm{k}\Omega$ and 189 $\mathrm{k}\Omega$ or the single-mode predictions of 7.7 $\mathrm{k}\Omega$ and 208 $\mathrm{k}\Omega$, respectively). The reason of this inaccuracy is the thermodynamic inconsistency behind the equation $R_l^{opt} = 1/\omega_r C_{\tilde{p}}^{eq}$. This expression is obtained for the simple electrical engineering representation of a piezoceramic layer as an electrical source: either a *current source in parallel with its internal capacitance* (Norton representation) or a *voltage source in series with its internal capacitance* (Thévenin representation). One should note that the Norton representation was reached in the derivations steps of the analytical model (Fig. 3.2b). In Fig. 3.2b, if one assumes a constant current amplitude oscillating at frequency ω_r (i.e. $i_p(t) = I_p e^{j\omega_r t}$) and proceeds to obtain the optimum load for maximum power generation using the circuit equation, that load turns out to be $R_l^{opt} = 1/\omega_r C_{\tilde{p}}^{eq}$. However, note that the electric current in Eq. (3.28) is a function of the velocity response of the structure due to Eq. (3.29). Therefore, the current source in this Norton representation is *not* constant and it strongly depends on the load resistance because the vibration response strongly depends on the load resistance as shown both theoretically and experimentally in Chapters 3 and 4. Therefore, using $R_l^{opt} = 1/\omega_r C_{\tilde{p}}^{eq}$ implies that there is no shunt damping effect in the structure, i.e. there is no converse piezoelectric effect although one generates electricity with the direct piezoelectric effect. A figure demonstrating the meaning of ignoring piezoelectric coupling in the mechanical equation is shown in Fig. 5.6 for excitation at the fundamental short-circuit resonance frequency of the cantilever discussed here. As the load resistance is changed from the smallest load to the largest load, the correct peak of the power in the FRF increases, moves to the right (on the frequency axis) and then decreases. This trend is completely due to the feedback received in the mechanical domain. If the electrical term in the mechanical domain was artificially set equal to zero to simulate the aforementioned inconsistent scenario, the dashed curves in Figs. 5.6a and 5.6b are obtained. Therefore, if the piezoelectric coupling in the mechanical equation is ignored, the power amplitude in Fig. 5.6a increases much more than the real case (and there is no frequency shift). Indeed, when the variation of the peak power with load resistance is plotted as shown in Fig. 5.6, the optimum load

resistance turns out to be this incorrect estimate ($R_l^{opt} = 1/\omega_r C_{\tilde{p}}^{eq}$) and the peak power is orders of magnitude larger than the experimental measurement as well as the model prediction with backward coupling in the mechanical equation.

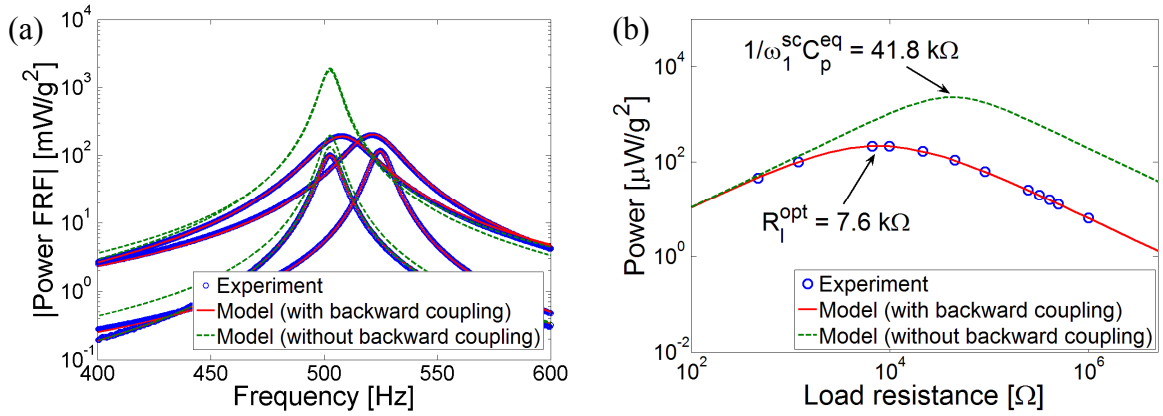

Figure 5.6 Comparison of the coupled and uncoupled distributed-parameter model predictions; (a) electrical power FRFs for 4 different resistive loads and (b) variation of the electrical power amplitude with load resistance for resonance excitation

5.5 Summary and Conclusions

Detailed mathematical analyses of the single-mode electromechanical relations are presented. Focus is placed on the voltage output and vibration response FRFs per translational base acceleration input. The complex forms single-mode relations derived in Chapter 3 (based on the multi-mode solutions) are first expressed in the modulus-phase form and then they are represented with dimensionless terms. After expressing the asymptotic trends of the single voltage and tip displacement FRFs, closed-form expressions are obtained for their short-circuit and open-circuit resonance frequencies. It is shown that the short-circuit resonance frequencies of the voltage FRF and the tip displacement FRF are slightly different. The linear asymptotes of the voltage and tip displacement for the extreme conditions of the load resistance (observed in the previous chapters) are mathematically verified here. Closed-form expressions for the optimum electrical loads for the maximum power generation at the short-circuit and the open-circuit resonance frequencies at extracted. It is shown that, for excitations at these two

frequencies, the intersections of the linear voltage asymptotes correspond to the respective optimum load resistance. Based on this observation, a simple technique is introduced to identify the optimum load resistance of a piezoelectric energy harvester using a single resistive load along with an open circuit voltage measurement. Relations are given to estimate the variation of the tip vibration response as the load resistance is changed between the two extreme conditions. The experimental case study for a PZT-5H bimorph is revisited and the major closed-form relations derived here are validated. An important issue related to estimation of the optimum load resistance from the Norton and Thévenin representations of the piezoceramic is clarified.

CHAPTER 6

EFFECTS OF MATERIAL CONSTANTS AND MECHANICAL DAMPING ON PIEZOELECTRIC ENERGY HARVESTING – A COMPARATIVE STUDY

This chapter investigates the effects of material constants and mechanical damping on piezoelectric energy harvesting. The discussion is given here with a focus on the most popular monolithic piezoceramics (PZT-5A and PZT-5H) and the novel single crystals (PMN-PT and PMN-PZT).[*] The motivation of the following analysis is to understand the effects of piezoelectric, elastic and dielectric constants as well as mechanical damping on piezoelectric power generation and to clarify whether or not the substantially large piezoelectric strain constants (particularly the d_{31} constant) of single crystals result in a substantially large power generation performance compared to commonly employed monolithic piezoceramics. It is therefore aimed to check whether the well-known d_{31} constant alone is a sufficient parameter to choose an active material for piezoelectric energy harvesting. The performance comparisons made for this purpose are presented for PZT-5A, PZT-5H, PMN-PT (with 30% PT), PMN-PT (with 33% PT) and PMN-PZT type piezoelectric materials. Piezoelectric, elastic and dielectric properties of these active materials differ from each other considerably. Individual effects of these properties are investigated using the analytical model developed in this dissertation. The reduced properties of these piezoelectric materials are obtained based on the plane-stress assumption for a thin beam. The plane-stress constants are compared and the importance of the elastic compliance as well as its effect on the reduced piezoelectric constant are highlighted. The effect of mechanical damping on piezoelectric power generation is also discussed. An experimental comparison between a PZT-5A bimorph and a PZT-5H bimorph is given in order to verify some of the conclusions drawn here based on the analytical model simulations.

[*] PMN stands for *lead magnesium niobate*.

6.1 Properties of Typical Monolithic Piezoceramics and Single Crystals

Typical properties of monolithic PZT-5A and PZT-5H can be found in several sources on the web [62] or the literature [63] and their data are listed in Appendix B. At room temperature, PZT-5A has $d_{31} = -171\,\text{pm/V}$ (piezoelectric constant), $s_{11}^E = 16.4\,\text{pm}^2/\text{N}$ (elastic compliance) and $\varepsilon_{33}^T / \varepsilon_0 = 1700$ (dielectric constant) whereas PZT-5A has $d_{31} = -274\,\text{pm/V}$, $s_{11}^E = 16.5\,\text{pm}^2/\text{N}$ and $\varepsilon_{33}^T / \varepsilon_0 = 3400$ (where $\varepsilon_0 = 8.854\,\text{pF/m}$ is the absolute permittivity of free space [26]).

The single-crystal technology is relatively new compared to the conventional PZT-5A and PZT-5H monolithic piezoceramics which are widely used in engineering applications. Limited literature is available for the material data of single-crystal piezoceramics. Cao et al. [64] reported the relevant constants for a PMN-PT with 30% PT as $d_{31} = -921\,\text{pm/V}$, $s_{11}^E = 52\,\text{pm}^2/\text{N}$ and $\varepsilon_{33}^T / \varepsilon_0 = 7800$ whereas they reported $d_{31} = -1330\,\text{pm/V}$, $s_{11}^E = 69\,\text{pm}^2/\text{N}$ and $\varepsilon_{33}^T / \varepsilon_0 = 8200$ for a PMN-PT with 33% PT. Properties of a relatively new single crystal PMN-PZT are reported by the manufacturer [65] as (product: CPSC200-115) as $d_{31} = -2252\,\text{pm/V}$, $s_{11}^E = 127\,\text{pm}^2/\text{N}$ and $\varepsilon_{33}^T / \varepsilon_0 = 5000$.[†]

The relevant piezoelectric, elastic and dielectric data of these five different piezoelectric materials (PZT-5A, PZT-5H, PMN-PT with 30% PT, PMN-PT with 33% PT and PMN-PZT) are listed in Tables 6.1 and 6.2 along with the average value of each property. The mass densities of these piezoceramics are also given in Table 6.2. The effective piezoelectric, elastic and dielectric terms for the plane-stress conditions of a thin beam are also obtained (Appendix A.2) since the reduced forms of the three-dimensional constants determine the performance of a thin generator.

As can be seen in Fig. 6.1, the piezoelectric constant d_{31} increases by more than an order of magnitude from PZT-5A to PMN-PZT. It is observed that the large d_{31} constant comes with large elastic compliance as plotted in Fig. 6.2. Approximately an order of magnitude difference is seen between the elastic compliance values of PZT-5A to PMN-PZT.

[†] Composition of this PMN-PZT [65] is the company's proprietary information.

Table 6.1 Piezoelectric and elastic properties of different piezoceramics

	d_{31} [pm/V]	s_{11}^E [pm^2/N]	$\overline{e}_{31}$ [C/m^2]
PZT-5A	-171	16.4	-10.4
PZT-5H	-274	16.5	-16.6
PMN-PT (30% PT)	-921	52	-17.7
PMN-PT (33% PT)	-1330	69	-19.3
PMN-PZT	-2252	127	-17.7
Average	**-989.6**	**56.2**	**-16.3**

Table 6.2 Mass densities and dielectric constants of different piezoceramics

	ρ [kg/m^3]	$\varepsilon_{33}^T / \varepsilon_0$	$\overline{\varepsilon}_{33}^S$ [nF/m]
PZT-5A	7750	1700	13.3
PZT-5H	7500	3400	25.6
PMN-PT (30% PT)	8040	7800	52.7
PMN-PT (33% PT)	8060	8200	47.0
PMN-PZT	7900	5000	4.34
Average	**7850**	**5220**	**28.6**

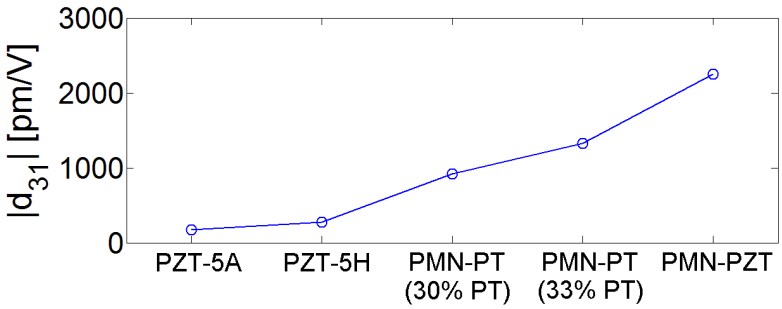

Fig. 6.1 Variation of the piezoelectric strain constant for different piezoceramics

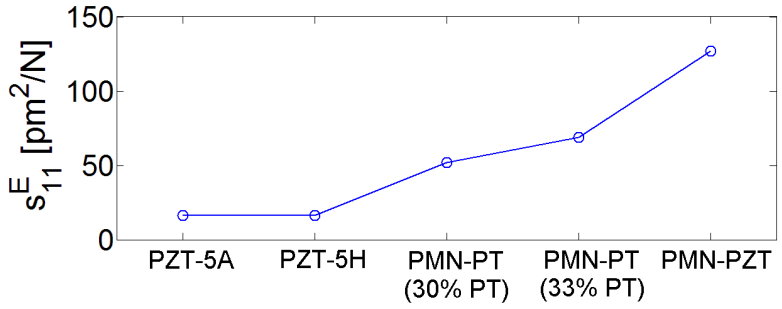

Fig. 6.2 Variation of the elastic compliance for different piezoceramics

6.2 Reduced Piezoelectric, Elastic and Permittivity Constants for a Thin Beam

For the plane-stress conditions of a thin beam, the elastic modulus at constant electric field is obtained from $\overline{c}_{11}^E = 1/s_{11}^E$ whereas the effective piezoelectric stress constant is obtained from $\overline{e}_{31} = d_{31}/s_{11}^E$ (Appendix A.2). It is important to note that $\overline{e}_{31}$ is the piezoelectric constant that appears in the reduced (plane-stress) piezoelectric constitutive relations of the analytical model (Chapter 3). The elastic modulus at constant electric field is simply the reciprocal of the elastic compliance shown in Fig. 6.2 and it is plotted in Fig. 6.3 for different piezoceramics. Clearly, the single-crystal piezoceramics with large d_{31} constants have low elastic moduli. Since it is the product of d_{31} and $\overline{c}_{11}^E$ (which exhibit opposite trends in Figs. 6.1 and 6.3), the plane-stress piezoelectric constant $\overline{e}_{31}$ for the piezoceramics considered here have values of the same order of magnitude (Fig. 6.4). For instance, even though the d_{31} constant of PMN-PZT is more than 10 times that of PZT-5A, its $\overline{e}_{31}$ constant is only 1.7 times that of the latter. From the mathematical point of view, d_{31} never appears alone in the formulation given in Chapter 3. It is the $\overline{e}_{31}$ constant that appears in the coupling terms (i.e. the multiplication of d_{31} and $\overline{c}_{11}^E$ for a thin beam). For this reason, very large d_{31} constants of single-crystal piezoceramics might *not* necessarily imply very large power generation performance as the stiffness of the piezoceramic affects the resulting electromechanical coupling. The PMN-PT with 33% PT has the largest $\overline{e}_{31}$ among the samples considered here.

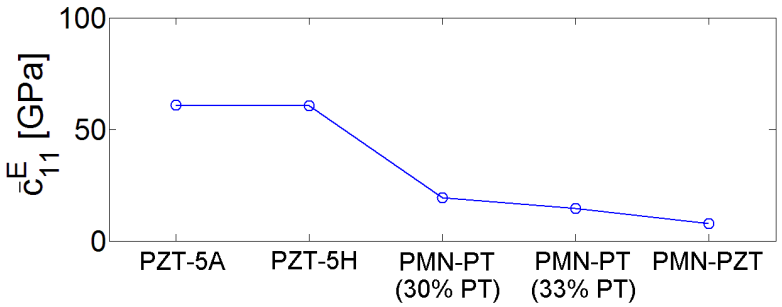

Fig. 6.3 Variation of the reduced elastic modulus for different piezoceramics

Variation of the plane-stress permittivity at constant strain (obtained from $\bar{\varepsilon}_{33}^{S} = \varepsilon_{33}^{T} - d_{31}^{2} / s_{11}^{E}$) is also plotted for different piezoceramics (Fig. 6.5). The dielectric constant $(\varepsilon_{33}^{T} / \varepsilon_{0})$ increases from PZT-5A until PMN-PT with 33% PT in Table 2. However, the permittivity component at constant strain ($\bar{\varepsilon}_{33}^{S}$) decreases after PMN-PT with 30% PT. It is interesting to note that the permittivity of PMN-PZT at constant strain is lower than that of all the other piezoceramics considered here. Mass densities of these piezoceramics are very similar to each other as shown in Fig. 6.6.

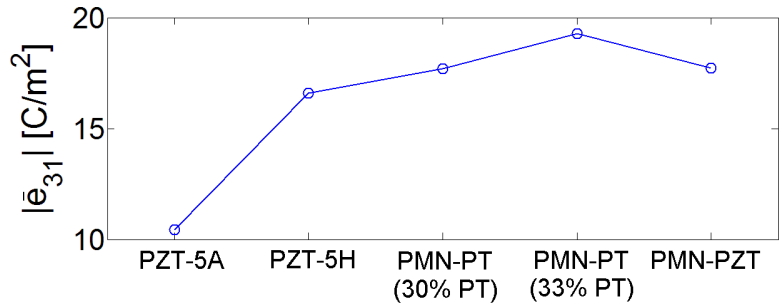

Fig. 6.4 Variation of the reduced piezoelectric stress constant for different piezoceramics

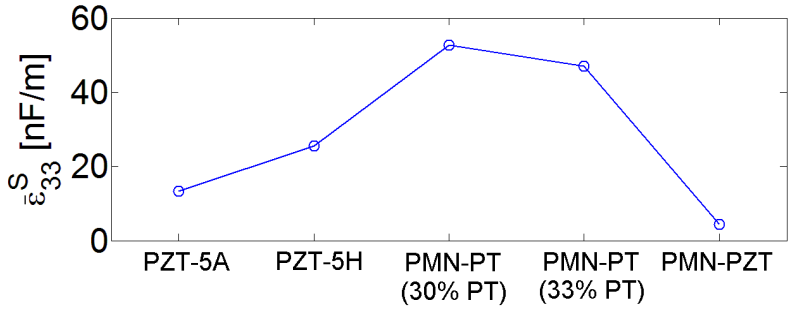

Fig. 6.5 Variation of the reduced permittivity constant for different piezoceramics

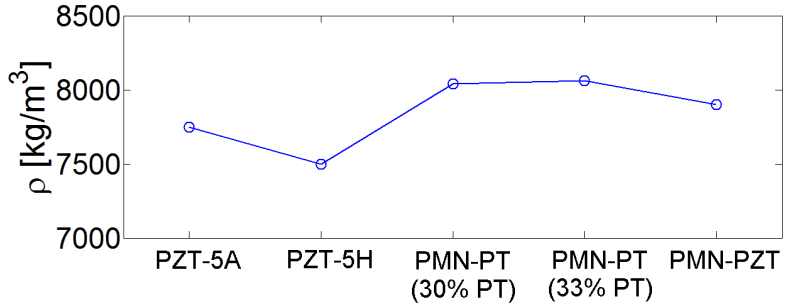

Fig. 6.6 Variation of the mass density for different piezoceramics

6.3 Theoretical Case Study for Performance Comparison of Various Monolithic Piezoceramics and Single Crystals

6.3.1 Properties of the Bimorph Cantilevers. In this section, power generation performances of bimorph cantilevers with identical dimensions and substrate materials using PZT-5A, PZT-5H, PMN-PT (with 30% PT and with 33% PT) and PMN-PZT are compared. The piezoceramic layers of each bimorph cantilever are assumed to be connected in parallel (Fig. 3.1b). The substrate material in all cases is aluminum with identical dimensions and properties ($Y = 70$ GPa, $\rho = 2700$ kg/m^3). For all cases considered here, the dimensions of the bimorph cantilever are as given in Table 6.3.

Table 6.3 Geometric properties of the bimorph cantilevers

	Piezoceramic	**Substructure**
Length (L) [mm]	40	40
Width (b) [mm]	6	6
Thickness (h_p , h_s) [mm]	0.2 (each)	0.1

The bimorph energy harvester model developed in Chapter 3 (experimentally validated in Chapter 4) is used here. As the electrical load resistance is increased from zero to infinity, the resonance frequencies of a bimorph shift from the short-circuit resonance frequencies to the open-circuit resonance frequencies. The short-circuit resonance frequency ω_r^{sc} (for $R_l \to 0$) of the *r*-th mode in the voltage FRF is the undamped natural frequency ω_r as shown in Chapter 5. As $R_l \to \infty$, the resonance frequency moves to the open-circuit resonance frequency (ω_r^{oc}). The short-circuit and the open-circuit resonance frequencies of the fundamental vibration mode ($r = 1$) of the five bimorphs with identical dimensions are listed in Table 6.4 (where $f = \omega / 2\pi$). Recall from Chapter 5 that the resonance frequency shift from the short-circuit to the open-circuit conditions is as a measure of electromechanical coupling. Among the piezoceramics considered here, with the second largest $\overline{e}_{31}$ constant and the smallest $\overline{\varepsilon}_{33}^{S}$ (as well as the smallest ω_r due to low stiffness), expectedly, PMN-PZT bimorph exhibits the largest relative resonance frequency shift (recall Eq. (5.18)).

Table 6.4 Short-circuit and open-circuit resonance frequencies of the bimorph cantilevers

	f_1^{sc} [Hz] (short circuit)	f_1^{oc} [Hz] (open circuit)
PZT-5A cantilever	151.9	157.0
PZT-5H cantilever	153.8	160.5
PMN-PT (30% PT) cantilever	84.7	90.7
PMN-PT (33% PT) cantilever	73.8	82.2
PMN-PZT cantilever	55.8	83.6

6.3.2 Performance Comparison of the Original Configurations. Figure 6.7a displays the power versus load resistance curves of these five bimorphs for excitation at the short-circuit resonance frequency of each bimorph. The outputs are normalized with respect to the base acceleration (in terms of the gravitation acceleration, g). Note that the modal mechanical damping ratio is assumed to be identical ($\zeta_1 = 0.01$) for all bimorphs. The PMN-PZT bimorph gives the largest power output (1.73 mW/g^2) and it is followed by the PMN-PT bimorph with 33% PT (1.33 mW/g^2) and the PMN-PT bimorph with 30% PT (1.15 mW/g^2). The PZT-5A bimorph generates 0.61 mW/g^2 whereas the PZT-5H bimorph generates 0.59 mW/g^2. The order of the power outputs might seem to agree with the order of the d_{31} constants (Fig. 6.1). However, in spite of its larger d_{31} constant, the PZT-5H bimorph gives slightly lower power output compared to the PZT-5A bimorph. Moreover, the largest power is less than only three times the smallest power (unlike the order of magnitude difference between the d_{31} constants).

Due to the large variance of the elastic compliance constants (Fig. 6.2), the natural frequencies of the bimorphs differ considerably, except for the PZT-5A and PZT-5H bimorphs, which have similar elastic compliances. Figure 6.7b shows the tip vibration response of the bimorphs in short-circuit conditions. Clearly, as it has the lowest stiffness (and therefore the lowest natural frequency), PMN-PZT bimorph exhibits the largest dynamic flexibility. The tip deflection of the PMN-PZT bimorph at resonance is about 7.5 times that of the PZT-5H bimorph for the same mechanical damping ratio (without any electrical damping, since $R_l \to 0$ in Fig. 6.7b). Therefore, since the power curves in Fig. 6.7a are obtained for the resonance excitation of each bimorph, it is not possible to claim that the order of the maximum power outputs in Fig. 6.7a is due to the order of the d_{31} constants. In addition, the PZT-5A bimorph has larger mass (which affects the forcing term in the base excitation problem), it exhibits slightly larger dynamic flexibility at its resonance than PZT-5H in Fig. 6.7b, which might be the reason of its larger power output in spite of its smaller d_{31} and $\bar{e}_{31}$ constants.

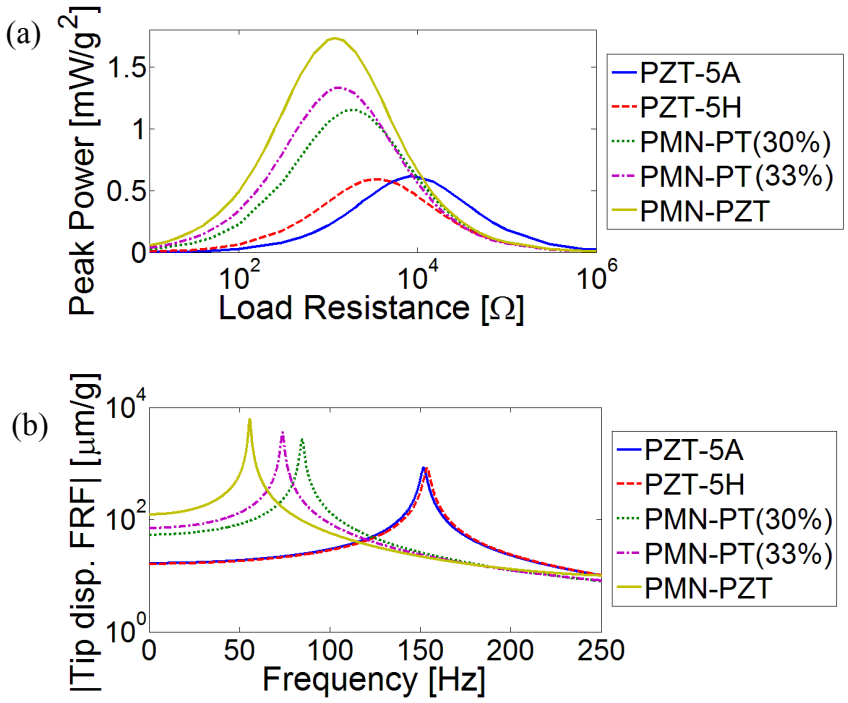

Fig. 6.7 (a) Power vs. load resistance curves for excitation at the fundamental short-circuit resonance frequency of each bimorph and the (b) vibration FRFs of the bimorphs for $R_l \to 0$ ($\zeta_1 = 1\%$ for all bimorphs)

6.3.3 On the Effect of Piezoelectric Strain Constant. In order to understand the role of the d_{31} constant in piezoelectric power generation, $d_{31} = -989.6\,\text{pm/V}$ is assumed for all bimorphs (which is the average of the d_{31} constants of these five piezoceramics as shown in Table 6.1). The geometry of the bimorph and the modal mechanical damping ratio are unchanged. Figure 6.8 shows the simulation results for this *artificial* case. The optimum loads are highly affected (as the optimum electrical load depends on electromechanical coupling) but the maximum power outputs are affected very slightly and the order of the power outputs is the same for the bimorphs. This observation supports the idea that the large power outputs in Fig. 6.7a are due to large dynamic flexibilities (originating from the large elastic compliance values) of the respective bimorphs at their individual resonances rather than the substantial difference in the d_{31} constants.

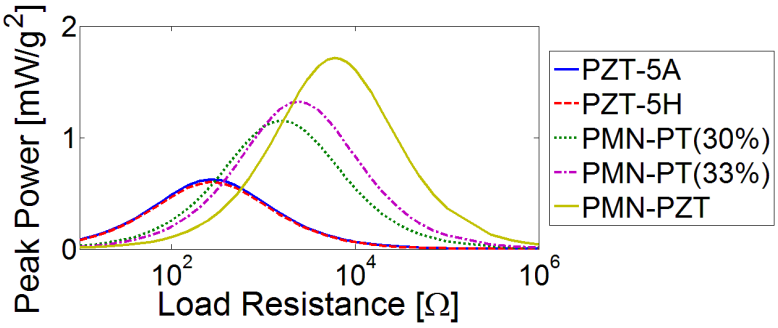

Fig. 6.8 Power versus load resistance curves for excitation at the fundamental short-circuit resonance frequency of each bimorph ($\zeta_1 = 1\%$ and $d_{31} = -989.6$ for all bimorphs)

6.3.4 On the Effect of Elastic Compliance. It is a useful practice to assume that all these bimorphs have the average compliance ($s_{11}^E = 56.2\,\text{pm}^2/\text{N}$) and average mass density ($\rho = 7850\,\text{kg/m}^3$) values shown in Tables 6.1 and 6.2. Then the fundamental short-circuit resonance frequencies of these bimorphs become identical in this second artificial case. Thus, the dynamic flexibilities of these bimorphs for resonance excitation are expected to be very similar in this case. Along with the remaining parameters, d_{31} values are kept at their original values and the power curves in Fig. 6.9a are obtained for resonance excitation. Figure 6.9b verifies that the dynamic flexibilities of these samples are indeed very similar for $R_l \to 0$. The maximum power output is obtained with the PMN-PZT bimorph as $1.16\,\text{mW}/g^2$ and the minimum power output is obtained with the PZT-5A bimorph as $0.94\,\text{mW}/g^2$. Therefore, in this particular case where the natural frequencies and therefore the dynamic flexibilities are forced to be identical, the power outputs of the bimorphs are in the same order of magnitude and they are indeed very similar to each other (yet the optimum loads differ considerably).

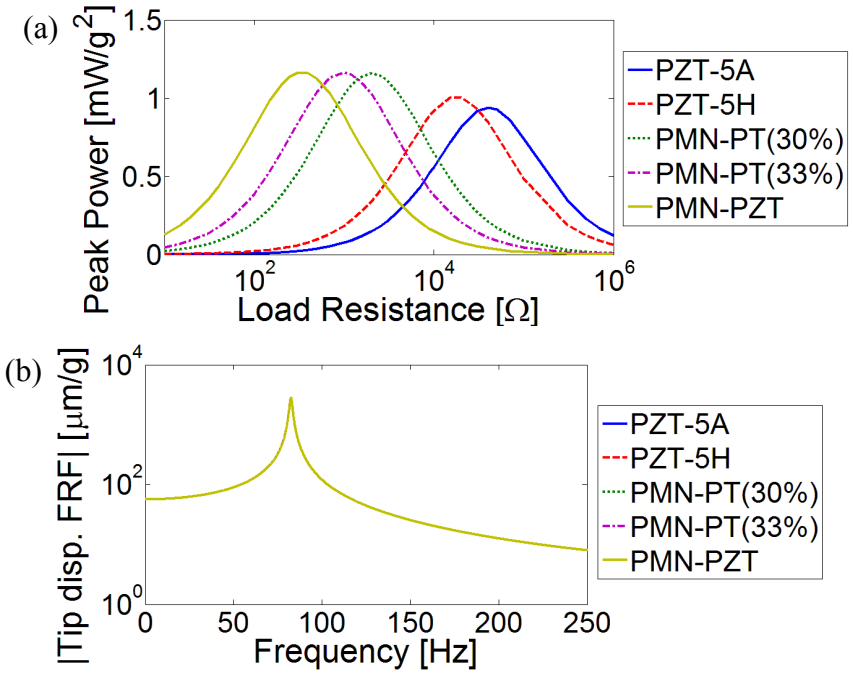

Fig. 6.9 (a) Power versus load resistance curves for excitation at the fundamental short-circuit resonance frequency of each bimorph and (b) vibration FRFs of the bimorphs for $R_l \to 0$ ($\zeta_1 = 1\%$, $s_{11}^E = 56.2$ and $\rho = 7850\,\text{kg/m}^3$ for all bimorphs)

The discussion so far shows that the order of magnitude difference in the electrical power outputs is *not* like the order of magnitude difference between the d_{31} constants. The electrical power outputs differ in the same order of magnitude (just like the $\overline{e}_{31}$ constants) and the dynamic flexibility of the cantilever plays an important role.

6.3.5 On the Effect of Permittivity Constant. The last artificial case is to assume that the constant stress dielectric constants are identical and equal to the average value given in Table 6.2 ($\varepsilon_{33}^T / \varepsilon_0 = 5220$) to study how the difference in the relative permittivity affects the results. As can be seen in Fig. 6.10, the qualitative order (in terms of the amplitude-wise results) is not changed considerably compared to the original graph given by Fig. 6.7a except for the PZT-5A and PZT-5H bimorphs. Now the PZT-5H bimorph gives slightly larger power output. Thus, the slightly larger power output of the PZT-5A bimorph (compared to the PZT-5H bimorph) in the original

case (Fig. 6.7a) might partially be due to its smaller relative permittivity, in addition to its slightly larger mass and dynamic flexibility.

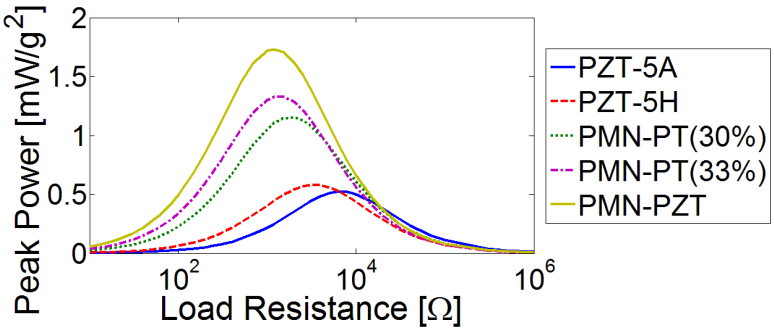

Fig. 6.10 Power versus load resistance curves for excitation at the fundamental short-circuit resonance frequency of each bimorph ($\zeta_1 = 1\%$ and $\varepsilon_{33}^T / \varepsilon_0 = 5220$ for all bimorphs)

6.3.6 On the Effect of the Overhang Length. For the original piezoelectric, elastic and dielectric properties of these bimorphs (Tables 6.1 and 6.2), it is possible to obtain the same short-circuit natural frequencies for different overhang lengths. Suppose that one is interested in designing these bimorphs for an excitation frequency of 60 Hz and the length dimension can be varied for this purpose (all the other parameters are the original parameters in Tables 6.1-6.3). In order to obtain a short-circuit resonance frequency of 60 Hz for the identical cross-sectional geometry described in Table 6.3, the lengths of the bimorphs must be as given in Fig. 6.11a. Note that the vibration response amplitudes of the bimorphs to the same excitation input are almost identical (Fig. 6.11b). Note that the original picture (Fig. 6.7) for the identical lengths (of 40 mm) is now reversed in Fig. 6.11a. In this particular design problem of tuning the resonance frequency of a bimorph cantilever to an excitation frequency (with design flexibility in the length dimension), the PZT-5A and PZT-5H bimorphs generate larger power. Similar to the discussion given in Section 6.3.4 (identical elastic compliances), this demonstration also agrees with the fact that the larger power outputs of the single crystals in the original case of Fig. 6.7a are indeed due to their larger dynamic flexibilities depicted in Fig. 6.7b. When the overhang lengths of the bimorphs with monolithic piezoceramics are increased to achieve the same dynamic flexibility, the monolithic piezoceramics generate larger power according to Fig. 6.11a.

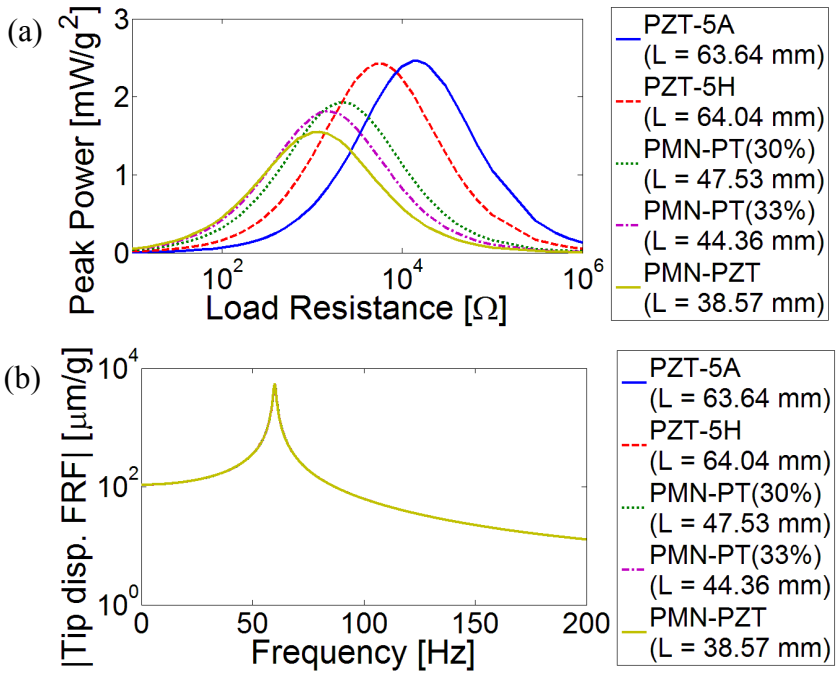

Fig. 6.11 (a) Power versus load resistance curves for excitation at the fundamental short-circuit resonance frequency of each bimorph and (b) vibration FRFs of the bimorphs for $R_l \to 0$ ($\zeta_1 = 1\%$ and the lengths are chosen to satisfy $f_1^{sc} = 60$ Hz for all bimorphs)

6.3.7 On the Effect of Mechanical Damping. The final discussion in this section demonstrates the sensitivity of the performance results to mechanical damping (which is not very easy to predict and control in practice). For the original parameters of this case study (which yield Fig. 6.7a), if one assumes the damping ratios shown in Fig. 6.12 (instead of $\zeta_1 = 1\%$ for all bimorphs), identical maximum power outputs are obtained. Note that these damping ratios are typical values one can identify in practice. Although the individual loss factors of the piezoceramic and the substructure layers can provide some insight, adhesive layers and clamped interfaces are important sources of mechanical damping which can dominate the damping due to the loss factors of the individual layers of a generator. The particular reason for the sensitivity of the results to mechanical damping is because the electrical power outputs already have the same order of magnitude. For instance, the favorable power output of the flexible PMN-PZT bimorph in Fig. 6.7a can become worse than that of the PZT-5H bimorph if the bonding layer and/or the clamped boundary of the PMN-PZT bimorph causes larger mechanical damping.

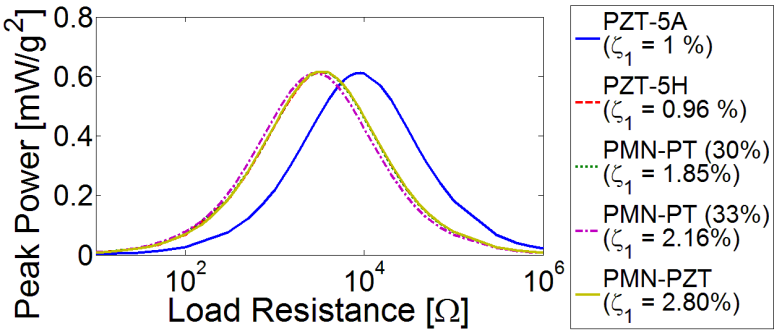

Fig. 6.12 Power versus load resistance curves for excitation at the fundamental short-circuit resonance frequency of each bimorph showing the sensitivity of the power output to mechanical damping ratio

6.4 Experimental Demonstration for PZT-5A and PZT-5H Cantilevers

6.4.1 Experimental Setup. A PZT-5A bimorph and a PZT-5H bimorph are tested under base excitation as shown in Fig. 6.13. The setup used for base excitation is very similar to the one described in Section 4.1.1 and the focus is placed here directly on the voltage frequency response measurements per base acceleration input. The excitation is provided using an electromagnetic LDS [66] shaker and the base acceleration is measured with a small PCB [47] accelerometer. The PZT-5A and PZT-5H bimorphs (T226-A4-203X and T226-H4-203X models) are manufactured by Piezo Systems, Inc. [45] and the properties of PZT-5A and the PZT-5H piezoceramics are listed in Tables 6.1 and 6.2. The layers of each bimorph are oppositely poled and the brass substructure layer provides electrical conductivity (for the series connection of the piezoceramic layers). When clamping these cantilevers, the overhang lengths are adjusted to have similar short-circuit resonance frequencies. The PZT-5A cantilever is clamped with an overhang length of 24.20 mm whereas the PZT-5H is clamped with an overhang length of 24.39 mm.

(a) 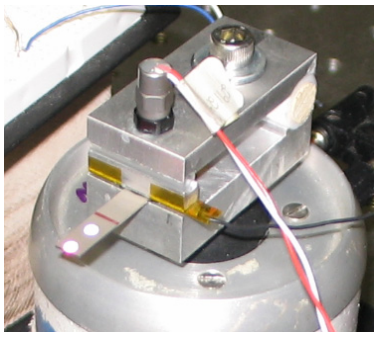 (b) 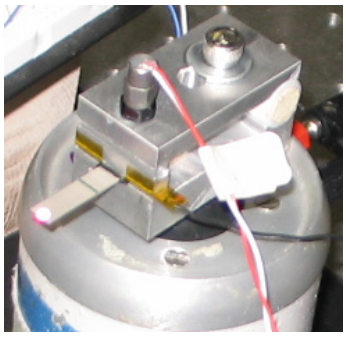

Fig. 6.13 (a) PZT-5A and (b) PZT-5H bimorph cantilevers under base excitation (photos by A. Erturk, 2009)

Table 6.5 Geometric properties of the PZT-5A and PZT-5H bimorph cantilevers

	PZT-5A cantilever	PZT-5H cantilever
Length (L) [mm]	24.20	24.39
Width (b) [mm]	6.4	6.4
Thickness (h_p , h_s) [mm]	0.265 (each)	0.140

6.4.2 Identification of Mechanical Damping and Model Predictions. The fundamental short circuit resonance frequencies of the PZT-5A and PZT-5H cantilevers are measured for a $100\,\Omega$ load resistance as 511.3 Hz and 508.1 Hz. For this lowest value of load resistance, the mechanical damping ratios of the fundamental vibration mode are identified for the PZT-5A and the PZT-5H cantilevers as $\zeta_1 = 0.0091$ and $\zeta_1 = 0.0141$, respectively. The possible sources of the difference in these identified damping ratios might be difference between the overall loss factors of the composite structures as well as slightly different clamping conditions in the experiments. As can be seen from Fig. 6.13, both cantilevers have non-conductive black tapes[‡] at their roots, which might act as a source of uneven mechanical damping in these two separate

[‡] These non-conductive tapes are preferred in the experiments not only to avoid shorting of the electrodes but also to minimize the possible stress concentration due to the direct contact of the aluminum clamp and the brittle piezoceramic layers.

configurations. Therefore these identified damping ratios are not purposely tuned and they are not easy to control. No effort has been made to obtain a similar mechanical damping effect in the experiments.

The voltage FRFs of the PZT-5A cantilever obtained for a set of resistive loads (ranging from 100 Ω to 248 kΩ) are shown in Fig. 6.14. The fundamental short-circuit resonance frequency of the PZT-5A cantilever is predicted by the model as 511.5 Hz. As the load resistance is increased from 100 Ω to 248 kΩ, the experimental value of the resonance frequency in Fig. 6.14 moves to 528.1 Hz and the analytical model predicts this frequency as 527.9 Hz. Note that, for the bandwidth of 0-2000 Hz, the frequency resolution of the SigLab [49] data acquisition system automatically adjust itself to give a frequency increment is 0.625 Hz. Therefore, both the short-circuit and the open-circuit resonance frequency readings from the FRFs include experimental error as in the cases discussed in Chapter 4.

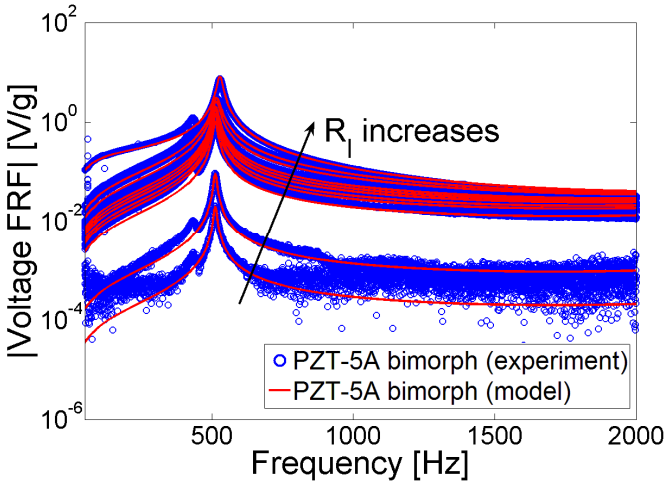

Fig. 6.14 Voltage FRFs of the PZT-5A cantilever for a set of resistive loads (experimental measurements and model predictions)

For the same set of load resistance, the model predictions for the PZT-5H cantilever are plotted in Fig. 6.15 along with the experimental voltage FRFs. The model prediction of the fundamental short-circuit resonance frequency is 508.4 Hz. In Fig. 6.15, as the load resistance is increased from 100 Ω to 248 kΩ, the experimental value of the resonance frequency moves to 530.6 Hz and the model predicts this frequency as 530.3 Hz. The short-circuit and the open-

circuit resonance frequencies of the PZT-5A and PZT-5H cantilevers are listed in Table 6.6. Predictions of the analytical model are very good in both cases.

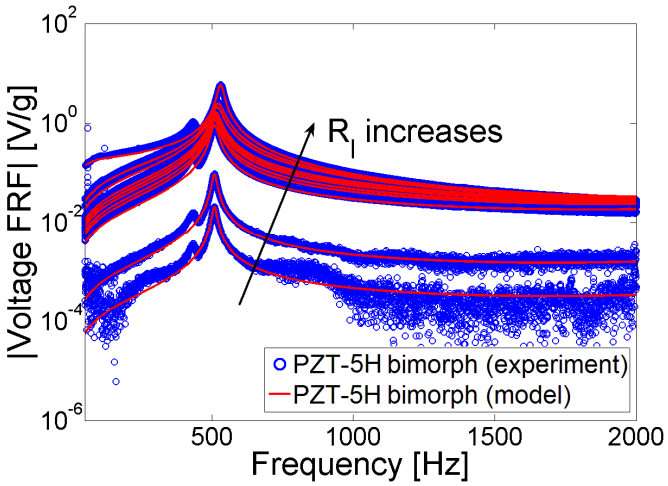

Fig. 6.15 Voltage FRFs of the PZT-5H cantilever for a set of resistive loads (experimental measurements and model predictions)

Table 6.6 Fundamental short-circuit resonance frequencies of the PZT-5A and PZT-5H bimorph cantilevers

	PZT-5A cantilever	PZT-5H cantilever
Experiment [Hz]	511.3	508.1
Model [Hz]	511.5	508.4

6.4.3 Performance Comparison of the PZT-5A and PZT-5H Cantilevers. Hereafter, the focus is placed on the fundamental short-circuit resonance frequencies of these cantilevers in order to compare their electrical performance results. For excitations at these frequencies, the variations of the voltage and current outputs with load resistance are shown in Figs. 6.16 and 6.17, respectively. Only for very low values of load resistance, the PZT-5H cantilever generates slightly larger voltage and current. For a wide range of load resistance, the PZT-5A cantilever generates considerably larger voltage and current.

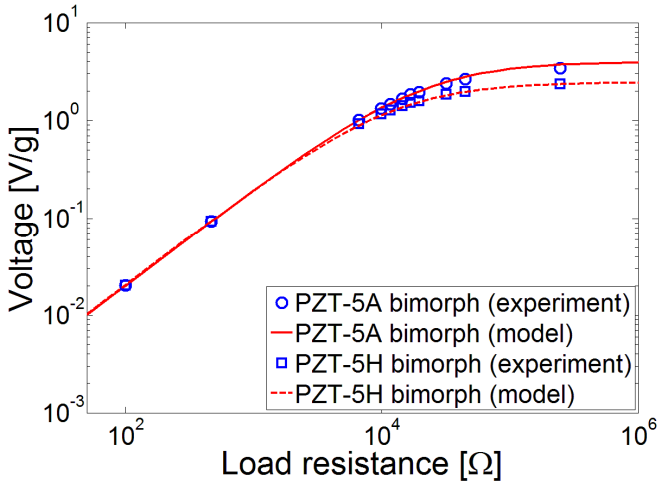

Fig. 6.16 Voltage vs. load resistance curves of the PZT-5A and PZT-5H cantilevers for excitation at the fundamental short-circuit resonance frequency (experimental measurements and model predictions)

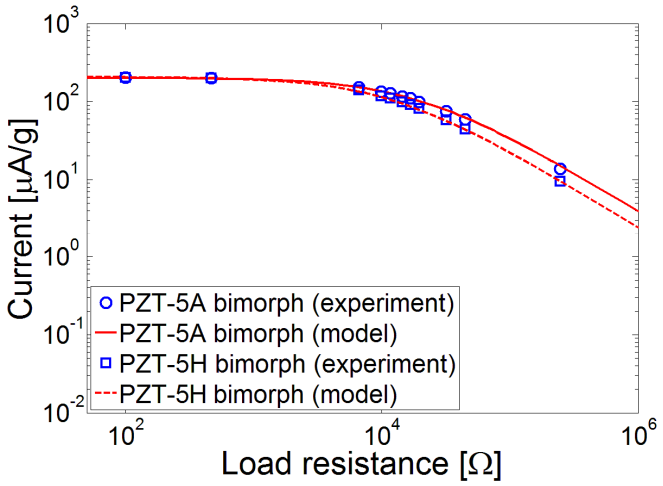

Fig. 6.17 Current vs. load resistance curves of the PZT-5A and PZT-5H cantilevers for excitation at the fundamental short-circuit resonance frequency (experimental measurements and model predictions)

Using the voltage data for excitations at the fundamental short-circuit resonance frequencies of the cantilevers, variations of the power output with load resistance are plotted in Fig. 6.18. The maximum experimental power output of the PZT-5A cantilever is obtained as

0.202 mW/g^2 (for a load resistance of 17.8 kΩ - the optimum value among the resistors used). The maximum experimental power output of the PZT-5H cantilever is 0.140 mW/g^2 (for a load resistance of 11.7 kΩ - the optimum value among the resistors used). Since the overhang volumes and masses of these cantilevers are slightly different, the power density and the specific power values are also reported in Table 6.7.

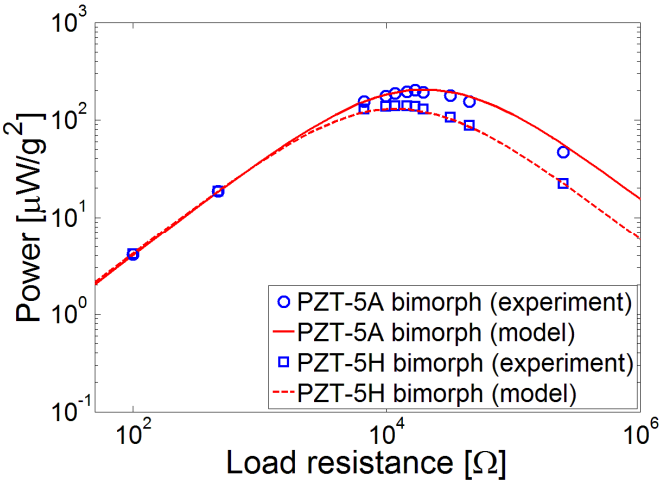

Fig. 6.18 Power vs. load resistance curves of the PZT-5A and PZT-5H cantilevers for excitation at the fundamental short-circuit resonance frequency (experimental measurements and model predictions)

As can be seen from Table 6.7, the maximum power density of the PZT-5A cantilever is about 45 % larger than that of the PZT-5H cantilever. If the maximum specific power outputs are compared, it is obtained that the PZT-5A cantilever generates 42 % larger specific power. Therefore, choosing the PZT-5H cantilever due to its larger d_{31} constant (larger by 60 % compared to that of PZT-5A) could result in surprising results in terms of the power output as the mechanical damping can change the entire picture. Since the modal damping ratio of the PZT-5H cantilever turns out to be 55 % larger than that of the PZT-5A cantilever (in this particular experiment), the power output is controlled by mechanical damping. Recall from the theoretical discussion given with Fig. 6.7a that, for the same amount of mechanical damping, the power outputs of the PZT-5A and PZT-5H cantilevers are very similar. However, 55 % larger mechanical damping relative to the PZT-5A cantilever results in 45 % less power density for

resonance excitation of the PZT-5H cantilever. This simple practice shows the importance of mechanical damping in piezoelectric energy harvesting. Mechanical damping is probably the most difficult parameter to control in the system (as in several other vibration engineering problems) and it can change the entire picture regardless of the piezoelectric material of being used.

Table 6.7 Maximum power outputs and identified mechanical damping ratios

	PZT-5A cantilever	PZT-5H cantilever
Max. Power [mW/g^2]	0.202	0.140
Max. Power Density [mW/(g^2cm^3)]	1.95	1.34
Max. Specific Power [mW/(g^2g)]]	0.243	0.171
Mechanical Damping [%]	0.91	1.41

6.5 Summary and Conclusions

In this chapter, the effects of materials constants and mechanical damping on the power generation performances of conventional piezoceramics (PZT-5A and PZT-5H) and novel single crystals (PMN-PT and PMN-PZT) are investigated. The material constants of interest are the piezoelectric, elastic and the dielectric constants. It is shown that the large piezoelectric strain constants of the commercially available single crystals are associated with very large elastic compliance and the combination of these two properties does *not* result in a substantial increase in the effective piezoelectric stress constant ($\overline{e}_{31}$) for a thin energy harvester beam. Although the d_{31} constants can change by an order of magnitude from PZT-5A to PMN-PZT, the effective piezoelectric constants of these active materials are in the same order of magnitude. Consequently, the substantially large d_{31} constants of the commercially available single crystals do *not* necessarily imply substantially large power output in energy harvesting. The concepts of dynamic flexibility and mechanical damping are shown to be very important as far as the maximum power output is concerned. When geometrically identical bimorphs employing these piezoelectric materials are forced to have the same dynamic flexibility, the power outputs are observed to be very similar. It is also observed that the power output under resonance excitation

is extremely sensitive to mechanical damping (which is a very difficult parameter to control in practice). It is shown with an experimental case study using a PZT-5A bimorph and a PZT-5H bimorph that the former cantilever gives 45 % larger power density when the latter has 55 % larger mechanical damping ratio (although the d_{31} constant of PZT-5H is 60 % larger than that of PZT-5A). Therefore, designing and manufacturing the energy harvester beam to have less damping can be more important than the piezoelectric material being used.

CHAPTER 7

EFFECTS OF STRAIN NODES AND ELECTRODE CONFIGURATION ON PIEZOELECTRIC ENERGY HARVESTING

As briefly mentioned in the analytical derivations, vibration modes of a cantilevered beam other than the first mode have certain strain nodes where the dynamic strain distribution changes in the direction of the beam length. In this chapter, it is theoretically discussed and experimentally demonstrated that covering the strain nodes of vibration modes with continuous electrodes results in strong cancellation of the electrical outputs. After a brief review of the mathematical background, a detailed dimensionless analysis is given for predicting the locations of the strain nodes of a uniform thin cantilever in the absence of a tip mass. The dimensionless derivations and results are then presented for predicting the strain node positions and their variations in the presence of a tip mass. Since the cancellation problem is not peculiar to clamped-free boundary conditions, dimensionless data of modal strain nodes are tabulated for some other practical boundary condition pairs as well. The locations of strain nodes tabulated in this chapter are important also for applications of modal actuation since covering these positions with piezoelectric actuators might require dramatically high voltage inputs, yielding inefficient actuation processes. It is experimentally shown that the voltage output due to the second mode excitation can be increased substantially if segmented electrodes are used instead of continuous electrodes. The relationship between the discussion given here and a recent study on piezoelectric energy harvesting from the static deflection of a clamped circular plate is also explained. The use of segmented electrode pairs to avoid cancellations is described for single-mode and multi-mode vibrations of a cantilevered piezoelectric energy harvester. Alternative circuitry-based approaches can be investigated to handle the cancellation problem for multi-mode excitations.

7.1 Mathematical Background

Recall from Chapter 3 that the circuit equation of a piezoceramic layer under dynamic bending (such as the one shown in Fig. 3.2a) is obtained from the Gauss's law as

$$\frac{d}{dt}\left(\int_A \mathbf{D}\cdot\mathbf{n}dA\right)=\frac{v(t)}{R_l} \tag{7.1}$$

where the electrodes are connected to a resistive load* of R_l, $v(t)$ is the voltage output, $\mathbf{D}$ is the vector of electric displacements components in the piezoceramic layer, $\mathbf{n}$ is the unit outward normal and the integration is performed over the electrode area A. Since the only non-zero component of the inner product in Eq. (7.1) is $D_3 n_3$ due to the electrode placement on the thin layer (Appendix A.2), Eq. (7.1) reduces to†

$$\frac{\overline{\varepsilon}_{33}^{S} bL}{h_{\tilde{p}}}\frac{dv(t)}{dt}+\frac{v(t)}{R_l}=-\overline{e}_{31}h_{\tilde{p}c}b\int_0^L\frac{\partial^3 w_{rel}(x,t)}{\partial x^2\partial t}dx \tag{7.2}$$

As the vibration response is expanded in terms of the eigenfunctions of the undamped problem, Eq. (7.2) is expressed as a first order circuit equation excited by all vibration modes:

$$C_{\tilde{p}}^{eq}\frac{dv(t)}{dt}+\frac{v(t)}{R_l}=\sum_{r=1}^{\infty}\tilde{\theta}_r\frac{d\eta_r(t)}{dt} \tag{7.3}$$

where the electromechanical coupling term is

$$\tilde{\theta}_r=\Im\int_0^L\frac{d^2\phi_r(x)}{dx^2}dx=\Im\left.\frac{d\phi_r(x)}{dx}\right|_{x=L} \tag{7.4}$$

Here, $\Im=-\overline{e}_{31}bh_{\tilde{p}c}$ for the series connection and $\Im=-2\overline{e}_{31}bh_{\tilde{p}c}$ for the parallel connection of the piezoceramic layers for a bimorph (Table 3.1). The equivalent capacitance term also depends on the way the piezoceramic layers are connected as given in Table 3.1.

---

* If the circuit includes more linear elements than a resistive load, the $1/R_l$ term on the right hand side is simply replaced by the electrical admittance seen across the electrodes. Note that this electrical admittance should exclude the admittance due to the inherent capacitance of the piezoceramic, which emerges from the electric displacement term.

† In agreement with the analytical formulation given in Chapter 3, it is assumed that the widths of the substructure, piezoceramic and the electrodes are identical.

In Eq. (7.3), the forcing function on the right hand side is a modal summation where the contribution from the *r*-th vibration mode is the product of $\tilde{\theta}_r$ and $d\eta_r(t)/dt$. The modal velocity response, $d\eta_r(t)/dt$, is also an output of the system to the base vibration input and it is indeed affected by the voltage response due to the backward electromechanical coupling (Chapter 3). A more critical term is the modal coupling term $\tilde{\theta}_r$, which is not only a function of geometric, material and piezoelectric parameters of the energy harvester beam but also the *bending slope (cross-section rotation) eigenfunction* evaluated at the boundaries of the electrodes. In the foregoing derivation, since each of the electrodes is assumed to be covering the entire respective surface of the piezoceramic layer (the top or the bottom) and since the slope at the clamped end of the beam is already zero, the contribution to the forcing function from the *r*-th vibration mode simply depends on the slope at the free end as in Eq. (7.4). If the electrodes cover only a certain region $x_1 \le x \le x_2$ over the piezoceramic (which is still structurally continuous), the boundaries of the integral in Eq. (7.5) change and the resulting expression for $\tilde{\theta}_r$ becomes‡

$$\tilde{\theta}_r = \Im \frac{d\phi_r(x)}{dx}\bigg|_{x=x_1}^{x=x_2} \tag{7.5}$$

According to Eq. (7.5), the modal electromechanical coupling term (which is a measure of the modal forcing function in the circuit equation) depends on the region covered by the electrodes on the surface of the piezoceramic. Therefore, the contribution to the forcing function in Eq. (7.3) from the *r*-th vibration mode will be large if the difference of the slopes at the boundaries of the electrodes for that particular mode is large and vice versa. As a consequence, depending on the locations of the electrodes, modal electromechanical coupling and therefore the contribution from certain vibration modes can be large or small. If it is aimed to harvest energy from a specific vibration mode (say, from the *r*-th mode) by exciting the system harmonically at the *r*-th natural frequency (ω_r), the main contribution to the forcing function in the circuit will be from the *r*-th term at the right hand side of Eq. (7.3), yielding

‡ In Eq. (7.5), the eigenfunction term can be updated according to the piecewise-defined electrical boundary conditions (which will affect the elastic modulus of the piezoceramic) to be more precise.

$$C_{\tilde{p}}^{eq}\frac{dv(t)}{dt}+\frac{v(t)}{R_l}=\tilde{\theta}_r A_r e^{j\omega_r t} \tag{7.6}$$

where $A_r e^{j\omega_r t}$ is the modal velocity response ($A_r = j\omega \mathrm{H}_r$ in terms of the complex modal mechanical response H_r defined in Chapter 3) and it is indeed a function of the voltage response given by $v(t)$ as shown in the analytical derivations of Chapter 3. Therefore, if the beam vibrates under resonance excitation, the electrical circuit may or may not be excited very strongly depending on the respective mode shape. Clearly, one prefers a large $\tilde{\theta}_r$ for a stronger excitation of the circuit.

7.2 Physical and Historical Backgrounds

It turns out from the foregoing derivation that the bending slopes (cross-section rotations) at the boundaries of the electrodes constitute a strong parameter in piezoelectric energy harvesting problem. If the slopes at the boundaries of continuous electrodes are very close to each other for a particular mode shape, the contribution to the electrical output from that mode is very low. Furthermore, the above derivation also directly shows that certain boundary conditions are not useful for harvesting energy using continuous electrodes (e.g. clamped-clamped).

The physics behind this discussion is related to the strain distribution throughout the length of the beam. If the strain distribution over the length of the beam changes sign (i.e. if its phase changes by 180 degrees) for a certain vibration mode, collecting the charge developed by using continuous electrodes results in cancellation of the electrical outputs in harvesting energy from that vibration mode. The mechanism of cancellation is more obvious in the first term of Eq. (7.4), where the integrand is the *curvature eigenfunction* (which is a measure of *bending strain* for a symmetric thin beam). Hence, if the curvature changes sign for a vibration mode, the net electric charge output is reduced due to cancellation of the positive and the negative areas under the curvature eigenfunction in integrating the electric displacement over the electrode area. Therefore a physical solution that allows handling the integration in a piecewise sense should be preferred to using continuous electrodes.

The concept of strain nodes was formerly discussed in the literature of structural actuation. Crawley and de Luis [67] addressed the importance of strain nodes in their work

(which focuses on the converse piezoelectric effect for actuation) with the following words: "*…the first mode has no strain nodes. Therefore, if this were the only mode to be excited, the actuators could be placed anywhere along the beam. For maximum effectiveness, they would be placed as near to the root as possible. The second mode has a strain node at x = 0.216L. The PZA's (piezoelectric actuators) must be placed away from this point, so that the strain applied over the entire length of the actuator has a constant phase with respect to the homogeneous strain in the beam in this mode. If not, the modal force produced by the actuator will be decreased, since one section of the actuator will be opposing the other… This reasoning also indicates why it is necessary to use segmented actuators for the control of flexible structures. For the second mode of a cantilevered beam, a PZA located at x<0.216 must be driven 180 deg out of phase with a PZA located at x>0.2l6L".* It should be noted that the results of the above formulation in the "direct sense" are in agreement with the observation of Crawley and de Luis [67] in the "converse sense" of using piezoceramics in actuation for structural excitation and control.

Indeed, more than 60 years ago, Cady [68] discussed this phenomenon for (longitudinal) vibrations of crystals: "*There is no external piezoelectric reaction due to longitudinal deformations when rods with full-length electrodes are excited at an even multiple of the fundamental frequency, since the effects of compressions and extensions in the various segments cancel exactly*". He adds in another section of the same book on piezoelectric resonators that "*by the use of short (segmented) electrodes, however, intense vibrations, with correspondingly strong electric reactions, can be secured at any value of h (mode number), even or odd… Resonators with any number of pairs of electrodes can be prepared by silvering or evaporating a uniform metallic deposit on the opposite sides of the bar and then dissolving away metal in the proper regions to produce the desired number of pairs of separate electrodes*". Note that his reasoning on even and odd modes is for longitudinal vibrations and the boundary conditions he uses. However, the idea is the same and the "proper regions" he mentions are just the strain nodes.

In harvesting energy from the bending vibrations of a cantilevered thin beam like the one shown in Fig. 3.1, the location of the electrodes and/or the piezoceramic layers can be very important. The positions on the beam where the bending strain distribution (at a constant level from the neutral axis) changes sign for a vibration mode are called the *strain nodes*. Since the bending strain at a point is proportional to the curvature in the thin-beam theory, strain nodes of a

vibration mode are simply the *inflection points* of the respective eigenfunction. For a cantilevered beam, all vibration modes other than the first mode have certain strain nodes. The following section presents the dimensionless strain nodes of a cantilevered thin-beam based on the Euler-Bernoulli beam theory.

7.3 Strain Nodes of a Thin Cantilever without a Tip Mass

For a symmetric cantilever, the curvature eigenfunction is a direct measure of bending strain distribution and it is simply the second derivative of the displacement eigenfunction given by Eq. (2.10). Therefore the case without a tip mass is considered first ($M_t = I_t = 0$). Since the system is positive definite ($\lambda_r > 0$), positions of the strain nodes are the roots of the following equation in the interval $0 < \bar{x} < 1$:

$$\cosh \lambda_r \bar{x} + \cos \lambda_r \bar{x} - \sigma_r \left(\sinh \lambda_r \bar{x} + \sin \lambda_r \bar{x} \right) = 0 \tag{7.7}$$

where $\bar{x} = x / L$ is the dimensionless position on the beam axis. Using Eq. (7.7) along with Eqs. (2.11) and (2.12) gives the dimensionless positions of the strain nodes over the length of the beam for the first five modes as shown in Table 7.1. For convenience, the frequency numbers of the first five vibration modes are also provided in Table 1 and they can be used in Eq. (3.19) to predict the undamped natural frequencies of the harvester beam in short-circuit conditions (i.e. for $R_l \to 0$). As can be seen from Table 7.1, the *r*-th vibration mode has $r-1$ strain nodes and the only vibration mode of a cantilevered beam without strain nodes is the fundamental mode.

Table 7.1 Frequency numbers and dimensionless positions of the strain nodes for a cantilevered thin beam without a tip mass for the first five vibration modes

Mode	Freq. Num. (λ_r)	Strain node positions on x-axis ($\bar{x} = x / L$)			
1	1.87510407	-	-	-	-
2	4.69409113	0.2165	-	-	-
3	7.85475744	0.1323	0.4965	-	-
4	10.9955407	0.0944	0.3559	0.6417	-
5	14.1371684	0.0735	0.2768	0.5001	0.7212

The normalized displacement mode shapes and the strain mode shapes of the first three vibration modes of a cantilevered beam without a tip mass are displayed in Fig. 7.1. In agreement with Table 7.1, the strain node of the second vibration mode is located at $\bar{x} = 0.2165$, and the third vibration mode has two strain nodes at $\bar{x} = 0.1323$ and $\bar{x} = 0.4965$. These positions give an idea about how to locate the segmented electrodes for harvesting energy from these modes without cancellation. For instance, to avoid cancellation in harvesting energy from the second vibration mode, two electrode pairs should be used to cover the regions $0 \le \bar{x} < 0.2165$ and $0.2165 < \bar{x} \le 1$ separately. The voltage outputs of these electrode pairs will be out of phase with each other by 180 degrees and they should be combined accordingly in the electrical circuit. Otherwise, as can be seen in Fig. 7.1b, if continuous electrodes cover the entire length of the beam $(0 \le \bar{x} \le 1)$, the negative area $(0 \le \bar{x} < 0.2165)$ under the strain curve cancels a considerable portion of the positive area $(0.2165 < \bar{x} \le 1)$, yielding a reduced voltage output from the harvester.

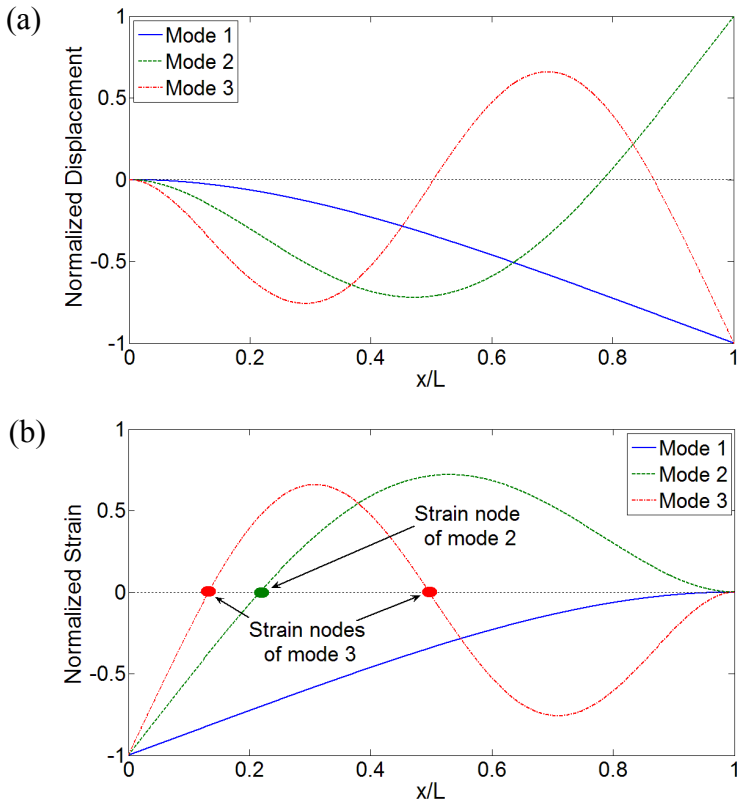

Fig. 7.1 (a) Normalized displacement and (b) normalized strain mode shapes of a cantilevered thin beam without a tip mass for the first three vibration modes

The discussion so far has focused on a cantilevered beam without a tip mass. In some energy harvesting applications, it is required to use a tip mass to tune the fundamental natural frequency of the harvester beam to a dominant excitation frequency or just to reduce its natural frequencies and increase its dynamic flexibility especially in micro-scale applications. The effect of a tip mass on the strain nodes of a cantilever is investigated in the following section.

7.4 Effect of Using a Tip Mass on the Strain Nodes of a Thin Cantilever

If a tip mass M_t of negligible rotary inertia ($I_t = 0$) is attached rigidly at $x = L$ to the cantilevered beam shown in Fig. 3.1, the eigenfunctions and the eigenvalues are referred from Eqs. (2.41) and (2.44), respectively. The curvature eigenfunction is the second derivative of Eq. (2.41) with respect to *x*. It is then possible to study the effect of a tip mass on the strain nodes in a dimensionless basis. As an example, Fig. 7.2a shows the variation of the displacement mode shape whereas Fig. 7.2b displays the variation of the strain distribution of the second vibration mode with increasing M_t / mL. The shift of the strain node position due to increasing M_t / mL is shown in Fig. 7.2b. As the M_t / mL ratio goes from 0 to 10, the strain node of the second mode moves from $\bar{x} = 0.2165$ to $\bar{x} = 0.2632$.

Figure 7.3a shows the strain node positions of the second and the third vibration modes versus M_t / mL ratio. As the M_t / mL ratio increases from 0 to 10, the only strain node of the second mode moves from $\bar{x} = 0.2165$ to $\bar{x} = 0.2632$ whereas the two strain nodes of the third vibration mode move from $\bar{x} = 0.1323$ and $\bar{x} = 0.4965$ to $\bar{x} = 0.1468$ and $\bar{x} = 0.5530$, respectively. It is also useful to investigate the variation of the frequency numbers with the M_t / mL ratio which is given in Fig. 7.3b for the first five vibration modes. Note that these frequency numbers give the natural frequencies when they are used in Eq. (3.19). As can be seen from Figs. 7.3a and 7.3b, the strain nodes move toward the free end of the beam and the frequency numbers decrease with increasing M_t / mL ratio. The positions of the strain nodes are more sensitive to the variations in M_t / mL ratio in the relatively low M_t / mL region (i.e. for $0 \le M_t / mL \le 1$).

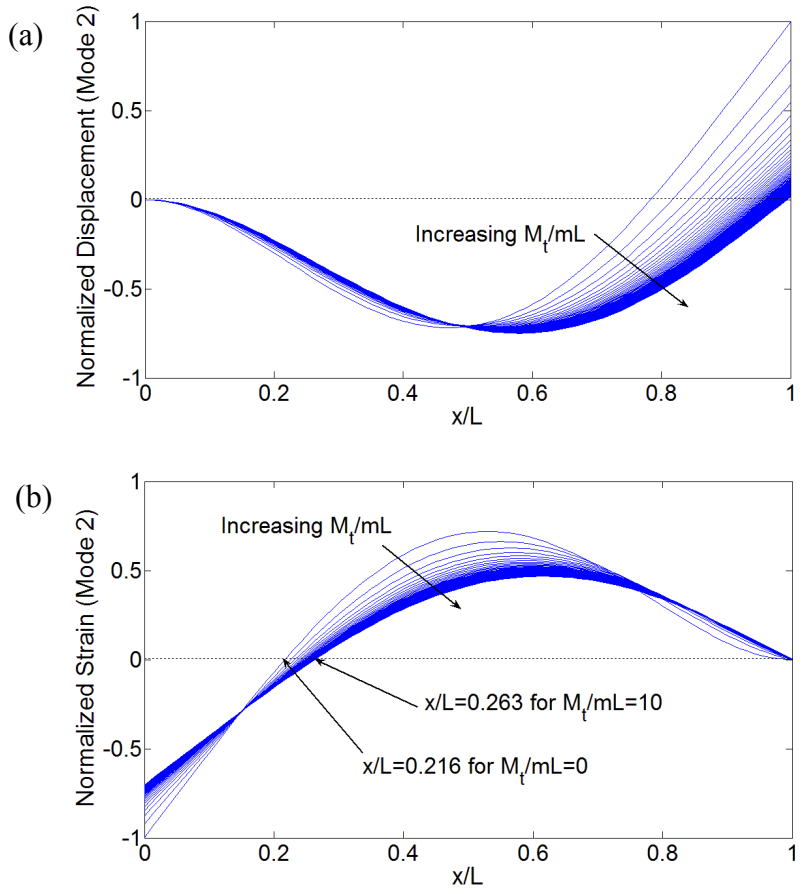

Fig. 7.2 Variation of the (a) normalized displacement and (b) normalized strain mode shapes of the second vibration mode with tip mass – to – beam mass ratio

As far as the frequency numbers given in Fig. 7.3b are concerned, other than the frequency number of the first vibration mode, all the frequency numbers converge to a nonzero value as $M_t/mL \to \infty$. A careful investigation shows that, as $M_t/mL \to \infty$, the frequency number of the *r*-th mode of a clamped-free beam with a tip mass converges to that of the $(r-1)$-th mode of a clamped-pinned beam without a tip mass[§] (except for the first frequency number λ_1, which goes to zero with a very slow rate). That the boundary conditions of a cantilevered harvester beam with a tip mass shift from clamped-free to clamped-pinned as $M_t/mL \to \infty$ makes sense, as the rotary inertia of the tip mass is neglected. Therefore, the direct consideration

[§] The dominating term in Eq. (2.44) for $M_t/mL \to \infty$ is the characteristic equation of a clamped-pinned beam: $\tanh\lambda - \tan\lambda = 0$ (because the system is positive definite, $\lambda \neq 0$ in the dominating term).

of the strain nodes of a clamped-pinned beam should give a good estimate of the strain nodes (of modes $r \geq 2$) for very large values of M_t/mL in modes other than the first mode. However, if the rotary inertia of the tip mass is not negligible and if it increases uniformly as $M_t/mL \to \infty$, the boundary conditions shift from clamped-free to clamped-clamped and it becomes more reasonable to estimate the strain node positions (of modes $r \geq 2$) from the eigenfunctions of a clamped-clamped beam for large values of M_t/mL. Hence, it is also insightful to examine the characteristic equation of a thin cantilevered beam where the rotary inertia (I_t) of the tip mass is also considered (Eq. (3.20)).

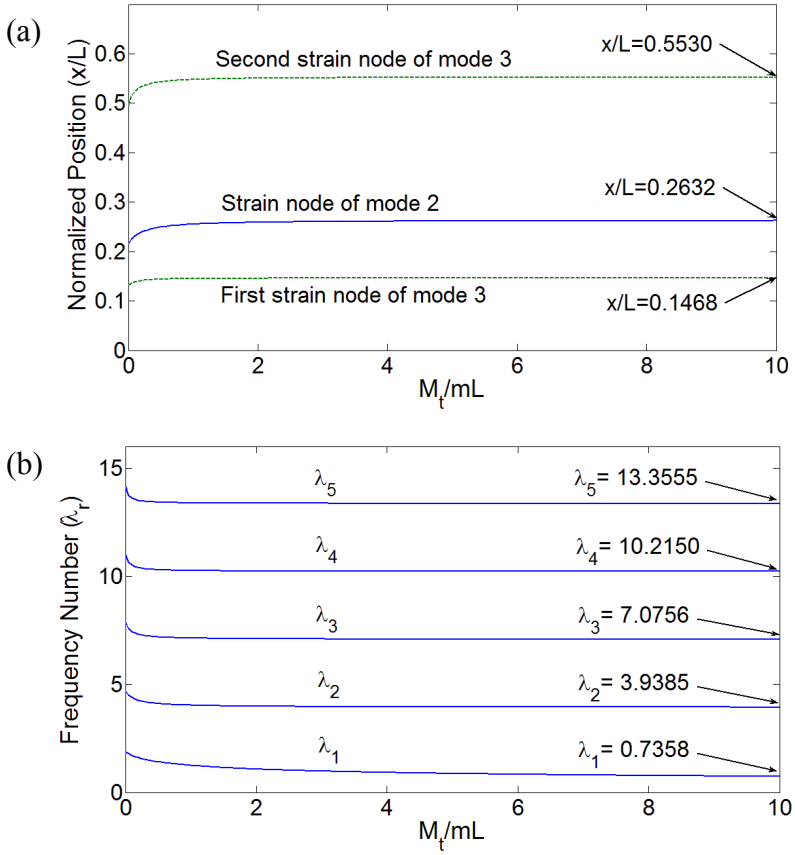

Fig. 7.3 (a) Variation of the strain node positions of the second and the third vibration modes and (b) variation of the frequency numbers of the first five vibration modes with tip mass – to – beam mass ratio

In Eq. (3.20), the rotary inertia of the tip mass can be normalized with respect to the rotary inertia of the free rigid beam about its centroid (or that of a rigid pendulum about its pivot) and a similar dimensionless analysis can be performed. As can be seen from Eq. (3.20), the rotary inertia of the tip mass introduces two additional terms to Eq. (2.44). The form of the eigenfunction expression given by Eq. (2.41) is still the same; however, the eigenvalues to be used in this equation should be extracted from Eq. (2.44). As mentioned before, for a large tip mass and tip rotary inertia, the free end of the beam also acts as a clamped end. This fact is also evident from the dominating term in Eq. (3.20) for $(M_t/mL)(I_t/mL^3)\to\infty$, which is the characteristic equation of a uniform thin-beam beam with clamped-clamped boundary conditions ($1-\cos\lambda\cosh\lambda=0$). Clamped-clamped boundary conditions may cause strong cancellations in the electrical outputs if full electrodes are used for covering the piezoceramic layer(s). Therefore, employing a large tip mass for reducing the natural frequencies of a cantilevered harvester has the side effect of drastically reducing the electrical response of the vibration modes other than the fundamental mode. If higher vibrations of a cantilevered energy harvester are to be excited in a practical application (which is the case for the ambient vibration energy with random, varying frequency or impulse-type excitation characteristics), addition of a tip mass results in a trade-off, as it has an undesired effect on the vibration modes other than the first mode.

7.5 Strain Nodes for Other Boundary Conditions

Since the literature of energy harvesting [25,69] and the literature dealing with piezoelectric beams [70] have considered boundary conditions other than clamped-free as well, the numerical data of the strain node positions for some other practical boundary conditions are tabulated in this section. The boundary condition pairs investigated in this section are pinned-pinned, clamped-clamped and clamped-pinned pairs. Tables 7.2-7.4 display the positions of the strain nodes for the first five vibration modes of uniform thin beams with these three boundary condition pairs. The frequency numbers are also provided and they can be used in Eq. (3.19) to predict the undamped natural frequencies (which are the resonance frequencies of the voltage FRF in short-circuit conditions as shown in Chapter 5).

Since the pinned-pinned (Table 7.2) and clamped-clamped (Table 7.3) boundary conditions are symmetric boundary conditions (yielding symmetric and antisymmetric mode shapes for odd and even modes, respectively), the positions of the strain nodes (inflection points of the mode shapes) are symmetric with respect to the center $\overline{x} = 0.5$ of the beam. However, for the clamped-pinned boundary conditions (Table 7.4), no such symmetry exists. It should be noted that it is safe to cover the entire surface with continuous electrodes for harvesting energy from the first vibration mode of a pinned-pinned beam. The rule for the pinned-pinned case is the same as the clamped-free case, i.e. the *r*-th vibration mode has $r-1$ strain nodes (Table 7.2). However, a beam with clamped-clamped boundary conditions has two strain nodes in the first vibration mode. According to Table 7.3, the *r*-th vibration mode of a clamped-clamped beam has $r+1$ strain nodes. Hence, three electrode pairs (with discontinuities at $\overline{x} = 0.2242$ and at $\overline{x} = 0.7758$) can be used to extract the electrical outputs of a clamped-clamped energy harvester without cancellation for vibrations with the first mode shape. Table 7.4 shows that the *r*-th vibration mode has r strain nodes for a clamped-pinned beam. Thus, two electrode pairs (with a discontinuity at $\overline{x} = 0.2642$) can handle the cancellation issue for the fundamental mode excitation of a harvester beam with clamped-pinned boundary conditions. Note that, in the clamped-pinned case, the clamped boundary is the $\overline{x} = 0$ point.

Among the boundary conditions investigated here, the clamped-clamped boundary condition pair constitutes a unique case. Theoretically, for excitations at all vibration modes of a clamped-clamped beam, the modal forcing term $\tilde{\theta}_r$ in the electrical equation and therefore the voltage response is zero, if full (continuous) electrodes cover the entire beam surface (see Eq. (7.5)). A similar issue (of total cancellation) is expected for the *even* vibration modes ($r = 2, 4, 6, ..., 2n$ where *n* is an integer) of the pinned-pinned case, if full electrodes cover the entire beam length. For the even modes of a beam with pinned-pinned boundary conditions, the slopes at the pinned boundaries are not zero, but they are equal to each other, yielding a total cancellation at these modes due to Eq. (7.5).

Table 7.2 Strain nodes of a thin beam with pinned-pinned boundary conditions

Mode	Freq. Num. (λ_r)	Strain node positions on x-axis ($\bar{x} = x/L$)			
1	π	-	-	-	-
2	2π	$1/2$	-	-	-
3	3π	$1/3$	$2/3$	-	-
4	4π	$1/4$	$1/2$	$3/4$	-
5	5π	$1/5$	$2/5$	$3/5$	$4/5$

Table 7.3 Strain nodes of a thin beam with clamped-clamped boundary conditions

Mode	Freq. Num. (λ_r)	Strain node positions on x-axis ($\bar{x} = x/L$)					
1	4.73004074	0.2242	0.7758	-	-	-	-
2	7.85320462	0.1321	0.5000	0.8679	-	-	-
3	10.9956079	0.0944	0.3558	0.6442	0.9056	-	-
4	14.1371655	0.0735	0.2768	0.5000	0.7232	0.9265	-
5	17.2787597	0.0601	0.2265	0.4091	0.5909	0.7735	0.9399

Table 7.4 Strain nodes of a thin beam with clamped-pinned boundary conditions

Mode	Freq. Num. (λ_r)	Strain node positions on x-axis ($\bar{x} = x/L$)			
1	3.92660231	0.2642	-	-	-
2	7.06858275	0.1469	0.5536	-	-
3	10.2101761	0.1017	0.3832	0.6924	-
4	13.3517688	0.0778	0.2931	0.5295	0.7647
5	16.4933614	0.0630	0.2372	0.4286	0.6190

The data provided in Tables 7.1-7.4 are also useful for modal actuation of beams with these boundary conditions because the coupling term $\tilde{\theta}_r$ (given by Eq. (7.5)) appears in the modal equation for the beam response (Section 3.6). According to Table 4.1, the fundamental mode of a clamped-free beam can be excited by locating the piezoelectric actuator(s) at anywhere along the beam. One should prefer a location close to the clamped end (see the strain distribution in Fig. 7.2b) in order to minimize the required actuation input as previously discussed by Crawley and de Luis [67]. However, excitation of the fundamental mode of a clamped-clamped beam is more critical as the piezoelectric actuators should not cover the positions $\bar{x} = 0.2242$ and $\bar{x} = 0.7758$ (Table 7.4). Covering one of these strain nodes with an actuator might require dramatically high voltage inputs for actuating the fundamental mode of a clamped-clamped beam piezoelectrically.

7.6 Experimental Demonstration

The cantilevered beam shown in Fig. 7.4 is used in order to demonstrate the effect of strain nodes on the voltage output briefly. The length, width and the height of the steel beam are 600 mm, 19.1 mm and 3.05 mm, respectively. An electromagnetic shaker with a stinger is used to excite the cantilevered beam at its first two natural frequencies. Since the main purpose is to demonstrate the importance of the strain nodes on energy harvesting by using cantilevered beams with piezoceramic layers/patches, the dimensions of the beam are selected arbitrarily and the importance is given only to justify the Euler-Bernoulli beam assumptions (i.e. the thin-beam theory). Hence, although the demonstration is given for a configuration that would not typically be used as an energy harvester, the results of the following study are valid for all micro-scale and macro-scale cantilevered piezoelectric energy harvesters which can be modeled based on the Euler-Bernoulli beam assumptions.

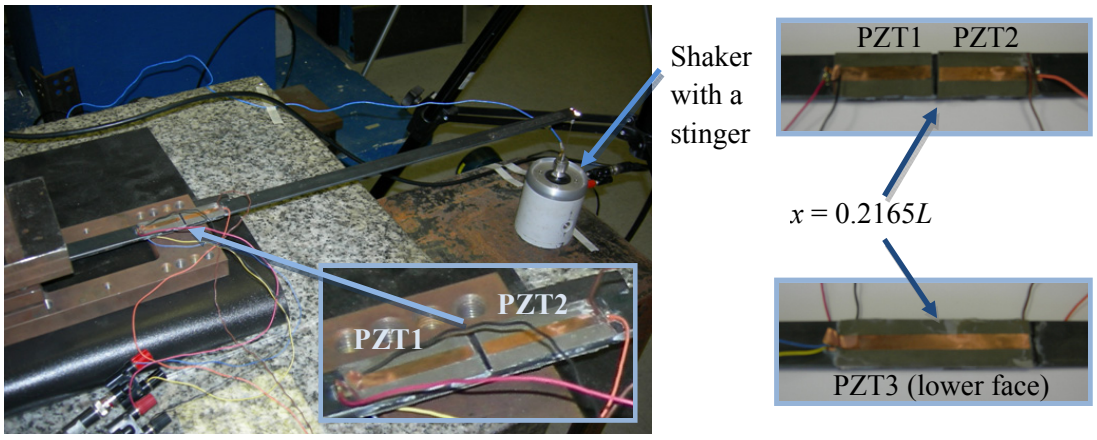

Fig. 7.4 Experimental setup for demonstration of the effect of strain nodes on the voltage output (photos by A. Erturk, 2009)

The first two vibration modes are considered for a simple demonstration of the voltage cancellation at higher vibration modes. Note that the experimental validations of the analytical model have already been given for several cases in Chapter 4. Hence the experimental demonstration of cancellation given here does not aim to verify the electrical circuit equations given in Section 7.1 quantitatively. The goal of this section is to provide a qualitative verification of voltage cancellation at higher modes excitations, which is expected from the theory. For convenience, small PZT-5A patches are used instead of covering the entire surface of the beam. Since the first vibration mode has no strain nodes, we focus on the strain node of the second mode, which is at $x = 0.2165L$ as given in Table 7.1. Therefore, *theoretically*, the distance of this strain node is approximately 130 mm from the clamped end of the beam. Two PZT-5A patches of dimensions $72\ \text{mm} \times 19.1\ \text{mm} \times 0.265\ \text{mm}$ are obtained from a PZT-5A sheet by Piezo Systems Inc. [45] (as the width of the beam is 19.1 mm and the lengths of the PZT-5A sheets are restricted with 72 mm by the manufacturer). The piezoceramic sheets come from the manufacturer with continuous nickel electrodes. Therefore, in order to realize the *segmented-electrodes* configuration, one should either etch the electrodes from the surface of the piezoceramic at the desired location or cut the piezoceramic directly to remove the electrical conductivity of the electrodes at the strain node of the beam. The second option is preferred for convenience and one of the two patches is cut into two identical parts to obtain two patches of dimensions $36\ \text{mm} \times 19.1\ \text{mm}$. First the small patches (PZT1 and PZT2) are attached onto the

opposite sides of the strain node on the upper surface of the beam (Fig. 7.4). Then, the longer patch (PZT3) is attached to the lower face of the beam such that the strain node coincides with the center of this patch as shown in Fig. 7.4. Hence, approximately the same region ($94 \le x \le 166$ mm) is covered on the upper and the lower surfaces of the beam, and theoretically, the strain node of the second mode is around the center of this region (at $x = 130$ mm).[**] Therefore, the piezoceramic and the electrodes are continuous on the lower surface whereas they are discontinuous on the upper surface at the theoretically predicted location of the strain node. In the following discussion, the open circuit voltage across the electrodes is measured in all cases without connecting the electrodes to an energy harvesting circuit ($R_l \to \infty$ in the theoretical discussion). For shaker excitations at both vibration modes, the voltage input to the electromagnetic shaker is kept the same (at 0.8 volts).

If the beam vibrates with its first mode shape, there is no strain node throughout the length of the beam. Although the excitation frequency is the first natural frequency (which is measured to be 7.1 Hz), slight contributions to the response are expected from the neighboring modes in response to excitation at the tip with the stinger of the shaker. In other words, the response of the beam is not perfectly the first mode shape; however, the major contribution to the response is from the first mode shape. Therefore, the dynamic strain distribution in PZT3 is expected to be in phase throughout its length. Hence the amplitude of the voltage response across the electrode pair of PZT3 should be identical to the combined amplitude of the voltage responses across the individual electrode pairs of PZT1 and PZT2. The voltage histories across the electrode pairs of PZT1 and PZT2 are shown in Figs. 7.5a and 7.5b, respectively. It is clear from Fig. 7.5 that the voltage responses of PZT1 and PZT2 are *in phase* and their amplitudes are also very close to each other.

[**] As an approximation, it is assumed that the attachment of the thin piezoceramic patches onto the uniform steel beam does not change the inflection point of the second mode shape considerably.

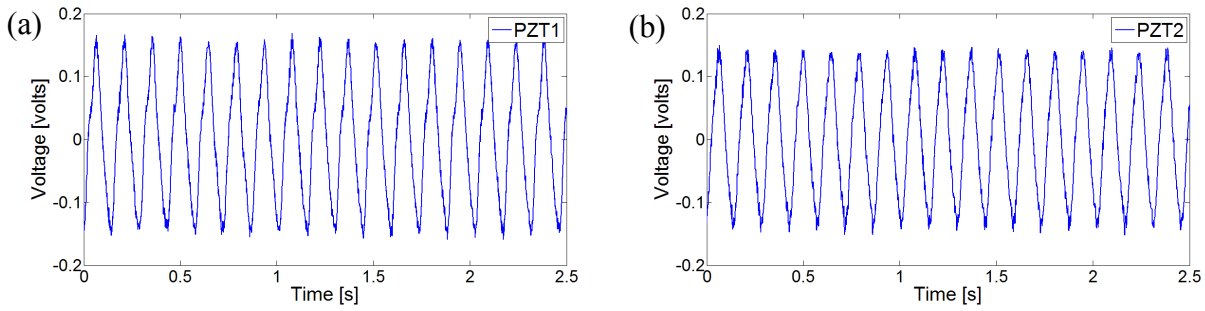

Fig. 7.5 Voltage responses across the electrodes of (a) PZT1 and (b) PZT2 for excitation at the first natural frequency of the beam

Figure 7.6 shows the voltage response of PZT3 along with the summation of the voltage responses of PZT1 and PZT2 for excitation at the first natural frequency. As expected, the voltage amplitude of PZT3 (which has the continuous electrode pair) is approximately identical to the summation of the voltage amplitudes across the electrode pairs of PZT1 and PZT2 as they are in phase. Also, the voltage response of PZT3 is 180 degrees out of phase with the summation of PZT1 and PZT2 since the lower face of the beam is in tension when the upper face is in compression, and vice versa. The slight difference in the amplitudes (Fig. 7.6) is expected to be due to experimental imperfections. The PZTs were cut by hand and there is a finite spacing between PZT1 and PZT2 as shown in Fig. 7.4 (so that the region covered by PZT1+PZT2 exceeds $94 \le x \le 166$ mm slightly). Figure 7.6 is therefore a verification of the fact that the piezoceramic patches with continuous electrodes can be used safely for harvesting energy from the first vibration mode since the strain distribution is always in phase over the length of a cantilevered beam.

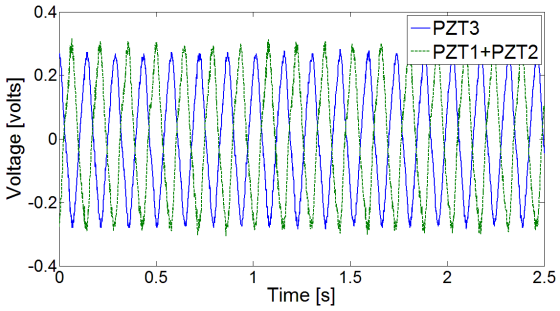

Fig. 7.6 Voltage response across the continuous electrodes of PZT3 and the maximum voltage response obtained by combining the electrodes of PZT1 and PZT2 for excitation at the first natural frequency

If the beam is excited at its second natural frequency (which is measured as 40.8 Hz), the dominant vibration mode in the response is the second mode. The voltage outputs of PZT1 and PZT2 are displayed in Fig.7.7 for excitation at the second natural frequency. Unlike the voltage outputs for excitation at the first natural frequency, as expected, the voltage outputs of these patches are now 180 degrees out of phase with each other. During the vibratory motion, when PZT1 is in compression, PZT 2 is in tension, and vice versa. The phase difference in the mechanical domain determines the phase difference in the voltage outputs. Note that the voltage amplitudes of PZT1 and PZT2 are not identical, which means that the strain distributions at different sides of $x = 130$ mm are not identical for excitation at the second natural frequency.

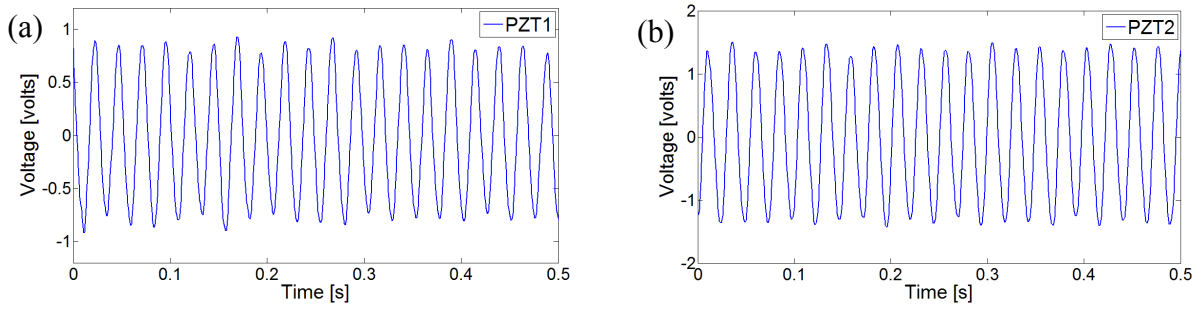

Fig. 7.7 Voltage responses across the electrodes of (a) PZT1 and (b) PZT2 for excitation at the second natural frequency of the beam

The continuous electrodes of PZT3 cover the entire region on the strain node of the second mode. For excitation at the second natural frequency, the voltage response across the electrodes of PZT3 is shown in Fig. 7.8 along with appropriate combination of PZT1 and PZT2 outputs for maximum voltage output. Since the charge developed in PZT3 is collected by continuous electrodes, the phase difference in the strain distribution at opposite sides of the second mode results in cancellation. Therefore the voltage output of PZT3 is less than even the individual outputs of PZT1 and PZT2 for the same mechanical input (compare the solid line in Fig. 7.8 with Figs. 7.7a and 7.7b). Clearly, it is not preferable to cover the strain node of a harvester beam with continuous electrodes. In order to obtain the maximum voltage output from this sample region ($94 \le x \le 166$ mm) for excitation at the second natural frequency, one should collect the electric charge developed in regions $94 \le x \le 130$ mm and $130 \le x \le 166$ mm with separate electrode pairs to obtain the individual voltage outputs given in Fig. 7.7. These voltage outputs can then be combined by considering the phase difference (mathematically, by subtracting the voltage outputs: PZT1-PZT2) to obtain the maximum voltage amplitude (dashed line Fig. 7.8). The physical combination of these voltage outputs (i.e. realization of the subtraction PZT1-PZT2) is done by combining the correct leads coming from the respective segmented electrode pairs. According to Fig. 7.8, the voltage amplitude of the preferable combination of PZT1 and PZT2 is more than 4 times the amplitude of the voltage response of PZT3.

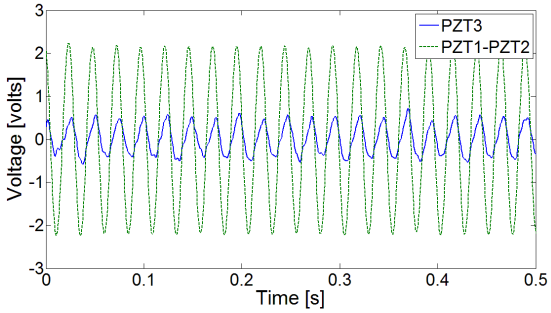

Fig. 7.8 Voltage response across the continuous electrodes of PZT3 and the maximum voltage response obtained by combining the electrodes of PZT1 and PZT2 for excitation at the second natural frequency

In this simple example, the continuous electrode pair covering the strain node yielded some voltage output because there is no total cancellation at the opposite sides of $x = 130$ mm for PZT3 (since PZT1 and PZT2 outputs do not have the same amplitude in Fig. 7.7). It is worth adding that the position of the strain node ($x = 130$ mm) is predicted theoretically (for the geometrically uniform configuration without the patches) and the patches were located on the beam according to this position. Scanning the second mode shape of the beam experimentally and locating the patches according to the exact position of the strain node of the experimental mode shape would give more accurate results. In addition, the piezoceramics were cut by hand and the region covered by PZT1+PZT2 is not identical to that covered by PZT3 due to the discontinuity between PZT1 and PZT2. Regardless of these experimental imperfections, the qualitative results discussed based on this simple experiment are in perfect agreement with the theory. In conclusion, depending on how they are located on the harvester beam, using continuous electrodes may result in dramatically lower voltage outputs in piezoelectric energy harvesting from cantilevered beams at higher vibration modes. Although the experimental demonstration is given here for clamped-free boundary conditions, the cancellation problem for other boundary conditions (see Section 7.5) can be solved a similar manner.

7.7 Relationship with the Energy Harvesting Literature

Recently, Kim et al. [71,72] studied energy harvesting from a clamped circular plate due to a pressure drop in an air chamber. Even though their system was not a beam and although they considered the deflection of the plate due to a uniform static pressure rather than its vibrations, Kim et al. [71,72] also observed the cancellation of the electrical outputs when continuous electrodes are used. Based on their theoretical analysis which uses the energy method, Kim et al. [71] found that no net charge output is obtained if their unimorph circular plate is fully covered by continuous electrodes. They obtained theoretically that, if the electrodes were "regrouped" after $0.707r$ (where r is the radius of the plate), the optimum electrical output could be extracted from the deflection of the piezoceramic due to constant static pressure. Although Kim et al. [71] also mentioned that the problem can be handled by collecting the charge developed in different regions separately and reversing the leads in the electrical circuit, they used the concept of "patterned poling" by changing the direction of polarization of the outer piezoceramic region

(that is the region outside a specific radius) in their experimental work [72]. Changing the poling direction implies etching the electrodes at a specific region (at $0.5r$ and $0.75r$ in two separate cases of their work) and then applying a very high electric field in the desired portion of the piezoceramic (in general, at a temperature above the Curie temperature of the piezoelectric material). After the patterned poling process is completed, Kim et al. [72] used a conductive pen to reconstruct the electrodes at the etched regions. Finally, the electric charge is collected using the reconstructed full electrodes and improved results are obtained. They observed experimentally that patterned poling after $0.75r$ gave the best results when compared to the cases of patterned poling after $0.5r$ and the original case with full electrodes and unmodified polarization (in agreement with their theoretical work [71] which predicted the optimum radius as $0.707r$ which is close to $0.75r$). It should also be added that the unmodified case with full electrodes still gave some nonzero electric charge output in the order of magnitude of the other cases, most likely because of some physical imperfections, such as the difficulty in realization of the clamped boundary [72].

Although the approach preferred by Kim et al. [72] appears to be a relatively complicated way of solving the cancellation problem, it is worthwhile to relate it to our discussion on cantilevered beams. The optimum location for etching the electrodes is where the electric displacement changes sign and it corresponds to a *strain node* line in our study on cantilevered harvesters. Once patterned polarization process is completed, continuous electrodes can be used for collecting the charge output. Mathematically, as far as our relevant equations for beams are concerned, the piezoelectric constant ($\overline{e}_{31}$) changes sign in the modified region after the patterned polarization process. The issue of cancellation in the integral given by Eq. (7.2) was due to the opposite sign of the curvature at the opposite sides of the strain nodes when $\overline{e}_{31}$ had the same sign throughout the length of the beam. The new polarization at one side of the strain node makes the sign of the product of the piezoelectric constant and the curvature the same at the opposite sides of the strain node. Hence no cancellation takes place during the integration of the electric displacement over the continuous electrode area. Briefly, in order to avoid the cancellation, either the polarization at one side of the strain node must be reversed (by patterned poling) so that continuous electrodes can be used or the electrodes must be discontinuous at the strain node if the polarization is to be kept the same over the length of the beam (as demonstrated in the previous section).

Although the patterned polarization approach solved the *static* deflection problem of Kim et al. [72] *permanently*, it may not be a flexible approach as far as the *dynamic* (vibration) problem is concerned, since the deflection pattern changes with vibration modes. For a simple explanation, consider the second vibration mode of a cantilevered energy harvester. If the polarization of the harvester is reversed at one side of the strain node (which is located at $\bar{x} = 0.2165$), one can use continuous electrodes (covering $0 \le \bar{x} \le 1$) to collect the charge developed in the piezoceramic and this avoids the cancellation in the integral of Eq. (7.4) for vibrations with the second mode shape. After patterned poling, if the beam with continuous electrodes is used for harvesting energy at the first vibration mode, one ends up with a strong cancellation although there is no strain node in the first vibration mode. Even though the curvature has the same sign throughout the beam length for the first mode shape (Fig. 7.1b), the change in the sign of $\bar{e}_{31}$ at $\bar{x} = 0.2165$ makes it necessary to consider the integral in Eq. (7.4) in two parts where a drastic cancellation occurs between the two areas ($0 \le \bar{x} < 0.2165$ and $0.2165 < \bar{x} \le 1$) as far as the resultant of the inner product in Eq. (7.1) is concerned. Therefore, in the dynamic problem, the patterned poling process can be favorable for a single vibration mode only. Otherwise, one has to repeat the patterned poling process again in order to use the same harvester beam (which was patterned poled for a certain mode shape) for excitations with another mode shape.

Based on the above discussion, it is reasonable to claim that switching the leads of the segmented electrodes (as demonstrated in Section 7.6) is more *flexible* and *reversible* compared to the patterned poling process in the *vibration-based* energy harvesting problem. The patterned poling process can be useful for static problems as a permanent solution since (for a given loading) a single deflection pattern exists in linear static problems, unlike the vibration problems (where the deflection pattern depends on the vibration mode). Using segmented electrodes is easier to implement as the cancellation problem is mainly solved in the electrical circuit by combining the leads of the electrodes accordingly. Moreover, considering the fact that most piezoceramic patches come with integrated electrodes from the manufacturer, one may not have to apply an etching process to obtain a discontinuity at the strain node of the harvester. In most cases, it might be possible to cut the piezoceramic patch (and therefore its electrodes) as done in the simple experimental demonstration of the previous section. The following section discusses a

first approach for handling of the cancellation issue in the electrical circuit for harvesting energy from multiple vibration modes with the same cantilevered harvester.

7.8 Avoiding Cancellation in the Electrical Circuit with Segmented Electrodes

The configuration shown in Fig. 7.9 is the commonly employed [23-25] AC-to-DC conversion circuit through a full-wave rectifier as a primary step in the electrical engineering design and analysis for implementing piezoelectric energy harvesting in order to charge a battery or a capacitor. The electrodes bracketing the piezoceramic layers are connected to a diode bridge to remove the sign alternation of the electrical output. In general, a smoothing capacitor is used at the DC side in order to bring the pulsating rectified voltage to a relatively constant value for the purpose of battery/capacitor charging. Usually a DC-to-DC converter (step-up or step-down) is also required to adjust the voltage level after the rectifier and the smoothing capacitor to the voltage level required to charge a given battery or a capacitor. These electrical engineering aspects are beyond the scope of this dissertation and the particular interest here is to avoid the cancellation of the alternating voltage output of the piezoceramic (which is the *source* to the circuit) before it is supplied to a simple or a sophisticated harvesting circuit. Hence, for convenience, the leads of the DC side are left open in Fig. 7.9. In addition, let the piezoceramic layers of the bimorph in Fig. 7.9 be poled in the opposite directions so that this configuration is the series connection case (Fig. 3.1a).

As mentioned previously, if the harvester beam vibrates with the first mode shape, the strain distribution (and therefore the electric displacement distribution) is in phase throughout the length of the beam. Hence, it is possible to collect the charge developed in the piezoceramic with continuous electrodes without any cancellation. Considering the strain mode shape of the first mode in Fig. 7.1b, it can be observed that the main contribution to the electrical output is from the region which is close to the clamped end of the beam. However, covering the entire (top and bottom) faces of the piezoceramic with a continuous electrode pair gives the maximum electrical output and this classical configuration with continuous electrodes (Fig. 7.9) can safely be used as the first vibration mode has no strain nodes.

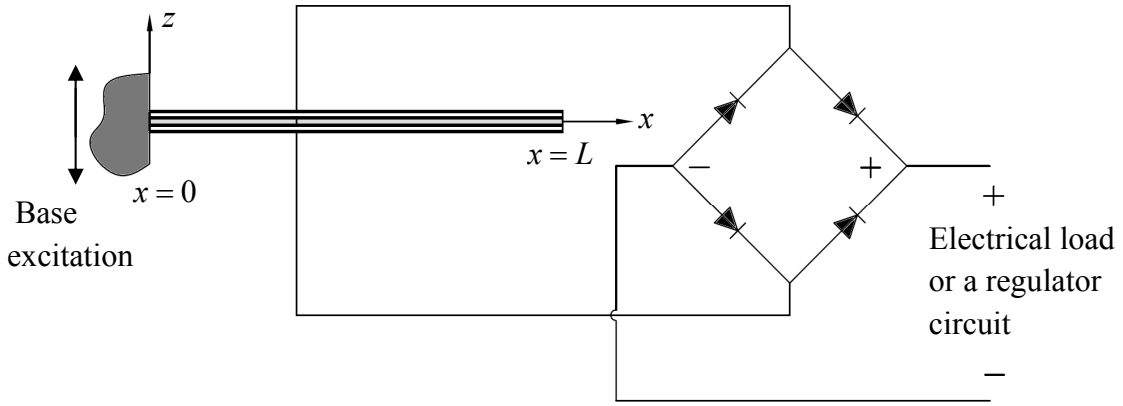

Fig. 7.9 Continuous electrodes are connected to a full-wave rectifier for harvesting energy from the first vibration mode (causes cancellation in mode 2)

If the harvester beam vibrates with the second mode shape, using the configuration with continuous electrodes (Fig. 7.9) results in cancellation of the electrical outputs as theoretically discussed and experimentally demonstrated in this paper. In order to avoid the cancellation in a simple manner, segmented electrodes can be used. Figure 7.10 shows two segmented electrode pairs used for collecting the electric charge developed in $0 \le x < 0.2165L$ and $0.2165L < x \le L$ separately. Note that the bottom electrodes are connected to each other whereas the top electrodes are connected to the diode bridge. This configuration prevents cancellation in harvesting energy from the second vibration mode because the polarization of the electrodes in these two regions is the opposite of each other all the time during the vibratory motion (i.e. when the top electrode in $0 \le x < 0.2165L$ is $(+)$, the bottom electrode in $0.2165L < x \le L$ is also $(+)$, and vice versa). However, if one intends to use the segmented electrode configuration shown in Fig. 7.10 for harvesting energy from the first vibration mode, cancellation occurs because of the way the voltage outputs of $0 \le x < 0.2165L$ and $0.2165L < x \le L$ are combined. Therefore, the configuration displayed in Fig. 7.10 is suitable for vibrations with the second mode shape but it is not preferable for vibrations with the first mode shape.

The configuration given in Fig. 7.9 is suitable for harvesting energy from the first mode (but it causes cancellation in the second mode) whereas the configuration of Fig. 7.10 is suitable for harvesting energy from the second mode (and it is causes cancellation in the first mode). However, it is not difficult to combine the outputs of the segmented electrode pairs in Fig. 7.10 to come up with a configuration that can be used both for the first mode and second mode

vibrations. In the configuration of Fig. 7.11, the electrode pairs are connected to two separate diode bridges so that cancellation is prevented regardless of the instantaneous polarization in $0 \le x < 0.2165L$ and $0.2165L < x \le L$ regions.

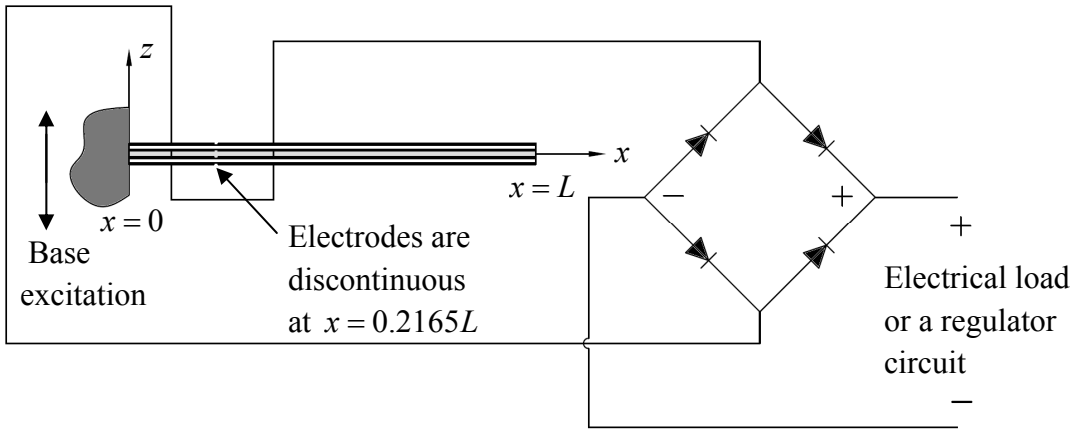

Fig. 7.10 Segmented electrode pairs are connected to a full-wave rectifier for harvesting energy from the second vibration mode (causes cancellation in mode 1)

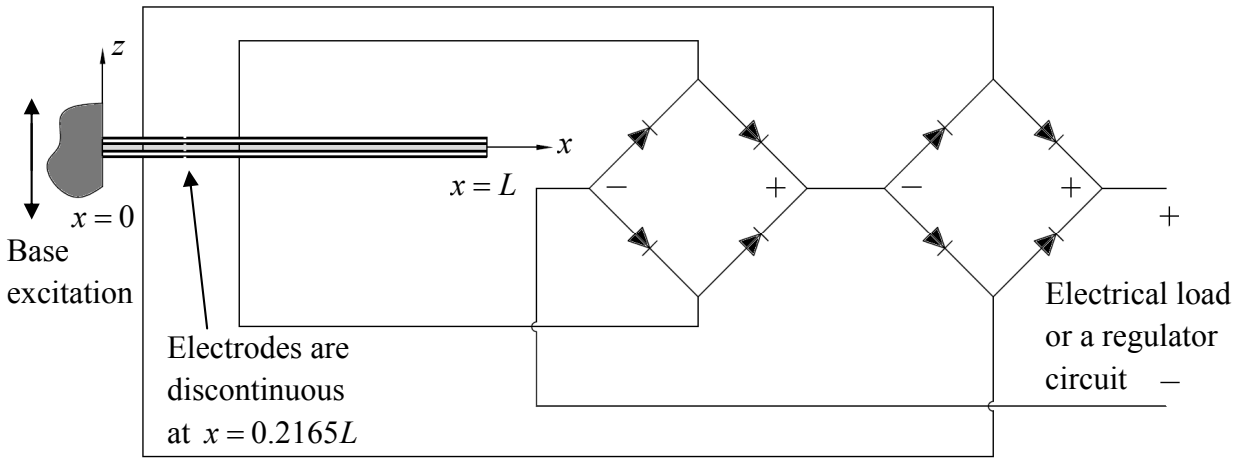

Fig. 7.11 Segmented electrode pairs are connected to two separate full-wave rectifiers for harvesting energy from the first or the second vibration modes (avoids cancellation both in mode 1 and mode 2)

The foregoing approach of avoiding the cancellation issue appears to be easier and more flexible than the patterned poling technique [72]. Here, the only requirements are the removal of electrodes at the strain nodes and simple considerations in the electrical circuit. The idea described here is not limited to the first two vibration modes and it can easily be extended to higher vibration modes and other boundary conditions. Alternative circuitry-based approaches can be investigated to handle the cancellation problem for multi-mode excitations with less number of diodes as the presence of diodes creates losses in the electrical circuit.

7.9 Summary and Conclusions

The positions of the beam where the dynamic strain distribution changes sign are called the strain nodes. It is theoretically discussed and experimentally demonstrated that covering the strain nodes of vibration modes with continuous electrodes results in cancellation of the electrical outputs in piezoelectric energy harvesting. A detailed dimensionless analysis is given for predicting the locations of the strain nodes of a thin cantilever in the absence of a tip mass. Dimensionless derivations and results are then presented for predicting the strain node positions and their variations in the presence of a tip mass. As the cancellation issue is not peculiar to clamped-free boundary conditions, dimensionless data of modal strain nodes are tabulated for some other practical boundary condition pairs as well. The locations of strain nodes tabulated in this work are important also for applications of modal actuation since covering these positions with piezoelectric actuators might require very high voltage inputs. It is experimentally demonstrated that the voltage output due to the second mode excitation can be increased dramatically if segmented electrodes are used instead of continuous electrodes. The relationship between the discussion given here and a recent study on piezoelectric energy harvesting from the static deflection of a clamped circular plate is also explained. The use of segmented electrode pairs to avoid cancellations is described for single-mode and multi-mode vibrations of a cantilevered harvester and alternative circuitry-based approaches can be investigated to handle the cancellation problem for multi-mode excitations.

CHAPTER 8

APPROXIMATE DISTRIBUTED-PARAMETER MODELING OF PIEZOELECTRIC ENERGY HARVESTERS USING THE ELECTROMECHANICAL ASSUMED-MODES METHOD

This chapter covers the approximate distributed-parameter formulation of cantilevered piezoelectric energy harvester beams under base excitation. Since the closed-form analytical solutions for bimorph configurations were obtained in Chapter 3, this chapter provides derivations with a focus on the unimorph configuration (Fig. 8.1). The technique used here is an electromechanical version of the assumed-modes method[*], which is based on the extended Hamilton's principle for electromechanical media. After obtaining the distributed-parameter energy expressions, extended Hamilton's principle is used to derive the discretized electromechanical Lagrange equations. In order to model the asymmetric unimorph structure precisely, an axial displacement variable is introduced to account for coupling of axial and transverse displacement variables due to asymmetric laminates. The derivations are given in this chapter in three parts: (1) the Euler-Bernoulli formulation, (2) the Rayleigh formulation and (3) the Timoshenko formulation. The first type of formulation neglects the rotary inertia and the transverse shear deformation effects whereas the second type includes the rotary inertia effect but neglects the transverse shear deformation. The third solution type accounts for the influences of both the transverse shear deformation and rotary inertia on the resulting electromechanical behavior. Therefore the Euler-Bernoulli solution is valid for thin beams whereas the Timoshenko solution is valid for moderately thick beams (and the Rayleigh solution lies in between). Experimental validations are given for the thin-beam case by comparing the assumed-modes predictions with the experimental and analytical results for different number of modes.

[*] As discussed by Meirovitch [41], the assumed-modes method for distributed-parameter systems is closely related to the Rayleigh-Ritz method. Indeed the resulting discretized equations obtained in both methods are identical for the same admissible functions. The difference is that the Rayleigh-Ritz method is concerned with spatial discretization of the differential eigenvalue problem whereas the assumed-modes method directly begins with spatial discretization of the boundary-value problem in an implicit manner.

8.1 Unimorph Piezoelectric Energy Harvester Configuration

Consider the piezoelectric energy harvester configuration shown in Fig. 8.1. The configuration has a single piezoceramic layer bonded onto a substructure layer, therefore it is a unimorph cantilever. The perfectly conductive electrode pair (of negligible thickness) fully covers the upper and the lower faces of the piezoceramic and is connected to a resistive electrical load. The layers are perfectly bonded to each other so there is no relative sliding at the interface. The purpose is to find the voltage output of the piezoceramic ($v_p(t)$) across the load resistance in response to imposed base excitation. As done in Chapter 3 (where the analytical solutions for symmetric bimorph configurations were given), the base motion is represented as translation in the transverse direction with superimposed small rotation. Deformations are assumed to be small and the material behavior is assumed to be linear elastic. Note that the x, y and z directions, respectively, are coincident with the 1, 2 and 3 directions of piezoelectricity (y-direction is into the page). These directional subscripts are used interchangeably as the former is preferred for mechanical derivations whereas the latter is used in the piezoelectric constitutive relations (Appendix A). Note that the following Euler-Bernoulli, Rayleigh and Timoshenko type derivations can handle modeling of beams with varying cross-section and changing material properties in x-direction. The coupling between the axial and transverse displacement components due to structural asymmetry is taken into consideration in all cases. The harvester beam shown in Fig. 8.1 has no tip mass. The effect of a tip mass (with mass moment of inertia) on the following formulation is discussed after the basic derivations (in Section 8.6).

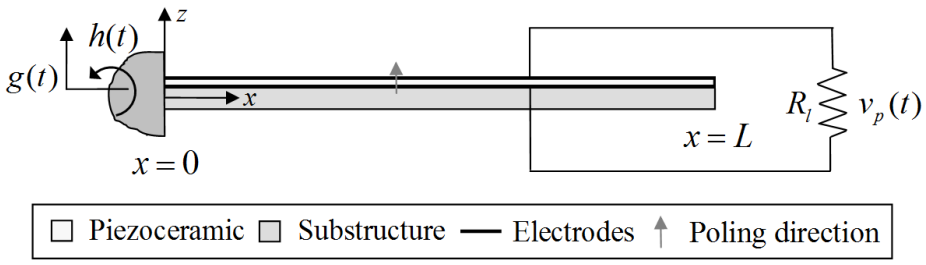

Fig. 8.1 Unimorph piezoelectric energy harvester with varying cross-section

8.2 Electromechanical Euler-Bernoulli Model with Axial Deformations

8.2.1 Distributed-parameter Electromechanical Energy Formulation. The effective base displacement acting on the beam is given by Eq. (3.1) as

$$w_b(x,t) = g(t) + xh(t) \tag{8.1}$$

where $g(t)$ is the translation in the transverse direction and $h(t)$ is the superimposed small rotation.

The displacement field in the beam relative to the moving base can be given by

$$u(x,z,t) = u^0(x,t) - z\frac{\partial w^0(x,t)}{\partial x} \tag{8.2}$$

$$v(x,z,t) = 0 \tag{8.3}$$

$$w(x,z,t) = w^0(x,t) \tag{8.4}$$

where $u^0(x,t)$ and $w^0(x,t)$ are the axial displacement and transverse displacement of the neutral axis at point x and time t relative to the moving base.[†]

The vector form of the displacement field is

$$\mathbf{u} = \begin{bmatrix} u^0(x,t) - z\dfrac{\partial w^0(x,t)}{\partial x} & 0 & w^0(x,t) \end{bmatrix}^t \tag{8.5}$$

where superscript t stands for transpose (otherwise it is time). From this displacement field, the only non-zero strain component can be extracted as

$$S_{xx}(x,z,t) = \frac{\partial u(x,z,t)}{\partial x} = \frac{\partial u^0(x,t)}{\partial x} - z\frac{\partial^2 w^0(x,t)}{\partial x^2} \tag{8.6}$$

The total potential energy in the structure is

$$U = \frac{1}{2}\left(\int_{V_s} \mathbf{S}^t \mathbf{T} dV_s + \int_{V_p} \mathbf{S}^t \mathbf{T} dV_p \right) \tag{8.7}$$

where $\mathbf{S}$ is the vector of engineering strain components, $\mathbf{T}$ is the vector of engineering stress components, the subscripts s and p stand for substructure and piezoceramic, respectively, and the integrations are performed in the volume (V) of the respective material.

[†] The subscript *rel* (used to denote the relative motion) used in Chapters 2 and 3 has been removed here to avoid notation complexity. These terms are defined relative to the moving base throughout this chapter.

The isotropic substructure obeys Hooke's law:

$$T_{xx}(x,z,t) = Y_s S_{xx}(x,z,t) \tag{8.8}$$

where Y_s is the elastic modulus of the substructure layer.

The constitutive relation for the stress component in the piezoceramic is (Appendix A.2)

$$T_{xx}(x,z,t) = T_1 = \overline{c}_{11}^E S_1 - \overline{e}_{31} E_3 = \overline{c}_{11}^E S_{xx}(x,z,t) + \overline{e}_{31} \frac{v_p(t)}{h_p} \tag{8.9}$$

Here, the electric field is given in terms of the voltage across the load (i.e. $E_3(t) = -v_p(t)/h_p$ where $v_p(t)$ is the voltage across the electrodes and h_p is the thickness of the piezoceramic), the reduced elastic modulus, piezoelectric stress constant and the permittivity constant expressions are $\overline{c}_{11}^E = 1/s_{11}^E$, $\overline{e}_{31} = d_{31}/s_{11}^E$ and $\overline{\varepsilon}_{33}^S = \varepsilon_{33}^T - d_{31}^2/s_{11}^E$, respectively (Appendix A.2).

Equation (8.7) becomes

$$\begin{aligned} U = & \frac{1}{2}\int_{V_s} Y_s \left(\frac{\partial u^0(x,t)}{\partial x} - z\frac{\partial^2 w^0(x,t)}{\partial x^2} \right)^2 dV_s \\ & + \frac{1}{2}\int_{V_p} \left[\overline{c}_{11}^E \left(\frac{\partial u^0(x,t)}{\partial x} - z\frac{\partial^2 w^0(x,t)}{\partial x^2} \right)^2 + \overline{e}_{31}\frac{v_p(t)}{h_p}\left(\frac{\partial u^0(x,t)}{\partial x} - z\frac{\partial^2 w^0(x,t)}{\partial x^2} \right) \right] dV_p \end{aligned} \tag{8.10}$$

The total kinetic energy of the system can be given by

$$T = \frac{1}{2}\left(\int_{V_s} \rho_s \frac{\partial \mathbf{u}_m^t}{\partial t}\frac{\partial \mathbf{u}_m}{\partial t} dV_s + \int_{V_p} \rho_p \frac{\partial \mathbf{u}_m^t}{\partial t}\frac{\partial \mathbf{u}_m}{\partial t} dV_p \right) \tag{8.11}$$

where ρ_s and ρ_p are the mass densities of the substructure and piezoceramic layers, and $\mathbf{u}_m$ is the modified displacement vector that is the superposition of the base displacement input given by Eq. (8.1) and the displacement vector $\mathbf{u}$:‡

$$\mathbf{u}_m = \begin{bmatrix} u^0(x,t) - z\dfrac{\partial w^0(x,t)}{\partial x} & 0 & w^0(x,t) + w_b(x,t) \end{bmatrix}^t \tag{8.12}$$

‡ Note that the external forcing on the structure is due to the base motion. Since the total kinetic energy is written for the velocity field of the beam relative to the absolute reference frame, the forcing function on the beam (in terms of $w_b(x,t)$) will emerge from this kinetic energy expression. Alternatively, one could express the total kinetic energy relative to the moving base and include the (virtual) work done by the inertial excitation term (due to base displacement $w_b(x,t)$) as a non-conservative effect.

Then the total kinetic energy becomes

$$T = \frac{1}{2}\int_{V_s} \rho_s \left[\left(\frac{\partial u^0(x,t)}{\partial t} - z\frac{\partial^2 w^0(x,t)}{\partial t \partial x} \right)^2 + \left(\frac{\partial w^0(x,t)}{\partial t} + \frac{\partial w_b(x,t)}{\partial t} \right)^2 \right] dV_s$$
$$+ \int_{V_p} \rho_p \left[\left(\frac{\partial u^0(x,t)}{\partial t} - z\frac{\partial^2 w^0(x,t)}{\partial t \partial x} \right)^2 + \left(\frac{\partial w^0(x,t)}{\partial t} + \frac{\partial w_b(x,t)}{\partial t} \right)^2 \right] dV_p \tag{8.13}$$

The total potential energy can be re-expressed as follows:

$$U = \frac{1}{2}\int_0^L \left\{ Y_s \left[A_s \left(\frac{\partial u^0(x,t)}{\partial x} \right)^2 + I_s \left(\frac{\partial^2 w^0(x,t)}{\partial x^2} \right)^2 - 2H_s \frac{\partial u^0(x,t)}{\partial x}\frac{\partial^2 w^0(x,t)}{\partial x^2} \right] \right.$$
$$+ \bar{c}_{11}^E \left[A_p \left(\frac{\partial u^0(x,t)}{\partial x} \right)^2 + I_p \left(\frac{\partial^2 w^0(x,t)}{\partial x^2} \right)^2 - 2H_p \frac{\partial u^0(x,t)}{\partial x}\frac{\partial^2 w^0(x,t)}{\partial x^2} \right] \cdots \tag{8.14}$$
$$\left. + B_p v_p(t)\frac{\partial u^0(x,t)}{\partial x} + J_p v_p(t)\frac{\partial^2 w^0(x,t)}{\partial x^2} \right\} dx$$

The total kinetic energy in the expanded form is

$$T = \frac{1}{2}\int_0^L \left\{ \rho_s \left[A_s \left(\frac{\partial u^0(x,t)}{\partial t} \right)^2 + A_s \left(\frac{\partial w^0(x,t)}{\partial t} \right)^2 + 2A_s \frac{\partial w^0(x,t)}{\partial t}\frac{\partial w_b(x,t)}{\partial t} + A_s \left(\frac{\partial w_b(x,t)}{\partial t} \right)^2 \right. \right. \cdots$$
$$-2H_s \frac{\partial u^0(x,t)}{\partial t}\frac{\partial^2 w^0(x,t)}{\partial t \partial x} + \cancel{I_s \left(\frac{\partial^2 w^0(x,t)}{\partial t \partial x} \right)^2} \cdots$$
$$+ \rho_p \left[A_p \left(\frac{\partial u^0(x,t)}{\partial t} \right)^2 + A_p \left(\frac{\partial w^0(x,t)}{\partial t} \right)^2 + 2A_p \frac{\partial w^0(x,t)}{\partial t}\frac{\partial w_b(x,t)}{\partial t} + A_p \left(\frac{\partial w_b(x,t)}{\partial t} \right)^2 \cdots \right. \tag{8.15}$$
$$\left. \left. -2H_p \frac{\partial u^0(x,t)}{\partial t}\frac{\partial^2 w^0(x,t)}{\partial t \partial x} + \cancel{I_p \left(\frac{\partial^2 w^0(x,t)}{\partial t \partial x} \right)^2} \right] \right\} dx$$

where the kinetic energy contributions from the rotary inertia are neglected but the terms which might cause inertial coupling between the axial and transverse displacement components due to asymmetric laminates are kept. Here, the zero-th, first and the second moments of area for the substructure and piezoceramic cross-sections at an arbitrary point *x* are

$$\{A_s, H_s, I_s\} = \iint_s \{1, z, z^2\} dydz \tag{8.16}$$

$$\{A_p, H_p, I_p\} = \iint_p \{1, z, z^2\} dydz \tag{8.17}$$

where H_s and H_p vanish for a structure that is symmetric with respect to the neutral axis of the beam (just like a bimorph or any symmetric multi-morph). Therefore, for a symmetric structure, there is no coupling between $u^0(x,t)$ and $w^0(x,t)$. As a result, in a symmetric structure, the axial displacement $u^0(x,t)$ cannot be excited by the imposed base displacement $w_b(x,t)$, which simplifies the problem (and allows analytical solutions as in Chapter 3). It is worth adding that, in the foregoing expressions as well as in the following, $A_s = A_s(x)$, $A_p = A_p(x)$, $H_s = H_s(x)$, $H_p = H_p(x)$, $I_s = I_s(x)$ and $I_p = I_p(x)$ are allowed.

The terms related to piezoelectric coupling are

$$B_p = \iint_p \frac{\overline{e}_{31}}{h_p} dydz \tag{8.18}$$

$$J_p = -\iint_p \frac{\overline{e}_{31}}{h_p} zdydz \tag{8.19}$$

where B_p couples the voltage and the extension component and J_p couples the voltage and the curvature component according to Eq. (8.14).

The internal electrical energy in the piezoceramic layer is

$$W_{ie} = \frac{1}{2}\int_{V_p} \mathbf{E}^t \mathbf{D} dV_p \tag{8.20}$$

where $\mathbf{E}$ is the vector of electric field components and $\mathbf{D}$ is the vector of electric displacement components. Substituting the respective terms (the non-zero electric field and the electric displacement components from Appendix A.2) gives

$$\begin{aligned} W_{ie} &= -\frac{1}{2}\int_{V_p} \frac{v_p(t)}{h_p}\left[\overline{e}_{31}\left(\frac{\partial u^0(x,t)}{\partial x} - z\frac{\partial^2 w^0(x,t)}{\partial x^2}\right) - \overline{\varepsilon}_{33}^S \frac{v_p(t)}{h_p}\right] dV_p \\ &= -\frac{1}{2}\int_0^L \left(B_p v_p(t)\frac{\partial u^0(x,t)}{\partial x} + J_p v_p(t)\frac{\partial^2 w^0(x,t)}{\partial x^2}\right) dx + \frac{1}{2} C_p \left[v_p(t)\right]^2 \end{aligned} \tag{8.21}$$

Here, C_p is the internal capacitance of the piezoceramic given by

$$C_p = \overline{\varepsilon}_{33}^S \frac{A_p}{h_p} \tag{8.22}$$

where A_p is the electrode area.

In order to account for mechanical damping, Rayleigh's dissipation function [41] can be used. Alternatively, a damping matrix proportional to the resulting mass and stiffness matrices can be introduced later (i.e. after the system is discretized in the assumed-modes solution procedure). The second approach is preferred here for simplicity.

The extended Hamilton's principle [30] with the internal electrical energy is

$$\int_{t_1}^{t_2} \left(\delta L + \delta W_{ie} + \delta W_{nc} \right) dt = 0 \tag{8.23}$$

where L is the Lagrangian,

$$L = T - U \tag{8.24}$$

Here, δL and δW_{ie} are the first variations [54] of the Lagrangian and the inertial electrical energy, and δW_{nc} is the virtual work of the non-conservative mechanical force and electric charge components. Since the effect of base excitation is considered in the total kinetic energy term and the mechanical damping effect is to be introduced later, the only non-conservative virtual work is due to the electric charge output ($Q(t)$):

$$\delta W_{nc} = \delta W_{nce} = Q(t)\delta v_p(t) \tag{8.25}$$

Following the regular procedure of the assumed-modes method [41], the next step is to discretize the components of the extended Hamilton's principle, which are the Lagrangian, internal electrical energy and the virtual work of the non-conservative electric charge.

8.2.2 Spatial Discretization of the Energy Equations. The distributed-parameter variables in the mechanical domain are $w^0(x,t)$ and $u^0(x,t)$ while the electrical variable is $v_p(t)$. Let the following two finite series represent the two components of vibration response:

$$w^0(x,t) = \sum_{r=1}^{N} a_r(t)\phi_r(x) \tag{8.26}$$

$$u^0(x,t) = \sum_{r=1}^{N} b_r(t)\alpha_r(x) \tag{8.27}$$

where $\phi_r(x)$ and $\alpha_r(x)$ are the kinematically admissible trial functions which satisfy the respective essential boundary conditions (Appendix D.1), $a_r(t)$ and $b_r(t)$ are the unknown generalized coordinates. Using Eqs. (8.26) and (8.27) in Eq. (8.14), the total potential energy equation becomes

$$U=\frac{1}{2}\sum_{r=1}^{N}\sum_{l=1}^{N}\left\{a_r a_l\int_0^L\left(Y_s I_s+\overline{c}_{11}^E I_p\right)\phi_r''(x)\phi_l''(x)dx+b_r b_l\int_0^L\left(Y_s A_s+\overline{c}_{11}^E A_p\right)\alpha_r'(x)\alpha_l'(x)dx...\right.$$
$$\left.-2a_r b_l\int_0^L\left(Y_s H_s+\overline{c}_{11}^E H_p\right)\phi_r''(x)\alpha_l'(x)dx+b_r v_p(t)\int_0^L B_p\alpha_r'(x)dx+a_r v_p(t)\int_0^L J_p\phi_r''(x)dx\right\} \tag{8.28}$$

where a *prime* represents ordinary differentiation with respect to space (variable x). Similarly, the total kinetic energy expression given by Eq. (8.15) can be discretized to give

$$T=\frac{1}{2}\sum_{r=1}^{N}\sum_{l=1}^{N}\left\{\dot{a}_r\dot{a}_l\int_0^L\left(\rho_s A_s+\rho_p A_p\right)\phi_r(x)\phi_l(x)dx+2\dot{a}_r\int_0^L\left(\rho_s A_s+\rho_p A_p\right)\phi_r(x)\frac{\partial w_b(x,t)}{\partial t}dx...\right.$$
$$+\int_0^L\left(\rho_s A_s+\rho_p A_p\right)\left(\frac{\partial w_b(x,t)}{\partial t}\right)^2dx+\dot{b}_r\dot{b}_l\int_0^L\left(\rho_s A_s+\rho_p A_p\right)\alpha_r(x)\alpha_l(x)dx... \tag{8.29}$$
$$\left.-2\dot{a}_r\dot{b}_l\int_0^L\left(\rho_s H_s+\rho_p H_p\right)\phi_r'(x)\alpha_l(x)dx\right\}$$

where an *over-dot* represents ordinary differentiation with respect to time (variable t).

Substituting Eqs. (8.26) and (8.27) into Eq. (8.21), the internal electrical energy expression becomes

$$W_{ie}=-\frac{1}{2}\sum_{r=1}^{N}\left\{b_r v_p(t)\int_0^L B_p\alpha_r'(x)dx+a_r v_p(t)\int_0^L J_p\phi_r''(x)dx-C_p\left[v_p(t)\right]^2\right\} \tag{8.30}$$

Equations (8.28)-(8.30) can be written as

$$U=\frac{1}{2}\sum_{r=1}^{N}\sum_{l=1}^{N}\left(a_r a_l k_{rl}^{aa}+b_r b_l k_{rl}^{bb}-2a_r b_l k_{rl}^{ab}+a_r v_p\tilde{\theta}_r^a+b_r v_p\tilde{\theta}_r^b\right) \tag{8.32}$$

$$T=\frac{1}{2}\sum_{r=1}^{N}\sum_{l=1}^{N}\left(\dot{a}_r\dot{a}_l m_{rl}^{aa}+\dot{b}_r\dot{b}_l m_{rl}^{bb}-2\dot{a}_r\dot{b}_l m_{rl}^{ab}+2\dot{a}_r p_r\right)+\int_0^L\left(\rho_s A_s+\rho_p A_p\right)\left(\frac{\partial w_b(x,t)}{\partial t}\right)^2dx \tag{8.31}$$

$$W_{ie}=-\frac{1}{2}\sum_{r=1}^{N}\left(a_r v_p\tilde{\theta}_r^a+b_r v_p\tilde{\theta}_r^b-C_p v_p^2\right) \tag{8.33}$$

Here,

$$m_{rl}^{aa}=\int_0^L\left(\rho_s A_s+\rho_p A_p\right)\phi_r(x)\phi_l(x)dx \tag{8.34}$$

$$m_{rl}^{bb}=\int_0^L\left(\rho_s A_s+\rho_p A_p\right)\alpha_r(x)\alpha_l(x)dx \tag{8.35}$$

$$m_{rl}^{ab} = \int_0^L \left(\rho_s H_s + \rho_p H_p\right) \phi_r'(x) \alpha_l(x) dx \tag{8.36}$$

$$p_r = \int_0^L \left(\rho_s A_s + \rho_p A_p\right) \phi_r(x) \frac{\partial w_b(x,t)}{\partial t} dx \tag{8.37}$$

$$k_{rl}^{aa} = \int_0^L \left(Y_s I_s + \overline{c}_{11}^E I_p\right) \phi_r''(x) \phi_l''(x) dx \tag{8.38}$$

$$k_{rl}^{bb} = \int_0^L \left(Y_s I_s + \overline{c}_{11}^E I_p\right) \alpha_r'(x) \alpha_l'(x) dx \tag{8.39}$$

$$k_{rl}^{ab} = \int_0^L \left(Y_s H_s + \overline{c}_{11}^E H_p\right) \phi_r''(x) \alpha_l'(x) dx \tag{8.40}$$

$$\tilde{\theta}_r^a = \int_0^L J_p \phi_r''(x) dx \tag{8.41}$$

$$\tilde{\theta}_r^b = \int_0^L B_p \alpha_r'(x) dx \tag{8.42}$$

where $r = 1,...,N$ and $l = 1,...,N$.

8.2.3 Electromechanical Lagrange Equations. The electromechanical Lagrange equations based on the extended Hamilton's principle given by Eq. (8.23) are (Appendix E)

$$\frac{d}{dt}\left(\frac{\partial T}{\partial \dot{a}_i}\right) - \frac{\partial T}{\partial a_i} + \frac{\partial U}{\partial a_i} - \frac{\partial W_{ie}}{\partial a_i} = 0 \tag{8.43}$$

$$\frac{d}{dt}\left(\frac{\partial T}{\partial \dot{b}_i}\right) - \frac{\partial T}{\partial b_i} + \frac{\partial U}{\partial b_i} - \frac{\partial W_{ie}}{\partial b_i} = 0 \tag{8.44}$$

$$\frac{d}{dt}\left(\frac{\partial T}{\partial \dot{v}_p}\right) - \frac{\partial T}{\partial v_p} + \frac{\partial U}{\partial v_p} - \frac{\partial W_{ie}}{\partial v_p} = Q \tag{8.45}$$

where Q is the electric charge output of the piezoceramic layer. Recall that the mechanical forcing function due to base excitation is expected to come out from the total kinetic energy and the mechanical dissipation effects will be introduced in the form of proportional damping later in this section.

The non-zero components of Eq. (8.43) are

$$\frac{\partial T}{\partial \dot{a}_i} = \frac{1}{2}\sum_{r=1}^{N}\sum_{l=1}^{N}\left[\left(\frac{\partial \dot{a}_r}{\partial \dot{a}_i}\dot{a}_l + \frac{\partial \dot{a}_l}{\partial \dot{a}_i}\dot{a}_r\right)m_{rl}^{aa} - 2\frac{\partial \dot{a}_r}{\partial \dot{a}_i}\dot{b}_l m_{rl}^{ab} + 2\frac{\partial \dot{a}_r}{\partial \dot{a}_i}p_r\right]$$
$$= \frac{1}{2}\sum_{r=1}^{N}\sum_{l=1}^{N}\left[\left(\delta_{ri}\dot{a}_l + \delta_{li}\dot{a}_r\right)m_{rl}^{aa} - 2\delta_{ri}\dot{b}_l m_{rl}^{ab} + 2\delta_{ri}p_r\right] = \sum_{l=1}^{N}\left(m_{il}^{aa}\dot{a}_l - m_{il}^{ab}\dot{b}_l + p_i\right) \tag{8.46}$$

$$\frac{\partial U}{\partial a_i} = \frac{1}{2}\sum_{r=1}^{N}\sum_{l=1}^{N}\left[\left(\frac{\partial a_r}{\partial a_i}a_l + \frac{\partial a_l}{\partial a_i}a_r\right)k_{rl}^{aa} - 2\frac{\partial a_r}{\partial a_i}b_l k_{rl}^{ab} + \frac{\partial a_r}{\partial a_i}v_p\tilde{\theta}_r^a\right]$$
$$= \frac{1}{2}\sum_{r=1}^{N}\sum_{l=1}^{N}\left[\left(\delta_{ri}a_l + \delta_{li}a_r\right)k_{rl}^{aa} - 2\delta_{ri}b_l k_{rl}^{ab} + \delta_{ri}v_p\tilde{\theta}_r^a\right] = \sum_{l=1}^{N}\left(k_{il}^{aa}a_l - k_{il}^{ab}b_l\right) + \frac{1}{2}\tilde{\theta}_i^a v_p \tag{8.47}$$

$$\frac{\partial W_{ie}}{\partial a_i} = -\frac{1}{2}\sum_{r=1}^{N}\frac{\partial a_r}{\partial a_i}v_p\tilde{\theta}_r^a = -\frac{1}{2}\sum_{r=1}^{N}\delta_{ri}v_p\tilde{\theta}_r^a = -\frac{1}{2}\tilde{\theta}_i^a v_p \tag{8.48}$$

Then the first set of Lagrange equations (for the generalized coordinate a_l) become

$$\sum_{l=1}^{N}\left(m_{il}^{aa}\ddot{a}_l - m_{il}^{ab}\ddot{b}_l + k_{il}^{aa}a_l - k_{il}^{ab}b_l + \tilde{\theta}_i^a v_p - f_i\right) = 0 \tag{8.49}$$

where f_i is the forcing component due to base excitation

$$f_i = -\frac{\partial p_i}{\partial t} = -\int_0^L\left(\rho_s A_s + \rho_p A_p\right)\phi_i(x)\frac{\partial^2 w_b(x,t)}{\partial t^2}dx$$
$$= -\frac{d^2 g(t)}{dt^2}\int_0^L\left(\rho_s A_s + \rho_p A_p\right)\phi_i(x)dx - \frac{d^2 h(t)}{dt^2}\int_0^L\left(\rho_s A_s + \rho_p A_p\right)x\phi_i(x)dx \tag{8.50}$$

Similarly, the non-zero components in Eq. (8.44) are

$$\frac{\partial T}{\partial \dot{b}_i} = \frac{1}{2}\sum_{r=1}^{N}\sum_{l=1}^{N}\left[\left(\frac{\partial \dot{b}_r}{\partial \dot{b}_i}\dot{b}_l + \frac{\partial \dot{b}_l}{\partial \dot{b}_i}\dot{b}_r\right)m_{rl}^{bb} - 2\frac{\partial \dot{b}_r}{\partial \dot{b}_i}\dot{a}_l m_{rl}^{ab}\right]$$
$$= \frac{1}{2}\sum_{r=1}^{N}\sum_{l=1}^{N}\left[\left(\delta_{ri}\dot{b}_l + \delta_{li}\dot{b}_r\right)m_{rl}^{bb} - 2\delta_{ri}\dot{a}_l m_{rl}^{ab}\right] = \sum_{l=1}^{N}\left(m_{il}^{bb}\dot{b}_l - m_{il}^{ab}\dot{a}_l\right) \tag{8.51}$$

$$\frac{\partial U}{\partial b_i} = \frac{1}{2}\sum_{r=1}^{N}\sum_{l=1}^{N}\left[\left(\frac{\partial b_r}{\partial b_i}b_l + \frac{\partial b_l}{\partial b_i}b_r\right)k_{rl}^{bb} - 2\frac{\partial b_r}{\partial b_i}a_l k_{rl}^{ab} + \frac{\partial b_r}{\partial b_i}v_p\tilde{\theta}_r^b\right]$$
$$= \frac{1}{2}\sum_{r=1}^{N}\sum_{l=1}^{N}\left[\left(\delta_{ri}b_l + \delta_{li}b_r\right)k_{rl}^{bb} - 2\delta_{ri}a_l k_{rl}^{ab} + \delta_{ri}v_p\tilde{\theta}_r^b\right] = \sum_{l=1}^{N}\left(k_{il}^{bb}b_l - k_{il}^{ab}a_l\right) + \frac{1}{2}\tilde{\theta}_i^b v_p \tag{8.52}$$

$$\frac{\partial W_{ie}}{\partial b_i} = -\frac{1}{2}\sum_{r=1}^{N}\frac{\partial b_r}{\partial b_i}v_p\tilde{\theta}_r^b = -\frac{1}{2}\sum_{r=1}^{N}\delta_{ri}v_p\tilde{\theta}_r^b = -\frac{1}{2}\tilde{\theta}_i^b v_p \tag{8.53}$$

The Lagrange equation for the generalized coordinate b_l is

$$\sum_{l=1}^{N}\left(m_{il}^{bb}\ddot{b}_l - m_{il}^{ab}\ddot{a}_l + k_{il}^{bb}b_l - k_{il}^{ab}a_l + \tilde{\theta}_i^b v_p\right) = 0 \tag{8.54}$$

The non-zero components on the left hand side of Eq. (8.45) are

$$\frac{\partial U}{\partial v_p} = \frac{1}{2}\sum_{r=1}^{N}\left(a_r\tilde{\theta}_r^a + b_r\tilde{\theta}_r^b\right) \tag{8.55}$$

$$\frac{\partial W_{ie}}{\partial v_p} = C_p v_p - \frac{1}{2}\sum_{r=1}^{N}\left(a_r\tilde{\theta}_r^a + b_r\tilde{\theta}_r^b\right) \tag{8.56}$$

yielding

$$C_p v_p + Q - \sum_{r=1}^{N}\left(a_r\tilde{\theta}_r^a + b_r\tilde{\theta}_r^b\right) = 0 \tag{8.57}$$

Taking the time derivative of Eq. (8.57) gives

$$C_p\dot{v}_p + \dot{Q} - \sum_{r=1}^{N}\left(\dot{a}_r\tilde{\theta}_r^a + \dot{b}_r\tilde{\theta}_r^b\right) = 0 \tag{8.58}$$

where the time rate of change of charge is the electric current passing through the resistor:

$$\dot{Q} = \frac{v_p}{R_l} \tag{8.59}$$

The Lagrange equation for v_p becomes

$$C_p\dot{v}_p + \frac{v_p}{R_l} - \sum_{r=1}^{N}\left(\dot{a}_r\tilde{\theta}_r^a + \dot{b}_r\tilde{\theta}_r^b\right) = 0 \tag{8.60}$$

The first two Lagrange equations (Eqs. (8.49) and (8.54)) can be given in the matrix form as

$$\begin{bmatrix}\mathbf{m}^{aa} & \mathbf{-m}^{ab}\\ \mathbf{-m}^{ab} & \mathbf{m}^{bb}\end{bmatrix}\begin{Bmatrix}\ddot{\mathbf{a}}\\ \ddot{\mathbf{b}}\end{Bmatrix} + \begin{bmatrix}\mathbf{k}^{aa} & \mathbf{-k}^{ab}\\ \mathbf{-k}^{ab} & \mathbf{k}^{bb}\end{bmatrix}\begin{Bmatrix}\mathbf{a}\\ \mathbf{b}\end{Bmatrix} + \begin{Bmatrix}\tilde{\boldsymbol{\theta}}^{a}\\ \tilde{\boldsymbol{\theta}}^{b}\end{Bmatrix}v_p = \begin{Bmatrix}\mathbf{f}\\ \mathbf{0}\end{Bmatrix} \tag{8.61}$$

Introducing Rayleigh damping to represent the dissipative electromechanical system as a normal-mode system:

$$\begin{bmatrix}\mathbf{m}^{aa} & \mathbf{-m}^{ab}\\ \mathbf{-m}^{ab} & \mathbf{m}^{bb}\end{bmatrix}\begin{Bmatrix}\ddot{\mathbf{a}}\\ \ddot{\mathbf{b}}\end{Bmatrix} + \begin{bmatrix}\mathbf{d}^{aa} & \mathbf{-d}^{ab}\\ \mathbf{-d}^{ab} & \mathbf{d}^{bb}\end{bmatrix}\begin{Bmatrix}\dot{\mathbf{a}}\\ \dot{\mathbf{b}}\end{Bmatrix} + \begin{bmatrix}\mathbf{k}^{aa} & \mathbf{-k}^{ab}\\ \mathbf{-k}^{ab} & \mathbf{k}^{bb}\end{bmatrix}\begin{Bmatrix}\mathbf{a}\\ \mathbf{b}\end{Bmatrix} + \begin{Bmatrix}\tilde{\boldsymbol{\theta}}^{a}\\ \tilde{\boldsymbol{\theta}}^{b}\end{Bmatrix}v_p = \begin{Bmatrix}\mathbf{f}\\ \mathbf{0}\end{Bmatrix} \tag{8.62}$$

where the damping matrix is

$$\begin{bmatrix}\mathbf{d}^{aa} & \mathbf{-d}^{ab}\\ \mathbf{-d}^{ab} & \mathbf{d}^{bb}\end{bmatrix} = \mu\begin{bmatrix}\mathbf{m}^{aa} & \mathbf{-m}^{ab}\\ \mathbf{-m}^{ab} & \mathbf{m}^{bb}\end{bmatrix} + \gamma\begin{bmatrix}\mathbf{k}^{aa} & \mathbf{-k}^{ab}\\ \mathbf{-k}^{ab} & \mathbf{k}^{bb}\end{bmatrix} \tag{8.63}$$

Here, μ and γ are the constants of mass and stiffness proportionality, respectively.

The electrical circuit equation given by Eq. (8.60) becomes

$$C_p \dot{v}_p + \frac{v_p}{R_l} - \left(\tilde{\boldsymbol{\theta}}^{\mathbf{a}}\right)^t \dot{\mathbf{a}} - \left(\tilde{\boldsymbol{\theta}}^{\mathbf{b}}\right)^t \dot{\mathbf{b}} = 0 \tag{8.64}$$

Equations (8.62) and (8.64) are the discretized equations of the distributed-parameter electromechanical system. Here, the $N \times 1$ vectors of generalized coordinates are

$$\mathbf{a} = \begin{bmatrix} a_1 & a_2 & \dots & a_N \end{bmatrix}^t, \ \mathbf{b} = \begin{bmatrix} b_1 & b_2 & \dots & b_N \end{bmatrix}^t \tag{8.65}$$

and the $N \times 1$ vectors of electromechanical coupling are

$$\tilde{\boldsymbol{\theta}}^{\mathbf{a}} = \begin{bmatrix} \tilde{\theta}_1^a & \tilde{\theta}_2^a & \dots & \tilde{\theta}_N^a \end{bmatrix}^t, \ \tilde{\boldsymbol{\theta}}^{\mathbf{b}} = \begin{bmatrix} \tilde{\theta}_1^b & \tilde{\theta}_2^b & \dots & \tilde{\theta}_N^b \end{bmatrix}^t \tag{8.66}$$

and the mass, stiffness and damping sub-matrices ($\mathbf{m}^{\mathbf{aa}}$, $\mathbf{m}^{\mathbf{bb}}$, $\mathbf{m}^{\mathbf{ab}}$, $\mathbf{k}^{\mathbf{aa}}$, $\mathbf{k}^{\mathbf{bb}}$, $\mathbf{k}^{\mathbf{ab}}$, $\mathbf{d}^{\mathbf{aa}}$, $\mathbf{d}^{\mathbf{bb}}$ and $\mathbf{d}^{\mathbf{ab}}$) are $N \times N$ matrices and the forcing vector $\mathbf{f}$ is an $N \times 1$ vector whose elements are given by Eq. (8.50).

8.2.4 Solution of the Electromechanical Lagrange Equations. The electromechanical Lagrange equations given by Eqs. (8.62) and (8.64) can be re-expressed as

$$\mathbf{m}^{\mathbf{aa}}\ddot{\mathbf{a}} - \mathbf{m}^{\mathbf{ab}}\ddot{\mathbf{b}} + \mathbf{d}^{\mathbf{aa}}\dot{\mathbf{a}} - \mathbf{d}^{\mathbf{ab}}\dot{\mathbf{b}} + \mathbf{k}^{\mathbf{aa}}\mathbf{a} - \mathbf{k}^{\mathbf{ab}}\mathbf{b} + \tilde{\boldsymbol{\theta}}^{\mathbf{a}} v_p = \mathbf{f} \tag{8.67}$$

$$-\mathbf{m}^{\mathbf{ab}}\ddot{\mathbf{a}} + \mathbf{m}^{\mathbf{bb}}\ddot{\mathbf{b}} - \mathbf{d}^{\mathbf{ab}}\dot{\mathbf{a}} + \mathbf{d}^{\mathbf{bb}}\dot{\mathbf{b}} - \mathbf{k}^{\mathbf{ab}}\mathbf{a} + \mathbf{k}^{\mathbf{bb}}\mathbf{b} + \tilde{\boldsymbol{\theta}}^{\mathbf{b}} v_p = \mathbf{0} \tag{8.68}$$

$$C_p \dot{v}_p + \frac{v_p}{R_l} = \left(\tilde{\boldsymbol{\theta}}^{\mathbf{a}}\right)^t \dot{\mathbf{a}} + \left(\tilde{\boldsymbol{\theta}}^{\mathbf{b}}\right)^t \dot{\mathbf{b}} \tag{8.69}$$

If the base displacement is harmonic of the form $g(t) = W_0 e^{j\omega t}$ and $h(t) = \theta_0 e^{j\omega t}$, then the components of the forcing vector become

$$\mathbf{f} = \mathbf{F} e^{j\omega t} \tag{8.70}$$

Here,

$$F_r = -\sigma_r \omega^2 W_0 - \tau_r \omega^2 \theta_0 \tag{8.71}$$

where

$$\sigma_r = -\int_0^L \left(\rho_s A_s + \rho_p A_p\right) \phi_r(x) dx \tag{8.72}$$

$$\tau_r = -\int_0^L \left(\rho_s A_s + \rho_p A_p\right) x \phi_r(x) dx \tag{8.73}$$

Based on the linear electromechanical system assumption, the generalized coordinates and the voltage output at steady state are $\mathbf{a} = \mathbf{A}e^{j\omega t}$, $\mathbf{b} = \mathbf{B}e^{j\omega t}$ and $v_p = V_p e^{j\omega t}$ (where $\mathbf{A} = \begin{bmatrix} A_1 & A_2 & \ldots & A_N \end{bmatrix}^t$, $\mathbf{B} = \begin{bmatrix} B_1 & B_2 & \ldots & B_N \end{bmatrix}^t$ and V_p are complex valued). Equations (8.67)-(8.69) become

$$\left(-\omega^2 \mathbf{m}^{\mathbf{aa}} + j\omega \mathbf{d}^{\mathbf{aa}} + \mathbf{k}^{\mathbf{aa}}\right)\mathbf{A} - \left(-\omega^2 \mathbf{m}^{\mathbf{ab}} + j\omega \mathbf{d}^{\mathbf{ab}} + \mathbf{k}^{\mathbf{ab}}\right)\mathbf{B} + \tilde{\boldsymbol{\theta}}^{\mathbf{a}} V_p = \mathbf{F} \tag{8.74}$$

$$-\left(-\omega^2 \mathbf{m}^{\mathbf{ab}} + j\omega \mathbf{d}^{\mathbf{ab}} + \mathbf{k}^{\mathbf{ab}}\right)\mathbf{A} + \left(-\omega^2 \mathbf{m}^{\mathbf{bb}} + j\omega \mathbf{d}^{\mathbf{bb}} + \mathbf{k}^{\mathbf{bb}}\right)\mathbf{B} + \tilde{\boldsymbol{\theta}}^{\mathbf{b}} V_p = \mathbf{0} \tag{8.75}$$

$$\left(j\omega C_p + \frac{1}{R_l}\right) V_p = j\omega \left[\left(\tilde{\boldsymbol{\theta}}^{\mathbf{a}}\right)^t \mathbf{A} + \left(\tilde{\boldsymbol{\theta}}^{\mathbf{b}}\right)^t \mathbf{B}\right] \tag{8.76}$$

From Eq. (8.76):

$$V_p = j\omega \left(j\omega C_p + \frac{1}{R_l}\right)^{-1} \left[\left(\tilde{\boldsymbol{\theta}}^{\mathbf{a}}\right)^t \mathbf{A} + \left(\tilde{\boldsymbol{\theta}}^{\mathbf{b}}\right)^t \mathbf{B}\right] \tag{8.77}$$

Substituting Eq. (8.77) into Eqs. (8.74) and (8.75) gives

$$\boldsymbol{\Gamma}^{\mathbf{aa}} \mathbf{A} - \boldsymbol{\Gamma}^{\mathbf{ab}} \mathbf{B} = \mathbf{F} \tag{8.78}$$

$$-\boldsymbol{\Gamma}^{\mathbf{ba}} \mathbf{A} + \boldsymbol{\Gamma}^{\mathbf{bb}} \mathbf{B} = \mathbf{0} \tag{8.79}$$

where

$$\boldsymbol{\Gamma}^{\mathbf{aa}} = -\omega^2 \mathbf{m}^{\mathbf{aa}} + j\omega \mathbf{d}^{\mathbf{aa}} + \mathbf{k}^{\mathbf{aa}} + j\omega \left(j\omega C_p + \frac{1}{R_l}\right)^{-1} \tilde{\boldsymbol{\theta}}^{\mathbf{a}} \left(\tilde{\boldsymbol{\theta}}^{\mathbf{a}}\right)^t \tag{8.80}$$

$$\boldsymbol{\Gamma}^{\mathbf{bb}} = -\omega^2 \mathbf{m}^{\mathbf{bb}} + j\omega \mathbf{d}^{\mathbf{bb}} + \mathbf{k}^{\mathbf{bb}} + j\omega \left(j\omega C_p + \frac{1}{R_l}\right)^{-1} \tilde{\boldsymbol{\theta}}^{\mathbf{b}} \left(\tilde{\boldsymbol{\theta}}^{\mathbf{b}}\right)^t \tag{8.81}$$

$$\boldsymbol{\Gamma}^{\mathbf{ab}} = -\omega^2 \mathbf{m}^{\mathbf{ab}} + j\omega \mathbf{d}^{\mathbf{ab}} + \mathbf{k}^{\mathbf{ab}} - j\omega \left(j\omega C_p + \frac{1}{R_l}\right)^{-1} \tilde{\boldsymbol{\theta}}^{\mathbf{a}} \left(\tilde{\boldsymbol{\theta}}^{\mathbf{b}}\right)^t \tag{8.82}$$

$$\boldsymbol{\Gamma}^{\mathbf{ba}} = -\omega^2 \mathbf{m}^{\mathbf{ab}} + j\omega \mathbf{d}^{\mathbf{ab}} + \mathbf{k}^{\mathbf{ab}} - j\omega \left(j\omega C_p + \frac{1}{R_l}\right)^{-1} \tilde{\boldsymbol{\theta}}^{\mathbf{b}} \left(\tilde{\boldsymbol{\theta}}^{\mathbf{a}}\right)^t \tag{8.83}$$

From Eq. (8.79):

$$\mathbf{B} = \left(\boldsymbol{\Gamma}^{\mathbf{bb}}\right)^{-1} \boldsymbol{\Gamma}^{\mathbf{ba}} \mathbf{A} \tag{8.84}$$

Substituting Eq. (8.84) into Eq. (8.78) gives the complex generalize coordinate amplitudes A_r:

$$\mathbf{A} = \left[\boldsymbol{\Gamma}^{\mathbf{aa}} - \boldsymbol{\Gamma}^{\mathbf{ab}} \left(\boldsymbol{\Gamma}^{\mathbf{bb}} \right)^{-1} \boldsymbol{\Gamma}^{\mathbf{ba}} \right]^{-1} \mathbf{F} \tag{8.85}$$

Back substitution of Eq. (8.85) into Eq. (8.84) gives the complex generalized coordinate amplitudes B_r:

$$\mathbf{B} = \left(\boldsymbol{\Gamma}^{\mathbf{bb}} \right)^{-1} \boldsymbol{\Gamma}^{\mathbf{ba}} \left[\boldsymbol{\Gamma}^{\mathbf{aa}} - \boldsymbol{\Gamma}^{\mathbf{ab}} \left(\boldsymbol{\Gamma}^{\mathbf{bb}} \right)^{-1} \boldsymbol{\Gamma}^{\mathbf{ba}} \right]^{-1} \mathbf{F} \tag{8.86}$$

Eventually, the complex voltage amplitude V_p is obtained from Eq. (8.77) as

$$V_p = j\omega \left(j\omega C_p + \frac{1}{R_l} \right)^{-1} \left[\left(\tilde{\boldsymbol{\theta}}^{\mathbf{a}} \right)^t + \left(\tilde{\boldsymbol{\theta}}^{\mathbf{b}} \right)^t \left(\boldsymbol{\Gamma}^{\mathbf{bb}} \right)^{-1} \boldsymbol{\Gamma}^{\mathbf{ba}} \right] \left[\boldsymbol{\Gamma}^{\mathbf{aa}} - \boldsymbol{\Gamma}^{\mathbf{ab}} \left(\boldsymbol{\Gamma}^{\mathbf{bb}} \right)^{-1} \boldsymbol{\Gamma}^{\mathbf{ba}} \right]^{-1} \mathbf{F} \tag{8.87}$$

Substituting the elements of **A** and **B** into Eqs. (8.26) and (8.27) gives the transverse displacement and axial displacement response expressions at steady state as

$$w^0(x,t) = \sum_{r=1}^{N} A_r e^{j\omega t} \phi_r(x) \tag{8.88}$$

$$u^0(x,t) = \sum_{r=1}^{N} B_r e^{j\omega t} \alpha_r(x) \tag{8.89}$$

The steady-state voltage response is

$$v_p(t) = j\omega \left(j\omega C_p + \frac{1}{R_l} \right)^{-1} \left[\left(\tilde{\boldsymbol{\theta}}^{\mathbf{a}} \right)^t + \left(\tilde{\boldsymbol{\theta}}^{\mathbf{b}} \right)^t \left(\boldsymbol{\Gamma}^{\mathbf{bb}} \right)^{-1} \boldsymbol{\Gamma}^{\mathbf{ba}} \right] \left[\boldsymbol{\Gamma}^{\mathbf{aa}} - \boldsymbol{\Gamma}^{\mathbf{ab}} \left(\boldsymbol{\Gamma}^{\mathbf{bb}} \right)^{-1} \boldsymbol{\Gamma}^{\mathbf{ba}} \right]^{-1} \mathbf{F} e^{j\omega t} \tag{8.90}$$

Following the procedure of Chapter 3, one can use the split form of the base excitation given by Eq. (8.71) ($\mathbf{F} = -\boldsymbol{\sigma}\omega^2 W_0 - \boldsymbol{\tau}\omega^2 \theta_0$) and define 6 electromechanical FRFs for the 3 steady-state response expressions given by Eqs. (8.88)-(8.90) per base acceleration components. These FRFs are

$$\frac{w^0(x,t)}{-\omega^2 W_0 e^{j\omega t}},\ \frac{u^0(x,t)}{-\omega^2 W_0 e^{j\omega t}},\ \frac{v_p(t)}{-\omega^2 W_0 e^{j\omega t}},\ \frac{w^0(x,t)}{-\omega^2 \theta_0 e^{j\omega t}},\ \frac{u^0(x,t)}{-\omega^2 \theta_0 e^{j\omega t}},\ \frac{v_p(t)}{-\omega^2 \theta_0 e^{j\omega t}} \tag{8.91}$$

It is worth mentioning that the short-circuit and the open-circuit natural frequencies of the system can be obtained from the homogeneous form of Eqs. (8.78) and (8.79) by setting the mechanical damping terms equal to zero ($\mathbf{d} \to \mathbf{0}$) and considering the $R_l \to 0$ and $R_l \to \infty$ cases, respectively:

$$\begin{bmatrix} \boldsymbol{\Gamma}^{\mathbf{aa}} & -\boldsymbol{\Gamma}^{\mathbf{ab}} \\ -\boldsymbol{\Gamma}^{\mathbf{ba}} & \boldsymbol{\Gamma}^{\mathbf{bb}} \end{bmatrix} \begin{Bmatrix} \mathbf{A} \\ \mathbf{B} \end{Bmatrix} = \begin{Bmatrix} \mathbf{0} \\ \mathbf{0} \end{Bmatrix} \tag{8.92}$$

The characteristic equation is obtained from the determinant

$$\begin{vmatrix} \mathbf{\Gamma^{aa}} & \mathbf{-\Gamma^{ab}} \\ \mathbf{-\Gamma^{ba}} & \mathbf{\Gamma^{bb}} \end{vmatrix} = 0 \tag{8.93}$$

After removing the mechanical damping terms in the sub-matrices $\mathbf{\Gamma^{aa}}$, $\mathbf{\Gamma^{ab}}$, $\mathbf{\Gamma^{ba}}$, $\mathbf{\Gamma^{bb}}$, if one sets $R_l \to 0$, the electrical coupling terms simply vanish and the resulting natural frequencies obtained from Eq. (8.93) are the short-circuit natural frequencies (natural frequencies at the constant electric field condition). If one sets $R_l \to \infty$, the resulting natural frequencies are the open-circuit natural frequencies (natural frequencies at the constant electric displacement condition) as the effective stiffness increases due to electromechanical coupling.

8.3 Electromechanical Rayleigh Model with Axial Deformations

8.3.1 Distributed-parameter Electromechanical Energy Formulation. The form of the total potential energy is the same as that of the Euler-Bernoulli formulation:

$$\begin{aligned} U = \frac{1}{2}\int_0^L \Bigg\{ & Y_s \left[A_s \left(\frac{\partial u^0(x,t)}{\partial x} \right)^2 + I_s \left(\frac{\partial^2 w^0(x,t)}{\partial x^2} \right)^2 - 2H_s \frac{\partial u^0(x,t)}{\partial x} \frac{\partial^2 w^0(x,t)}{\partial x^2} \right] \dots \\ & + \bar{c}_{11}^E \left[A_p \left(\frac{\partial u^0(x,t)}{\partial x} \right)^2 + I_p \left(\frac{\partial^2 w^0(x,t)}{\partial x^2} \right)^2 - 2H_p \frac{\partial u^0(x,t)}{\partial x} \frac{\partial^2 w^0(x,t)}{\partial x^2} \right] \dots \\ & + B_p v_p(t) \frac{\partial u^0(x,t)}{\partial x} + J_p v_p(t) \frac{\partial^2 w^0(x,t)}{\partial x^2} \Bigg\} dx \end{aligned} \tag{8.94}$$

The main difference in the Rayleigh formulation is that the rotary inertia terms are kept in the total kinetic energy expression:

$$\begin{aligned} T = \frac{1}{2}\int_0^L \Bigg\{ & \rho_s \left[A_s \left(\frac{\partial u^0(x,t)}{\partial t} \right)^2 + A_s \left(\frac{\partial w^0(x,t)}{\partial t} \right)^2 + 2A_s \frac{\partial w^0(x,t)}{\partial t} \frac{\partial w_b(x,t)}{\partial t} + A_s \left(\frac{\partial w_b(x,t)}{\partial t} \right)^2 \dots \right. \\ & \left. - 2H_s \frac{\partial u^0(x,t)}{\partial t} \frac{\partial^2 w^0(x,t)}{\partial t \partial x} + I_s \left(\frac{\partial^2 w^0(x,t)}{\partial t \partial x} \right)^2 \dots \right] \\ & + \rho_p \left[A_p \left(\frac{\partial u^0(x,t)}{\partial t} \right)^2 + A_p \left(\frac{\partial w^0(x,t)}{\partial t} \right)^2 + 2A_p \frac{\partial w^0(x,t)}{\partial t} \frac{\partial w_b(x,t)}{\partial t} + A_p \left(\frac{\partial w_b(x,t)}{\partial t} \right)^2 \dots \right. \end{aligned}$$

$$-2H_p\frac{\partial u^0(x,t)}{\partial t}\frac{\partial^2 w^0(x,t)}{\partial t\partial x}+I_p\left(\frac{\partial^2 w^0(x,t)}{\partial t\partial x}\right)^2\Bigg]\Bigg\}dx \tag{8.95}$$

The internal electrical energy and the non-conservative work of the charge output are also the same as in the previous discussion:

$$\begin{aligned}W_{ie}&=-\frac{1}{2}\int_{V_p}\frac{v_p(t)}{h_p}\left[\overline{e}_{31}\left(\frac{\partial u^0(x,t)}{\partial x}-z\frac{\partial^2 w^0(x,t)}{\partial x^2}\right)-\overline{\varepsilon}_{33}^S\frac{v_p(t)}{h_p}\right]dV_p\\&=-\frac{1}{2}\int_0^L\left(B_p v_p(t)\frac{\partial u^0(x,t)}{\partial x}+J_p v_p(t)\frac{\partial^2 w^0(x,t)}{\partial x^2}\right)dx+\frac{1}{2}C_p\left[v_p(t)\right]^2\end{aligned} \tag{8.96}$$

$$\delta W_{nc}=\delta W_{nce}=Q(t)\delta v_p(t) \tag{8.97}$$

8.3.2 Spatial Discretization of the Energy Equations. The assumed vibration response expressions are given by Eqs. (8.26) and (8.27), which discretize Eqs. (8.94)-(8.96) into

$$U=\frac{1}{2}\sum_{r=1}^N\sum_{l=1}^N\left(a_r a_l k_{rl}^{aa}+b_r b_l k_{rl}^{bb}-2a_r b_l k_{rl}^{ab}+a_r v_p\tilde{\theta}_r^a+b_r v_p\tilde{\theta}_r^b\right) \tag{8.98}$$

$$T=\frac{1}{2}\sum_{r=1}^N\sum_{l=1}^N\left(\dot{a}_r\dot{a}_l m_{rl}^{aa}+\dot{b}_r\dot{b}_l m_{rl}^{bb}-2\dot{a}_r\dot{b}_l m_{rl}^{ab}+2\dot{a}_r p_r\right)+\int_0^L\left(\rho_s A_s+\rho_p A_p\right)\left(\frac{\partial w_b(x,t)}{\partial t}\right)^2dx \tag{8.99}$$

$$W_{ie}=-\frac{1}{2}\sum_{r=1}^N\left(a_r v_p\tilde{\theta}_r^a+b_r v_p\tilde{\theta}_r^b-C_p v_p^2\right) \tag{8.100}$$

where

$$m_{rl}^{aa}=\int_0^L\left[\left(\rho_s A_s+\rho_p A_p\right)\phi_r(x)\phi_l(x)+\left(\rho_s I_s+\rho_p I_p\right)\phi_r'(x)\phi_l'(x)\right]dx \tag{8.101}$$

and the rest of the mass, stiffness and damping terms are as given by Eqs. (8.35)-(8.42). Therefore, the rotary inertia effect modifies m_{rl}^{aa} only.

8.3.3 Electromechanical Lagrange Equations. Since the discretized form of the electromechanical equations does not change (other than the modification in the m_{rl}^{aa} term), the resulting Lagrange equations are

$$\mathbf{m^{aa}\ddot{a}-m^{ab}\ddot{b}+d^{aa}\dot{a}-d^{ab}\dot{b}+k^{aa}a-k^{ab}b+\tilde{\theta}^a v_p=f} \tag{8.102}$$

$$\mathbf{-m^{ab}\ddot{a}+m^{bb}\ddot{b}-d^{ab}\dot{a}+d^{bb}\dot{b}-k^{ab}a+k^{bb}b+\tilde{\theta}^b v_p=0} \tag{8.103}$$

$$C_p \dot{v}_p + \frac{v_p}{R_l} = \left(\tilde{\boldsymbol{\theta}}^{\mathbf{a}}\right)^t \dot{\mathbf{a}} + \left(\tilde{\boldsymbol{\theta}}^{\mathbf{b}}\right)^t \dot{\mathbf{b}} \tag{8.104}$$

8.3.4 Solution of the Electromechanical Lagrange Equations. For harmonic base excitation ($g(t) = W_0 e^{j\omega t}$ and $h(t) = \theta_0 e^{j\omega t}$ so that $\mathbf{f} = \mathbf{F}e^{j\omega t}$), the vectors of complex generalized coordinate amplitudes are

$$\mathbf{A} = \left[\boldsymbol{\Gamma}^{\mathbf{aa}} - \boldsymbol{\Gamma}^{\mathbf{ab}}\left(\boldsymbol{\Gamma}^{\mathbf{bb}}\right)^{-1}\boldsymbol{\Gamma}^{\mathbf{ba}}\right]^{-1}\mathbf{F} \tag{8.105}$$

$$\mathbf{B} = \left(\boldsymbol{\Gamma}^{\mathbf{bb}}\right)^{-1}\boldsymbol{\Gamma}^{\mathbf{ba}}\left[\boldsymbol{\Gamma}^{\mathbf{aa}} - \boldsymbol{\Gamma}^{\mathbf{ab}}\left(\boldsymbol{\Gamma}^{\mathbf{bb}}\right)^{-1}\boldsymbol{\Gamma}^{\mathbf{ba}}\right]^{-1}\mathbf{F} \tag{8.106}$$

The complex voltage amplitude is

$$V_p = j\omega\left(j\omega C_p + \frac{1}{R_l}\right)^{-1}\left[\left(\tilde{\boldsymbol{\theta}}^{\mathbf{a}}\right)^t + \left(\tilde{\boldsymbol{\theta}}^{\mathbf{b}}\right)^t\left(\boldsymbol{\Gamma}^{\mathbf{bb}}\right)^{-1}\boldsymbol{\Gamma}^{\mathbf{ba}}\right]\left[\boldsymbol{\Gamma}^{\mathbf{aa}} - \boldsymbol{\Gamma}^{\mathbf{ab}}\left(\boldsymbol{\Gamma}^{\mathbf{bb}}\right)^{-1}\boldsymbol{\Gamma}^{\mathbf{ba}}\right]^{-1}\mathbf{F} \tag{8.107}$$

Equations (8.105)-(8.107) can be used in Eqs. (8.88)-(8.90) to express the steady-state response of the system. The discussion related to obtaining the short-circuit and the open-circuit natural frequencies is the same as in the Euler-Bernoulli formulation. Hence, the only difference in the foregoing equations is due to m_{rl}^{aa} which includes the rotary inertia effect based on the Rayleigh formulation.

8.4 Electromechanical Timoshenko Model with Axial Deformations

8.4.1 Distributed-parameter Electromechanical Energy Formulation. The displacement field in the Timoshenko formulation is

$$u(x,z,t) = u^0(x,t) - z\psi^0(x,t) \tag{8.108}$$

$$v(x,z,t) = 0 \tag{8.109}$$

$$w(x,z,t) = w^0(x,t) \tag{8.110}$$

where $u^0(x,t)$ and $w^0(x,t)$ are the axial displacement and transverse displacement at point x on the neutral axis relative to the moving base and $\psi^0(x,t)$ is the cross-section rotation.

The vector form of the displacement field is then

$$\mathbf{u} = \begin{bmatrix} u^0(x,t) - z\psi^0(x,t) & 0 & w^0(x,t) \end{bmatrix}^t \tag{8.111}$$

The two non-zero strain components based on the given displacement field are

$$S_{xx}(x,z,t) = \frac{\partial u(x,z,t)}{\partial x} = \frac{\partial u^0(x,t)}{\partial x} - z\frac{\partial \psi^0(x,t)}{\partial x} \tag{8.112}$$

$$S_{xz}(x,t) = \frac{\partial u(x,z,t)}{\partial z} + \frac{\partial w(x,z,t)}{\partial x} = \frac{\partial w^0(x,t)}{\partial x} - \psi^0(x,t) \tag{8.113}$$

where $S_{xx}(x,z,t)$ is the axial strain component and $S_{xz}(x,t)$ is the transverse engineering shear strain component.

The isotropic substructure has the following constitutive relations:

$$T_{xx}(x,z,t) = Y_s S_{xx}(x,z,t) \tag{8.114}$$

$$T_{xz}(x,t) = \kappa G_s S_{xz}(x,t) \tag{8.115}$$

where κ is the cross-section dependent shear correction factor introduced by Timoshenko [73,74] and it accounts for the non-uniform distribution of the shear stress over the cross-section [73-83].[§] Moreover, G_s is the shear modulus of the substructure layer and it is related to the elastic modulus of the substructure layer through

$$G_s = \frac{Y_s}{2(1+\nu_s)} \tag{8.116}$$

where ν_s is the Poisson's ratio for the substructure layer.

The constitutive relation for the piezoceramic layer is (Appendix A.3)

$$T_{xx}(x,z,t) = T_1 = \bar{c}_{11}^E S_1 - \bar{e}_{31} E_3 = \bar{c}_{11}^E S_{xx}(x,z,t) + \bar{e}_{31}\frac{v_p(t)}{h_p} \tag{8.117}$$

[§] Various expressions [73-83] for the shear correction factor κ have been derived in the literature since Timoshenko's beam theory [73] was established in 1921. A review of the shear correction factors proposed in 1921-1975 was presented by Kaneko [78], concluding that the expressions derived by Timoshenko [74] should be preferred. For rectangular cross-sections, Timoshenko [74] derived $\kappa = (5+5\nu_s)/(6+5\nu_s)$ theoretically whereas Mindlin [75,76] obtained $\kappa = \pi^2/12$ experimentally (for crystal plates). Cowper's [77] solution is also widely used and it differs slightly from Timoshenko's solution: $\kappa = (10+10\nu_s)/(12+11\nu_s)$. The effect of width-to-depth ratio of the cross-section has been taken into account by Stephen [80,81] and more recently by Hutchinson [82]. Recently, an experimental study on the effect of width-to-depth ratio of the cross-section has been presented by Puchegger et al. [83].

$$T_{xz}(x,z,t) = T_5 = \kappa \overline{c}_{55}^E S_5 = \kappa \overline{c}_{55}^E S_{xz}(x,t) \tag{8.118}$$

where $\overline{c}_{55}^E$ is the shear modulus of the piezoceramic ($\overline{c}_{55}^E = 1/s_{55}^E$).

The total potential energy in the structure is

$$U = \frac{1}{2}\left(\int_{V_s} \mathbf{S}^t \mathbf{T} dV_s + \int_{V_p} \mathbf{S}^t \mathbf{T} dV_p \right) \tag{8.119}$$

yielding

$$\begin{aligned} U = {} & \frac{1}{2}\int_{V_s}\left[Y_s\left(\frac{\partial u^0(x,t)}{\partial x} - z\frac{\partial \psi^0(x,t)}{\partial x} \right)^2 + \kappa G_s\left(\frac{\partial w^0(x,t)}{\partial x} - \psi^0(x,t) \right)^2 \right] dV_s \\ & + \frac{1}{2}\int_{V_p}\left[\overline{c}_{11}^E\left(\frac{\partial u^0(x,t)}{\partial x} - z\frac{\partial \psi^0(x,t)}{\partial x} \right)^2 + \kappa \overline{c}_{55}^E\left(\frac{\partial w^0(x,t)}{\partial x} - \psi^0(x,t) \right)^2 \cdots \right. \\ & \left. + \overline{e}_{31}\frac{v_p(t)}{h_p}\left(\frac{\partial u^0(x,t)}{\partial x} - z\frac{\partial \psi^0(x,t)}{\partial x} \right) \right] dV_p \end{aligned} \tag{8.120}$$

The total kinetic energy of the system can be given by

$$T = \frac{1}{2}\left(\int_{V_s} \rho_s \frac{\partial \mathbf{u}_m^t}{\partial t}\frac{\partial \mathbf{u}_m}{\partial t} dV_s + \int_{V_p} \rho_p \frac{\partial \mathbf{u}_m^t}{\partial t}\frac{\partial \mathbf{u}_m}{\partial t} dV_p \right) \tag{8.121}$$

where the modified displacement vector (including the base displacement) is

$$\mathbf{u}_m = \left[u^0(x,t) - z\psi^0(x,t) \quad 0 \quad w^0(x,t) + w_b(x,t) \right]^t \tag{8.122}$$

Then the total kinetic energy becomes

$$\begin{aligned} T = {} & \frac{1}{2}\int_{V_s} \rho_s \left[\left(\frac{\partial u^0(x,t)}{\partial t} - z\frac{\partial \psi^0(x,t)}{\partial t} \right)^2 + \left(\frac{\partial w^0(x,t)}{\partial t} + \frac{\partial w_b(x,t)}{\partial t} \right)^2 \right] dV_s \\ & + \int_{V_p} \rho_p \left[\left(\frac{\partial u^0(x,t)}{\partial t} - z\frac{\partial \psi^0(x,t)}{\partial t} \right)^2 + \left(\frac{\partial w^0(x,t)}{\partial t} + \frac{\partial w_b(x,t)}{\partial t} \right)^2 \right] dV_p \end{aligned} \tag{8.123}$$

Equations (8.120) can be written as

$$\begin{aligned} U = {} & \frac{1}{2}\int_0^L \left\{ Y_s\left[A_s\left(\frac{\partial u^0(x,t)}{\partial x} \right)^2 + I_s\left(\frac{\partial \psi^0(x,t)}{\partial x} \right)^2 - 2H_s\frac{\partial u^0(x,t)}{\partial x}\frac{\partial \psi^0(x,t)}{\partial x} \right] \cdots \right. \\ & \left. + \kappa G_s A_s\left[\left(\frac{\partial w^0(x,t)}{\partial x} \right)^2 + \left(\psi^0(x,t) \right)^2 - 2\psi^0(x,t)\frac{\partial w^0(x,t)}{\partial x} \right] \cdots \right. \end{aligned}$$

$$+\overline{c}_{11}^{E}\left[A_p\left(\frac{\partial u^0(x,t)}{\partial x}\right)^2+I_p\left(\frac{\partial \psi^0(x,t)}{\partial x}\right)^2-2H_p\frac{\partial u^0(x,t)}{\partial x}\frac{\partial \psi^0(x,t)}{\partial x}\right]...$$
$$+\kappa\overline{c}_{55}^{E}A_p\left[\left(\frac{\partial w^0(x,t)}{\partial x}\right)^2+\left(\psi^0(x,t)\right)^2-2\psi^0(x,t)\frac{\partial w^0(x,t)}{\partial x}\right]... \tag{8.124}$$
$$+B_p v_p(t)\frac{\partial u^0(x,t)}{\partial x}+J_p v_p(t)\frac{\partial \psi^0(x,t)}{\partial x}\Bigg\}dx$$

where B_p and J_p are as given by Eqs. (8.18) and (8.19), respectively.

Equations (8.123) becomes

$$T=\frac{1}{2}\int_0^L\Bigg\{\rho_s\left[A_s\left(\frac{\partial u^0(x,t)}{\partial t}\right)^2+A_s\left(\frac{\partial w^0(x,t)}{\partial t}\right)^2+2A_s\frac{\partial w^0(x,t)}{\partial t}\frac{\partial w_b(x,t)}{\partial t}+A_s\left(\frac{\partial w_b(x,t)}{\partial t}\right)^2...\right.$$
$$-2H_s\frac{\partial u^0(x,t)}{\partial t}\frac{\partial \psi^0(x,t)}{\partial t}+I_s\left(\frac{\partial \psi^0(x,t)}{\partial t}\right)^2...$$
$$+\rho_p\left[A_p\left(\frac{\partial u^0(x,t)}{\partial t}\right)^2+A_p\left(\frac{\partial w^0(x,t)}{\partial t}\right)^2+2A_p\frac{\partial w^0(x,t)}{\partial t}\frac{\partial w_b(x,t)}{\partial t}+A_p\left(\frac{\partial w_b(x,t)}{\partial t}\right)^2...\right. \tag{8.125}$$
$$\left.\left.-2H_p\frac{\partial u^0(x,t)}{\partial t}\frac{\partial \psi^0(x,t)}{\partial t}+I_p\left(\frac{\partial \psi^0(x,t)}{\partial t}\right)^2\right]\right\}dx$$

where the kinetic energy contributions from the rotary inertia are kept. The area moments in the foregoing equations are as given by Eqs. (8.16) and (8.17) and the argument related to decoupling of $u^0(x,t)$ from the equations mentioned in the Euler-Bernoulli formulation is still valid. That is, for a symmetric structure, $H_s=H_p=0$ and $u^0(x,t)$ is not excited due to the transverse vibrations of the beam.

The internal electrical energy in the piezoceramic layer is

$$W_{ie}=\frac{1}{2}\int_{V_p}\mathbf{E}^t\mathbf{D}dV_p=-\frac{1}{2}\int_{V_p}\frac{v_p(t)}{h_p}\left[\overline{e}_{31}\left(\frac{\partial u^0(x,t)}{\partial x}-z\frac{\partial \psi^0(x,t)}{\partial x}\right)-\overline{\varepsilon}_{33}^{S}\frac{v_p(t)}{h_p}\right]dV_p$$
$$=-\frac{1}{2}\int_0^L\left(B_p v_p(t)\frac{\partial u^0(x,t)}{\partial x}+G_p v_p(t)\frac{\partial \psi^0(x,t)}{\partial x}\right)dx+\frac{1}{2}C_p\left[v_p(t)\right]^2 \tag{8.126}$$

where the internal capacitance of the piezoceramic is given by Eq. (8.22).

As done in Section 8.2, the mechanical dissipation effects will be included in the form of proportional damping after the equations are discretized. Therefore the only virtual work of non-

conservative forces in the extended Hamilton's principle given by Eq. (8.23) is that of the electric charge given by Eq. (8.25).

8.4.2 Spatial Discretization of the Energy Equations. The distributed-parameter variables in the mechanical domain are $w^0(x,t)$, $u^0(x,t)$ and $\psi^0(x,t)$ and the electrical variable is $v_p(t)$. Let the following finite series represent the components of vibration response:

$$w^0(x,t) = \sum_{r=1}^{N} a_r(t)\phi_r(x) \tag{8.127}$$

$$u^0(x,t) = \sum_{r=1}^{N} b_r(t)\alpha_r(x) \tag{8.128}$$

$$\psi^0(x,t) = \sum_{r=1}^{N} c_r(t)\beta_r(x) \tag{8.129}$$

where $\phi_r(x)$, $\alpha_r(x)$ and $\beta_r(x)$ are the kinematically admissible trial functions which satisfy the essential boundary conditions (Appendix D.2), $a_r(t)$, $b_r(t)$ and $c_r(t)$ are the unknown generalized coordinates. Using Eqs. (8.127)-(8.129) in Eq. (8.124), the total potential energy equation becomes

$$\begin{aligned} U = \frac{1}{2}\sum_{r=1}^{N}\sum_{l=1}^{N}\Bigg\{ & a_r a_l \int_0^L \kappa\left(G_s A_s + \bar{c}_{55}^E A_p\right)\phi_r'(x)\phi_l'(x)dx + b_r b_l \int_0^L \left(Y_s A_s + \bar{c}_{11}^E A_p\right)\alpha_r'(x)\alpha_l'(x)dx... \\ & + c_r c_l \int_0^L \left[\left(Y_s I_s + \bar{c}_{11}^E I_p\right)\beta_r'(x)\beta_l'(x) + \kappa\left(G_s A_s + \bar{c}_{55}^E A_p\right)\beta_r(x)\beta_l(x)\right]dx... \\ & - 2a_r c_l \int_0^L \kappa\left(G_s A_s + \bar{c}_{55}^E A_p\right)\phi_r'(x)\beta_l(x)dx - 2b_r c_l \int_0^L \left(Y_s H_s + \bar{c}_{11}^E H_p\right)\alpha_r'(x)\beta_l'(x)dx... \\ & + b_r v_p(t)\int_0^L B_p \alpha_r'(x)dx + c_r v_p(t)\int_0^L J_p \beta_r'(x)dx\Bigg\} \end{aligned} \tag{8.130}$$

Similarly, the total kinetic energy expression is discretized into

$$\begin{aligned} T = \frac{1}{2}\sum_{r=1}^{N}\sum_{l=1}^{N}\Bigg\{ & \dot{a}_r \dot{a}_l \int_0^L \left(\rho_s A_s + \rho_p A_p\right)\phi_r(x)\phi_l(x)dx + 2\dot{a}_r \int_0^L \left(\rho_s A_s + \rho_p A_p\right)\phi_r(x)\frac{\partial w_b(x,t)}{\partial t}dx... \\ & + \int_0^L \left(\rho_s A_s + \rho_p A_p\right)\left(\frac{\partial w_b(x,t)}{\partial t}\right)^2 dx + \dot{b}_r \dot{b}_l \int_0^L \left(\rho_s A_s + \rho_p A_p\right)\alpha_r(x)\alpha_l(x)dx... \end{aligned}$$

$$+\dot{c}_r\dot{c}_l\int_0^L\left(\rho_s I_s+\rho_p I_p\right)\beta_r(x)\beta_l(x)dx-2\dot{b}_r\dot{c}_l\int_0^L\left(\rho_s H_s+\rho_p H_p\right)\alpha_r(x)\beta_l(x)dx\Bigg\} \tag{8.131}$$

The discretized internal electrical energy is then

$$W_{ie}=-\frac{1}{2}\sum_{r=1}^{N}\left\{b_r v_p(t)\int_0^L B_p\alpha_r'(x)dx+c_r v_p(t)\int_0^L J_p\beta_r'(x)dx-C_p\left[v_p(t)\right]^2\right\} \tag{8.132}$$

Equations (8.130)-(8.132) can be written as

$$U=\frac{1}{2}\sum_{r=1}^{N}\sum_{l=1}^{N}\left(a_r a_l k_{rl}^{aa}+b_r b_l k_{rl}^{bb}+c_r c_l k_{rl}^{cc}-2a_r c_l k_{rl}^{ac}-2b_r c_l k_{rl}^{bc}+b_r v_p\tilde{\theta}_r^b+c_r v_p\tilde{\theta}_r^c\right) \tag{8.133}$$

$$T=\frac{1}{2}\sum_{r=1}^{N}\sum_{l=1}^{N}\left(\dot{a}_r\dot{a}_l m_{rl}^{aa}+\dot{b}_r\dot{b}_l m_{rl}^{bb}+\dot{c}_r\dot{c}_l m_{rl}^{cc}-2\dot{b}_r\dot{c}_l m_{rl}^{bc}+2\dot{a}_r p_r\right)+\int_0^L\left(\rho_s A_s+\rho_p A_p\right)\left(\frac{\partial w_b(x,t)}{\partial t}\right)^2 dx \tag{8.134}$$

$$W_{ie}=-\frac{1}{2}\sum_{r=1}^{N}\left(b_r v_p\tilde{\theta}_r^b+c_r v_p\tilde{\theta}_r^c-C_p v_p^2\right) \tag{8.135}$$

Here,

$$m_{rl}^{aa}=\int_0^L\left(\rho_s A_s+\rho_p A_p\right)\phi_r(x)\phi_l(x)dx \tag{8.136}$$

$$m_{rl}^{bb}=\int_0^L\left(\rho_s A_s+\rho_p A_p\right)\alpha_r(x)\alpha_l(x)dx \tag{8.137}$$

$$m_{rl}^{cc}=\int_0^L\left(\rho_s I_s+\rho_p I_p\right)\beta_r(x)\beta_l(x)dx \tag{8.138}$$

$$m_{rl}^{bc}=\int_0^L\left(\rho_s H_s+\rho_p H_p\right)\alpha_r(x)\beta_l(x)dx \tag{8.139}$$

$$p_r=\int_0^L\left(\rho_s A_s+\rho_p A_p\right)\phi_r(x)\frac{\partial w_b(x,t)}{\partial t}dx \tag{8.140}$$

$$k_{rl}^{aa}=\int_0^L\kappa\left(G_s A_s+\overline{c}_{55}^E A_p\right)\phi_r'(x)\phi_l'(x)dx \tag{8.141}$$

$$k_{rl}^{bb}=\int_0^L\left(Y_s A_s+\overline{c}_{11}^E A_p\right)\alpha_r'(x)\alpha_l'(x)dx \tag{8.142}$$

$$k_{rl}^{cc}=\int_0^L\left[\left(Y_s I_s+\overline{c}_{11}^E I_p\right)\beta_r'(x)\beta_l'(x)+\kappa\left(G_s A_s+\overline{c}_{55}^E A_p\right)\beta_r(x)\beta_l(x)\right]dx \tag{8.143}$$

$$k_{rl}^{ac} = \int_0^L \kappa\left(G_s A_s + \overline{c}_{55}^E A_p\right)\phi_r'(x)\beta_l(x)dx \tag{8.144}$$

$$k_{rl}^{bc} = \int_0^L \left(Y_s H_s + \overline{c}_{11}^E H_p\right)\alpha_r'(x)\beta_l'(x)dx \tag{8.145}$$

$$\tilde{\theta}_r^b = \int_0^L B_p \alpha_r'(x)dx \tag{8.146}$$

$$\tilde{\theta}_r^c = \int_0^L J_p \beta_r'(x)dx \tag{8.147}$$

where $r = 1,...,N$ and $l = 1,...,N$.

8.4.3 Electromechanical Lagrange Equations. The electromechanical Lagrange equations are expressed based on the extended Hamilton's principle as

$$\frac{d}{dt}\left(\frac{\partial T}{\partial \dot{a}_i}\right) - \frac{\partial T}{\partial a_i} + \frac{\partial U}{\partial a_i} - \frac{\partial W_{ie}}{\partial a_i} = 0 \tag{8.148}$$

$$\frac{d}{dt}\left(\frac{\partial T}{\partial \dot{b}_i}\right) - \frac{\partial T}{\partial b_i} + \frac{\partial U}{\partial b_i} - \frac{\partial W_{ie}}{\partial b_i} = 0 \tag{8.149}$$

$$\frac{d}{dt}\left(\frac{\partial T}{\partial \dot{c}_i}\right) - \frac{\partial T}{\partial c_i} + \frac{\partial U}{\partial c_i} - \frac{\partial W_{ie}}{\partial c_i} = 0 \tag{8.150}$$

$$\frac{d}{dt}\left(\frac{\partial T}{\partial \dot{v}_p}\right) - \frac{\partial T}{\partial v_p} + \frac{\partial U}{\partial v_p} - \frac{\partial W_{ie}}{\partial v_p} = Q \tag{8.151}$$

where Q is the electric charge output and the forcing component due to base excitation will be obtained from the total kinetic energy (more precisely from $\partial T / \partial \dot{a}_i$).

The non-zero components of Eq. (8.148) are

$$\begin{aligned}\frac{\partial T}{\partial \dot{a}_i} &= \frac{1}{2}\sum_{r=1}^{N}\sum_{l=1}^{N}\left[\left(\frac{\partial \dot{a}_r}{\partial \dot{a}_i}\dot{a}_l + \frac{\partial \dot{a}_l}{\partial \dot{a}_i}\dot{a}_r\right)m_{rl}^{aa} + 2\frac{\partial \dot{a}_r}{\partial \dot{a}_i}p_r\right] \\ &= \frac{1}{2}\sum_{r=1}^{N}\sum_{l=1}^{N}\left[\left(\delta_{ri}\dot{a}_l + \delta_{li}\dot{a}_r\right)m_{rl}^{aa} + 2\delta_{ri}p_r\right] = \sum_{l=1}^{N}\left(m_{il}^{aa}\dot{a}_l + p_i\right)\end{aligned} \tag{8.152}$$

$$\frac{\partial U}{\partial a_i} = \frac{1}{2}\sum_{r=1}^{N}\sum_{l=1}^{N}\left[\left(\frac{\partial a_r}{\partial a_i}a_l + \frac{\partial a_l}{\partial a_i}a_r\right)k_{rl}^{aa} - 2\frac{\partial a_r}{\partial a_i}c_l k_{rl}^{ac}\right]$$
$$= \frac{1}{2}\sum_{r=1}^{N}\sum_{l=1}^{N}\left[\left(\delta_{ri}a_l + \delta_{li}a_r\right)k_{rl}^{aa} - 2\delta_{ri}c_l k_{rl}^{ac}\right] = \sum_{l=1}^{N}\left(k_{il}^{aa}a_l - k_{il}^{ac}c_l\right) \tag{8.153}$$

Then the first set of Lagrange equations (for the generalized coordinate a_l) become

$$\sum_{l=1}^{N}\left(m_{il}^{aa}\ddot{a}_l + k_{il}^{aa}a_l - k_{il}^{ac}c_l - f_i\right) = 0 \tag{8.154}$$

where the forcing component due to base excitation is

$$f_i = -\frac{\partial p_i}{\partial t} = -\int_0^L \left(\rho_s A_s + \rho_p A_p\right)\phi_i(x)\frac{\partial^2 w_b(x,t)}{\partial t^2}dx$$
$$= -\frac{d^2 g(t)}{dt^2}\int_0^L \left(\rho_s A_s + \rho_p A_p\right)\phi_i(x)dx - \frac{d^2 h(t)}{dt^2}\int_0^L \left(\rho_s A_s + \rho_p A_p\right)x\phi_i(x)dx \tag{8.155}$$

The non-zero components in Eq. (8.149) are

$$\frac{\partial T}{\partial \dot{b}_i} = \frac{1}{2}\sum_{r=1}^{N}\sum_{l=1}^{N}\left[\left(\frac{\partial \dot{b}_r}{\partial \dot{b}_i}\dot{b}_l + \frac{\partial \dot{b}_l}{\partial \dot{b}_i}\dot{b}_r\right)m_{rl}^{bb} - 2\frac{\partial \dot{b}_r}{\partial \dot{b}_i}\dot{c}_l m_{rl}^{bc}\right]$$
$$= \frac{1}{2}\sum_{r=1}^{N}\sum_{l=1}^{N}\left[\left(\delta_{ri}\dot{b}_l + \delta_{li}\dot{b}_r\right)m_{rl}^{bb} - 2\delta_{ri}\dot{c}_l m_{rl}^{bc}\right] = \sum_{l=1}^{N}\left(m_{il}^{bb}\dot{b}_l - m_{il}^{bc}\dot{c}_l\right) \tag{8.156}$$

$$\frac{\partial U}{\partial b_i} = \frac{1}{2}\sum_{r=1}^{N}\sum_{l=1}^{N}\left[\left(\frac{\partial b_r}{\partial b_i}b_l + \frac{\partial b_l}{\partial b_i}b_r\right)k_{rl}^{bb} - 2\frac{\partial b_r}{\partial b_i}c_l k_{rl}^{bc} + \frac{\partial b_r}{\partial b_i}v_p\tilde{\theta}_r^b\right]$$
$$= \frac{1}{2}\sum_{r=1}^{N}\sum_{l=1}^{N}\left[\left(\delta_{ri}b_l + \delta_{li}b_r\right)k_{rl}^{bb} - 2\delta_{ri}c_l k_{rl}^{bc} + \delta_{ri}v_p\tilde{\theta}_r^b\right] = \sum_{l=1}^{N}\left(k_{il}^{bb}b_l - k_{il}^{bc}c_l\right) + \frac{1}{2}\tilde{\theta}_i^b v_p \tag{8.157}$$

$$\frac{\partial W_{ie}}{\partial b_i} = -\frac{1}{2}\sum_{r=1}^{N}\frac{\partial b_r}{\partial b_i}v_p\tilde{\theta}_r^b = -\frac{1}{2}\sum_{r=1}^{N}\delta_{ri}v_p\tilde{\theta}_r^b = -\frac{1}{2}\tilde{\theta}_i^b v_p \tag{8.158}$$

The Lagrange equation for the generalized coordinate b_l is

$$\sum_{l=1}^{N}\left(m_{il}^{bb}\ddot{b}_l - m_{il}^{bc}\ddot{c}_l + k_{il}^{bb}b_l - k_{il}^{bc}c_l + \tilde{\theta}_i^b v_p\right) = 0 \tag{8.159}$$

The non-zero components in Eq. (8.150) are

$$\frac{\partial T}{\partial \dot{b}_i} = \frac{1}{2}\sum_{r=1}^{N}\sum_{l=1}^{N}\left[\left(\frac{\partial \dot{c}_r}{\partial \dot{c}_i}\dot{c}_l + \frac{\partial \dot{c}_l}{\partial \dot{c}_i}\dot{c}_r\right)m_{rl}^{cc} - 2\frac{\partial \dot{c}_r}{\partial \dot{c}_i}\dot{b}_l m_{rl}^{bc}\right]$$
$$= \frac{1}{2}\sum_{r=1}^{N}\sum_{l=1}^{N}\left[\left(\delta_{ri}\dot{c}_l + \delta_{li}\dot{c}_r\right)m_{rl}^{cc} - 2\delta_{ri}\dot{b}_l m_{rl}^{bc}\right] = \sum_{l=1}^{N}\left(m_{il}^{cc}\dot{c}_l - m_{il}^{bc}\dot{b}_l\right) \tag{8.160}$$

$$\frac{\partial U}{\partial b_i} = \frac{1}{2}\sum_{r=1}^{N}\sum_{l=1}^{N}\left[\left(\frac{\partial c_r}{\partial c_i}c_l + \frac{\partial c_l}{\partial c_i}c_r\right)k_{rl}^{cc} - 2\frac{\partial c_r}{\partial c_i}a_l k_{rl}^{ac} - 2\frac{\partial c_r}{\partial c_i}b_l k_{rl}^{bc} + \frac{\partial c_r}{\partial c_i}v_p\tilde{\theta}_r^c\right]$$

$$= \frac{1}{2}\sum_{r=1}^{N}\sum_{l=1}^{N}\left[\left(\delta_{ri}c_l + \delta_{li}c_r\right)k_{rl}^{cc} - 2\delta_{ri}a_l k_{rl}^{ac} - 2\delta_{ri}b_l k_{rl}^{bc} + \delta_{ri}v_p\tilde{\theta}_r^c\right] \tag{8.161}$$

$$= \sum_{l=1}^{N}\left(k_{il}^{cc}c_l - k_{il}^{ac}a_l - k_{il}^{bc}b_l\right) + \frac{1}{2}\tilde{\theta}_i^c v_p$$

$$\frac{\partial W_{ie}}{\partial c_i} = -\frac{1}{2}\sum_{r=1}^{N}\frac{\partial c_r}{\partial c_i}v_p\tilde{\theta}_r^c = -\frac{1}{2}\sum_{r=1}^{N}\delta_{ri}v_p\tilde{\theta}_r^c = -\frac{1}{2}\tilde{\theta}_i^c v_p \tag{8.162}$$

Hence the Lagrange equation for the generalized coordinate c_l is

$$\sum_{l=1}^{N}\left(m_{il}^{cc}\ddot{c}_l - m_{il}^{bc}\ddot{b}_l + k_{il}^{cc}c_l - k_{il}^{ac}a_l - k_{il}^{bc}b_l + \tilde{\theta}_i^c v_p\right) = 0 \tag{8.163}$$

The non-zero components on the left hand side of Eq. (8.151) are

$$\frac{\partial U}{\partial v_p} = \frac{1}{2}\sum_{r=1}^{N}\left(b_r\tilde{\theta}_r^b + c_r\tilde{\theta}_r^c\right) \tag{8.164}$$

$$\frac{\partial W_{ie}}{\partial v_p} = C_p v_p - \frac{1}{2}\sum_{r=1}^{N}\left(b_r\tilde{\theta}_r^b + c_r\tilde{\theta}_r^c\right) \tag{8.165}$$

yielding

$$C_p v_p + Q - \sum_{r=1}^{N}\left(b_r\tilde{\theta}_r^b + c_r\tilde{\theta}_r^c\right) = 0 \tag{8.166}$$

Taking the time derivative of Eq. (8.166) and using $\dot{Q} = v_p / R_l$ gives the Lagrange equation for v_p as

$$C_p\dot{v}_p + \frac{v_p}{R_l} - \sum_{r=1}^{N}\left(\dot{b}_r\tilde{\theta}_r^b + \dot{c}_r\tilde{\theta}_r^c\right) = 0 \tag{8.167}$$

The first three Lagrange equations can be given in the matrix form as

$$\begin{bmatrix} \mathbf{m}^{aa} & \mathbf{0} & \mathbf{0} \\ \mathbf{0} & \mathbf{m}^{bb} & -\mathbf{m}^{bc} \\ \mathbf{0} & -\mathbf{m}^{bc} & \mathbf{m}^{cc} \end{bmatrix}\begin{Bmatrix} \ddot{\mathbf{a}} \\ \ddot{\mathbf{b}} \\ \ddot{\mathbf{c}} \end{Bmatrix} + \begin{bmatrix} \mathbf{k}^{aa} & \mathbf{0} & -\mathbf{k}^{ac} \\ \mathbf{0} & \mathbf{k}^{bb} & -\mathbf{k}^{bc} \\ -\mathbf{k}^{ac} & -\mathbf{k}^{bc} & \mathbf{k}^{cc} \end{bmatrix}\begin{Bmatrix} \mathbf{a} \\ \mathbf{b} \\ \mathbf{c} \end{Bmatrix} + \begin{Bmatrix} \mathbf{0} \\ \tilde{\boldsymbol{\theta}}^b \\ \tilde{\boldsymbol{\theta}}^c \end{Bmatrix} v_p = \begin{Bmatrix} \mathbf{f} \\ \mathbf{0} \\ \mathbf{0} \end{Bmatrix} \tag{8.168}$$

Rayleigh damping is introduced to account for the mechanical dissipative effects by preserving the normal-mode system:

$$\begin{bmatrix} \mathbf{m}^{aa} & \mathbf{0} & \mathbf{0} \\ \mathbf{0} & \mathbf{m}^{bb} & -\mathbf{m}^{bc} \\ \mathbf{0} & -\mathbf{m}^{bc} & \mathbf{m}^{cc} \end{bmatrix} \begin{Bmatrix} \ddot{\mathbf{a}} \\ \ddot{\mathbf{b}} \\ \ddot{\mathbf{c}} \end{Bmatrix} + \begin{bmatrix} \mathbf{d}^{aa} & \mathbf{0} & -\mathbf{d}^{ac} \\ \mathbf{0} & \mathbf{d}^{bb} & -\mathbf{d}^{bc} \\ -\mathbf{d}^{ac} & -\mathbf{d}^{bc} & \mathbf{d}^{cc} \end{bmatrix} \begin{Bmatrix} \dot{\mathbf{a}} \\ \dot{\mathbf{b}} \\ \dot{\mathbf{c}} \end{Bmatrix} + \begin{bmatrix} \mathbf{k}^{aa} & \mathbf{0} & -\mathbf{k}^{ac} \\ \mathbf{0} & \mathbf{k}^{bb} & -\mathbf{k}^{bc} \\ -\mathbf{k}^{ac} & -\mathbf{k}^{bc} & \mathbf{k}^{cc} \end{bmatrix} \begin{Bmatrix} \mathbf{a} \\ \mathbf{b} \\ \mathbf{c} \end{Bmatrix} + \begin{Bmatrix} \mathbf{0} \\ \tilde{\boldsymbol{\theta}}^{b} \\ \tilde{\boldsymbol{\theta}}^{c} \end{Bmatrix} v_p = \begin{Bmatrix} \mathbf{f} \\ \mathbf{0} \\ \mathbf{0} \end{Bmatrix} \tag{8.169}$$

Here the damping matrix is

$$\begin{bmatrix} \mathbf{d}^{aa} & \mathbf{0} & -\mathbf{d}^{ac} \\ \mathbf{0} & \mathbf{d}^{bb} & -\mathbf{d}^{bc} \\ -\mathbf{d}^{ac} & -\mathbf{d}^{bc} & \mathbf{d}^{cc} \end{bmatrix} = \mu \begin{bmatrix} \mathbf{m}^{aa} & \mathbf{0} & \mathbf{0} \\ \mathbf{0} & \mathbf{m}^{bb} & -\mathbf{m}^{bc} \\ \mathbf{0} & -\mathbf{m}^{bc} & \mathbf{m}^{cc} \end{bmatrix} + \gamma \begin{bmatrix} \mathbf{k}^{aa} & \mathbf{0} & -\mathbf{k}^{ac} \\ \mathbf{0} & \mathbf{k}^{bb} & -\mathbf{k}^{bc} \\ -\mathbf{k}^{ac} & -\mathbf{k}^{bc} & \mathbf{k}^{cc} \end{bmatrix} \tag{8.170}$$

where μ and γ are the constants of mass and stiffness proportionality.

Equation (8.167) can be expressed as

$$C_p \dot{v}_p + \frac{v_p}{R_l} - \left(\tilde{\boldsymbol{\theta}}^{b}\right)^t \dot{\mathbf{b}} - \left(\tilde{\boldsymbol{\theta}}^{c}\right)^t \dot{\mathbf{c}} = 0 \tag{8.171}$$

Equations (8.169) and (8.171) are the discretized equations of the distributed-parameter electromechanical system where the $N \times 1$ vectors of generalized coordinates are

$$\mathbf{a} = \begin{bmatrix} a_1 & a_2 & \dots & a_N \end{bmatrix}^t, \ \mathbf{b} = \begin{bmatrix} b_1 & b_2 & \dots & b_N \end{bmatrix}^t, \ \mathbf{c} = \begin{bmatrix} c_1 & c_2 & \dots & c_N \end{bmatrix}^t \tag{8.172}$$

and the $N \times 1$ vectors of electromechanical coupling are

$$\tilde{\boldsymbol{\theta}}^{b} = \begin{bmatrix} \tilde{\theta}_1^b & \tilde{\theta}_2^b & \dots & \tilde{\theta}_N^b \end{bmatrix}^t, \ \tilde{\boldsymbol{\theta}}^{c} = \begin{bmatrix} \tilde{\theta}_1^c & \tilde{\theta}_2^c & \dots & \tilde{\theta}_N^c \end{bmatrix}^t \tag{8.173}$$

8.4.4 Solution of the Electromechanical Lagrange Equations. Rewriting the discretized equations of the electromechanical system as

$$\mathbf{m}^{aa}\ddot{\mathbf{a}} + \mathbf{d}^{aa}\dot{\mathbf{a}} - \mathbf{d}^{ac}\dot{\mathbf{c}} + \mathbf{k}^{aa}\mathbf{a} - \mathbf{k}^{ac}\mathbf{c} = \mathbf{f} \tag{8.174}$$

$$\mathbf{m}^{bb}\ddot{\mathbf{b}} - \mathbf{m}^{bc}\ddot{\mathbf{c}} + \mathbf{d}^{bb}\dot{\mathbf{b}} - \mathbf{d}^{bc}\dot{\mathbf{c}} + \mathbf{k}^{bb}\mathbf{b} - \mathbf{k}^{bc}\mathbf{c} + \tilde{\boldsymbol{\theta}}^{b} v_p = \mathbf{0} \tag{8.175}$$

$$-\mathbf{m}^{bc}\ddot{\mathbf{b}} + \mathbf{m}^{cc}\ddot{\mathbf{c}} - \mathbf{d}^{ac}\dot{\mathbf{a}} - \mathbf{d}^{bc}\dot{\mathbf{b}} + \mathbf{d}^{cc}\dot{\mathbf{c}} - \mathbf{k}^{ac}\mathbf{a} - \mathbf{k}^{bc}\mathbf{b} + \mathbf{k}^{cc}\mathbf{c} + \tilde{\boldsymbol{\theta}}^{c} v_p = \mathbf{0} \tag{8.176}$$

$$C_p \dot{v}_p + \frac{v_p}{R_l} = \left(\tilde{\boldsymbol{\theta}}^{b}\right)^t \dot{\mathbf{b}} + \left(\tilde{\boldsymbol{\theta}}^{c}\right)^t \dot{\mathbf{c}} \tag{8.177}$$

For harmonic base displacement of the form $g(t) = W_0 e^{j\omega t}$ and $h(t) = \theta_0 e^{j\omega t}$, the components of the forcing vector become

$$\mathbf{f} = \mathbf{F} e^{j\omega t} \tag{8.178}$$

Here,

$$F_r = -\sigma_r \omega^2 W_0 - \tau_r \omega^2 \theta_0 \tag{8.179}$$

where

$$\sigma_r = -\int_0^L \left(\rho_s A_s + \rho_p A_p\right) \phi_r(x) dx \tag{8.180}$$

$$\tau_r = -\int_0^L \left(\rho_s A_s + \rho_p A_p\right) x \phi_r(x) dx \tag{8.181}$$

The steady-state generalized coordinates and the voltage output are $\mathbf{a} = \mathbf{A}e^{j\omega t}$, $\mathbf{b} = \mathbf{B}e^{j\omega t}$, $\mathbf{c} = \mathbf{C}e^{j\omega t}$ and $v_p = V_p e^{j\omega t}$ (where the elements of $\mathbf{A}$, $\mathbf{B}$ and $\mathbf{C}$ as well as V_p are complex valued).

The steady-state form of Eqs. (8.174)-(8.177) are then

$$\left(-\omega^2 \mathbf{m}^{\mathbf{aa}} + j\omega \mathbf{d}^{\mathbf{aa}} + \mathbf{k}^{\mathbf{aa}}\right)\mathbf{A} - \left(j\omega \mathbf{d}^{\mathbf{ac}} + \mathbf{k}^{\mathbf{ac}}\right)\mathbf{C} = \mathbf{F} \tag{8.182}$$

$$\left(-\omega^2 \mathbf{m}^{\mathbf{bb}} + j\omega \mathbf{d}^{\mathbf{bb}} + \mathbf{k}^{\mathbf{bb}}\right)\mathbf{B} - \left(-\omega^2 \mathbf{m}^{\mathbf{bc}} + j\omega \mathbf{d}^{\mathbf{bc}} + \mathbf{k}^{\mathbf{bc}}\right)\mathbf{C} + \tilde{\boldsymbol{\theta}}^{\mathbf{b}} V_p = 0 \tag{8.183}$$

$$-\left(j\omega \mathbf{d}^{\mathbf{ac}} + \mathbf{k}^{\mathbf{ac}}\right)\mathbf{A} - \left(-\omega^2 \mathbf{m}^{\mathbf{bc}} + j\omega \mathbf{d}^{\mathbf{bc}} + \mathbf{k}^{\mathbf{bc}}\right)\mathbf{B} + \left(-\omega^2 \mathbf{m}^{\mathbf{cc}} + j\omega \mathbf{d}^{\mathbf{cc}} + \mathbf{k}^{\mathbf{cc}}\right)\mathbf{C} + \tilde{\boldsymbol{\theta}}^{\mathbf{c}} V_p = \mathbf{0} \tag{8.184}$$

$$\left(j\omega C_p + \frac{1}{R_l}\right) V_p = j\omega \left[\left(\tilde{\boldsymbol{\theta}}^{\mathbf{b}}\right)^t \mathbf{B} + \left(\tilde{\boldsymbol{\theta}}^{\mathbf{c}}\right)^t \mathbf{C}\right] \tag{8.185}$$

From Eq. (8.185):

$$V_p = j\omega \left(j\omega C_p + \frac{1}{R_l}\right)^{-1} \left[\left(\tilde{\boldsymbol{\theta}}^{\mathbf{b}}\right)^t \mathbf{B} + \left(\tilde{\boldsymbol{\theta}}^{\mathbf{c}}\right)^t \mathbf{C}\right] \tag{8.186}$$

Substituting Eq. (8.186) into Eqs. (8.182)-(8.184) gives

$$\boldsymbol{\Gamma}^{\mathbf{aa}} \mathbf{A} - \boldsymbol{\Gamma}^{\mathbf{ac}} \mathbf{C} = \mathbf{F} \tag{8.187}$$

$$-\boldsymbol{\Gamma}^{\mathbf{bc}} \mathbf{C} + \boldsymbol{\Gamma}^{\mathbf{bb}} \mathbf{B} = \mathbf{0} \tag{8.188}$$

$$-\boldsymbol{\Gamma}^{\mathbf{ca}} \mathbf{A} - \boldsymbol{\Gamma}^{\mathbf{cb}} \mathbf{B} + \boldsymbol{\Gamma}^{\mathbf{cc}} \mathbf{C} = \mathbf{0} \tag{8.189}$$

where

$$\boldsymbol{\Gamma}^{\mathbf{aa}} = -\omega^2 \mathbf{m}^{\mathbf{aa}} + j\omega \mathbf{d}^{\mathbf{aa}} + \mathbf{k}^{\mathbf{aa}} \tag{8.190}$$

$$\boldsymbol{\Gamma}^{\mathbf{bb}} = -\omega^2 \mathbf{m}^{\mathbf{bb}} + j\omega \mathbf{d}^{\mathbf{bb}} + \mathbf{k}^{\mathbf{bb}} + j\omega \left(j\omega C_p + \frac{1}{R_l}\right)^{-1} \tilde{\boldsymbol{\theta}}^{\mathbf{b}} \left(\tilde{\boldsymbol{\theta}}^{\mathbf{b}}\right)^t \tag{8.191}$$

$$\boldsymbol{\Gamma}^{\mathbf{cc}} = -\omega^2 \mathbf{m}^{\mathbf{cc}} + j\omega \mathbf{d}^{\mathbf{cc}} + \mathbf{k}^{\mathbf{cc}} + j\omega \left(j\omega C_p + \frac{1}{R_l} \right)^{-1} \tilde{\boldsymbol{\theta}}^{\mathbf{c}} \left(\tilde{\boldsymbol{\theta}}^{\mathbf{c}} \right)^t \tag{8.192}$$

$$\boldsymbol{\Gamma}^{\mathbf{ac}} = \boldsymbol{\Gamma}^{\mathbf{ca}} = j\omega \mathbf{d}^{\mathbf{ac}} + \mathbf{k}^{\mathbf{ac}} \tag{8.193}$$

$$\boldsymbol{\Gamma}^{\mathbf{bc}} = -\omega^2 \mathbf{m}^{\mathbf{bc}} + j\omega \mathbf{d}^{\mathbf{bc}} + \mathbf{k}^{\mathbf{bc}} - j\omega \left(j\omega C_p + \frac{1}{R_l} \right)^{-1} \tilde{\boldsymbol{\theta}}^{\mathbf{b}} \left(\tilde{\boldsymbol{\theta}}^{\mathbf{c}} \right)^t \tag{8.194}$$

$$\boldsymbol{\Gamma}^{\mathbf{cb}} = -\omega^2 \mathbf{m}^{\mathbf{bc}} + j\omega \mathbf{d}^{\mathbf{bc}} + \mathbf{k}^{\mathbf{bc}} - j\omega \left(j\omega C_p + \frac{1}{R_l} \right)^{-1} \tilde{\boldsymbol{\theta}}^{\mathbf{c}} \left(\tilde{\boldsymbol{\theta}}^{\mathbf{b}} \right)^t \tag{8.195}$$

From Eq. (8.188):

$$\mathbf{B} = \left(\boldsymbol{\Gamma}^{\mathbf{bb}} \right)^{-1} \boldsymbol{\Gamma}^{\mathbf{bc}} \mathbf{C} \tag{8.196}$$

Substituting Eq. (8.196) into Eq. (8.189) gives

$$\mathbf{A} = \left(\boldsymbol{\Gamma}^{\mathbf{ca}} \right)^{-1} \left[\boldsymbol{\Gamma}^{\mathbf{cc}} - \boldsymbol{\Gamma}^{\mathbf{cb}} \left(\boldsymbol{\Gamma}^{\mathbf{bb}} \right)^{-1} \boldsymbol{\Gamma}^{\mathbf{bc}} \right] \mathbf{C} \tag{8.197}$$

Using Eq. (8.197) in Eq. (8.187) gives the vector of complex generalized coordinate amplitudes $\mathbf{C}$ as

$$\mathbf{C} = \left\{ \boldsymbol{\Gamma}^{\mathbf{aa}} \left(\boldsymbol{\Gamma}^{\mathbf{ca}} \right)^{-1} \left[\boldsymbol{\Gamma}^{\mathbf{cc}} - \boldsymbol{\Gamma}^{\mathbf{cb}} \left(\boldsymbol{\Gamma}^{\mathbf{bb}} \right)^{-1} \boldsymbol{\Gamma}^{\mathbf{bc}} \right] - \boldsymbol{\Gamma}^{\mathbf{ac}} \right\}^{-1} \mathbf{F} \tag{8.198}$$

which can be substituted into Eq. (8.196) to give vector $\mathbf{B}$:

$$\mathbf{B} = \left(\boldsymbol{\Gamma}^{\mathbf{bb}} \right)^{-1} \boldsymbol{\Gamma}^{\mathbf{bc}} \left\{ \boldsymbol{\Gamma}^{\mathbf{aa}} \left(\boldsymbol{\Gamma}^{\mathbf{ca}} \right)^{-1} \left[\boldsymbol{\Gamma}^{\mathbf{cc}} - \boldsymbol{\Gamma}^{\mathbf{cb}} \left(\boldsymbol{\Gamma}^{\mathbf{bb}} \right)^{-1} \boldsymbol{\Gamma}^{\mathbf{bc}} \right] - \boldsymbol{\Gamma}^{\mathbf{ac}} \right\}^{-1} \mathbf{F} \tag{8.199}$$

Similarly, the vector of complex generalized coordinate amplitudes $\mathbf{A}$ is obtained as

$$\mathbf{A} = \left(\boldsymbol{\Gamma}^{\mathbf{ca}} \right)^{-1} \left[\boldsymbol{\Gamma}^{\mathbf{cc}} - \boldsymbol{\Gamma}^{\mathbf{cb}} \left(\boldsymbol{\Gamma}^{\mathbf{bb}} \right)^{-1} \boldsymbol{\Gamma}^{\mathbf{bc}} \right] \left\{ \boldsymbol{\Gamma}^{\mathbf{aa}} \left(\boldsymbol{\Gamma}^{\mathbf{ca}} \right)^{-1} \left[\boldsymbol{\Gamma}^{\mathbf{cc}} - \boldsymbol{\Gamma}^{\mathbf{cb}} \left(\boldsymbol{\Gamma}^{\mathbf{bb}} \right)^{-1} \boldsymbol{\Gamma}^{\mathbf{bc}} \right] - \boldsymbol{\Gamma}^{\mathbf{ac}} \right\}^{-1} \mathbf{F} \tag{8.200}$$

and the complex voltage amplitude is

$$V_p = j\omega \left(j\omega C_p + \frac{1}{R_l} \right)^{-1} \left[\left(\tilde{\boldsymbol{\theta}}^{\mathbf{b}} \right)^t \left(\boldsymbol{\Gamma}^{\mathbf{bb}} \right)^{-1} \boldsymbol{\Gamma}^{\mathbf{bc}} + \left(\tilde{\boldsymbol{\theta}}^{\mathbf{c}} \right)^t \right] \left\{ \boldsymbol{\Gamma}^{\mathbf{aa}} \left(\boldsymbol{\Gamma}^{\mathbf{ca}} \right)^{-1} \left[\boldsymbol{\Gamma}^{\mathbf{cc}} - \boldsymbol{\Gamma}^{\mathbf{cb}} \left(\boldsymbol{\Gamma}^{\mathbf{bb}} \right)^{-1} \boldsymbol{\Gamma}^{\mathbf{bc}} \right] - \boldsymbol{\Gamma}^{\mathbf{ac}} \right\}^{-1} \mathbf{F} \tag{8.201}$$

Substituting the elements of $\mathbf{A}$, $\mathbf{B}$ and $\mathbf{C}$ into Eqs. (8.127)-(8.129) gives the transverse displacement, axial displacement and the cross-section rotation response at steady state as

$$w^0(x,t) = \sum_{r=1}^{N} A_r e^{j\omega t} \phi_r(x) \tag{8.202}$$

$$u^0(x,t)=\sum_{r=1}^{N}B_r e^{j\omega t}\alpha_r(x) \tag{8.203}$$

$$\psi^0(x,t)=\sum_{r=1}^{N}C_r e^{j\omega t}\beta_r(x) \tag{8.204}$$

The steady-state voltage response is

$$V_p=j\omega\left(j\omega C_p+\frac{1}{R_l}\right)^{-1}\left[\left(\tilde{\boldsymbol{\theta}}^{\mathbf{b}}\right)^t\left(\boldsymbol{\Gamma}^{\mathbf{bb}}\right)^{-1}\boldsymbol{\Gamma}^{\mathbf{bc}}+\left(\tilde{\boldsymbol{\theta}}^{\mathbf{c}}\right)^t\right]\left\{\boldsymbol{\Gamma}^{\mathbf{aa}}\left(\boldsymbol{\Gamma}^{\mathbf{ca}}\right)^{-1}\left[\boldsymbol{\Gamma}^{\mathbf{cc}}-\boldsymbol{\Gamma}^{\mathbf{cb}}\left(\boldsymbol{\Gamma}^{\mathbf{bb}}\right)^{-1}\boldsymbol{\Gamma}^{\mathbf{bc}}\right]-\boldsymbol{\Gamma}^{\mathbf{ac}}\right\}^{-1}\mathbf{F}e^{j\omega t} \tag{8.205}$$

One can use the form of the base excitation given by Eq. (8.179) ($\mathbf{F}=-\boldsymbol{\sigma}\omega^2W_0-\boldsymbol{\tau}\omega^2\theta_0$) and define the following 8 electromechanical FRFs for the 4 steady-state response expressions given by Eqs. (8.202)-(8.205)

$$\frac{w^0(x,t)}{-\omega^2W_0e^{j\omega t}},\ \frac{u^0(x,t)}{-\omega^2W_0e^{j\omega t}},\ \frac{\psi^0(x,t)}{-\omega^2W_0e^{j\omega t}},\ \frac{v_p(t)}{-\omega^2W_0e^{j\omega t}},\ \frac{w^0(x,t)}{-\omega^2\theta_0e^{j\omega t}},\ \frac{u^0(x,t)}{-\omega^2\theta_0e^{j\omega t}},\ \frac{\psi^0(x,t)}{-\omega^2\theta_0e^{j\omega t}},\ \frac{v_p(t)}{-\omega^2\theta_0e^{j\omega t}} \tag{8.206}$$

The short-circuit and the open-circuit natural frequencies of the system can be obtained by setting the mechanical damping terms equal to zero ($\mathbf{d}\to\mathbf{0}$) and considering the $R_l\to 0$ and $R_l\to\infty$ cases, respectively, in the following characteristic equation obtained from the free vibration ($\mathbf{F}=\mathbf{0}$) problem:

$$\begin{vmatrix}\boldsymbol{\Gamma}^{\mathbf{aa}} & \mathbf{0} & -\boldsymbol{\Gamma}^{\mathbf{ac}}\\ \mathbf{0} & \boldsymbol{\Gamma}^{\mathbf{bb}} & -\boldsymbol{\Gamma}^{\mathbf{bc}}\\ -\boldsymbol{\Gamma}^{\mathbf{ca}} & -\boldsymbol{\Gamma}^{\mathbf{cb}} & \boldsymbol{\Gamma}^{\mathbf{cc}}\end{vmatrix}=\mathbf{0} \tag{8.207}$$

8.5 Modeling of Symmetric Configurations

8.5.1 Euler-Bernoulli and Rayleigh Models. For a geometrically symmetric configuration (i.e. symmetric laminates) such as the bimorph configurations shown in Fig. 3.1, the H_s and H_p terms causing the coupling between the transverse displacement and axial displacement vanish, reducing the governing discretized equations of the system (given by Eqs. (8.67)-(8.69)) to

$$\mathbf{m}^{\mathbf{aa}}\ddot{\mathbf{a}}+\mathbf{d}^{\mathbf{aa}}\dot{\mathbf{a}}+\mathbf{k}^{\mathbf{aa}}\mathbf{a}+\tilde{\boldsymbol{\theta}}^{\mathbf{a}}v_p=\mathbf{f} \tag{8.208}$$

$$C_p\dot{v}_p + \frac{v_p}{R_l} = \left(\tilde{\boldsymbol{\theta}}^{\mathbf{a}}\right)^t \dot{\mathbf{a}} \tag{8.209}$$

This simplest form is similar to the symmetric thin bimorph equations derived using the Rayleigh-Ritz technique [16,21]. Following the well-known procedure with the assumption of harmonic excitation ($\mathbf{f} = \mathbf{F}e^{j\omega t}$), the steady-state response expressions are harmonic of the forms $\mathbf{a} = \mathbf{A}e^{j\omega t}$ and $v_p = V_p e^{j\omega t}$, yielding

$$\left(-\omega^2\mathbf{m}^{\mathbf{aa}} + j\omega\mathbf{d}^{\mathbf{aa}} + \mathbf{k}^{\mathbf{aa}}\right)\mathbf{A} + \tilde{\boldsymbol{\theta}}^{\mathbf{a}}V_p = \mathbf{F} \tag{8.210}$$

$$V_p = j\omega\left(j\omega C_p + \frac{1}{R_l}\right)^{-1}\left(\tilde{\boldsymbol{\theta}}^{\mathbf{a}}\right)^t \mathbf{A} \tag{8.211}$$

which give the complex generalized coordinate vector **A** and the complex voltage amplitude as

$$\mathbf{A} = \left(\boldsymbol{\Gamma}^{\mathbf{aa}}\right)^{-1}\mathbf{F} \tag{8.212}$$

$$V_p = j\omega\left(j\omega C_p + \frac{1}{R_l}\right)^{-1}\left(\tilde{\boldsymbol{\theta}}^{\mathbf{a}}\right)^t\left(\boldsymbol{\Gamma}^{\mathbf{aa}}\right)^{-1}\mathbf{F} \tag{8.213}$$

8.5.2 Timoshenko Model. For a symmetric bimorph cantilever, Eq. (8.175) decouples from the electromechanical equations of the system:

$$\mathbf{m}^{\mathbf{aa}}\ddot{\mathbf{a}} + \mathbf{d}^{\mathbf{aa}}\dot{\mathbf{a}} - \mathbf{d}^{\mathbf{ac}}\dot{\mathbf{c}} + \mathbf{k}^{\mathbf{aa}}\mathbf{a} - \mathbf{k}^{\mathbf{ac}}\mathbf{c} = \mathbf{f} \tag{8.214}$$

$$\mathbf{m}^{\mathbf{cc}}\ddot{\mathbf{c}} - \mathbf{d}^{\mathbf{ac}}\dot{\mathbf{a}} + \mathbf{d}^{\mathbf{cc}}\dot{\mathbf{c}} - \mathbf{k}^{\mathbf{ac}}\mathbf{a} + \mathbf{k}^{\mathbf{cc}}\mathbf{c} + \tilde{\boldsymbol{\theta}}^{\mathbf{c}}v_p = \mathbf{0} \tag{8.215}$$

$$C_p\dot{v}_p + \frac{v_p}{R_l} = \left(\tilde{\boldsymbol{\theta}}^{\mathbf{c}}\right)^t \dot{\mathbf{c}} \tag{8.216}$$

With the assumption of harmonic excitation ($\mathbf{f} = \mathbf{F}e^{j\omega t}$) the steady-state response expressions are $\mathbf{a} = \mathbf{A}e^{j\omega t}$, $\mathbf{c} = \mathbf{C}e^{j\omega t}$ and $v_p = V_p e^{j\omega t}$. One obtains from Eqs. (8.214)-(8.216) that

$$\mathbf{A} = \left(\boldsymbol{\Gamma}^{\mathbf{ca}}\right)^{-1}\boldsymbol{\Gamma}^{\mathbf{cc}}\left[\boldsymbol{\Gamma}^{\mathbf{aa}}\left(\boldsymbol{\Gamma}^{\mathbf{ca}}\right)^{-1}\boldsymbol{\Gamma}^{\mathbf{cc}} - \boldsymbol{\Gamma}^{\mathbf{ac}}\right]^{-1}\mathbf{F} \tag{8.217}$$

$$\mathbf{C} = \left[\boldsymbol{\Gamma}^{\mathbf{aa}}\left(\boldsymbol{\Gamma}^{\mathbf{ca}}\right)^{-1}\boldsymbol{\Gamma}^{\mathbf{cc}} - \boldsymbol{\Gamma}^{\mathbf{ac}}\right]^{-1}\mathbf{F} \tag{8.218}$$

$$V_p = j\omega\left(j\omega C_p + \frac{1}{R_l}\right)^{-1}\left(\tilde{\boldsymbol{\theta}}^{\mathbf{c}}\right)^t\left[\boldsymbol{\Gamma}^{\mathbf{aa}}\left(\boldsymbol{\Gamma}^{\mathbf{ca}}\right)^{-1}\boldsymbol{\Gamma}^{\mathbf{cc}} - \boldsymbol{\Gamma}^{\mathbf{ac}}\right]^{-1}\mathbf{F} \tag{8.219}$$

8.6 Presence of a Tip Mass in the Euler-Bernoulli, Rayleigh and Timoshenko Models

If the energy harvester configuration shown in Fig. 8.1 has a tip mass of M_t with a mass moment of inertia of I_t, the total kinetic energy expressions should be modified in the electromechanical models derived in this chapter.

In the Euler-Bernoulli and Rayleigh models, the total kinetic energy expression with the kinetic energy contribution of a tip mass located at $x = L$ becomes

$$\begin{aligned} T = & \frac{1}{2}\int_{V_s} \rho_s \left[\left(\frac{\partial u^0(x,t)}{\partial t} - z\frac{\partial^2 w^0(x,t)}{\partial t \partial x} \right)^2 + \left[\frac{\partial w^0(x,t)}{\partial t} + \frac{\partial w_b(x,t)}{\partial t} \right]^2 \right] dV_s \\ & + \int_{V_p} \rho_p \left[\left(\frac{\partial u^0(x,t)}{\partial t} - z\frac{\partial^2 w^0(x,t)}{\partial t \partial x} \right)^2 + \left[\frac{\partial w^0(x,t)}{\partial t} + \frac{\partial w_b(x,t)}{\partial t} \right]^2 \right] dV_p \\ & + \frac{1}{2} M_t \left[\left(\frac{\partial w^0(x,t)}{\partial t} + \frac{\partial w_b(x,t)}{\partial t} \right)\Bigg|_{x=L} \right]^2 + \frac{1}{2} I_t \left[\frac{\partial^2 w^0(x,t)}{\partial t \partial x}\Bigg|_{x=L} \right]^2 \end{aligned} \tag{8.220}$$

which modifies the sub-matrix m_{rl}^{aa} in the Euler-Bernoulli model to

$$m_{rl}^{aa} = \int_0^L \left(\rho_s A_s + \rho_p A_p \right) \phi_r(x) \phi_l(x) dx + M_t \phi_r(L) \phi_l(L) + I_t \phi_r'(L) \phi_l'(L) \tag{8.221}$$

and the sub-matrix m_{rl}^{aa} in the Rayleigh model becomes

$$m_{rl}^{aa} = \int_0^L \left[\left(\rho_s A_s + \rho_p A_p \right) \phi_r(x) \phi_l(x) + \left(\rho_s I_s + \rho_p I_p \right) \phi_r'(x) \phi_l'(x) \right] dx + M_t \phi_r(L) \phi_l(L) + I_t \phi_r'(L) \phi_l'(L) \tag{8.222}$$

In both Euler-Bernoulli and Rayleigh models, the term p_r derived from the total kinetic energy expression becomes

$$p_r = \int_0^L \left(\rho_s A_s + \rho_p A_p \right) \phi_r(x) \frac{\partial w_b(x,t)}{\partial t} dx + M_t \phi_r(L) \frac{\partial w_b(x,t)}{\partial t}\Bigg|_{x=L} \tag{8.223}$$

which alters the effective force due to base excitation as follows

$$f_r = -\frac{\partial p_r}{\partial t} = -\int_0^L \left(\rho_s A_s + \rho_p A_p\right)\phi_r(x)\frac{\partial^2 w_b(x,t)}{\partial t^2}dx - M_t\phi_r(L)\frac{\partial^2 w_b(x,t)}{\partial t^2}\bigg|_{x=L}$$
$$= -\frac{d^2 g(t)}{dt^2}\left[\int_0^L \left(\rho_s A_s + \rho_p A_p\right)\phi_r(x)dx + M_t\phi_r(L)\right] - \frac{d^2 h(t)}{dt^2}\left[\int_0^L \left(\rho_s A_s + \rho_p A_p\right)x\phi_r(x)dx + M_t L\phi_r(L)\right] \tag{8.224}$$

and it modifies the σ_r and τ_r terms accordingly in the split representation of the forcing term ($F_r = -\sigma_r\omega^2 W_0 - \tau_r\omega^2\theta_0$).

With the inclusions of the tip mass, the total kinetic energy expression in the Timoshenko model becomes

$$T = \frac{1}{2}\int_{V_s}\rho_s\left[\left(\frac{\partial u^0(x,t)}{\partial t} - z\frac{\partial \psi^0(x,t)}{\partial t}\right)^2 + \left[\frac{\partial w^0(x,t)}{\partial t} + \frac{\partial w_b(x,t)}{\partial t}\right]^2\right]dV_s$$
$$+\int_{V_p}\rho_p\left[\left(\frac{\partial u^0(x,t)}{\partial t} - z\frac{\partial \psi^0(x,t)}{\partial t}\right)^2 + \left[\frac{\partial w^0(x,t)}{\partial t} + \frac{\partial w_b(x,t)}{\partial t}\right]^2\right]dV_p \tag{8.225}$$
$$+\frac{1}{2}M_t\left[\left(\frac{\partial w^0(x,t)}{\partial t} + \frac{\partial w_b(x,t)}{\partial t}\right)\bigg|_{x=L}\right]^2 + \frac{1}{2}I_t\left[\frac{\partial \psi^0(x,t)}{\partial t}\bigg|_{x=L}\right]^2$$

The sub-matrices altered in the Timoshenko model due to this modification are m_{rl}^{aa} and m_{rl}^{cc}:

$$m_{rl}^{aa} = \int_0^L \left(\rho_s A_s + \rho_p A_p\right)\phi_r(x)\phi_l(x)dx + M_t\phi_r(L)\phi_l(L) \tag{8.226}$$

$$m_{rl}^{cc} = \int_0^L \left(\rho_s I_s + \rho_p I_p\right)\beta_r(x)\beta_l(x)dx + I_t\beta_r(L)\beta_l(L) \tag{8.227}$$

The base excitation related terms derived from the total kinetic energy take the forms given by Eqs. (8.223) and (8.224) (identical in Euler-Bernoulli, Rayleigh and Timoshenko models).

8.7 Comments on the Kinematically Admissible Trial Functions

8.7.1 Euler-Bernoulli and Rayleigh Models. The essential boundary conditions of a clamped-free beam in the Euler-Bernoulli and Rayleigh models are given in Appendix D.1. According to the kinematic boundary conditions at the clamped end, the admissible functions in Eqs. (8.26) and (8.27) should satisfy

$$\phi_r(0) = 0 \tag{8.228}$$

$$\phi_r'(0) = 0 \tag{8.229}$$

$$\alpha_r(0) = 0 \tag{8.230}$$

For the admissible functions $\phi_r(x)$ of the transverse displacement, one can use the eigenfunctions of the respective symmetric structure given in Chapter 3. Therefore,

$$\phi_r(x) = \cos\frac{\lambda_r}{L}x - \cosh\frac{\lambda_r}{L}x + \varsigma_r\left(\sin\frac{\lambda_r}{L}x - \sinh\frac{\lambda_r}{L}x\right) \tag{8.231}$$

where ς_r is obtained from

$$\varsigma_r = \frac{\sin\lambda_r - \sinh\lambda_r + \lambda_r\dfrac{M_t}{mL}\left(\cos\lambda_r - \cosh\lambda_r\right)}{\cos\lambda_r + \cosh\lambda_r - \lambda_r\dfrac{M_t}{mL}\left(\sin\lambda_r - \sinh\lambda_r\right)} \tag{8.232}$$

Here, λ_r is the *r*-th root of the transcendental equation

$$\begin{aligned}&1 + \cos\lambda\cosh\lambda + \lambda\frac{M_t}{mL}\left(\cos\lambda\sinh\lambda - \sin\lambda\cosh\lambda\right) - \frac{\lambda^3 I_t}{mL^3}\left(\cosh\lambda\sin\lambda + \sinh\lambda\cos\lambda\right)\\ &+ \frac{\lambda^4 M_t I_t}{m^2 L^4}\left(1 - \cos\lambda\cosh\lambda\right) = 0\end{aligned} \tag{8.233}$$

where *m* is the mass per length of the beam:

$$m = \int_0^L \left(\rho_s A_s + \rho_p A_p\right) dx \tag{8.234}$$

The foregoing expressions simplify considerably in the absence of a tip mass ($M_t = I_t = 0$). Indeed, even in the presence of a tip mass, one can use the form of the $\phi_r(x)$ for $M_t = I_t = 0$,

$$\phi_r(x) = \cos\frac{\lambda_r}{L}x - \cosh\frac{\lambda_r}{L}x + \frac{\sin\lambda_r - \sinh\lambda_r}{\cos\lambda_r + \cosh\lambda_r}\left(\sin\frac{\lambda_r}{L}x - \sinh\frac{\lambda_r}{L}x\right) \tag{8.235}$$

which is still kinematically admissible with λ_r obtained from

$$1 + \cos\lambda\cosh\lambda = 0 \tag{8.236}$$

However, in the presence of a tip mass, using the eigenvalues obtained from Eq. (8.233) might lead to faster convergence (with less number of modes) in the discretized system. Note that the foregoing admissible functions become the eigenfunctions for a symmetric structure.

If one prefers to avoid the hyperbolic functions appearing in the eigenfunctions of the symmetric structure, the following is a typical admissible function used for clamped-free boundary conditions [84]:

$$\phi_r(x) = 1 - \cos\left[\frac{(2r-1)\pi x}{2L}\right] \tag{8.237}$$

which satisfies Eqs. (8.228) and (8.229). Polynomial forms and static solutions can also be used to satisfy Eqs. (8.228) and (8.229).

Similarly, the eigenfunctions of the symmetric structure under longitudinal vibrations can be used as the admissible functions of the asymmetric structure here. From Chapter 2,

$$\alpha_r(x) = \sin\frac{\eta_r}{L}x \tag{8.238}$$

where η_r is the *r*-th root of the transcendental equation

$$\frac{M_t}{mL}\eta_r \sin\eta_r - \cos\eta_r = 0 \tag{8.239}$$

Alternatively, the roots of $\cos\eta_r = 0$ (i.e. $\eta_r = (2r-1)\pi/2$, $r = 1, 2, ..., N$) can be used in Eq. (8.238) for simplicity.

8.7.2 Timoshenko Model. The essential boundary conditions of a clamped-free Timoshenko beam are given in Appendix D.2. Based on the kinematic boundary conditions, the admissible functions in Eqs. (8.127)-(8.129) should satisfy

$$\phi_r(0) = 0 \tag{8.240}$$

$$\alpha_r(0) = 0 \tag{8.241}$$

$$\beta_r(0) = 0 \tag{8.242}$$

According to Eq. (8.240), one can use the form of $\phi_r(x)$ given by Eq. (8.231) since it satisfies Eq. (8.240). However, it is useful to note that $\phi_r'(0) = 0$ implies zero shear strain at the root (due to $\beta_r(0) = 0$), which is not realistic for a clamped boundary. A simple trigonometric function similar to Eq. (8.238) could be a better alternative compared to Eq. (8.231). Equations (8.241) and (8.242) also accept trigonometric forms. However, using similar trigonometric functions might result in cancellations of the cross-integrals in Eqs. (8.136)-(8.147) due to the orthogonality of trigonometric functions. Polynomial forms can be employed as an alternative.

Several other alternatives exist in the literature, such as implementations of the Chebyshev polynomials [85] and static solutions [86].

8.8 Experimental Validations of the Assumed-Modes Solution for a Bimorph Cantilever

8.8.1 PZT-5H Bimorph Cantilever without a Tip Mass. The experimental case study given for the PZT-5H bimorph cantilever with a tip mass in Section 4.1 is revisited here for validation of the electromechanical assumed-modes solution. The assumed-modes counterpart of the analytical thin-beam solution given in Chapter 4 is the Euler-Bernoulli formulation given in Section 8.2. Note that the structure is thin enough to neglect the effects of shear deformation and rotary inertia in modeling. For a device with moderate thickness, the Timoshenko formulation should be used. According to the geometric and materials properties of the cantilever given in Table 4.1, the coupling between the transverse and the longitudinal displacement components vanishes (i.e. due to the structural symmetry, $H_s = H_p = 0$). The admissible function used in all simulations is the trigonometric admissible function given by Eq. (8.237) (therefore the exact eigenfunction, although is available, is not used). All the comparisons here are given against the experimental measurements and the analytical solutions for the entire set of resistors used in Section 4.1.

Figure 8.2 shows the assumed-modes prediction with only one mode ($N = 1$). Both the voltage and the tip velocity predictions are highly inaccurate (especially in terms of the resonance frequency). If the number of modes in the assume-modes procedure is increased to $N = 3$, the predictions are improved substantially as observed in Fig. 8.3 (see Table 8.1). Further increase in the number of modes up to $N = 5$ (Fig. 8.4) and then to $N = 10$ (Fig. 8.5) provides uniform convergence to the analytical frequencies (but not as dramatic as the improvement from 3 modes to 10 modes). Although increasing the number of modes does not seem to be improving the model prediction considerably, including more number of modes improve the predictions of higher vibration modes which are not discussed here.

Note that, the fundamental natural frequency estimated using this technique gives an upper bound of the lowest natural frequency [41] (as in the Rayleigh-Ritz method) and approximate fundamental natural frequency cannot underestimate the analytical value regardless of the number of modes used.

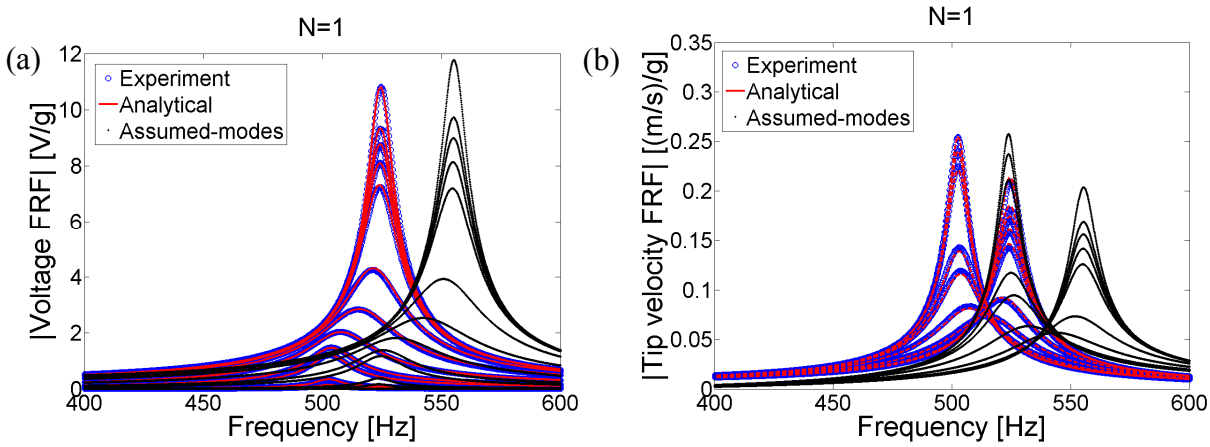

Fig. 8.2 Comparison of the (a) voltage FRFs and the (b) tip velocity FRFs of the PZT-5H bimorph cantilever without a tip mass against the experimental data and the analytical solution (1 mode is used in the assumed-modes solution)

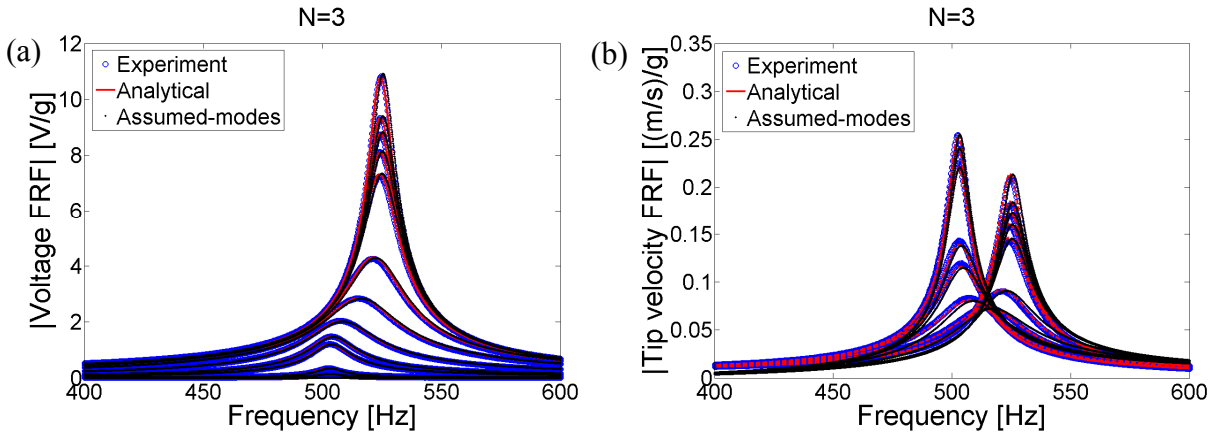

Fig. 8.3 Comparison of the (a) voltage FRFs and the (b) tip velocity FRFs of the PZT-5H bimorph cantilever without a tip mass against the experimental data and the analytical solution (3 modes are used in the assumed-modes solution)

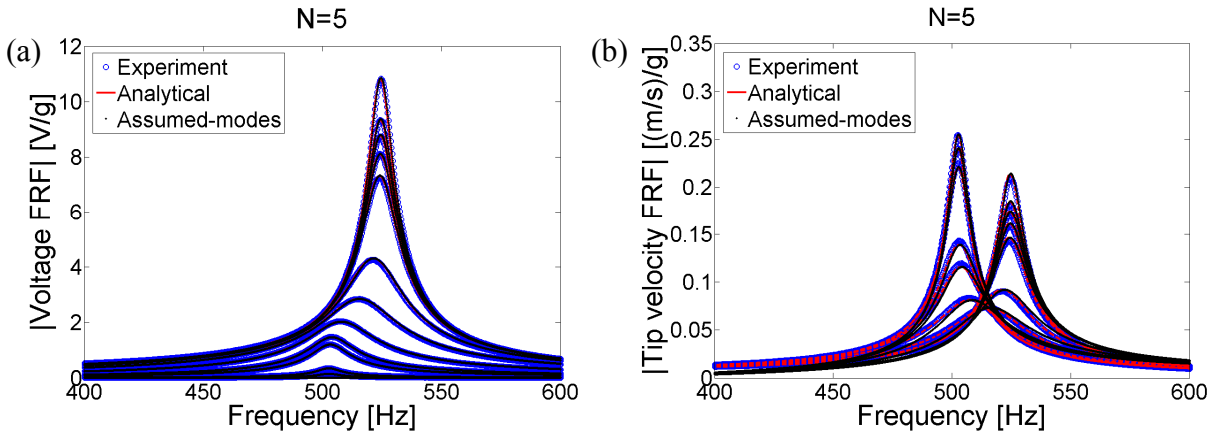

Fig. 8.4 Comparison of the (a) voltage FRFs and the (b) tip velocity FRFs of the PZT-5H bimorph cantilever without a tip mass against the experimental data and the analytical solution (5 modes are used in the assumed-modes solution)

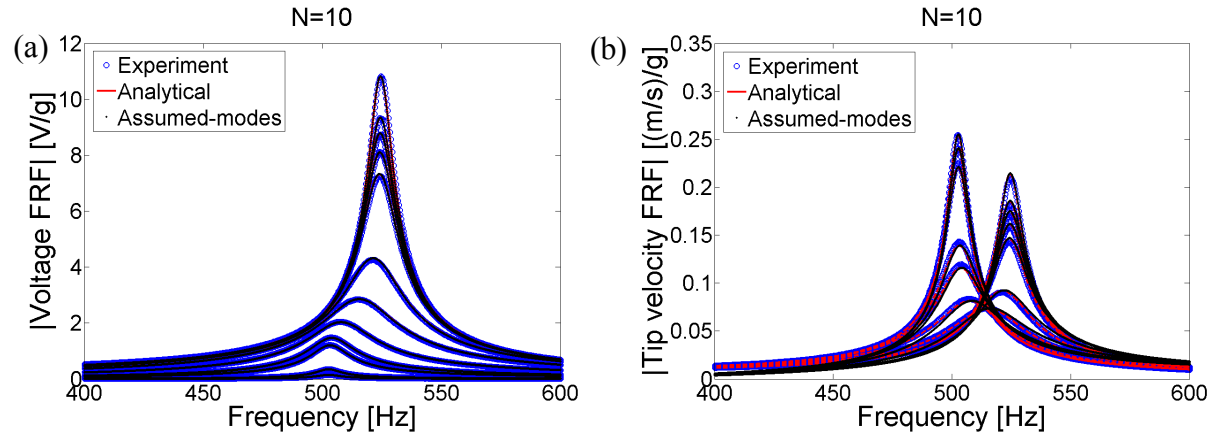

Fig. 8.5 Comparison of the (a) voltage FRFs and the (b) tip velocity FRFs of the PZT-5H bimorph cantilever without a tip mass against the experimental data and the analytical solution (10 modes are used in the assumed-modes solution)

Table 8.1 Assumed-mode predictions of the short-circuit and the open-circuit resonance frequencies of the voltage FRF for the PZT-5H bimorph cantilever without a tip mass

	f_1^{sc} [Hz]	f_1^{oc} [Hz]
Experimental	502.5	524.7
Analytical	502.6	524.5
Assumed-modes ($N=1$)	523.8	555.3
Assumed-modes ($N=3$)	503.2	525.5
Assumed-modes ($N=5$)	502.7	524.7
Assumed-modes ($N=10$)	502.6	524.5

8.8.2 PZT-5H Bimorph Cantilever with a Tip Mass. The configuration in Section 4.2 (the same cantilever of Section 8.8.1 with a tip mass attachment) is revisited next. The only difference in the formulation (compared to that of Section 8.8.1) is due to the contribution of the tip mass information and its mass moment of inertia to the mass matrix and the forcing vector as discussed in Section 8.6. Therefore, Eqs. (8.221) and (8.223) should be used in order to calculate the sub-matrix m_{rl}^{aa} and the forcing vector p_r in the assume-modes solution procedure of Section 8.2. Again, all resistors are considered in the comparisons against the analytical solutions and the experimental results. The same admissible function given by Eq. (8.237) is used in the assumed-modes simulations.

The assumed-modes prediction for only one mode ($N=1$) gives highly inaccurate predictions as shown in Fig. 8.6 (as in the previous case). Just like in the previous case (without the tip mass), if two mode modes added to the solution (so that $N=3$), the predictions are improved substantially as given in Fig. 8.7 which can also been seen from the predictions of the short-circuit resonance and the open-circuit resonance frequency predictions in Table 8.2. Further increase in the number of modes results in uniform convergence to the analytical frequencies as shown in Figs. 8.8 and 8.9.

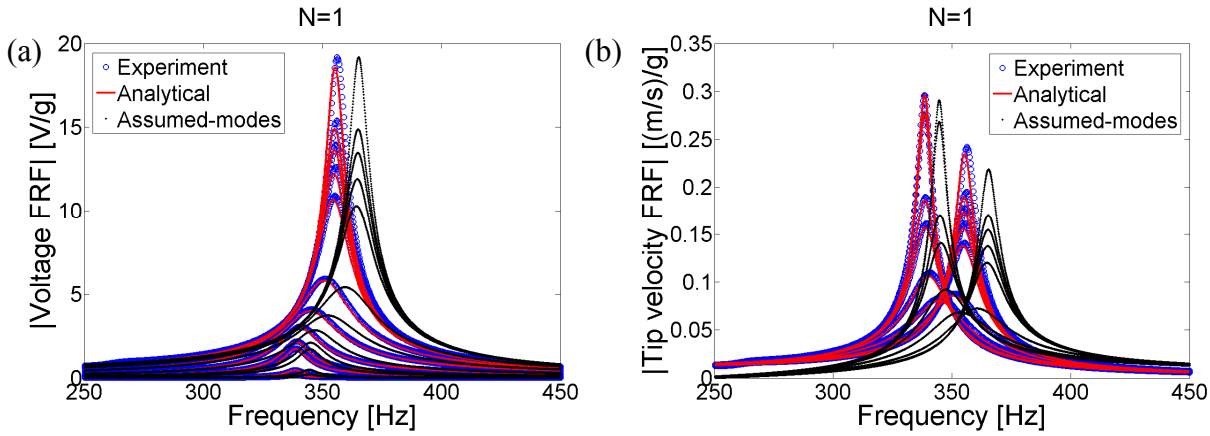

Fig. 8.6 Comparison of the (a) voltage FRFs and the (b) tip velocity FRFs of the PZT-5H bimorph cantilever with a tip mass against the experimental data and the analytical solution (1 mode is used in the assumed-modes solution)

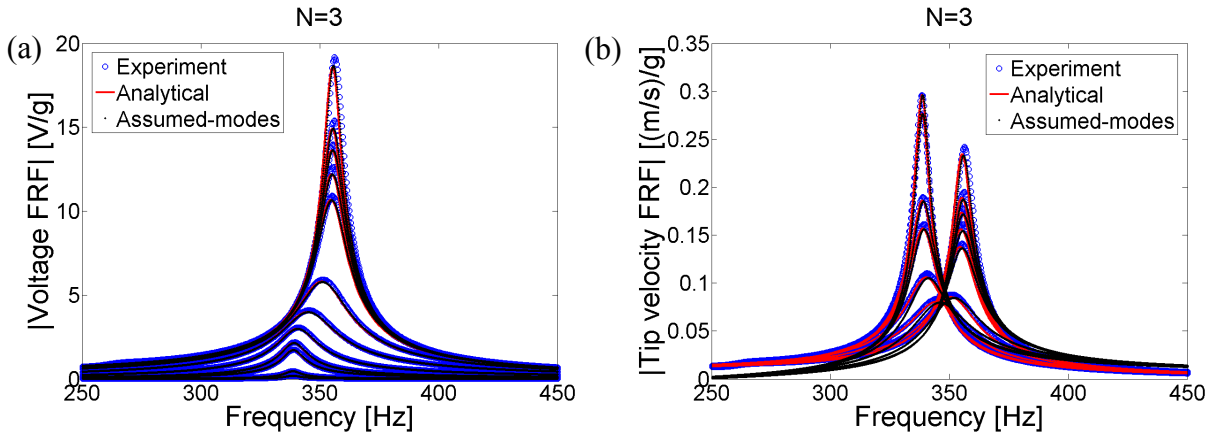

Fig. 8.7 Comparison of the (a) voltage FRFs and the (b) tip velocity FRFs of the PZT-5H bimorph cantilever with a tip mass against the experimental data and the analytical solution (3 modes are used in the assumed-modes solution)

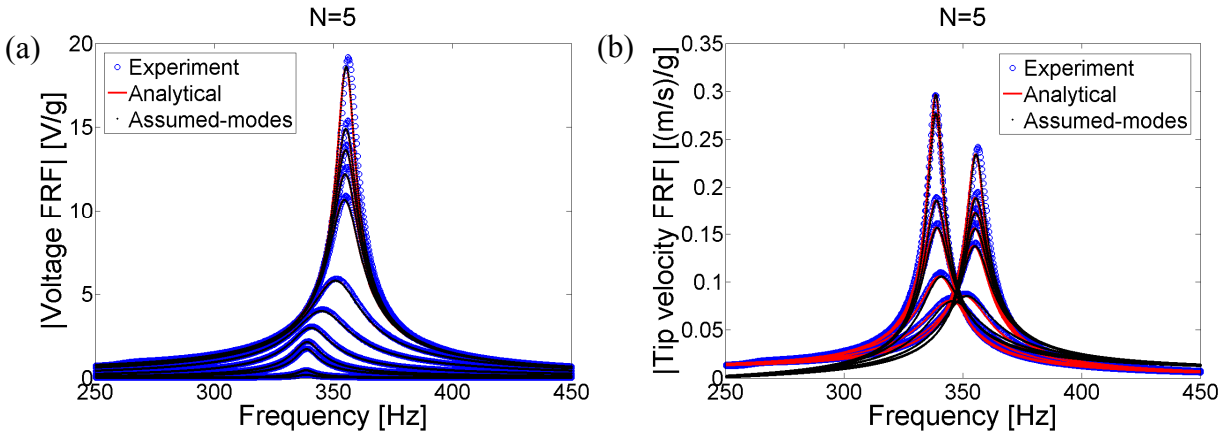

Fig. 8.8 Comparison of the (a) voltage FRFs and the (b) tip velocity FRFs of the PZT-5H bimorph cantilever with a tip mass against the experimental data and the analytical solution (5 modes are used in the assumed-modes solution)

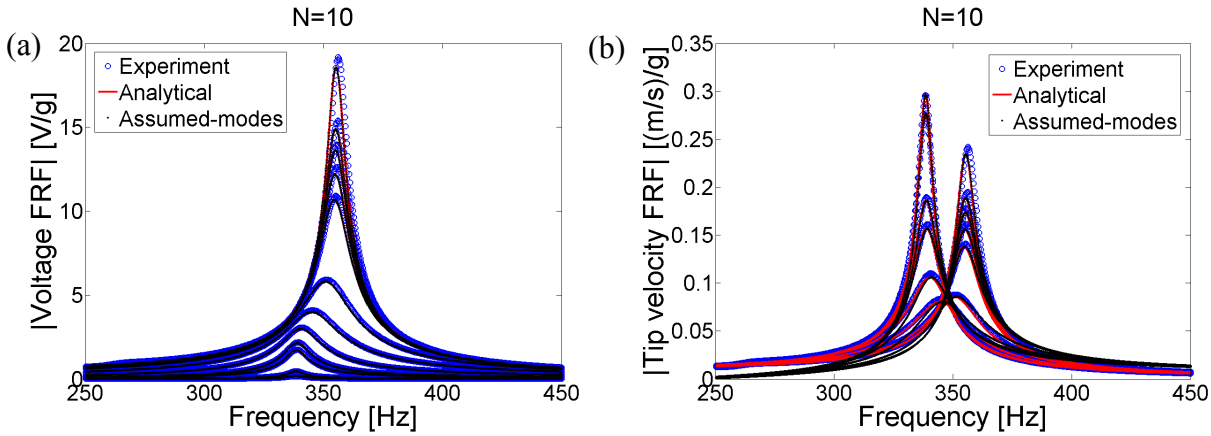

Fig. 8.9 Comparison of the (a) voltage FRFs and the (b) tip velocity FRFs of the PZT-5H bimorph cantilever with a tip mass against the experimental data and the analytical solution (10 modes are used in the assumed-modes solution)

Table 8.2 Assumed-mode predictions of the short-circuit and the open-circuit resonance frequencies of the voltage FRF for the PZT-5H bimorph cantilever with a tip mass

	f_1^{sc} [Hz]	f_1^{oc} [Hz]
Experimental	338.4	356.3
Analytical	338.5	355.4
Assumed-modes ($N=1$)	344.6	365.3
Assumed-modes ($N=3$)	338.7	355.8
Assumed-modes ($N=5$)	338.5	355.5
Assumed-modes ($N=10$)	338.5	355.4

8.9 Summary and Conclusions

Approximate distributed-parameter modeling of cantilevered piezoelectric energy harvesters is given in this chapter. An electromechanical version of the assumed-modes method of structural dynamics is used to discretize the energy equations into electromechanical Lagrange equations derived from the extended Hamilton's principle. The derivations are given based on the Euler-Bernoulli, Rayleigh and Timoshenko beam theories. In all cases, an axial displacement variable is defined to capture its coupling with the transverse displacement variable due to structural asymmetry. To demonstrate modeling of an asymmetric configuration, focus is placed on the unimorph configuration. Simplification of the governing equations for symmetric bimorph configurations is also shown and the effect of a tip mass on the resulting formulation is discussed. A short discussion regarding the kinematically admissible functions to be used in the models derived here is also provided. Finally the experimental case studies for a thin cantilever (without and with a tip mass) are revisited for validation of the assumed-modes solution using different number of admissible trigonometric functions. The predictions of the assumed-modes solution are also compared with the analytical solution and a very good agreement is observed. The approximate formulations given in this chapter can be used to predict the electromechanical response of cantilevers with asymmetric laminates, moderately thick cantilevers as well as cantilevers with varying cross-section.

CHAPTER 9

A NON-CONVENTIONAL BROADBAND VIBRATION ENERGY HARVESTER USING A BI-STABLE PIEZO-MAGNETO-ELASTIC STRUCTURE

A primary issue in resonant vibration energy harvesters discussed in the previous chapters is that the best performance of the device is limited to resonance excitation. That is, if the excitation frequency slightly deviates from the fundamental resonance frequency of the energy harvester, the power out is drastically reduced. In order to overcome this issue of the conventional *resonant* cantilever configuration, a *non-resonant* piezo-magneto-elastic energy harvester is introduced in this chapter. The magneto-elastic configuration is well known from the literature of nonlinear dynamics as a mechanical structure that exhibits chaotic strange attractor motions. Here, piezoelectric coupling is introduced to the structure in order to obtain a piezo-magneto-elastic configuration for vibration energy harvesting. First the lumped-parameter electromechanical equations describing the nonlinear system are given along with theoretical simulations to demonstrate the existence of high-energy orbits at different frequencies. It is shown that, over a range of frequencies, one can generate much larger voltage from the substantially large amplitude oscillations on these orbits. An experimental prototype is built and the presence of such high-energy orbits at several frequencies below the post-buckled natural frequency of the structure is verified. In qualitative agreement with the theory, the experiments show that the transient chaotic vibrations of the generator can turn into large-amplitude oscillations on a high-energy orbit, which can also be realized by applying a disturbance to the structure oscillating on a low-energy orbit around one of its foci. It is shown experimentally that, for the same excitation input, the open-circuit voltage output of the piezo-magneto-elastic energy harvester can be three times that of the conventional piezo-elastic cantilever configuration, yielding an order of magnitude larger power output over a range of frequencies.

9.1 Piezo-magneto-elastic Energy Harvester

9.1.1 Lumped-parameter Electromechanical Equations Describing the Nonlinear System Dynamics. The magneto-elastic structure shown in Fig. 9.1a was first investigated by Moon and Holmes [87] as a mechanical structure that exhibits *strange attractor*[*] motions [88]. The device consists of a ferromagnetic cantilevered beam with two permanent magnets located symmetrically near the free end and it is subjected to harmonic base excitation. The bifurcations of the static problem are described by a *butterfly catastrophe* [91] in the catastrophe theory with a sixth order magneto-elastic potential. Therefore, depending on the magnet spacing, the ferromagnetic beam may have five (with three stable), three (with two stable) or one (stable) equilibrium positions. For the case with three equilibrium positions (the *bi-stable* configuration), the governing lumped-parameter equation of motion has the form of the Duffing equation:

$$\ddot{x} + 2\zeta\dot{x} - \frac{1}{2}x\left(1 - x^2\right) = f\cos\Omega t \tag{9.1}$$

where x is the dimensionless tip displacement of the beam in the transverse direction, ζ is the mechanical damping ratio, Ω is the dimensionless excitation frequency, f is the dimensionless excitation force due to base acceleration ($f \propto \Omega^2 X_0$ where X_0 is the dimensionless base displacement amplitude) and an over-dot represents differentiation with respect to dimensionless time. The three equilibrium positions obtained from Eq. (9.1) are $\left(x,\dot{x}\right) = \left(0,0\right)$ (a saddle) and $\left(x,\dot{x}\right) = \left(\pm 1,0\right)$ (two centers). Detailed nonlinear analysis of the magneto-elastic structure shown in Fig. 9.1a can be found in the papers by Moon and Holmes [87,92].

In order to use this device as a piezoelectric energy harvester, we attach two piezoceramic layers onto the root of the cantilever and obtain a bimorph generator as depicted in Fig. 9.1b. The piezoceramic layers are connected to an electrical load (a resistor for simplicity)

[*] Although the main focus of this chapter is not the chaotic vibrations of the magneto-elastic configuration, it is worth recalling that the term *strange attractor* in chaos theory refers to a fractal set to which a dynamical system evolves after sufficiently long time. According to Lorenz [89], one of the pioneers best known for his early work on the nonlinear atmospheric phenomena [90], "*a strange attractor, when it exists, is truly the heart of a chaotic system…*" [89]. A concrete example of such an attractor with a practical value follows: "*…For one special complicated chaotic system – the global weather – the attractor is simply the climate, that is, the set of weather patterns that have at least some chance of occasionally occurring*."

and the voltage output of the generator across the load due to seismic excitation is the primary interest in energy harvesting. Introducing piezoelectric coupling into Eq. (9.1) and applying the Kirchhoff laws to the circuit with a resistive load (Fig. 9.1b) leads to the following electromechanical equations describing the system dynamics:

$$\ddot{x} + 2\zeta\dot{x} - \frac{1}{2}x\left(1 - x^2\right) - \chi v = f\cos\Omega t \tag{9.2}$$

$$\dot{v} + \lambda v + \kappa\dot{x} = 0 \tag{9.3}$$

where v is the dimensionless voltage across the load resistance, χ is the dimensionless piezoelectric coupling term in the mechanical equation, κ is the dimensionless piezoelectric coupling term in the electrical circuit equation and λ is the reciprocal of the dimensionless time constant ($\lambda \propto 1/R_l C_p$ where R_l is the load resistance and C_p is the equivalent capacitance of the piezoceramic layers). Note that the possible nonlinearity coming from piezoelectric coupling is ignored in Eqs. (9.2) and (9.3), assuming the standard form of the linear piezoelectric constitutive relations [26] (Appendix A).

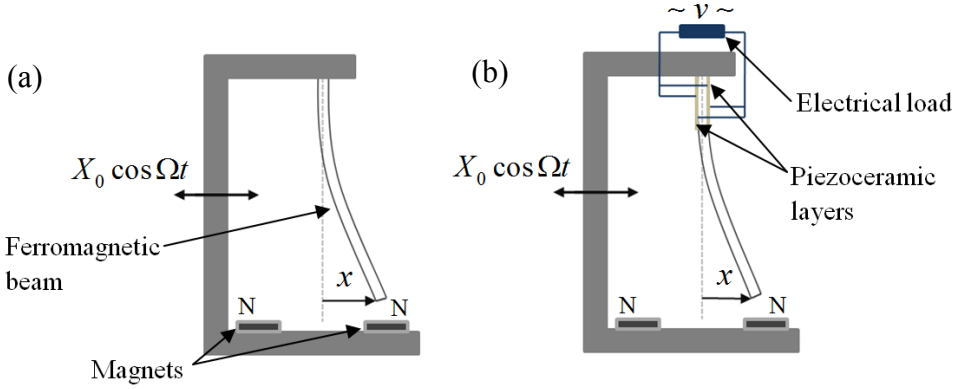

Fig. 9.1 Schematics of the (a) magneto-elastic structure investigated by Moon and Holmes [87] and the (b) piezo-magneto-elastic energy harvester proposed here

The state-space form of Eqs. (9.2) and (9.3) can be expressed as

$$\begin{Bmatrix} \dot{u}_1 \\ \dot{u}_2 \\ \dot{u}_3 \end{Bmatrix} = \begin{Bmatrix} u_2 \\ -2\zeta u_2 + \frac{1}{2}u_1\left(1 - u_1^2\right) + \chi u_3 + f\cos\Omega t \\ -\lambda u_3 - \kappa u_2 \end{Bmatrix} \tag{9.4}$$

where the state variables are $u_1 = x$, $u_2 = \dot{x}$ and $u_3 = v$. The electromechanically coupled equations given by Eq. (9.4) can be used in an ordinary differential equation solver for numerical simulations (the *ode45* command of MATLAB [44] is used here).

9.1.2 Time-domain Numerical Simulations of the Electromechanical Response. The time-domain voltage simulations shown in Figs. 9.2 and 9.3 are obtained using Eq. (9.4) with $\Omega = 0.8$, $\zeta = 0.01$, $\chi = 0.05$, $\kappa = 0.5$ and $\lambda = 0.05$ (close to open-circuit conditions). In the first case (Fig. 9.2a), the forcing term is $f = 0.083$ and the motion starts with an initial deflection at one of the stable equilibrium positions ($x(0) = 1$ with zero initial velocity and voltage: $\dot{x}(0) = v(0) = 0$). The resulting vibratory motion is on a chaotic strange attractor (yielding the chaotic voltage history shown in Fig. 9.2a) and the Poincaré map of this strange attractor motion is shown in Fig. 9.2b on its phase portrait.

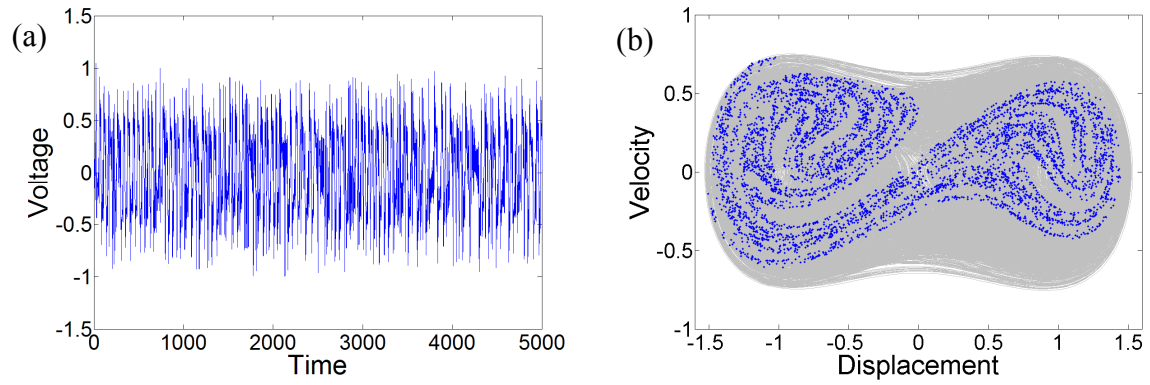

Fig. 9.2 (a) Theoretical voltage history exhibiting the strange attractor motion for and (b) its Poincaré map ($x(0) = 1$, $\dot{x}(0) = 0$, $v(0) = 0$, $f = 0.083$, $\Omega = 0.8$)

If the excitation amplitude is increased by keeping the same initial conditions, the transient chaotic behavior is followed by large-amplitude oscillations on a high-energy orbit with improved voltage response (Fig. 9.3a). More importantly, Fig. 9.3b shows that this type of large-amplitude voltage response can be obtained with the original excitation amplitude (of Fig. 9.2a) and different initial conditions (simply by imposing an initial velocity condition so that $x(0) = 1$, $\dot{x}(0) = 1.2$, $v(0) = 0$).

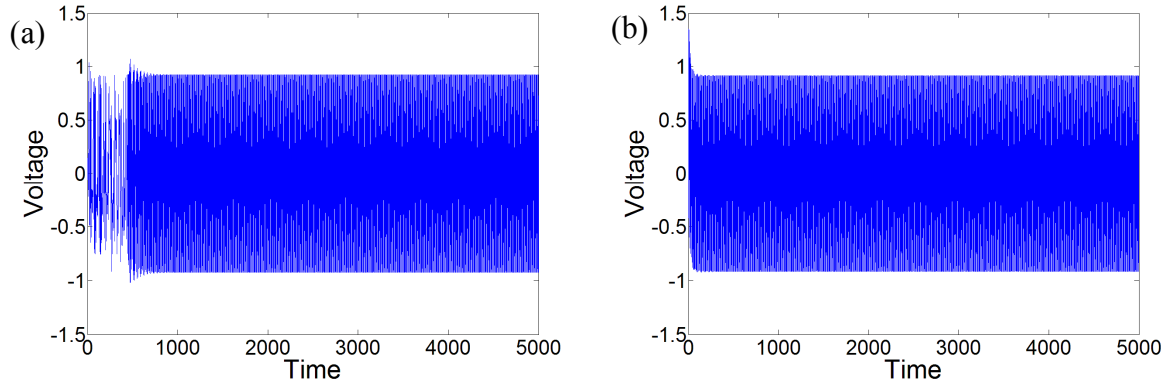

Fig. 9.3 Theoretical voltage histories: (a) Large-amplitude response due to the excitation amplitude ($x(0)=1$, $\dot{x}(0)=0$, $v(0)=0$, $f=0.115$, $\Omega=0.8$); (b) Large-amplitude response due to the initial conditions for a lower excitation amplitude ($x(0)=1$, $\dot{x}(0)=1.2$, $v(0)=0$, $f=0.083$, $\Omega=0.8$)

9.1.3 Performance Comparison of the Piezo-magneto-elastic and the Piezo-elastic Structures in the Phase Space. Having observed the large-amplitude electromechanical response obtained on high-energy orbits of the piezo-magneto-elastic energy harvester configuration described by Eqs. (9.2) and (9.3), a simple comparison can be made against the conventional piezo-elastic configuration (which is the *linear* cantilever configuration without the magnets causing the bi-stability).

The lumped-parameter equations of the linear piezo-elastic configuration are

$$\ddot{x}+2\zeta\dot{x}+x-\chi v=f\cos\Omega t \tag{9.5}$$

$$\dot{v}+\lambda v+\kappa\dot{x}=0 \tag{9.6}$$

which can be given in the state-space form as

$$\begin{Bmatrix}\dot{u}_1\\ \dot{u}_2\\ \dot{u}_3\end{Bmatrix}=\begin{Bmatrix}u_2\\ -2\zeta u_2-u_1+\chi u_3+f\cos\Omega t\\ -\lambda u_3-\kappa u_2\end{Bmatrix} \tag{9.7}$$

For the same numerical input ($\Omega=0.8$, $\zeta=0.01$, $\chi=0.05$, $\kappa=0.5$ and $\lambda=0.05$), initial conditions and the forcing amplitude of Fig. 9.3b ($x(0)=1$, $\dot{x}(0)=1.2$, $v(0)=0$, $f=0.083$), one can simulate the voltage response of the piezo-elastic configuration using Eq. (9.7).

Figure 9.4a shows the velocity vs. displacement phase portrait of the piezo-magneto-elastic and the piezo-elastic configurations. As can be seen from the steady-state orbits appearing in this figure, for the same excitation amplitude, system parameters and the forcing amplitude, the steady-state vibration amplitude of the piezo-magneto-elastic configuration can be much larger than that of the piezo-elastic configuration. Expectedly, the large-amplitude response on the high-energy orbit is also observed in the velocity vs. voltage phase portrait[†] shown in Fig. 9.4b.

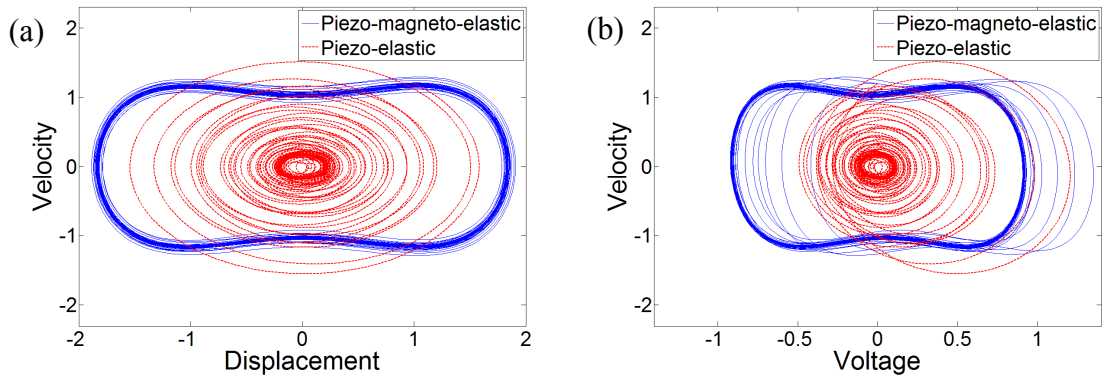

Fig. 9.4 Comparison of the (a) velocity vs. displacement and the (b) velocity vs. voltage phase portraits of the piezo-magneto-elastic and piezo-elastic configurations

$(x(0)=1, \dot{x}(0)=1.2, v(0)=0, f=0.083, \Omega=0.8)$

The superiority of the piezo-magneto-elastic configuration over the piezo-elastic configuration can be shown by plotting these trajectories at several other frequencies except for the resonance ($\Omega \cong 1$) case of the linear problem for which the piezo-elastic configuration generates more voltage. However, at several other frequencies (e.g. $\Omega=0.6, \Omega=0.7, \Omega=0.9$), a substantially

[†] For the system parameters used in these simulations, the phase between the voltage and the velocity is approximately 90 degrees because the system is close to open-circuit conditions. Therefore, in open-circuit conditions, it is reasonable to plot the velocity vs. voltage output as the *electromechanical phase portrait* (as an alternative to the conventional velocity vs. displacement phase portrait). From the experimental point of view, it is advantageous to plot these two independent measurements (voltage output of the piezoceramic vs. the velocity signal from the laser vibrometer) rather than integrating the experimental velocity history (as it typically results in a non-uniform drift).

amplified response similar to the case of $\Omega = 0.8$ can be obtained. The velocity vs. open-circuit voltage phase portraits of the piezo-magneto-elastic and the piezo-elastic configurations are plotted for $\Omega = 0.7$ and $\Omega = 0.9$ in Figs. 9.5a and 9.5b, respectively.

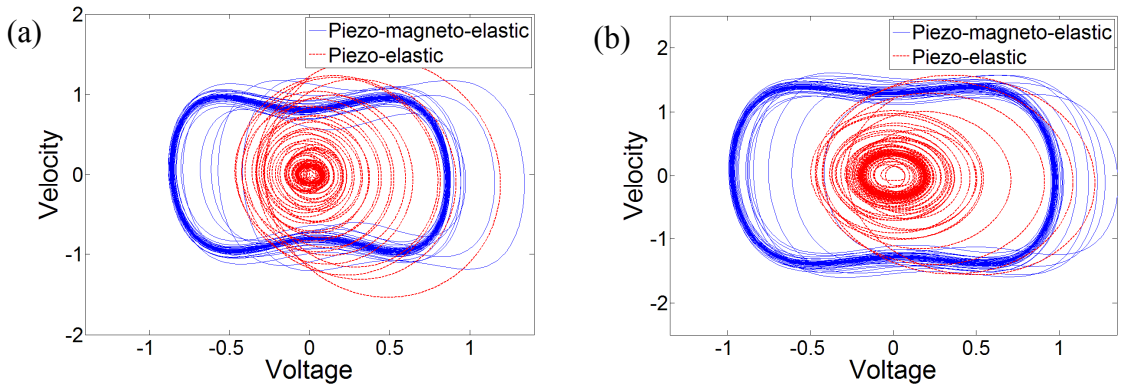

Fig 9.5 Comparison of the velocity vs. voltage phase portraits of the piezo-magneto-elastic and piezo-elastic configurations for (a) $\Omega = 0.7$ and (b) $\Omega = 0.9$
$(x(0) = 1, \dot{x}(0) = 1.2, v(0) = 0, f = 0.083)$

The three-dimensional voltage vs. velocity phase-space trajectories are given for the frequency range of $\Omega = 0.5 - 1$ in Fig. 9.6. In all cases, the system parameters, initial conditions and the forcing amplitude[‡] are the identical. In Fig. 9.6a, the electrical output of the piezo-magneto-elastic configuration is not considerably larger because the trajectory oscillates around one of its foci. That is, the forcing amplitude cannot overcome the attraction of the magnetic force at the respective focus. As a result, the piezo-magneto-elastic configuration oscillates on a low-energy orbit and its electrical response amplitude is indeed comparable to that of the piezo-elastic configuration. In Figs. 9.6b-9.6e, over the frequency range of $\Omega = 0.6 - 0.9$, the piezo-magneto-elastic configuration shows a very large amplitude electromechanical response on a high-energy orbit compared to the orbit of the piezo-elastic configuration. Note that the response amplitude of the piezo-elastic configuration grows as one moves close to the resonance ($\Omega \cong 1$)

[‡] Notice from the discussions in Chapter 3 that the forcing amplitude in the base excitation problem is proportional to the square of the frequency ($f \propto \Omega^2 X_0$). Keeping the forcing amplitude f constant at different frequencies implies keeping the base acceleration amplitude the same. Hence the base displacement amplitudes are different.

of the piezo-elastic configuration. Yet the piezo-magneto-elastic configuration generates dramatically larger steady-state voltage output in this frequency range ($\Omega = 0.6 - 0.9$).

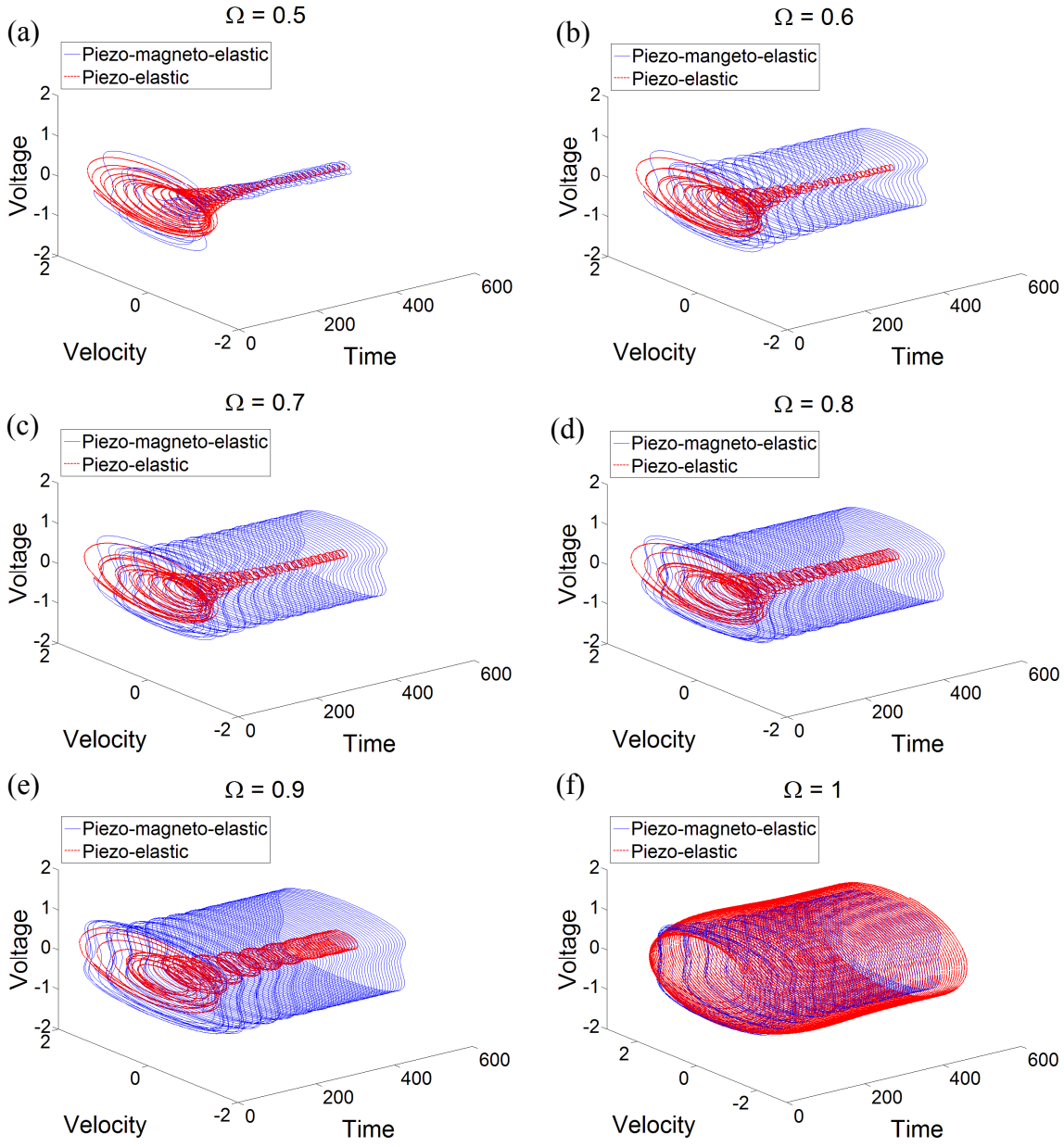

Fig. 9.6 Comparison of the voltage vs. velocity phase portraits of the piezo-magneto-elastic and piezo-elastic configurations for (a) $\Omega = 0.5$, (b) $\Omega = 0.6$, (c) $\Omega = 0.7$, (d) $\Omega = 0.8$, (e) $\Omega = 0.9$, (f) $\Omega = 1$ ($x(0) = 1, \dot{x}(0) = 1.2, v(0) = 0, f = 0.083$)

Expectedly, at $\Omega = 1$, the response amplitude of the piezo-elastic configuration is larger (Fig. 9.6f). It is worth adding that, at this particular frequency where the resonant configuration generates more voltage, the difference in the response amplitudes is not as dramatic as at other frequencies where the non-resonant configuration is much superior.

Experimental verifications of the concept (i.e. the presence of these high-energy orbits to utilize for piezoelectric energy harvesting) are given in the following sections.

9. 2 Experimental Setup and Performance Results

9.2.1 Experimental Setup. The piezo-magneto-elastic energy harvester and the setup used in the first set of experiments are shown in Fig. 9.7. Harmonic base excitation is provided by a seismic shaker (Acoustic Power Systems [93] APS-113), the acceleration at the base of the cantilever is measured by a small accelerometer (PCB Piezotronics [47] Model U352C67) and the velocity response of the cantilever is recorded by a laser vibrometer (Polytec [10] OFV303 laser head with OFV3001 vibrometer). The time history of the base acceleration, voltage and vibration responses are recorded by a National Instruments [94] NI cDAQ-9172 data acquisition system (with a sampling frequency of 2000 Hz). The ferromagnetic beam (made of tempered blue steel) is 145 mm long (overhang length), 26 mm wide and 0.26 mm thick. A lumped mass of 14 grams is attached close to the tip for improved dynamic flexibility. Two PZT-5A piezoceramic layers (QP16N, Midé Corporation [95]) are attached onto both faces of the beam at the root using a high – shear strength epoxy and they are connected in parallel. The spacing between the symmetrically located circular rare earth magnets is 50 mm (center to center) and this distance is selected to realize the three equilibrium case described by Eqs. (9.2) and (9.3). The tip deflection of the magnetically buckled beam in the static case to either side is approximately 15 mm relative to the unstable equilibrium position. The post-buckled fundamental resonance frequency of the beam is around 10.6 Hz (at both focus points) whereas the fundamental resonance frequency of the unbuckled beam (when the magnets are removed) is 7.4 Hz (both under the open-circuit conditions of piezoceramics – i.e. at constant electric displacement).

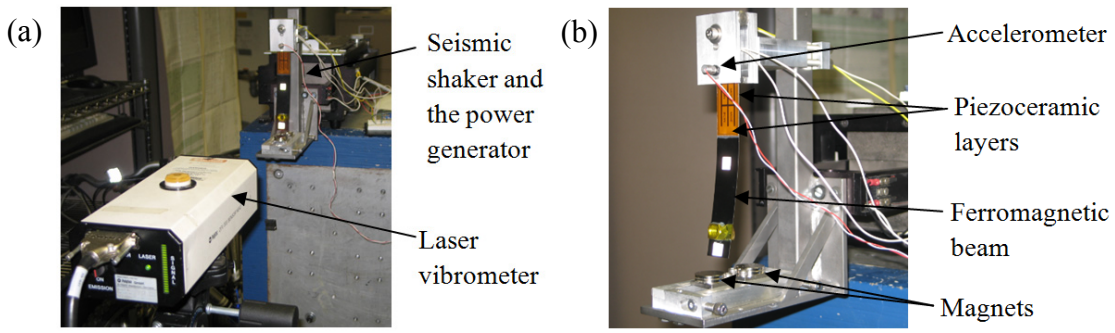

Fig. 9.7 (a) A view of the experimental setup and (b) the piezo-magneto-elastic energy harvester (photos by A. Erturk, 2009)

9.2.2 Performance Results. For a harmonic base excitation amplitude of 0.5*g* (where *g* is the gravitational acceleration: $g = 9.81$ m/s^2) at 8 Hz with an initial deflection at one of the stable equilibrium positions (15 mm to the shaker side), zero initial velocity and voltage, the chaotic open-circuit voltage response shown in Fig. 9.8a is obtained. The Poincaré map of the strange attractor motion is displayed in Fig. 9.8b. These figures are obtained from a measurement taken for about 15 minutes (1,784,400 data points due to a sampling frequency of 2000 Hz) and they exhibit very good qualitative agreement with the theoretical strange attractor given by Fig. 9.2.

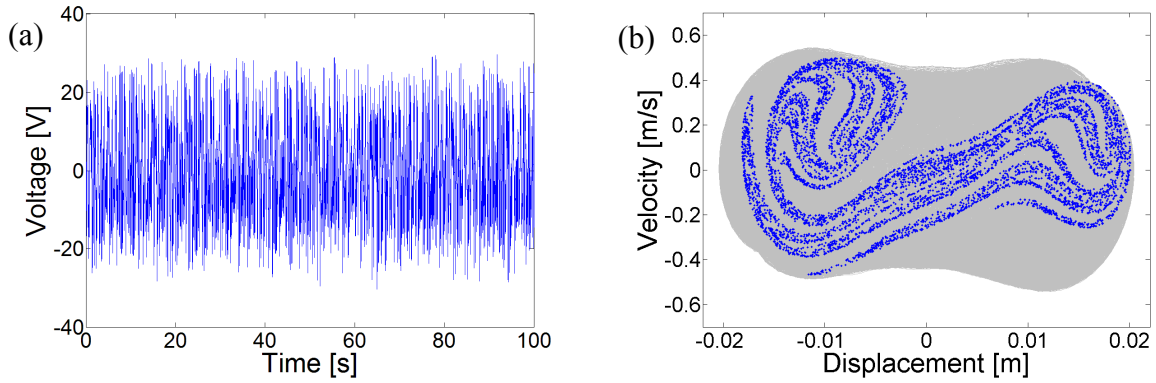

Fig. 9.8 (a) Experimental voltage history exhibiting the strange attractor motion for and (b) its Poincaré map (excitation: 0.5*g* at 8 Hz)

If the excitation amplitude is increased to 0.8*g* (at the same frequency), the structure goes from transient chaos into a large-amplitude periodic motion with a strong improvement in the voltage response as shown in Fig. 9.9a (i.e. the attractor is no longer a strange attractor). A

similar improvement is obtained in Fig. 9.9b where the excitation amplitude is kept as the original one ($0.5g$) and a disturbance (hand impulse) is applied at $t = 11\,\text{s}$ (as a simple alternative to creating a velocity initial condition). Such a disturbance can be realized in practice by applying an impulse type voltage input through one of the piezoceramic layers for once. The experimental evidence given with Fig. 9.9 is in agreement with the theoretical discussion given with Fig. 9.3. Noticing the large-amplitude steady-state voltage response obtained at an *off-resonance* frequency in Fig. 9.9, the broadband performance of the device is investigated and comparisons against the piezo-elastic configuration are given in the next section.

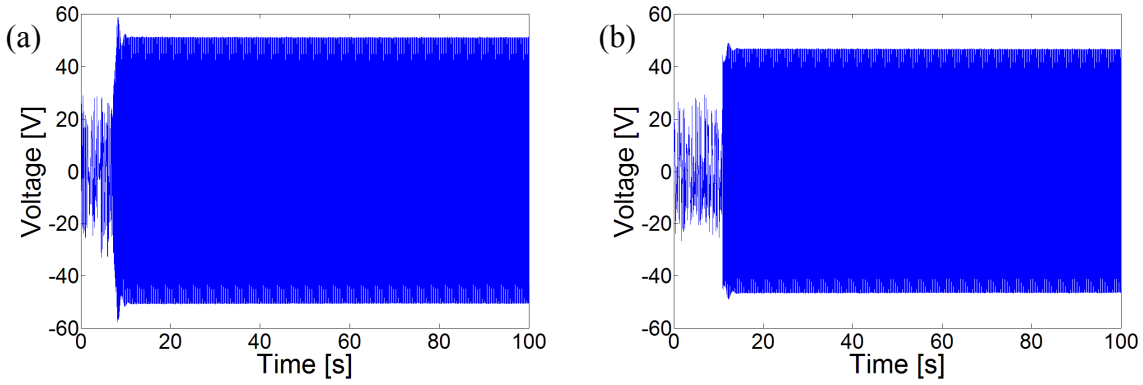

Fig. 9.9 Experimental voltage histories: (a) Large-amplitude response due to the excitation amplitude (excitation: $0.8g$ at 8 Hz); (b) Large-amplitude response due to a disturbance at $t = 11\,\text{s}$ for a lower excitation amplitude (excitation: $0.5g$ at 8 Hz)

9.3 Broadband Voltage Generation Using the Piezo-magneto-elastic Energy Harvester

9.3.1 Comments on the Chaotic and the Large-amplitude Regions in the Response. Before the comparisons of the piezo-magneto-elastic and piezo-elastic[§] configurations are given over a frequency range, reconsider the voltage history of Fig. 9.9b in two parts. The time history until the instant of the disturbance is chaotic, which would yield a strange attractor motion similar to what was shown in Fig. 9.8 if no disturbance was applied. After the disturbance is applied at $t = 11\,\text{s}$, the large-amplitude response on a high-energy orbit is obtained as the steady-state

[§] In the experiments, the piezo-elastic configuration is obtained simply by removing the magnets of the piezo-magneto-elastic configuration after the experiments the latter are completed.

response. In order to understand the advantage of the second region in the response history of Fig. 9.9b, the open-circuit voltage histories of the piezo-magneto-elastic and piezo-elastic configurations are compared for the same harmonic input (0.5*g* at 8 Hz). Figure 9.10a shows the acceleration input to the piezo-magneto-elastic and the piezo-elastic configurations at an arbitrary instant of time. The voltage input to the seismic shaker is identical for both configurations, yielding very similar base acceleration amplitudes (according to the signal output of the accelerometer) for a fair comparison. Figure 9.10b displays the comparison of the piezo-magneto-elastic and the piezo-elastic configurations where the former exhibits chaotic response and the latter has already reached its harmonic steady-state response amplitude at the input frequency. As a rough comparison, from Fig. 9.10b, it is not possible to claim that the chaotic response of the piezo-magneto-elastic configuration has any advantage over the harmonic response of the piezo-elastic configuration as their amplitudes look very similar (a more accurate comparison can be made through the RMS –root mean square [50,51] – amplitudes). Besides, one would definitely prefer a periodic signal to a chaotic signal when it comes to processing the harvested energy using an efficient energy harvesting circuit [23-25]. Figure 9.10c shows the voltage histories of these configurations some time after the disturbance is applied to the piezo-magneto-elastic configuration and the large-amplitude response is obtained. Obviously if the same disturbance is applied to the piezo-elastic configuration, the trajectory (in the phase space) returns to the same low-amplitude orbit after some transients. Therefore the response amplitude of the piezo-elastic configuration is identical in Figs. 9.10b and 9.10c. Although the chaotic response of the piezo-magneto-elastic structure has no considerable advantage according to Fig. 9.10b, the large-amplitude response of this structure can give more than 3 times larger RMS voltage output according to Fig. 9.10.c.

9.3.2 Comparison of the Piezo-magneto-elastic and Piezo-elastic Configurations for Voltage Generation. Figure 9.11a compares the velocity vs. voltage phase portraits of the piezo-magneto-elastic and piezo-elastic configurations for excitation at 8 Hz with 0.5*g*, showing the advantage of the large-amplitude orbit clearly. This figure is therefore analogous to the theoretical demonstration given by Fig. 9.4b (additional harmonics are present in the experimental data of the *distributed-parameter* piezo-magneto-elastic structure). The three-dimensional view of the electromechanical trajectory in the phase space is shown in Fig. 9.11b in

it shows good qualitative agreement with its simplified theoretical counterpart based on the lumped-parameter model (Fig. 9.6). The next step is to investigate different frequencies to see if similar high-energy orbits can be reached at other frequencies as well (as in the theoretical case).

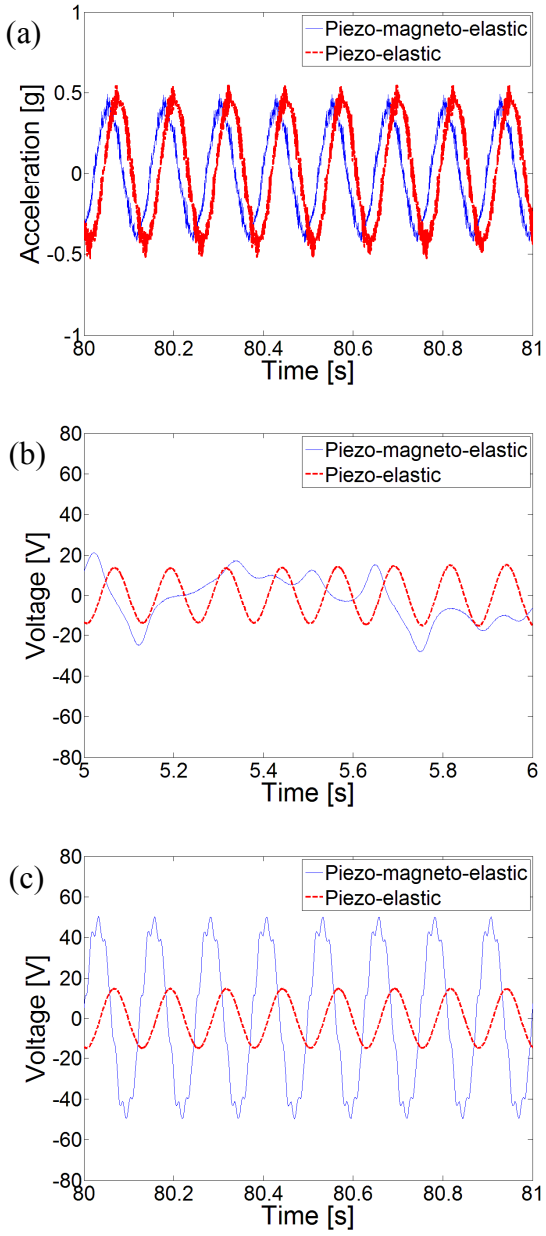

Fig. 9.10 Comparison of the input and the output time histories of the piezo-magneto-elastic and piezo-elastic configurations: (a) Input acceleration histories; (b) Voltage outputs in the chaotic response region of the piezo-magneto-elastic configuration; (c) Voltage outputs in the large-amplitude region of the piezo-magneto-elastic configuration (excitation: 0.5*g* at 8 Hz)

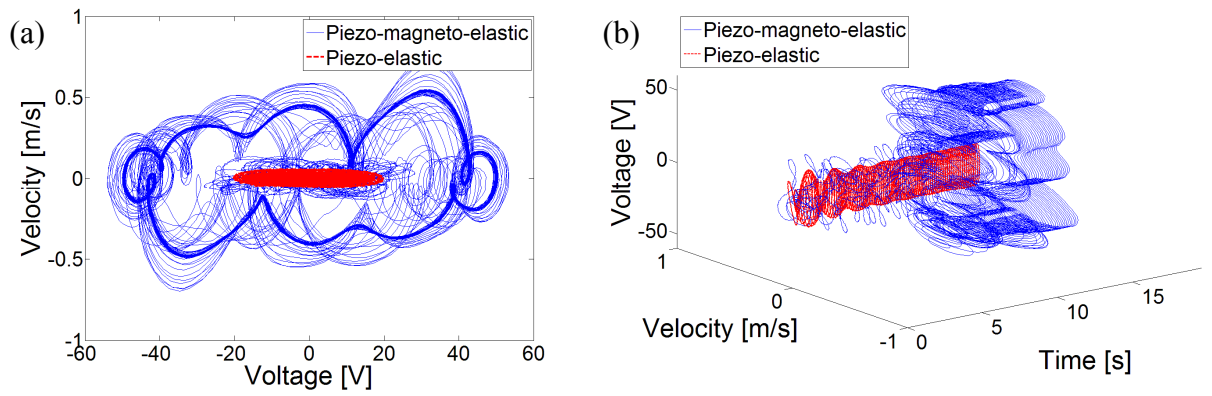

Fig. 9.11 (a) Two-dimensional and (b) three-dimensional comparison of the electromechanical (velocity vs. open-circuit voltage) phase portraits of the piezo-magneto-elastic and piezo-elastic configurations (excitation: 0.5*g* at 8 Hz)

For a harmonic base excitation amplitude of 0.5*g* (yielding an RMS acceleration of 0.35*g*), experiments are conducted at 4.5 Hz, 5 Hz, 5.5 Hz, 6 Hz, 6.5 Hz, 7 Hz, 7.5 Hz and 8 Hz. At each frequency, a large-amplitude response is obtained the same way as in Fig. 9.9b by applying a disturbance around $t = 11\text{s}$. Then the magnets are removed for comparison of the device performance with that of the conventional piezo-elastic configuration and the base excitation tests are repeated for the same frequencies with approximately the same input acceleration. The open-circuit RMS voltage outputs of the piezo-magneto-elastic and piezo-elastic configurations at each frequency are obtained considering the steady-state response in the 80s-100s time interval. The RMS values of the input base acceleration are also extracted for the same time interval.

Figure 9.12a shows that the excitation amplitudes of both configurations are indeed very similar (with an average RMS value of approximately 0.35*g*). The broadband voltage generation performance of the piezo-magneto-elastic energy harvester is shown in Fig. 9.12b. The resonant piezo-elastic device gives larger voltage output only when the excitation frequency is at or very close to its resonance frequency (7.4 Hz) whereas the voltage output of the piezo-magneto-elastic device can be 3 times that of the piezo-elastic device at several other frequencies below its post-buckled resonance frequency (10.6 Hz). It should be noted that power output is proportional to the square of the voltage. Hence an order of magnitude larger power output over a frequency range can be expected with this device.

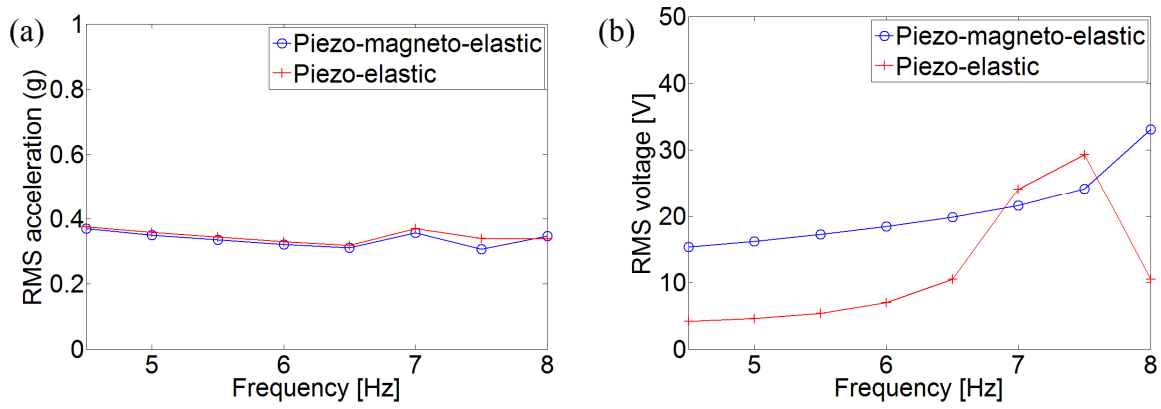

Fig. 9.12 (a) RMS acceleration input at different frequencies (average value: 0.35*g*); (b) Open-circuit RMS voltage output over a frequency range showing the broadband advantage of the piezo-magneto-elastic energy harvester

9. 4 Broadband Power Generation Performance and Comparisons against the Piezo-elastic Configuration

9.4.1 Experimental Setup. After the first set of experiments, another setup was prepared to compare the power generation performance of the piezo-magneto-elastic configuration with that of the piezo-elastic configuration to verify the order of magnitude increase in the power output. This section also aims to investigate whether or not the presence of a resistive load (which is known to create shunt damping effect as discussed in Chapters 3 and 4) considerably reduces the performance of the piezo-magneto-elastic configuration by modifying the attraction of the high-energy orbit discussed here. The experimental setup used for this purpose is shown in Fig. 9.13a and it is similar to the former setup shown in Fig. 9.7. These experiments have been conducted two months after the previous ones and the cantilever was unclamped and the magnets were removed in between (which is usually undesired). Therefore, effort has been made to clamp the beam with the same overhang length and to relocate the magnets in a similar way to stay in the same frequency range.

Figures 9.13b and 9.13c, respectively, display the piezo-magneto-elastic and piezo-elastic configurations tested for power generation under base excitation. A harmonic base excitation amplitude of 0.5*g* (yielding an RMS value of approximately 0.35*g*) is applied at frequencies of 5

Hz, 6 Hz, 7 Hz and 8 Hz. From the previous discussion related to the open-circuit voltage output given with Fig. 9.12b, it is expected to obtain an order of magnitude larger power with the piezo-magneto-elastic device at three of these frequencies (5 Hz, 6 Hz and 8 Hz). However, it is anticipated to obtain larger power from the piezo-elastic configuration around its resonance and 7 Hz is close to the resonance frequency of this linear system (as can be noted from Fig. 9.12b).

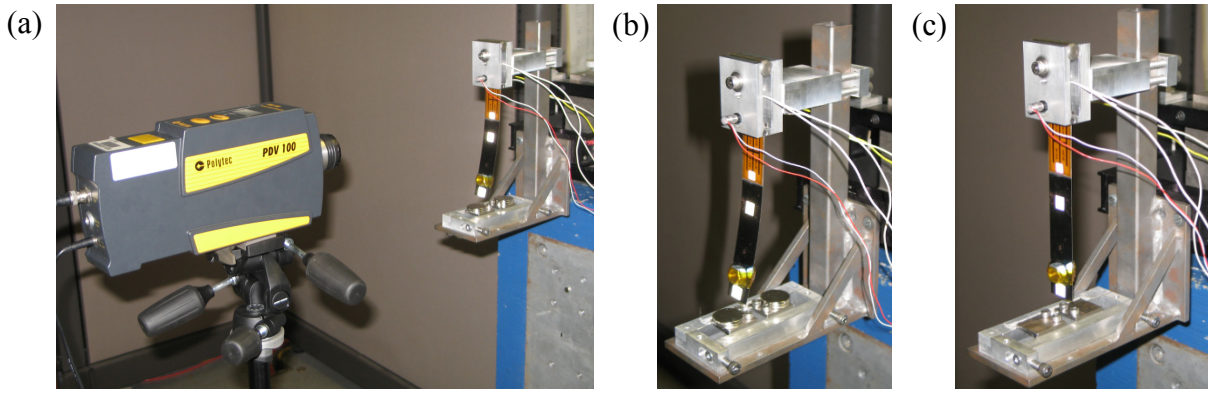

Fig. 9.13 (a) Experimental setup used for investigating the power generation performance of the piezo-magneto-elastic energy harvester; (b) Piezo-magneto-elastic configuration; (c) Piezo-elastic configuration (photos by A. Erturk, 2009)

9.4.2 Comparison of the Electrical Power Outputs. Figure 9.14 shows the comparison of the average steady-state power vs. load resistance graphs of the piezo-magneto-elastic and piezo-elastic configurations at the frequencies of interest. Note that the excitation amplitudes (i.e. the base acceleration) of both configurations are very similar in all cases. As anticipated, the piezo-magneto-elastic energy harvester gives an order of magnitude larger power at 5 Hz, 6 Hz and 8 Hz whereas the piezo-elastic configuration gives larger power only at 7 Hz (by a factor of 2.3). The average power outputs read from these graphs for the optimum values of load resistance are listed in Table 9.1.

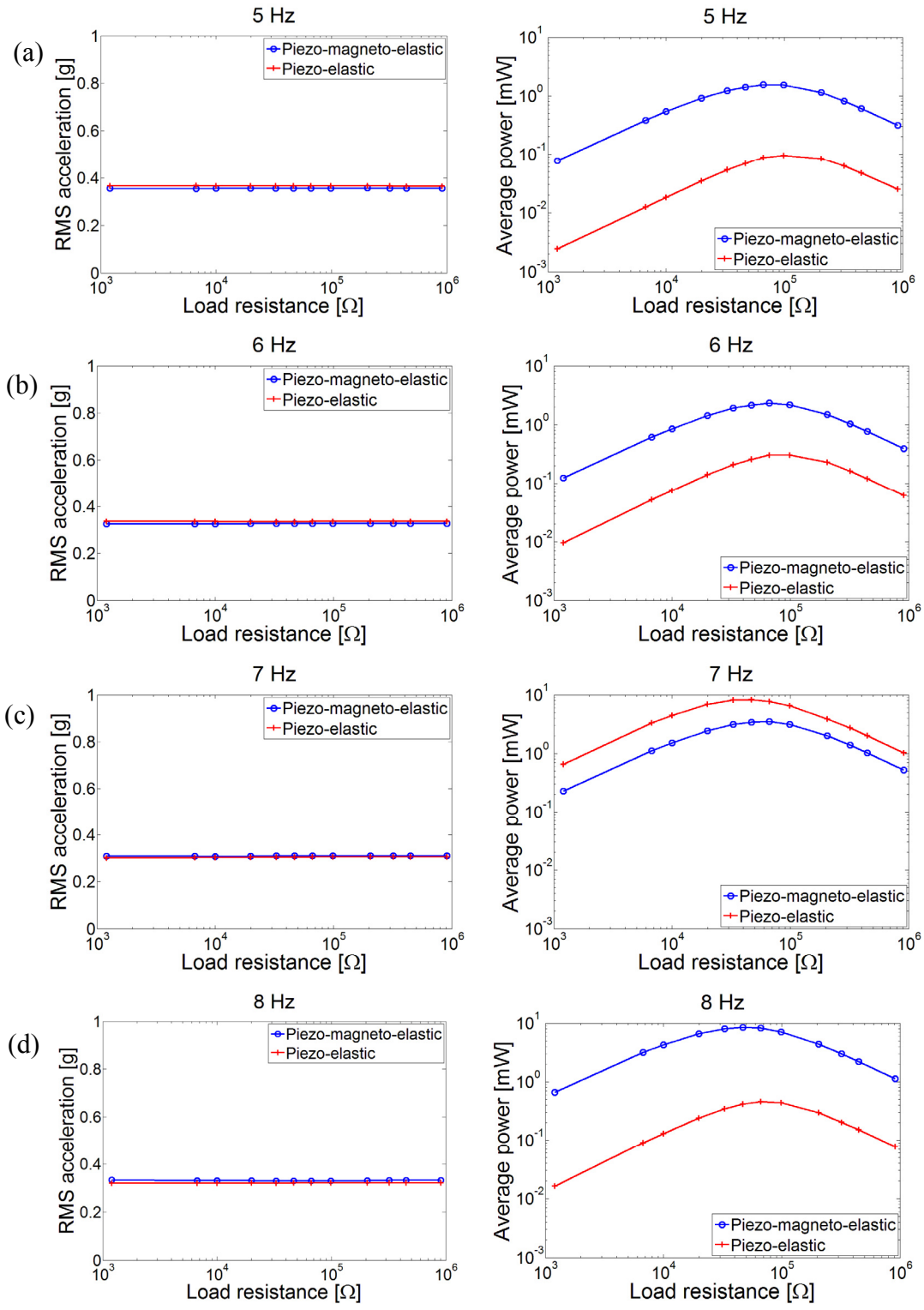

Fig. 9.14 Comparison of the acceleration input and power output of the piezo-magneto-elastic and piezo-elastic configurations at steady state for a range of excitation frequencies: (a) 5 Hz; (b) 6 Hz; (c) 7 Hz; (d) 8 Hz

Table 9.1 Comparison of the average power outputs of the piezo-magneto-elastic and piezo-elastic energy harvester configurations

Excitation frequency [Hz]	5	6	7	8
Piezo-magneto-elastic configuration [mW]	1.57	2.33	3.54	8.45
Piezo-elastic configuration [mW]	0.10	0.31	8.23	0.46

Variation of the average electrical power outputs of both configurations with the excitation frequency is plotted in Fig. 9.15 (including the frequencies 5.5 Hz, 6.5 Hz and 7.5 Hz). It is important to notice in this figure is that, at several frequencies, the *non-resonant* piezo-magneto-elastic energy harvester can indeed generate one order of magnitude more power for the same input. The *resonant* piezo-elastic energy harvester can generate larger power only within a narrow band around its fundamental resonance frequency. However, this power is not an order of magnitude larger than that of the piezo-magneto-elastic configuration (in qualitative agreement with Fig. 9.6).

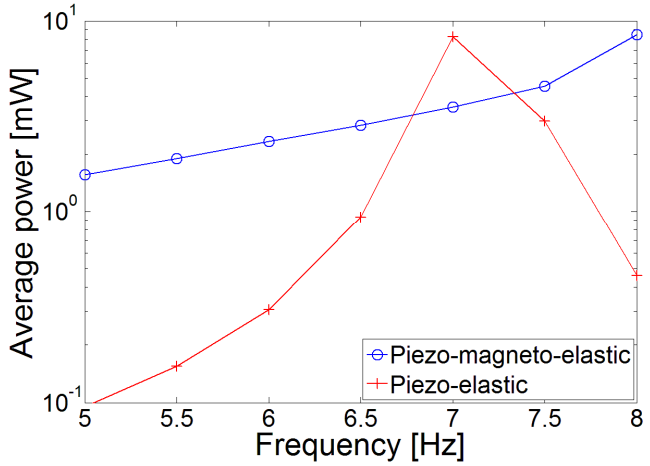

Fig. 9.15 Comparison of the average power output of the piezo-magneto-elastic and piezo-elastic energy harvester configurations (RMS acceleration input: 0.35*g*)

From to Fig. 9.15, it can be concluded that the piezo-magneto-elastic configuration exhibits a much better broadband power generation performance provided that the input excitation results in oscillations on its high-energy orbits in the frequency range of interest.

Given the frequency range and the amplitude of harmonic base excitation at these frequencies, the piezo-magneto-elastic energy harvester should be designed to catch these high-energy orbits at steady state.

9.5 Summary and Conclusions

In this chapter, a non-resonant piezo-magneto-elastic energy harvester is introduced for broadband vibration energy harvesting. The magneto-elastic configuration is known from the literature of chaos theory in structural mechanics. Here, piezoelectric coupling is introduced to the structure and a piezo-magneto-elastic vibration energy harvester is obtained. The lumped-parameter electromechanical equations describing the nonlinear system are given along with theoretical simulations. The existence of high-energy orbits at different frequencies is demonstrated. It is shown that, over a range of frequencies, one can obtain much larger voltage from the large amplitude oscillations on these orbits (compared to the conventional piezo-elastic configuration). An experimental prototype is built and the presence of such high-energy orbits at several frequencies below the post-buckled natural frequency of the structure is verified. It is shown experimentally that, the open-circuit voltage output of the piezo-magneto-elastic energy harvester can be three times that of the conventional piezo-elastic cantilever configuration, yielding an order of magnitude larger power output over a range of frequencies (for the same base acceleration input). The substantial broadband power generation performance of the magneto-elastic configuration is discussed here for piezoelectric energy harvesting and it can easily be extended to electromagnetic, electrostatic and magnetostrictive energy harvesting techniques as well as to their hybrid combinations.

CHAPTER 10

SUMMARY AND CONCLUSIONS

In the first chapter, distributed-parameter modeling of the base excitation problem is reviewed for cantilevered thin beams. The distributed-parameter displacement transmissibility function is compared with the well-known lumped-parameter transmissibility function and it is shown that the prediction of the lumped-parameter base excitation relation might have an error as high as 35 % in predicting the tip motion for a given base excitation input. The error in the lumped-parameter model is due to ignoring the contribution of the distributed inertia to the excitation amplitude. A correction factor is introduced to improve the predictions of the lumped-parameter representation and the variation of the correction factor with tip mass – to – beam mass ratio is investigated. It is shown that the original form of the lumped-parameter base excitation model can be used only if the tip mass is much larger than the beam mass (so that the contribution of the distributed mass to the excitation amplitude becomes negligible). Experimental validations of the corrected lumped-parameter model are given for a small cantilever in the absence and presence of a tip mass. Modeling of the base excitation problem is summarized for cantilevered bars under longitudinal vibrations and the lumped-parameter model of the longitudinal vibration case is also corrected. The correction factor is then introduced to the lumped-parameter electromechanical equations for energy harvesting and a theoretical case study is given.

Analytical modeling of bimorph piezoelectric energy harvesters with symmetric laminates is presented in the second chapter. The distributed-parameter electromechanical formulation is based on the Euler-Bernoulli beam theory and it is valid for thin piezoelectric energy harvesters for the typical vibration modes of interest in practice. The major steps of the analytical formulation are given for the series and parallel connection cases of the piezoceramic layers independently. An equivalent representation of the series and parallel connections is then given in a single form. The distributed-parameter electromechanical equations are first obtained for excitation at any arbitrary frequency by including all vibration modes in the analytical solution. Then, for the practical problem of resonance excitation, the multi-mode solutions are reduced to single-mode expressions (which are approximately valid only around the respective

resonance frequency). The electromechanical FRFs relating the steady-state electrical and mechanical response to the translational and rotational base acceleration components are extracted both from the multi-mode and single-mode solutions. A detailed theoretical case study is presented where simulations for the series and parallel connection cases are given using both multi-mode and single-mode electromechanical FRFs.

The analytical solutions derived in the Chapter 3 are validated for various experimental cases in Chapter 4. The first experimental case is given for a brass-reinforced PZT-5H bimorph cantilever without a tip mass. After validating the analytical model predictions using the voltage, current, power and the tip velocity FRFs for this configuration and providing an extensive electromechanical analysis, a tip mass is attached to create a configuration for the second case study. The variations of the fundamental short-circuit and open-circuit resonance frequencies after the attachment of the tip mass are successfully predicted by the model. Performance diagrams for excitations at the fundamental short-circuit and open-circuit resonance frequencies are extracted for both configurations (without and with the tip mass) and comparisons are made. Improvement of the overall power output (as well as the power density and the specific power) due to the addition of a tip mass is verified. Effect of the rotary inertia of the tip mass is also studied by providing further analytical simulations with the point mass assumption. It is shown that the resonance frequencies can be overestimated if the rotary inertia of the tip mass is neglected. The damping effect of piezoelectric power generation is discussed in detail based on the experimental measurements and the model predictions. The final case study is given for a brass-reinforced PZT-5A bimorph cantilever and the frequency range of interest is increased to cover the second vibration mode as well. Predictions of the multi-mode and the single-mode FRFs are provided (for the first two modes independently) and a very good agreement is observed with the experimental results.

In Chapter 5, detailed mathematical analyses of the single-mode electromechanical relations are presented. Focus is placed on the voltage output and vibration response FRFs per translational base acceleration. The single-mode relations derived in Chapter 3 (based on the multi-mode solutions) are first expressed in the modulus-phase form and then they are represented with dimensionless terms. After expressing the asymptotic trends of the single voltage and tip displacement FRFs, closed-form expressions are obtained for their short-circuit and open-circuit resonance frequencies. It is shown that the short-circuit resonance frequencies

of the voltage FRF and the tip displacement FRF are slightly different. The linear asymptotes of the voltage output and the tip displacement for the extreme conditions of load resistance (observed in the previous chapters) are mathematically verified here. Closed-form expressions for the optimum electrical loads for the maximum power generation at the short-circuit and the open-circuit resonance frequencies are extracted. It is shown that, for excitations at these two frequencies, the intersections of the linear voltage asymptotes correspond to the respective optimum load resistance. Based on this observation, a simple technique is introduced to identify the optimum load resistance of a piezoelectric energy harvester using a single resistive load along with an open-circuit voltage measurement. Relations are given to estimate the variation of the tip vibration response as the load resistance is changed between the two extreme conditions. The experimental case study for a PZT-5H bimorph is revisited and the major closed-form relations derived here are validated. An important issue related to estimation of the optimum load resistance from the Norton and Thévenin representations of the piezoceramic is clarified.

In Chapter 6, the effects of materials constants and mechanical damping on the power generation performances of conventional piezoceramics (PZT-5A and PZT-5H) and novel single crystals (PMN-PT and PMN-PZT) are investigated. It is shown that the large d_{31} strain constants of the commercially available single crystals are associated with very large elastic compliance and the combination of these two properties does *not* result in a substantial increase in the effective piezoelectric stress constant ($\overline{e}_{31}$) for a thin energy harvester beam. Although the d_{31} constants can change by an order of magnitude from PZT-5A to PMN-PZT, the effective piezoelectric constants of these active materials are in the same order of magnitude. Consequently, the substantially large d_{31} constants of the commercially available single crystals do *not* necessarily imply substantially large power output in energy harvesting. The concepts of dynamic flexibility and mechanical damping are shown to be very important as far as the maximum power output is concerned. When geometrically identical bimorphs using these piezoelectric materials are forced to have the same dynamic flexibility, the power outputs are observed to be very similar. It is also observed that the power output under resonance excitation is extremely sensitive to mechanical damping (which is very difficult parameter control in practice). It is shown with an experimental case study using a PZT-5A bimorph and a PZT-5H bimorph that the former cantilever gives 45 % larger power density when the latter has 55 % larger mechanical damping ratio (although the d_{31} constant of PZT-5H is 60 % larger than that of

PZT-5A). Therefore, designing and manufacturing the energy harvester beam to have less damping can be more important than the piezoelectric material being used.

The concept of strain nodes and its effect on energy harvesting is discussed in Chapter 7. It is theoretically discussed and experimentally demonstrated that covering the strain nodes of vibration modes with continuous electrodes results in cancellation of the electrical outputs in energy harvesting. A detailed dimensionless analysis is given for predicting the locations of the strain nodes of a thin cantilever in the absence of a tip mass. Dimensionless derivations and results are then presented for predicting the strain node positions and their variations in the presence of a tip mass. Dimensionless data of modal strain nodes are tabulated for some other practical boundary condition pairs as well. It is experimentally demonstrated using a cantilever that the voltage output due to the second mode excitation can be increased dramatically if segmented electrodes are used instead of continuous electrodes. The relationship between the discussion given here and a recent study on piezoelectric energy harvesting from the static deflection of a clamped circular plate is also explained. The use of segmented electrode pairs to avoid cancellations is described for single-mode and multi-mode vibrations of a cantilevered harvester and alternative circuitry-based approaches can be investigated to handle the cancellation problem for multi-mode excitations.

In Chapter 8, approximate distributed-parameter modeling of cantilevered piezoelectric energy harvesters is given. An electromechanical version of the assumed-modes method of structural dynamics is used to discretize the energy equations into electromechanical Lagrange equations derived from the extended Hamilton's principle. The derivations are given based on the Euler-Bernoulli, Rayleigh and Timoshenko beam theories. In all cases, an axial displacement variable is defined to capture its coupling with the transverse displacement variable in the presence of structural asymmetry. To demonstrate modeling of an asymmetric configuration, focus is placed on the unimorph configuration. Simplification of the resulting equations for symmetric bimorph configurations is also shown and the effect of a tip mass on the resulting formulation is discussed. A short discussion regarding the kinematically admissible functions to be used in the models derived here is also provided. Finally the experimental case studies for a thin cantilever (without and with a tip mass) are revisited for validation of the assumed-modes solution using different number of admissible trigonometric functions. The predictions of the assumed-modes solution are also compared with the analytical solution and a very good

agreement is observed. The approximate formulations given in Chapter 8 can be used to predict the electromechanical response of asymmetric cantilevers, moderately thick cantilevers as well as cantilevers with varying cross-section.

In Chapter 9, a piezo-magneto-elastic energy harvester is introduced for broadband vibration energy harvesting. The magneto-elastic configuration is known from the literature of chaos theory in nonlinear structural mechanics. Here, piezoelectric coupling is introduced to the structure and a piezo-magneto-elastic vibration energy harvester is obtained. The lumped-parameter electromechanical equations describing the nonlinear system are given along with theoretical simulations. The existence of high-energy orbits at different frequencies is demonstrated. It is shown that, over a range of frequencies, one can generate much larger voltage from the large amplitude oscillations on these orbits (compared to the conventional piezo-elastic configuration). An experimental prototype is built and the presence of such high-energy orbits at several frequencies below the post-buckled natural frequency of the structure is verified. It is shown experimentally that, the open-circuit voltage output of the piezo-magneto-elastic energy harvester can be three times that of the conventional piezo-elastic cantilever configuration, yielding an order of magnitude larger power output over a range of frequencies. The substantial broadband power generation performance of the magneto-elastic configuration is discussed here for piezoelectric energy harvesting and it can easily be extended to other vibration energy harvesting techniques (e.g. electromagnetic, electrostatic, magnetostrictive) as well as to their hybrid combinations.

Each dissertation produced in the Department of Engineering Science and Mechanics at Virginia Tech must address the social impact. While harvesting energy at the level discussed here does not have a major impact on reducing the world's energy demands (compared to well-known forms of *green energy*, e.g. wind energy and solar energy) it does have the potential for substantially reducing the world's reliance on chemical batteries, thereby reducing the amount of chemical waste produced by conventional batteries.

Future applications of vibration energy harvesting that eliminate the requirement of battery replacement and the relevant maintenance efforts can lead to durable wireless sensor networks and similar low-power electronic components. It should be noted that the energy required to keep such wireless low-power systems running include the maintenance costs as well, which can be dramatically large in applications such as wireless damage detection systems in

critical civil engineering structures at remote locations. In addition, even though the power outputs are not in the same order of magnitude, vibration energy is often available when/where solar energy and wind energy are not available.

One of the limitations regarding the use of piezoelectric materials is their present cost, which can be reduced in mass production as the technology becomes mature. An environmental issue related to using PZT-based piezoceramics is the lead content in piezoelectric materials. There is ongoing research in the materials science domain of the problem for developing lead-free piezoceramics [96,97].

REFERENCES

[1] Timoshenko, S.P., 1953, *History of Strength of Materials (with a brief account of the history of theory of elasticity and theory of structures)*, McGraw-Hill Book Company, New York.

[2] Williams, C.B. and Yates, R.B., 1996, "Analysis of a Micro-electric Generator for Microsystems," Sensors and Actuators A, **52**, pp. 8–11.

[3] Glynne-Jones P., Tudor, M.J., Beeby, S.P. and White, N.M., 2004, "An Electromagnetic, Vibration-powered Generator for Intelligent Sensor Systems," Sensors and Actuators A, **110**, pp. 344-349.

[4] Arnold, D., 2007, "Review Of Microscale Magnetic Power Generation," IEEE Transactions on Magnetics, **43**, pp. 3940–3951.

[5] Mitcheson, P., Miao, P., Start, B., Yeatman, E., Holmes, A. and Green, T., 2004, "MEMS Electrostatic Micro-Power Generator for Low Frequency Operation," Sensors and Actuators A, **115**, pp. 523-529.

[6] Roundy, S., Wright, P. and Rabaey, J., 2003, *Energy Scavenging for Wireless Sensor Networks*, Kluwer Academic Publishers, Boston.

[7] Roundy, S., Wright, P.K. and Rabaey, J.M., 2003, "A Study of Low Level Vibrations as a Power Source for Wireless Sonsor Nodes," Computer Communications, **26**, pp.1131-1144.

[8] Jeon, Y. B., Sood, R., Jeong, J. H. and Kim, S., 2005, "MEMS Power Generator with Transverse Mode Thin Film PZT," Sensors & Actuators A, **122**, pp. 16-22.

[9] Beeby, S.P., Tudor, M.J. and White, N.M., 2006, "Energy Harvesting Vibration Sources for Microsystems Applications", Measurement Science and Technology, **17**, pp. R175-R195.

[10] Cook-Chennault, K.A., Thambi, N., Sastry, A.M., 2008, "Powering MEMS Portable Devices – a Review of Non-Regenerative and Regenerative Power Supply Systems with Emphasis on Piezoelectric Energy Harvesting Systems," Smart Materials and Structures, **17**, 043001 (33pp).

[11] Sodano, H., Park G. and Inman, D.J., 2004, "A Review of Power Harvesting from Vibration Using Piezoelectric Materials", Shock and Vibration Digest, **36**, pp. 197-205.

[12] Anton, S.R. and Sodano, H.A., 2007, "A Review of Power Harvesting Using Piezoelectric Materials (2003-2006)," Smart Materials and Structures, **16**, pp. R1-R21.

[13] Priya, S., 2007, "Advances in Energy Harvesting Using Low Profile Piezoelectric Transducers," Journal of Electroceramics, **19**, pp. 167–184.

[14] Choi, W.J., Jeon, Y., Jeong, J.H., Sood, R. and Kim, S.G., 2006, "Energy Harvesting MEMS Device Based on Thin Film Piezoelectric Cantilevers," Journal of Electroceramics, **17**, pp. 543–8.

[15] Roundy, S. and Wright, P.K., 2004, "A Piezoelectric Vibration Based Generator for Wireless Electronics," Smart Materials and Structures, **13**, pp.1131-1144.

[16] duToit, N.E., Wardle, B.L. and Kim, S., 2005, "Design Considerations for MEMS-Scale Piezoelectric Mechanical Vibration Energy Harvesters," Journal of Integrated Ferroelectrics, **71**, pp. 121-160.

[17] Sodano, H.A., Park, G. and Inman, D.J., 2004, "Estimation of Electric Charge Output for Piezoelectric Energy Harvesting," Strain, **40**, pp. 49-58.

[18] Lu, F., Lee, H.P. and Lim, S.P., 2004, "Modeling and Analysis of Micro Piezoelectric Power Generators for Micro-Electromechanical-Systems Applications," Smart Materials and Structures, **13**, pp. 57-63.

[19] Chen, S.-N., Wang, G.-J. and Chien, M.-C., 2006, "Analytical Modeling of Piezoelectric Vibration-Induced Micro Power Generator," Mechatronics, **16**, pp. 397-387.

[20] Lin, J.H., Wu, X.M., Ren, T.L. and Liu, L.T., 2007, "Modeling and Simulation of Piezoelectric MEMS Energy Harvesting Device," Integrated Ferroelectrics, **95**, pp. 128-141.

[21] duToit, N.E. and Wardle, B.L., 2007, "Experimental Verification of Models for Microfabricated Piezoelectric Vibration Energy Harvesters," AIAA Journal, **45**, pp. 1126-1137.

[22] Ajitsaria, J., Choe, S.Y., Shen, D. and Kim, D.J., 2007, "Modeling and Analysis of a Bimorph Piezoelectric Cantilever Beam for Voltage Generation," Smart Materials and Structures, **16**, pp. 447-454.

[23] Ottman, G.K., Hofmann, H.F., Bhatt, A.C. and Lesieutre, G.A., 2002, "Adaptive Piezoelectric Energy Harvesting Circuit for Wireless Remote Power Supply," IEEE Transactions on Power Electronics, **17**, pp. 669-676.

[24] Ottman, G.K., Hofmann, H.F., and Lesieutre, G.A., 2003, "Optimized Piezoelectric Energy Harvesting Circuit Using Step-down Converter in Discontinuous Conduction Mode," **18**, pp. 696-703.

[25] Guan, M.J. and Liao, W.H., 2007, "On the Efficiencies of Piezoelectric Energy Harvesting Circuits Towards Storage Device Voltages," Smart Materials and Structures, **16**, pp. 498-505.

[26] *IEEE Standard on Piezoelectricity*, 1987, IEEE, NY.

[27] Stephen, N.G., 2006, "On Energy Harvesting from Ambient Vibration," Journal of Sound and Vibration, **293**, pp. 409-425.

[28] Daqaq, F.M., Renno J.M., Farmer, J.R. and Inman, D.J., 2007, "Effects of System Parameters and Damping on an Optimal Vibration-Based Energy Harvester," Proceedings of the 48th AIAA/ASME/ASCE/AHS/ASC Structures, Structural Dynamics, and Materials Conference, 23 - 26 April 2007, Honolulu, Hawaii.

[29] Hagood, N.W., Chung, W.H. and Von Flotow, A., 1990, "Modelling of piezoelectric actuator dynamics for active structural control," Journal of Intelligent Material Systems and Structures, **1**, pp.327-354.

[30] Crandall, S.H., Karnopp, D.C., Kurtz, Jr. E.F. and Pridmore-Brown, D.C., 1968, *Dynamics of Mechanical and Electromechanical Systems*, McGraw-Hill, New York.

[31] Fang, H.-B., Liu, J.-Q., Xu, Z.-Y., Dong, L., Chen, D., Cai, B.-C. and Liu, Y., 2006, "A MEMS-Based Piezoelectric Power Generator for Low Frequency Vibration Energy Harvesting," Chinese Physics Letters, **23**, pp. 732-734.

[32] Lesieutre, G.A., Ottman, G.K. and Hofmann, H.F., 2004, "Damping as a Result of Piezoelectric Energy Harvesting," Journal of Sound and Vibration, **269**, pp. 991-1001.

[33] DeVoe, D.L. and Pisano, A.P., 1997, Modeling and Optimal Design of Piezoelectric Cantilever Microactuators," Journal of Microelectromechanical Systems, **6**, pp. 266–270.

[34] Timoshenko, S.P., 1925, "Analysis of Bi-metal Thermostats," Journal of Optical Society of America, **11**, pp. 233-56.

[35] Timoshenko, S., Young, D.H. and Weaver, W., 1974, *Vibration Problems in Engineering*, John Wiley and Sons, New York.

[36] Banks, H.T. and Inman D.J., 1991, "On Damping Mechanisms in Beams," ASME Journal of Applied Mechanics, **58**, pp. 716–723.

[37] Clough, R.W. and Penzien, J., 1975, *Dynamics of Structures*, John Wiley and Sons, New York.

[38] Caughey, T.K. and O'Kelly, M.E.J., 1965, "Classical Normal Modes in Damped Linear Dynamic Systems," ASME Journal of Applied Mechanics, **32**, pp. 583-588.

[39] Ewins, D.J., 2000, *Modal Testing: Theory, Practice and Application*, Research Studies Press, Baldock, Hertfordshire, UK.

[40] Strutt, J. W. (Lord Rayleigh), 1894, *The Theory of Sound*, MacMillan Company, London, UK.

[41] Meirovitch, L., 2001, *Fundamentals of Vibrations*, McGraw Hill, New York.

[42] Inman, D.J., 2007, *Engineering Vibration*, Prentice Hall, Englewood Cliffs, New Jersey.

[43] Banks, H.T., Luo, Z.H., Bergman, L.A. and Inman D.J., 1998, "On the Existence of Normal Modes of Damped Discrete-Continuous Systems," ASME Journal of Applied Mechanics, **65**, pp. 980–989.

[44] The MathWorks, Inc. http://www.mathworks.com.

[45] Piezo Systems, Inc. (www.piezo.com).

[46] TMC Solution http://www.tmcsolution.com.cn.

[47] PCB Piezotronics http://www.pcb.com.

[48] Polytec http://www.polytec.com.

[49] Spectral Dynamics, Inc. http://www.spectraldynamics.com.

[50] Bendat, J.S. and Piersol, A.G., 1986, *Random Data Analysis and Measurement Procedures*, John Wiley and Sons, New York.

[51] Newland, D.E., 1993, *Random Vibrations, Spectral and Wavelet Analysis*, John Wiley and Sons, New York.

[52] Wang, Q.M. and Cross, L.E., 1999, "Constitutive Equations of Symmetrical Triple Layer Piezoelectric Benders," *IEEE Transactions on Ultrasonics, Ferroelectrics, and Frequency Control*, **46**, pp. 1343–1351.

[53] Sokolnikoff, 1946, *Mathematical Theory of Elasticity*, McGraw-Hill, New York.

[54] Dym, C.L. and Shames, I.H., 1973, *Solid Mechanics: A Variational Approach*, McGraw–Hill, New York.

[55] Chopra, A.K., 2006, *Dynamics of Structures: Theory and Applications to Earthquake Engineering*, Prentice-Hall, Englewood Cliffs, New Jersey.

[56] Hyer, M.W., 1998, *Stress Analysis of Fiber-Reinforced Composite Materials*, McGraw–Hill, New York.

[57] Schwartz, L., 1978, *Théorie des Distributions*, Hermann, Paris, France.

[58] Friedlander, F.G., 1998, *Introduction to the Theory of Distributions*, Cambridge University Press, Cambridge (with additional material by M. Joshi).

[59] Hewlett-Packard Development Company http://www.hp.com.

[60] Magcraft Advanced Magnetic Materials http://www.magcraft.com.

[61] Meriam, J.L and Kraige, L.G., 2001, *Engineering Mechanics: Dynamics*, John Wiley and Sons, New York.

[62] Engineering Fundamentals, Inc. (www.efunda.com).

[63] Heinonen, E., Juuti, J. and Leppavuori, S., 2005, "Characterization and Modelling of 3D Piezoelectric Ceramic Structures with ATILA Software," Journal of European Ceramic Society, **25**, pp. 2467-2470.

[64] Cao, H., Schmidt, V. H., Zhang, R., Cao, W. and Luo, H., 2004, "Elastic, Piezoelectric, and Dielectric Properties of $0.58Pb(Mg_{1/3}Nb_{2/3})O_3$-$0.42PbTiO_3$ Single Crystal," *Journal of Applied Physics*, **96**, 549.

[65] Ceracomp Co., Ltd. www.ceracomp.com.

[66] LDS Group http://www.lds-group.com.

[67] Crawley, E.F. and de Luis, J., 1987, "Use of Piezoelectric Actuators as Elements of Intelligent Structures", AIAA Journal, **25**, pp.1373-1385.

[68] Cady, W.G., 1946, *Piezoelectricity: An Introduction to the Theory and Applications of Electromechanical Phenomena in Crystals*, McGraw-Hill, New York.

[69] Elvin, N. G., Elvin, A. A., and Spector, M., 2001, "A Self-Powered Mechanical Strain Energy Sensor," Smart Materials and Structures, **10**, pp. 293–299.

[70] Lesieutre, G.A. and Davis, C.L., 1997, "Can a Coupling Coefficient of a Piezoelectric Device Be Higher Than Its Active Material?," Journal of Intelligent Material Systems and Structures, **8**, pp. 859-867.

[71] Kim, S., Clark, W.W. and Wang, Q.M., 2005, "Piezoelectric Energy Harvesting with a Clamped Circular Plate: Analysis," Journal of Intelligent Material Systems and Structures, **16**, pp. 847-854.

[72] Kim, S., Clark, W.W. and Wang, Q.M., 2005, "Piezoelectric Energy Harvesting with a Clamped Circular Plate: Experimental Study," Journal of Intelligent Material Systems and Structures, **16**, pp. 855-863.

[73] Timoshenko, S.P., 1921, "On the Correction for Shear of the Differential Equation for Transverse Vibrations of Prismatic Bars," Philosophical Magazine, **41,** pp. 744–746.

[74] Timoshenko, S.P., 1922, "On the Transverse Vibrations of Bars of Uniform Cross-section," Philosophical Magazine, **43**, pp.125–131.

[75] Mindlin, R.D., 1951, "Thickness-shear and Flexural Vibrations of Crystal Plates," Journal of Applied Physics, **22**, pp. 316-323.

[76] Mindlin, R.D., 1952, "Forced Thickness-shear and Flexural Vibrations of Piezoelectric Crystal Plates," Journal of Applied Physics, **23**, pp. 83-88.

[77] Cowper, G.R., 1966, "The Shear Coefficient in Timoshenko Beam Theory," ASME Journal of Applied Mechanics, **33**, pp. 335-340.

[78] Kaneko, T., 1975, "On Timoshenko's Correction for Shear in Vibrating Beams," Journal of Physics D, **8**, pp. 1927-1936.

[79] Stephen, N.G., 1978, "On the Variation of Timoshenko's Shear Coefficient with Frequency," ASME Journal of Applied Mechanics, **45**, pp. 695-697.

[80] Stephen, N.G., 1980, "Timoshenko's Shear Coefficient from a Beam Subjected to Gravity Loading," ASME Journal of Applied Mechanics, **47**, pp. 121-127.

[81] Stephen, N.G. and Hutchinson, J.R., 2001, "Discussion: Shear Coefficients for Timoshenko Beam Theory," ASME Journal of Applied Mechanics, **68**, pp. 959–961.

[82] Hutchinson, J.R., 2001, "Shear Coefficients for Timoshenko Beam Theory," ASME Journal of Applied Mechanics, **68**, pp. 87-92.

[83] Puchegger, S., Bauer, S., Loidl, D., Kromp, K. and Peterlik, H., 2003, "Experimental Validation of the Shear Correction Factor," Journal of Sound and Vibration, **261**, pp. 177-184.

[84] Den Hartog, J.P., 1956, *Mechanical Vibrations*, McGraw-Hill, New York.

[85] Lee, J. and Schultz, W.W., 2004, "Eigenvalue Analysis of Timoshenko Beams and Axisymmetric Mindlin Plates by the Pseudospectral Method," Journal of Sound and Vibration, **269**, pp. 609-621.

[86] Zhou, D. and Cheung, Y. K., 2001, "Vibrations of Tapered Timoshenko Beams in Terms of Static Timoshenko Beam Functions," ASME Journal of Applied Mechanics, **68**, pp. 596-602.

[87] Moon, F.C. and Holmes P.J., 1979, "A Magnetoelastic Strange Attractor," Journal of Sound and Vibration, **65**, pp. 275-296.

[88] Moon, F.C., 1987, *Chaotic Vibrations*, John Wiley and Sons, New York.

[89] Lorenz, E.N., 1993, *The Essence of Chaos*, University of Washington Press, Seattle.

[90] Lorenz, E.N., 1963, "Deterministic Nonperiodic Flow," Journal of Atmospheric Sciences, **26**, pp. 636-646.

[91] Poston, T. and Stewart, O., 1978, *Catastrophe Theory and Its Applications*, Pitman, London.

[92] Holmes, P., 1979, "A Nonlinear Oscillator with a Strange Attractor," Philosophical Transactions of the Royal Society of London, Series A, **292**, pp. 419449.

[93] APS Dynamics http://www.apsdynamics.com.

[94] National Instruments http://www.ni.com.

[95] Midé Corporation http://www.mide.com.

[96] Saito, Y., Takao, H. Tani, I., Nonoyama, T., Takatori, K., Homma, T., Nagaya, T. and Nakamura, M., 2004, ''Lead-Free Piezoceramics,'' Nature, **432**, pp. 84-87.

[97] Shrout, T.R. and Zhang, S.J., 2007, "Lead-free Piezoelectric Ceramics – Alternatives for PZT?," Journal of Electroceramics, **19,** pp. 111–124.

APPENDIX A

CONSTITUTIVE EQUATIONS FOR A MONOLITHIC PIEZOCERAMIC

A.1 Three-dimensional Form of the Piezoelectric Constitutive Equations

In general, poled monolithic piezoceramics are transversely isotropic materials. To be in agreement with the IEEE Standard on Piezoelectricity [26], the plane of isotropy is defined here as the 12-plane (or the *xy*-plane). The piezoelectric material therefore exhibits symmetry about the 3-direction (or the *z*-direction), which is the poling direction of the material. The field variables are the stress components (T_{ij}), strain components (S_{ij}), electric field components (E_k) and the electric displacement components (D_k).

The standard form of the piezoelectric constitutive equations can be given in four different forms by taking either two of the four field variables as the independent variables. Consider the tensorial representation of the strain – electric displacement form [26] where the independent variables are the stress components and the electric field components:

$$S_{ij} = s^E_{ijkl} T_{kl} + d_{kij} E_k \tag{A.1}$$

$$D_i = d_{ikl} T_{kl} + \varepsilon^T_{ik} E_k \tag{A.2}$$

which is the preferred form of the piezoelectric constitutive relations for bounded media (to eliminate some of the stress components depending on the geometry and some of the electric field components depending on the placement of the electrodes). Equations (A.1) and (A.2) can be given in the matrix form as

$$\begin{Bmatrix} \mathbf{S} \\ \mathbf{D} \end{Bmatrix} = \begin{bmatrix} \mathbf{s}^E & \mathbf{d}^t \\ \mathbf{d} & \boldsymbol{\varepsilon}^T \end{bmatrix} \begin{Bmatrix} \mathbf{T} \\ \mathbf{E} \end{Bmatrix} \tag{A.3}$$

where superscripts *E* and *T* represent that the respective constants are evaluated at constant electric field and constant stress, respectively, and superscript *t* stands for the transpose. The expanded form of Eq. (A.3) is

$$\begin{Bmatrix} S_1 \\ S_2 \\ S_3 \\ S_4 \\ S_5 \\ S_6 \\ D_1 \\ D_2 \\ D_3 \end{Bmatrix} = \begin{bmatrix} s_{11}^E & s_{12}^E & s_{13}^E & 0 & 0 & 0 & 0 & 0 & d_{31} \\ s_{12}^E & s_{11}^E & s_{13}^E & 0 & 0 & 0 & 0 & 0 & d_{31} \\ s_{13}^E & s_{13}^E & s_{33}^E & 0 & 0 & 0 & 0 & 0 & d_{33} \\ 0 & 0 & 0 & s_{55}^E & 0 & 0 & 0 & d_{15} & 0 \\ 0 & 0 & 0 & 0 & s_{55}^E & 0 & d_{15} & 0 & 0 \\ 0 & 0 & 0 & 0 & 0 & s_{66}^E & 0 & 0 & 0 \\ 0 & 0 & 0 & 0 & d_{15} & 0 & \varepsilon_{11}^T & 0 & 0 \\ 0 & 0 & 0 & d_{15} & 0 & 0 & 0 & \varepsilon_{11}^T & 0 \\ d_{31} & d_{31} & d_{33} & 0 & 0 & 0 & 0 & 0 & \varepsilon_{33}^T \end{bmatrix} \begin{Bmatrix} T_1 \\ T_2 \\ T_3 \\ T_4 \\ T_5 \\ T_6 \\ E_1 \\ E_2 \\ E_3 \end{Bmatrix} \tag{A.4}$$

where the contracted notation (i.e. Voigt's notation: $11 \to 1$, $22 \to 2$, $33 \to 3$, $23 \to 4$, $13 \to 5$, $12 \to 6$) is used so that the vectors of strain and stress components are

$$\begin{Bmatrix} S_1 \\ S_2 \\ S_3 \\ S_4 \\ S_5 \\ S_6 \end{Bmatrix} = \begin{Bmatrix} S_{11} \\ S_{22} \\ S_{33} \\ 2S_{23} \\ 2S_{13} \\ 2S_{12} \end{Bmatrix}, \quad \begin{Bmatrix} T_1 \\ T_2 \\ T_3 \\ T_4 \\ T_5 \\ T_6 \end{Bmatrix} = \begin{Bmatrix} T_{11} \\ T_{22} \\ T_{33} \\ T_{23} \\ T_{13} \\ T_{12} \end{Bmatrix} \tag{A.5}$$

Therefore the shear strain components in the contracted notation are the engineering shear strains. It should be noted from the elastic, piezoelectric and dielectric constants in Eq. (A.4) that the poled piezoceramic considered here is a monolithic piezoceramic so that the symmetries of transversely isotropic material behavior ($s_{11}^E = s_{22}^E$, $d_{31} = d_{32}$, etc) are directly applied.

A.2 Reduced Equations for a Thin Beam

If the piezoelastic behavior of the thin monolithic structure is to be modeled as a thin beam based on the Euler-Bernoulli beam theory or Rayleigh beam theory, the only non-zero stress component is T_1 (stress component in the axial direction) so that

$$T_2 = T_3 = T_4 = T_5 = T_6 = 0 \tag{A.6}$$

Along with this simplification, if an electrode pair covers the faces perpendicular to 3-direction, Eq. (A.4) becomes

$$\begin{Bmatrix} S_1 \\ D_3 \end{Bmatrix} = \begin{bmatrix} s_{11}^E & d_{31} \\ d_{31} & \varepsilon_{33}^T \end{bmatrix} \begin{Bmatrix} T_1 \\ E_3 \end{Bmatrix} \tag{A.7}$$

which can be written as

$$\begin{bmatrix} s_{11}^E & 0 \\ -d_{31} & 1 \end{bmatrix} \begin{Bmatrix} T_1 \\ D_3 \end{Bmatrix} = \begin{bmatrix} 1 & -d_{31} \\ 0 & \varepsilon_{33}^T \end{bmatrix} \begin{Bmatrix} S_1 \\ E_3 \end{Bmatrix} \tag{A.8}$$

Therefore the stress – electric displacement form of the reduced constitutive equations for a thin beam is

$$\begin{Bmatrix} T_1 \\ D_3 \end{Bmatrix} = \begin{bmatrix} \overline{c}_{11}^E & -\overline{e}_{31} \\ \overline{e}_{31} & \overline{\varepsilon}_{33}^S \end{bmatrix} \begin{Bmatrix} S_1 \\ E_3 \end{Bmatrix} \tag{A.9}$$

where the reduced matrix of elastic, piezoelectric and dielectric constants is

$$\overline{\mathbf{C}} = \begin{bmatrix} \overline{c}_{11}^E & -\overline{e}_{31} \\ \overline{e}_{31} & \overline{\varepsilon}_{33}^S \end{bmatrix} = \begin{bmatrix} s_{11}^E & 0 \\ -d_{31} & 1 \end{bmatrix}^{-1} \begin{bmatrix} 1 & -d_{31} \\ 0 & \varepsilon_{33}^T \end{bmatrix} \tag{A.10}$$

Here and hereafter, an over-bar denotes that the respective constant is reduced from the three-dimensional form to the plane-stress condition. In Eq. (A.10),

$$\overline{c}_{11}^E = \frac{1}{s_{11}^E},\ \overline{e}_{31} = \frac{d_{31}}{s_{11}^E},\ \overline{\varepsilon}_{33}^S = \varepsilon_{33}^T - \frac{d_{31}^2}{s_{11}^E} \tag{A.11}$$

where superscript *S* denotes that the respective constant is evaluated at constant strain.

A.3 Reduced Equations for a Moderately Thick Beam

If the piezoelasticity of the monolithic structure is to be modeled as a moderately thick beam based on the Timoshenko beam theory, the only non-zero stress components are T_1 (stress component in the axial direction) and T_5 (transverse shear stress) so that

$$T_2 = T_3 = T_4 = T_6 = 0 \tag{A.12}$$

is applied in Eq. (A.4). Then,

$$\begin{Bmatrix} S_1 \\ S_5 \\ D_3 \end{Bmatrix} = \begin{bmatrix} s_{11}^E & 0 & d_{31} \\ 0 & s_{55}^E & 0 \\ d_{31} & 0 & \varepsilon_{33}^T \end{bmatrix} \begin{Bmatrix} T_1 \\ T_5 \\ E_3 \end{Bmatrix} \tag{A.13}$$

which can be written as

$$\begin{bmatrix} s_{11}^E & 0 & 0 \\ 0 & s_{55}^E & 0 \\ -d_{31} & 0 & 1 \end{bmatrix} \begin{Bmatrix} T_1 \\ T_5 \\ D_3 \end{Bmatrix} = \begin{bmatrix} 1 & 0 & -d_{31} \\ 0 & 1 & 0 \\ 0 & 0 & \varepsilon_{33}^T \end{bmatrix} \begin{Bmatrix} S_1 \\ S_5 \\ E_3 \end{Bmatrix} \tag{A.14}$$

Therefore the stress – electric displacement form of the reduced constitutive equations is

$$\begin{Bmatrix} T_1 \\ T_5 \\ D_3 \end{Bmatrix} = \begin{bmatrix} \overline{c}_{11}^E & 0 & -\overline{e}_{31} \\ 0 & \overline{c}_{55}^E & 0 \\ \overline{e}_{31} & 0 & \overline{\varepsilon}_{33}^S \end{bmatrix} \begin{Bmatrix} S_1 \\ S_5 \\ E_3 \end{Bmatrix} \tag{A.15}$$

Here, the reduced matrix of elastic, piezoelectric and permittivity constants are

$$\overline{\mathbf{C}} = \begin{bmatrix} \overline{c}_{11}^E & 0 & -\overline{e}_{31} \\ 0 & \overline{c}_{55}^E & 0 \\ \overline{e}_{31} & 0 & \overline{\varepsilon}_{33}^S \end{bmatrix} = \begin{bmatrix} s_{11}^E & 0 & 0 \\ 0 & s_{55}^E & 0 \\ -d_{31} & 0 & 1 \end{bmatrix}^{-1} \begin{bmatrix} 1 & 0 & -d_{31} \\ 0 & 1 & 0 \\ 0 & 0 & \varepsilon_{33}^T \end{bmatrix} \tag{A.16}$$

where

$$\overline{c}_{11}^E = \frac{1}{s_{11}^E},\ \overline{c}_{55}^E = \frac{1}{s_{55}^E},\ \overline{e}_{31} = \frac{d_{31}}{s_{11}^E},\ \overline{\varepsilon}_{33}^S = \varepsilon_{33}^T - \frac{d_{31}^2}{s_{11}^E} \tag{A.17}$$

Note that the transverse shear stress in Eq. (A.15) is corrected due to Timoshenko [73,74]

$$T_5 = \kappa \overline{c}_{55}^E S_5 \tag{A.18}$$

where κ is the shear correction factor [73-83].

A.4 Reduced Equations for a Thin Plate

If the thin monolithic structure is to be modeled as a thin plate (i.e. Kirchhoff plate), the normal stress through the thickness of the piezoceramic and the respective transverse shear stress components vanish:

$$T_3 = T_4 = T_5 = 0 \tag{A.19}$$

Equation (A.4) becomes

$$\begin{Bmatrix} S_1 \\ S_2 \\ S_6 \\ D_3 \end{Bmatrix} = \begin{bmatrix} s_{11}^E & s_{12}^E & 0 & d_{31} \\ s_{12}^E & s_{11}^E & 0 & d_{31} \\ 0 & 0 & s_{66}^E & 0 \\ d_{31} & d_{31} & 0 & \varepsilon_{33}^T \end{bmatrix} \begin{Bmatrix} T_1 \\ T_2 \\ T_6 \\ E_3 \end{Bmatrix} \tag{A.20}$$

which can be rearranged to give

$$\begin{bmatrix} s_{11}^E & s_{12}^E & 0 & 0 \\ s_{12}^E & s_{11}^E & 0 & 0 \\ 0 & 0 & s_{66}^E & 0 \\ -d_{31} & -d_{31} & 0 & 1 \end{bmatrix} \begin{Bmatrix} T_1 \\ T_2 \\ T_6 \\ D_3 \end{Bmatrix} = \begin{bmatrix} 1 & 0 & 0 & -d_{31} \\ 0 & 1 & 0 & -d_{31} \\ 0 & 0 & 1 & 0 \\ 0 & 0 & 0 & \varepsilon_{33}^T \end{bmatrix} \begin{Bmatrix} S_1 \\ S_2 \\ S_6 \\ E_3 \end{Bmatrix} \tag{A.21}$$

The stress – electric displacement form of the reduced constitutive equations becomes

$$\begin{Bmatrix} T_1 \\ T_2 \\ T_6 \\ D_3 \end{Bmatrix} = \begin{bmatrix} \overline{c}_{11}^E & \overline{c}_{12}^E & 0 & -\overline{e}_{31} \\ \overline{c}_{12}^E & \overline{c}_{11}^E & 0 & -\overline{e}_{31} \\ 0 & 0 & \overline{c}_{66}^E & 0 \\ \overline{e}_{31} & \overline{e}_{31} & 0 & \overline{\varepsilon}_{33}^S \end{bmatrix} \begin{Bmatrix} S_1 \\ S_2 \\ S_6 \\ E_3 \end{Bmatrix} \tag{A.22}$$

where

$$\overline{\mathbf{C}} = \begin{bmatrix} \overline{c}_{11}^E & \overline{c}_{12}^E & 0 & -\overline{e}_{31} \\ \overline{c}_{12}^E & \overline{c}_{11}^E & 0 & -\overline{e}_{31} \\ 0 & 0 & \overline{c}_{66}^E & 0 \\ \overline{e}_{31} & \overline{e}_{31} & 0 & \overline{\varepsilon}_{33}^S \end{bmatrix} = \begin{bmatrix} s_{11}^E & s_{12}^E & 0 & 0 \\ s_{12}^E & s_{11}^E & 0 & 0 \\ 0 & 0 & s_{66}^E & 0 \\ -d_{31} & -d_{31} & 0 & 1 \end{bmatrix}^{-1} \begin{bmatrix} 1 & 0 & 0 & -d_{31} \\ 0 & 1 & 0 & -d_{31} \\ 0 & 0 & 1 & 0 \\ 0 & 0 & 0 & \varepsilon_{33}^T \end{bmatrix} \tag{A.23}$$

Here, the reduced elastic, piezoelectric and permittivity constants are

$$\overline{c}_{11}^E = \frac{s_{11}^E}{\left(s_{11}^E + s_{12}^E\right)\left(s_{11}^E - s_{12}^E\right)} \tag{A.24}$$

$$\overline{c}_{12}^E = \frac{-s_{12}^E}{\left(s_{11}^E + s_{12}^E\right)\left(s_{11}^E - s_{12}^E\right)} \tag{A.25}$$

$$\overline{c}_{66}^E = \frac{1}{s_{66}^E} \tag{A.26}$$

$$\overline{e}_{31} = \frac{d_{31}}{s_{11}^E + s_{12}^E} \tag{A.27}$$

$$\overline{\varepsilon}_{33}^S = \overline{\varepsilon}_{33}^T - \frac{2d_{31}^2}{s_{11}^E + s_{12}^E} \tag{A.28}$$

For one-dimensional bending vibration of a thin plate without any torsional mode (due to the base excitation of a cantilever that is symmetric with respect to the central axis in *x*-direction), the relevant terms are Eqs. (A.24), (A.27) and (A.28).*

* Theoretically, the thin-plate parameters should be preferred for large width-to-thickness ratios to account for the Poisson effect. In the experimental case studies of this dissertation (Chapter 4), the thin-beam parameters given in Section A.2 are used as they exhibit substantially better agreement with the experimental results.

APPENDIX B

NUMERICAL DATA FOR MONOLITHIC PZT-5A AND PZT-5H PIEZOCERAMICS

PZT-5A and PZT-5H piezoceramics are the most commonly used engineering piezoceramics. Their typical three-dimensional piezoelastic properties can be found on the web [62] or in the literature [63] as given in Table B.1.

Table B.1 Three-dimensional properties of PZT-5A and PZT-5H

	PZT-5A	**PZT-5H**
s_{11}^E [pm^2/N]	16.4	16.5
s_{12}^E [pm^2/N]	-5.74	-4.78
s_{13}^E [pm^2/N]	-7.22	-8.45
s_{33}^E [pm^2/N]	18.8	20.7
s_{55}^E [pm^2/N]	47.5	43.5
s_{66}^E [pm^2/N]	44.3	42.6
d_{31} [pm/V]	-171	-274
d_{33} [pm/V]	374	593
d_{15} [pm/V]	584	741
$\varepsilon_{11}^T / \varepsilon_0$	1730	3130
$\varepsilon_{33}^T / \varepsilon_0$	1700	3400

In addition to these data, the mass densities of PZT-5A and PZT-5H are reported [62,63] as 7750 kg/m^3 and 7500 kg/m^3, respectively. The permittivity components at constant stress are given in Table B.1 in the form of the dielectric constants ($\varepsilon_{11}^T / \varepsilon_0$, $\varepsilon_{33}^T / \varepsilon_0$) where the permittivity of free

space is $\varepsilon_0 = 8.854$ pF/m [26]. The reduced constants for the Euler-Bernoulli and Rayleigh beam theories are obtained using Eq. (A.11) as listed in Table B.2 whereas those for the Timoshenko beam theory are obtained from Eqs. (A.17) as in Table B.3.

Table B.2 Reduced properties of PZT-5A and PZT-5H for the Euler-Bernoulli and Rayleigh beam theories

	PZT-5A	**PZT-5H**
$\overline{c}_{11}^{E}$ [MPa]	61.0	60.6
$\overline{e}_{31}$ [C/m^2]	-10.4	-16.6
$\overline{\varepsilon}_{33}^{S}$ [nF/m]	13.3	25.55

Table B.3 Reduced properties of PZT-5A and PZT-5H for the Timoshenko beam theory

	PZT-5A	**PZT-5H**
$\overline{c}_{11}^{E}$ [MPa]	61.0	60.6
$\overline{c}_{55}^{E}$ [MPa]	21.1	23.0
$\overline{e}_{31}$ [C/m^2]	-10.4	-16.6
$\overline{\varepsilon}_{33}^{S}$ [nF/m]	13.3	25.6

Table B.4 Reduced properties of PZT-5A and PZT-5H for the Kirchhoff plate theory

	PZT-5A	**PZT-5H**
$\overline{c}_{11}^{E}$ [MPa]	69.5	66.2
$\overline{c}_{12}^{E}$ [MPa]	24.3	19.2
$\overline{c}_{66}^{E}$ [MPa]	22.6	23.5
$\overline{e}_{31}$ [C/m^2]	-16.0	-23.4
$\overline{\varepsilon}_{33}^{S}$ [nF/m]	9.57	17.3

APPENDIX C

CONSTITUTIVE EQUATIONS FOR AN ISOTROPIC SUBSTRUCTURE

C.1 Three-dimensional Form of the Constitutive Equations for an Isotropic Material

The tensorial representation of the three-dimensional constitutive law for an isotropic substructure material is [53]

$$S_{ij} = \frac{1}{Y_s}\left[\left(1+\nu_s\right)T_{ij} - \nu_s T_{kk}\delta_{ij}\right] \tag{C.1}$$

where Y_s is the elastic modulus and ν_s is the Poisson's ratio (subscript s denotes the substructure). The expanded form of Eq. (C.1) can be given as

$$\begin{Bmatrix} S_1 \\ S_2 \\ S_3 \\ S_4 \\ S_5 \\ S_6 \end{Bmatrix} = \frac{1}{Y_s}\begin{bmatrix} 1 & -\nu_s & -\nu_s & 0 & 0 & 0 \\ -\nu_s & 1 & -\nu_s & 0 & 0 & 0 \\ -\nu_s & -\nu_s & 1 & 0 & 0 & 0 \\ 0 & 0 & 0 & 2\left(1+\nu_s\right) & 0 & 0 \\ 0 & 0 & 0 & 0 & 2\left(1+\nu_s\right) & 0 \\ 0 & 0 & 0 & 0 & 0 & 2\left(1+\nu_s\right) \end{bmatrix}\begin{Bmatrix} T_1 \\ T_2 \\ T_3 \\ T_4 \\ T_5 \\ T_6 \end{Bmatrix} \tag{C.2}$$

where the contracted notation is used and the shear strains are the engineering shear strains defined in Eq. (A.5).

C.2 Reduced Equations for a Thin Beam

If the elastic behavior of the thin substructure is to be modeled as a thin beam based on the Euler-Bernoulli or Rayleigh beam theory, the only non-zero stress component is T_1 so that

$$T_2 = T_3 = T_4 = T_5 = T_6 = 0 \tag{C.3}$$

Therefore, Eq. (C.2) simply reduces to

$$T_1 = Y_s S_1 \tag{C.4}$$

C.3 Reduced Equations for a Moderately Thick Beam

If the elasticity of the thin substructure is to be modeled as a moderately thick beam (based on the Timoshenko beam theory), the conditions on the stress are

$$T_2 = T_3 = T_4 = T_6 = 0 \tag{C.5}$$

Equation (C.2) can be rearranged to give

$$\begin{Bmatrix} T_1 \\ T_5 \end{Bmatrix} = \begin{bmatrix} Y_s & 0 \\ 0 & G_s \end{bmatrix} \begin{Bmatrix} S_1 \\ S_5 \end{Bmatrix} \tag{C.6}$$

Here, the shear modulus is defined in terms of the elastic modulus and the Poisson's ratio as

$$G_s = \frac{Y}{2(1+\nu_s)} \tag{C.7}$$

and the transverse shear stress in its corrected form [73-83] is

$$T_5 = \kappa G_s S_5 \tag{C.8}$$

C.4 Reduced Equations for a Thin Plate

If the elastic behavior of the substructure is modeled as a thin plate, the following stress components vanish:

$$T_3 = T_4 = T_5 = 0 \tag{C.9}$$

Equation (C.2) simplifies to

$$\begin{Bmatrix} S_1 \\ S_2 \\ S_6 \end{Bmatrix} = Y_s \begin{bmatrix} 1 & -\nu_s & 0 \\ -\nu_s & 1 & 0 \\ 0 & 0 & 2(1+\nu_s) \end{bmatrix} \begin{Bmatrix} T_1 \\ T_2 \\ T_6 \end{Bmatrix} \tag{C.10}$$

which can be rearranged to give stress components in terms of strain components as

$$\begin{Bmatrix} T_1 \\ T_2 \\ T_6 \end{Bmatrix} = \frac{Y_s}{1-\nu_s^2} \begin{bmatrix} 1 & \nu_s & 0 \\ \nu_s & 1 & 0 \\ 0 & 0 & (1-\nu_s)/2 \end{bmatrix} \begin{Bmatrix} S_1 \\ S_2 \\ S_6 \end{Bmatrix} \tag{C.11}$$

As far as one-dimensional bending vibration of a thin plate without any torsional mode is concerned (due to base excitation of a cantilever that is symmetric with respect to the central axis in *x*-direction), the relevant elastic term is the first element in Eq. (C.11).

APPENDIX D

ESSENTIAL BOUNDARY CONDITIONS FOR CANTILEVERED BEAMS

D.1 Euler-Bernoulli and Rayleigh Beam Theories

If the beam is clamped at $x = 0$ and free at $x = L$, the essential boundary conditions are defined at the clamped boundary as

$$w^0(0,t) = 0 \tag{D.1}$$

$$\left.\frac{\partial w^0(x,t)}{\partial x}\right|_{x=0} = 0 \tag{D.2}$$

$$u^0(0,t) = 0 \tag{D.3}$$

where $w^0(x,t)$ is the transverse displacement and $u^0(x,t)$ is the axial displacement of the neutral axis.

D.2 Timoshenko Beam Theory

The essential boundary conditions are given at the clamped end ($x = 0$) of a cantilevered Timoshenko beam as

$$w^0(0,t) = 0 \tag{D.4}$$

$$\psi^0(0,t) = 0 \tag{D.5}$$

$$u^0(0,t) = 0 \tag{D.6}$$

where $\psi^0(x,t)$ is the cross-section rotation.

APPENDIX E

ELECTROMECHANICAL LAGRANGE EQUATIONS BASED ON THE EXTENDED HAMILTON'S PRINCIPLE

This section summarizes derivation of the electromechanical Lagrange's equations from the extended Hamilton's principle. For the most general case [41], the total kinetic energy is given as a function of the generalized coordinates and their time derivatives:

$$T = T\left(q_1, q_2, ..., q_n, \dot{q}_1, \dot{q}_2, ..., \dot{q}_n\right) \tag{E.1}$$

The total potential energy and the internal electrical energy are functions of generalized coordinates only†

$$U = U\left(q_1, q_2, ..., q_n\right) \tag{E.2}$$

$$W_{ie} = W_{ie}\left(q_1, q_2, ..., q_n\right) \tag{E.3}$$

The first variations of Eqs. (E.1)-(E.3) are

$$\delta T = \sum_{k=1}^{n}\left(\frac{\partial T}{\partial q_k}\delta q_k + \frac{\partial T}{\partial \dot{q}_k}\delta \dot{q}_k\right) \tag{E.4}$$

$$\delta U = \sum_{k=1}^{n}\frac{\partial U}{\partial q_k}\delta q_k \tag{E.5}$$

$$\delta W_{ie} = \sum_{k=1}^{n}\frac{\partial W_{ie}}{\partial q_k}\delta q_k \tag{E.6}$$

The virtual work done by the generalized non-conservative forces (Q_k) is

$$\delta W_{nc} = \sum_{k=1}^{n} Q_k \delta q_k \tag{E.7}$$

The extended Hamilton's principle becomes

$$\int_{t_1}^{t_2}\left(\delta T - \delta U + \delta W_{ie} + \delta W_{nc}\right)dt = \int_{t_1}^{t_2}\sum_{k=1}^{n}\left[\left(\frac{\partial T}{\partial q_k} - \frac{\partial U}{\partial q_k} + \frac{\partial W_{ie}}{\partial q_k} + Q_k\right)\delta q_k + \frac{\partial T}{\partial \dot{q}_k}\delta \dot{q}_k\right]dt = 0 \tag{E.8}$$

† In the electromechanical Lagrange formulation given here, one of the generalized coordinates is the electrical across variable, i.e. the voltage output across the load.

with the auxiliary conditions $\delta q_k = 0$ ($k = 1, 2, ..., n$) at $t = t_1$ and $t = t_2$. Integration by parts is applied to the last term to give

$$\int_{t_1}^{t_2} \frac{\partial T}{\partial \dot{q}_k} \delta \dot{q}_k dt = \int_{t_1}^{t_2} \frac{\partial T}{\partial \dot{q}_k} \frac{d(\delta q_k)}{dt} dt = \frac{\partial T}{\partial \dot{q}_k} \delta q_k \Big|_{t_1}^{t_2} - \int_{t_1}^{t_2} \frac{d}{dt}\left(\frac{\partial T}{\partial \dot{q}_k}\right) \delta q_k dt = -\int_{t_1}^{t_2} \frac{d}{dt}\left(\frac{\partial T}{\partial \dot{q}_k}\right) \delta q_k dt \quad \text{(E.9)}$$

Using Eq. (E.9) in Eq. (E.8) gives

$$\int_{t_1}^{t_2} \sum_{k=1}^{n} \left[\frac{\partial T}{\partial q_k} - \frac{\partial U}{\partial q_k} + \frac{\partial W_{ie}}{\partial q_k} + Q_k - \frac{d}{dt}\left(\frac{\partial T}{\partial \dot{q}_k}\right) \right] \delta q_k dt = 0 \quad \text{(E.10)}$$

For the extended Hamilton's principle to hold for arbitrary virtual displacements, Eq. (E.10) reduces to the electromechanical Lagrange equations:

$$\frac{d}{dt}\left(\frac{\partial T}{\partial \dot{q}_k}\right) - \frac{\partial T}{\partial q_k} + \frac{\partial U}{\partial q_k} - \frac{\partial W_{ie}}{\partial q_k} = Q_k \quad \text{(E.11)}$$

where the dissipative effects can be represented as generalized non-conservative terms.